University of Cincinnati

Date: 12/1/2017

I, Dhananjay Radhakrishnan Subramaniam, hereby submit this original work as part of the requirements for the degree of Doctor of Philosophy in Aerospace Engineering.

It is entitled:

Role of Elasticity in Respiratory and Cardiovascular Flow

Student's name: **Dhananjay Radhakrishnan Subramaniam**

This work and its defense approved by:

Committee chair: Ephraim Gutmark, Ph.D.

Committee member: Shaaban Abdallah, Ph.D.

Committee member: Iris Gutmark-Little

Committee member: Mark Turner, Sc.D.

29132

Role of elasticity in respiratory and cardiovascular flow

A dissertation submitted to the

Graduate School

of the University of Cincinnati

in partial fulfillment of the

requirements for the degree of

Doctor of Philosophy (PhD)

in the Department of Aerospace Engineering and Engineering Mechanics

of the College of Engineering and Applied Science

by

Dhananjay Radhakrishnan Subramaniam

Master of Science (MS) Mechanical Engineering,

Rochester Institute of Technology, NY

Bachelor of Engineering (BE) Mechanical Engineering,

University of Pune, India

Committee Chair: Dr. Ephraim J. Gutmark

December 2017

Abstract

Interaction between a deformable elastic body and an internal or external fluid flow alters the flow pattern. This dissertation describes the effects of elasticity on flow in physiological scenarios. The first part of the thesis describes the influence of soft tissue compliance on flow in the upper airways of pediatric Down syndrome (DS) patients and adolescent Polycystic-Ovarian syndrome patients with obstructive sleep apnea (OSA). Computational fluid dynamics (CFD) of airflow is performed in pre and post-operative geometries of the DS pediatric airway to evaluate effectiveness of a surgery and address the importance of including the subject-specific tissue compliance. A tube law approach and a novel image analysis method are then presented to evaluate the circumferential variation in airway compliance for DS patients. An iterative finite element method is then described to non-invasively estimate patient-specific mechanical properties of the upper airway in these patients. The estimated mechanical properties for a single patient are applied to simulate airway obstruction during inspiratory airflow, before and after surgery. Sensitivity to different flow variables is analyzed and an operating map is created to establish the relationship between tissue elasticity and volumetric airflow. The necessity for performing fluid-structure interaction (FSI) in PCOS subjects with OSA is illustrated through a series of strain maps of upper airway tissue. An inverse methodology based on FSI simulations is described to characterize the soft-palate stiffness in these subjects. Differences in pre and post-operative airflow patterns and tissue motion in a PCOS patient are described using computational modeling and compared with the same for a healthy individual.

The second part of the study describes computational FSI modeling of aortic blood flow in Turner syndrome (TS). A continuous measurement tool is developed to automatically compute the longitudinal variation in maximum aortic diameter. Patient-specific, three-dimensional

geometric analysis of the aorta is then performed to evaluate localized changes in aorta morphology. A quasi-steady FSI modeling approach is described to estimate hemodynamic and biomechanical functional indices of cardiovascular disease in TS. Patterns of swirling flow, wall shear stress, aorta wall pressure, vessel wall displacement and mechanical stresses are compared for healthy and diseased aortas. The proposed computational technique is then applied to determine longitudinal changes in functional variables for multiple patients. The influence of including the aortic sinus is then addressed to obtain improved predictions of the spatial locations that are most vulnerable to progressive dilatation and vessel wall tear. FSI simulations of aortic blood flow with subject-specific flow boundary conditions and vessel wall stiffness derived from imaging is performed for individualized risk stratification in TS. A FSI methodology employing improved outflow conditions is then presented for TS patients and subjects diagnosed with aortic dissection. A longitudinal comparison of functional measures is presented for 2 TS subjects including the aortic root geometry, using a decoupled FSI methodology. Temporal variations in flow-induced shear and mechanical stress are then assessed using transient blood flow simulations. Finally, the influence of vessel wall thickness and blood rheology on functional indices is estimated in different aortic anomalies observed in TS.

Acknowledgements

I would like to thank my academic advisor, Professor Ephraim Gutmark for giving me this excellent opportunity to pursue my PhD research in an interdisciplinary field of study. I wish to convey my sincere gratitude to him for his encouragement, patience and guidance throughout my doctoral studies. I am indebted to him for his advice that has helped me improve my research abilities, written and presentation skills.

I would like to thank Dr. Iris Gutmark-Little for giving me the opportunity to work on the project involving aortic anomalies in Turner syndrome patients and for her encouragement, time and discussions. I am extremely grateful to Dr. Goutham Mylavarapu and Dr. Jie Chen for their mentorship during my PhD studies, to Dr. Liran Oren for providing research funding in the final year of study and office space at the Department of Otolaryngology-Head and Neck Surgery and to Dr. Charles Farboz De Luzan for his help and discussions. My discussions with Dr. Mylavarapu have significantly contributed to my understanding of fluid-structure interaction modeling using the Ansys software and in the development of my skills in image-based computational modeling. I would like to thank Professor Shaaban Abdallah and Professor Mark Turner for agreeing to be on my dissertation committee.

I am extremely thankful to all my research collaborators including Dr. Raouf Amin, Dr. Sally Shott, Dr. Robert Fleck, Keith McConnell, Dr. Claus Gravholt, Dr. Krisitian Mortensen, Dr. Steffen Ringgaard and Dr. Christian Trolle for their time, discussions and support. I would like to thank Dr. Raanan Arens and Dr. Mark Wagshul from the Albert Einstein College of Medicine for providing flow data and medical images of sleep apnea patients with polycystic ovarian syndrome.

I am thankful to my lab mates at the Department of Otolaryngology-Head and Neck Surgery and colleagues in the Gas Dynamics and Propulsion Lab including Bhupatindra, Vijay and William for their friendship, discussions and help. I would like to thank Hari, Kiran, Seezan, Abha, Divya, Shatrunjai, Sun, Sudhir, Gopi, Sreekara and Preeti for their friendship and making my graduate life in Cincinnati memorable.

I would like to convey my deepest gratitude to my father Dr. S Radhakrishnan, mother Ananthalakshmi Radhakrishnan and my sister Dr. Kirthi Radhakrishnan for their unconditional love and unwavering support, that has helped me achieve my academic objectives. They have motivated me to work hard and achieve higher goals throughout my graduate studies. I would also like to thank my aunt Dr. Kumari Santosh, cousins (Vidya, Srihari and Sadashiv Santosh, Ram V. Krishnan and his family) for their help and support.

I would like to acknowledge financial support from the National Institutes of Health (NIH) Grant R01HL105206-01, University Research Council (URC), Department of Aerospace Engineering and Engineering Mechanics and Bryan Medical Inc., for providing research funding and University of Cincinnati for the University Graduate Scholarship (UGS) that covered my tuition throughout my PhD studies. I would also like to acknowledge GyroTools LLC, Zurich, Switzerland for providing an evaluation version of the GTFlow software for phase-contrast MR image processing.

Contents

Figures

Tables

Chapter 1

Introduction

1.1 *Pharyngeal Airway Anatomy*

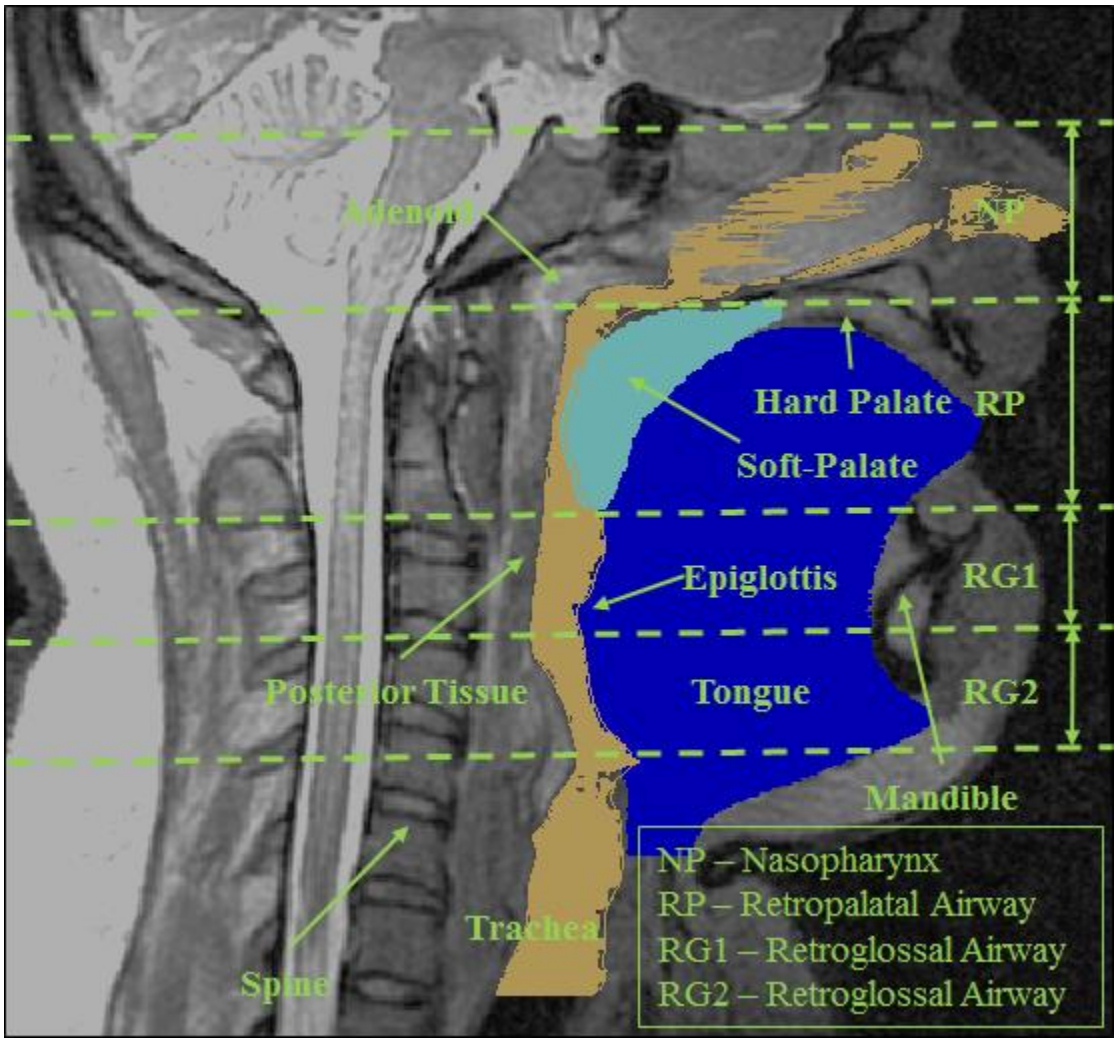

Figure 1.1: Anatomy of the human airway in the mid-sagittal plane (Note: Tongue – blue, Soft-Palate – cyan, Airway – yellow).

The human respiratory system has several functions including transport of air, conditioning, humidification, filtering, olfaction, phonation and deglutition [1]. The upper respiratory tract is

located outside the chest cavity and the lower respiratory tract is located inside the chest cavity. Figure 1.1 indicates the details of the human airway, including surrounding tissue and bony structures in the mid-sagittal plane. Details regarding anatomical plane definitions are given in Appendix A. The nasopharynx (NP) extends from the nostrils to the posterior end of the hard palate. The retropalatal (RP) or velopharyngeal airway extends from the choanae to the tip of the soft-palate (indicated in cyan in Fig.1.1). The retroglossal (RG) or oropharyngeal airway can be divided into two regions: RG1 – tip of the soft palate to the tip of epiglottis, RG2 – tip of epiglottis to base of the tongue. It should be noted that the trachea corresponds to the lower airway and is outside the domain of interest for the present study.

The pharynx includes the RP and RG airways as defined earlier and is the most compliant section of the upper airway. The pharyngeal airway is surrounded by soft-tissue including the tongue, soft-palate, posterior-wall mucosa, lateral tissue, fat-pads and blood vessels [1]. Bony or hard-structures including the mandible, hard palate and spine support the softer structures. The hard and soft-structures interact with one another in a complex manner during breathing. Diseases or disorders of the upper airway vary by location and range from mild to severe. For instance, rhinitis is caused by inflammation of the nasal cavity. Tonsillitis or inflammation of the lingual tonsils obstructs the pharyngeal airway. Sleep-disorders including snoring, obstructive sleep apnea and upper airway resistance syndrome cause cessation of airflow in the pharynx. Other respiratory infections of the upper airway include pharyngitis (i.e. inflammation of the throat) and laryngitis (inflammation of the vocal cords).

1.2 *Obstructive Sleep Apnea (OSA)*

Sleep is accompanied by the physiologic relaxation of the muscles and soft tissue supporting the upper airway. Obstructive sleep apnea (OSA) involves partial or complete occlusion of the

pharyngeal airway during sleep. Frequent collapse of the pharynx followed by arousal to maintain airway patency is a characteristic of sleep apnea [2]. OSA decreases cognitive performance and increases daytime sleepiness. Upper airway patency is controlled by a balance between forces in the soft tissue tending to dilate the airway and forces that promote airway collapse [3]. Airway narrowing or occlusion is likely to occur when the latter exceeds the former (Fig. 1.2). The degree of relaxation varies across individuals and determines the severity of OSA. Increased collapsibility of the upper airway in snorers and subjects with OSA could be attributed to neuromuscular deficiencies of the pharyngeal dilator muscles and abnormal stiffness of airway structures [4]. Upper airway obstruction in OSA has been frequently reported to occur in the velopharynx [5]. Negative pressures generated during inspiratory airflow have been hypothesized to result in upper airway collapse [6]. Additionally, narrow airways enhance the probability of sleep apnea [7].

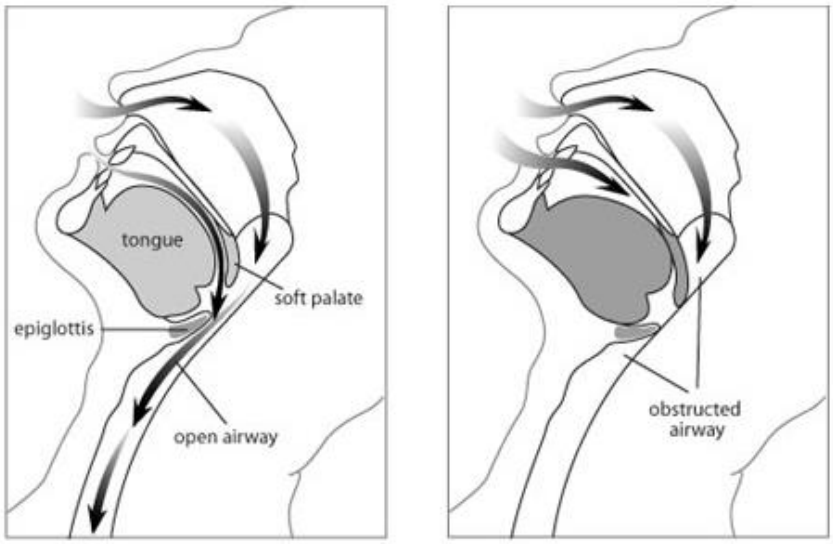

Figure 1.2: Normal inhalation compared to sleep-disordered breathing

(Source: http://www.irvinedentalcare.com/images/sleep-apnea-diagram.jpg).

Polysomnography (PSG) [8] and tracheal breath sound analysis [9] are some of the diagnostic tests for OSA. Several factors including ethanol ingestion [10] and presence of fat deposits [11]

result in reduced muscle tone during sleep thereby leading to an imbalance between dilatory and collapsing forces. The difference between the extraluminal tissue pressure and intraluminal pressure is known as transmural pressure. The value of transmural pressure at which the pharyngeal airway collapses completely is known as the critical transmural pressure (P_{crit}) [12]. Apnea-Hypopnea Index (AHI) is defined as the number of events per hour, when the airflow reduces (hypopnea) or ceases to flow (apnea) in the upper airway [13]. Both, P_{crit} and AHI indicate the level of OSA severity.

Down syndrome (DS) is a genetic disorder affecting 1 in every 1000 live births [14]. Hypotonia, obesity, midface hypoplasia, relative macroglossia, and excessively large tonsils and adenoids are some of the factors influencing pharyngeal airway collapse in DS pediatric patients [15]. Decrease in airway muscular tone associated with anesthesia and sedation [16], as well as the supine position, leading to changes in the anatomic positioning of structures that surround the airway is more pronounced in children with DS than other children. Polycystic ovarian syndrome (PCOS) is an endocrine disorder that affects 5 to 10% of pre-menopausal women and is often characterized by oligoanovulation and chronic hyperandrogenism [17]. It has been suggested previously that high androgen levels increase visceral fat in these subjects, subsequently resulting in obesity and sleep-disordered breathing [2]. However, high prevalence of OSA in PCOS [17] cannot be fully explained by elevated body mass index (BMI) or hyperandrogenism [18]. Treatment options for sleep apnea include non-invasive and invasive methods to increase airway caliber [4]. Non-invasive options include nasal continuous positive airway pressure (nCPAP) and surgical procedures such as removal of the tonsils and adenoids (T&A) are commonly used first line treatments for sleep apnea [4, 19]. For OSA persistent after T&A, other procedures such as midline posterior glossectomy and mandibular advancement are available.

Surgical treatment options have only had moderate success rates [15, 20]. Improved understanding of the interaction between flow-induced forces and upper airway soft tissue can guide treatment and improve surgical outcomes.

1.3 *Aorta Anatomy*

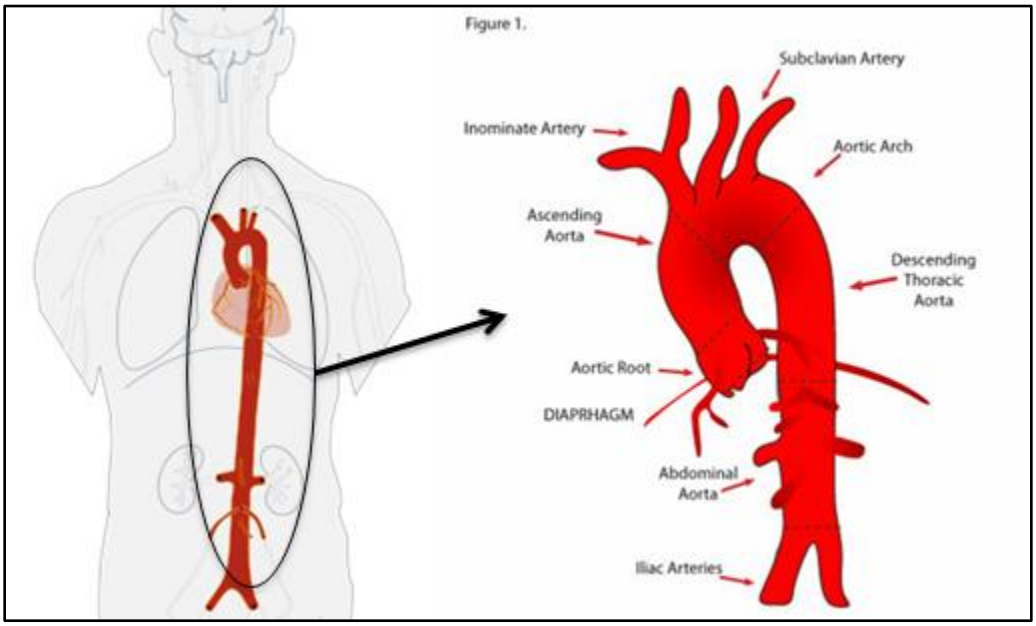

Figure 1.3: Anatomy of a normal aorta

(Source: http://en.wikipedia.org/wiki/Aorta, http://www.aortarepair.com/anatomy.html).

The aorta is the largest artery in the human body and is responsible for supplying oxygenated blood to other parts of the body through systemic circulation. The aorta is divided into different sections as indicated in Figure 1.3. The thoracic aorta runs from the heart to the diaphragm and is the focus of the present study. The portion of the aorta from the diaphragm extending downward in the abdomen to the aortic bifurcation is known as the abdominal aorta. The thoracic aorta primarily consists of the ascending aorta, aortic arch, descending aorta and daughter vessels in the transverse section. Blood flows superiorly (see Appendix A for anatomic directions) from the heart into the ascending aorta and encounters a sharp turn in the aortic arch. Blood then travels inferiorly in the descending segment. The ascending aorta originates at the opening of the aortic

valve in the left ventricle of the heart. At the root or base of the ascending aorta, the aorta lumen has three pockets between the cusps of the aortic valve in normal subjects and is referred to as the aortic sinuses or sinuses of the Valsalva. The right and left coronary arteries originate from the corresponding sinuses and supply the heart. Coronary arteries are not present on the posterior sinus. The ascending aorta transitions to the aortic arch at the pericardial reflection. The aortic arch which loops over the left pulmonary artery and bifurcation of the pulmonary trunk has three major branches from proximal to distal: innominate artery (IA), left-common carotid artery (LCCA) and left-sublcavian artery (LSCA). The IA supplies blood to the right side of the head and neck and the LCCA and LSCA supply blood to the left side of the same regions. The aortic arch transitions to the descending section at the level of the intervertebral disc.

1.4 *Turner syndrome*

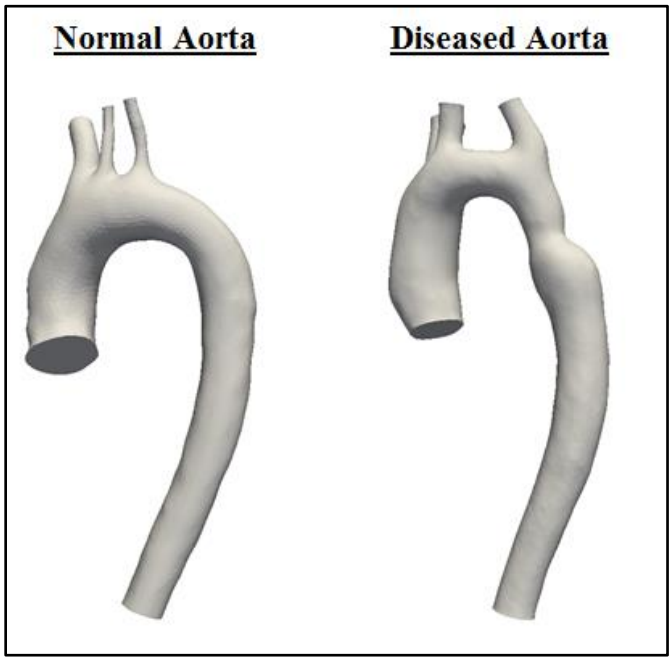

Figure 1.4: Comparison between normal and TS aorta.

Turner syndrome (TS) is a relatively common chromosomal disorder that affects approximately 1 in 2000 live born girls [21]. Common characteristics include short stature, webbed neck, and

gonadal dysgenesis [22]. Congenital heart defects, ischemic heart disease, hypertension and stroke are risks associated with the disorder [23]. Coarctation of the aorta (CoA) [24], bicuspid aortic valve (BAV) [25], aortic root dilatation [26] and elongation of the transverse aorta (ETA) [27, 28] are some of the heart defects observed in TS. The probability of aortic dissection is elevated in women and girls with TS [29] and can result in patient mortality. Hypertension in TS patients is thought to increase the probability of dissection, potentially related to progressive dilatation of the aorta [30]. Figure 1.4 compares the aorta geometries (excluding the root) for healthy individuals and TS patients. As can be seen, the ascending aorta for the diseased case is slightly dilated, followed by ETA and CoA, compared to the normal aorta. Tearing of the inner aorta wall results in aortic dissection. Blood flows through the tear causing the inner and outer layers of the aorta wall to separate. Rupture of the false lumen (i.e. blood-filled channel) can result in patient mortality. Aortic dissection is classified as Type-A or Type-B dissection as indicated in Figure 1.5. Type-A dissection involves the ascending aorta and/or the transverse section and in rare occasions the descending aorta. Type-B dissection occurs entirely in the descending aorta.

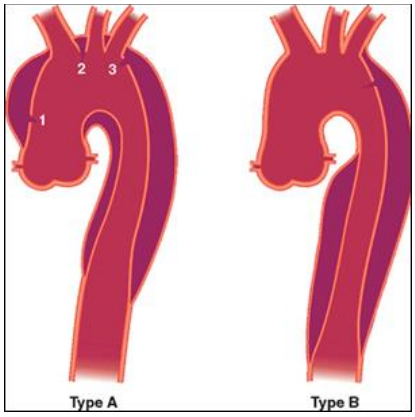

Figure 1.5: Type A and Type B Aortic Dissection (Source: http://www.clevelandclinicmeded.com).

Cardiovascular magnetic resonance (CMR) imaging is the gold standard for non-invasive assessment of thoracic aortic disease [28]. CMR has been employed previously in TS, to identify

structural aortic anomalies and to follow aortic changes over time [31]. Aortic diameter and growth are the only acknowledged risk markers for aortic dissection [32], and assessment of aortic dimensions using CMR is thereby the established clinical practice for cardiovascular risk assessment in TS [32]. Normative data on aortic dimensions in TS [33] is based on evaluation of aortic diameter at discrete measurement positions, with major determinants including aortic valve morphology, age and blood pressure [34, 35]. A statistical model, based on gold standard CMR, has been developed to assist in the identification of patients with rapid growth in aortic dimensions and to improve clinical decision making [32]. Consistent with international guidelines [36, 37], two-dimensional aortic measurements are performed manually or semi-automatically at discrete locations along the length of the thoracic aorta. Cardiovascular risk assessment in Turner syndrome (TS), particularly for aortic dissection, unfortunately has remained inadequate, which is due to a limited understanding of the pathophysiology of thoracic aortic disease in TS with aortic events occurring at dimensions classified as normal according to conventional size criteria [38].

1.5 *Dissertation Objectives*

Computational fluid dynamics (CFD) assumes a rigid pharynx and has been employed previously to calculate airflow patterns and variations in luminal pressure distribution in patients with OSA [39-41] and normal subjects [42]. CFD studies to obtain dynamic pressure and shear stress distributions on the pharyngeal wall in pre and post-operative airways have also been performed previously [43, 44]. Studies involving CFD have also described the use of 'virtual' surgery to assess the efficacy of a surgical procedure prior to application [45]. Flow-structure interaction (FSI) simulations have been performed to assess the effect of airflow on the passive deformation of soft tissue to simulate snoring [46] and velopharyngeal narrowing [47].

Furthermore, FSI studies have also been employed to calculate airflow patterns in the pharynx following nasal surgery [48] and mandibular advancement [49]. Besides, the aforementioned studies both limited the analysis to the soft-palate or the mucosal layer supporting the pharynx and employed elasticity values that were not subject-specific. Three-dimensional (3D) computational structural mechanics (CSM) simulations of pharyngeal narrowing in human [50] and animal models [51] with subject-specific mechanical properties have been performed for static pressure loads that do not consider the effects of airflow.

This dissertation firstly extends the CFD analysis described previously [45] to include virtual surgeries of the tongue, soft-palate and tonsils (Chapter 3) for pediatric subjects with DS. Compliance of the upper airway and its correlation with different severity measures of OSA (Section 1.2) is determined for sleep apnea patients with DS, using two novel approaches based on pressure-area relations (Chapter 4.1 and 4.2). A novel, iterative CSM method is presented to estimate patient-specific Young's modulus of soft-tissue in the upper airway in these subjects (Chapter 4.3). In order to illustrate the importance of including airway compliance to guide surgical treatment in DS patients, the derived values of tissue elasticity are employed for simulations of pre and post-operative airway narrowing in response to airflow (Chapter 4.4). The sensitivity of flow-induced deformations of upper airway tissue to flow variables and the importance of the same in predicting the outcome of the surgery are discussed. A deformable image registration methodology is presented in Chapter 5 to map the flow-induced shear strain of airway tissue in PCOS subjects with OSA. A computational FSI approach is presented to iteratively compute the biomechanical properties of the soft palate in these patients (Chapter 5.2). Virtual surgery is performed to estimate pre and post-operative airflow and tissue displacements in PCOS (Chapter 5.3).

Manual measurements of aortic caliber are labor-intensive and require multi-plane reformatting to obtain accurate measurements in the correct imaging planes [34], and techniques have been proposed to obtain aorta diameter as well as cross-sectional area automatically in order to overcome some of the challenges in obtaining precise geometric measures using the manual method [52, 53]. In addition, three-dimensional (3D) geometric markers employed previously to characterize abdominal aortic aneurysms [54] may further improve the ability to describe thoracic aortic disease in TS. Thinning of the vessel wall has been attributed to localized velocity gradients resulting from blood flow [55] and subsequent rupture of the vessel wall is dependent on arterial stiffness and cardiac pressure [56]. CFD simulations for patients with CoA, ETA and BAV have been performed previously in idealized [57] and patient-specific aorta geometries [58, 59] to characterize blood flow patterns in patients with TS. Computational structural mechanics (CSM) has been adopted to simulate vessel wall failure in response to static blood pressure in patients with BAV [55, 60], ascending and abdominal aortic aneurysms [61-64] and connective tissue disorders such as Marfan syndrome [65, 66]. However, the effects of blood flow were not considered in these aforementioned studies. Fully coupled flow structure interaction (FSI) simulations of the aorta can describe the effects of flow on vessel deformation and the influence of arterial wall motion on hemodynamic variables [67, 68].

This dissertation firstly describes a novel automatic method to measure aorta diameter continuously to overcome the shortcomings of the manual approach. The proposed approach is validated by comparing the dimensions with the same obtained using the manual method. Three-dimensional (3D) measures of aortic geometry are then presented and a registration scheme is proposed to estimate the 3D visit-to-visit change in aorta morphology (Chapter 6). Quasi-steady, fully-coupled FSI simulations of blood flow in healthy and TS aortas are presented to compare

the differences in hemodynamic variables obtained using CFD and to introduce biomechanical variables that could potentially serve as indicators of aortic dissection (Chapter 7.1). The study is then extended to evaluate longitudinal changes in hemodynamic and biomechanical variables in TS patients (Chapter 7.2). The importance of including the aortic sinus for cardiovascular risk assessment in TS is described for several aortic phenotypes observed in Turner syndrome (Chapter 8). Imaging of aortic flow patterns in healthy and TS subjects is then introduced and simulations of aortic blood flow using subject-specific flow boundary conditions and aortic wall stiffness is described in Chapter 9.1. A FSI methodology with improved outlet boundary conditions is then described to compute flow and mechanical variables for patients diagnosed with aortic dissection (Chapter 9.2). The FSI methodology described in Section 9.2 is then utilized to evaluate hemodynamic and biomechanical functional variables in normal subjects and TS patients using subject-specific flow conditions derived from imaging (Chapter 9.3). Chapter 10.1 introduces an alternative 2-way decoupled FSI methodology for longitudinal comparison of flow and biomechanical variables in Turner syndrome using the enhanced outflow boundary conditions described in Chapter 9.2. Chapter 10.2 describes transient simulations of blood flow in a compliant aorta and introduces functional variables based on temporal variations in the aortic flow and displacement of the vessel wall that could potentially provide an improved description of vessel wall failure in TS. The influence of variation in aortic wall thickness along the vessel length and shear-thinning behavior of blood, on cardiovascular risk factors is then studied for some commonly observed aortic phenotypes in TS (Chapter 10.3).

Chapter 2

Theory

2.1 *Computational Fluid Dynamics (CFD)*

2.1.1 *Governing Equations*

Physiological flows are associated with low Mach numbers (<<0.3) and can thereby be approximated as incompressible. The governing equations for fluid flow include conservation laws of mass, momentum and energy and are known as the Navier-Stokes (NS) equations. The NS equations for incompressible flow of a Newtonian fluid expressed in Einstein notation are as follows:

$$\frac{\partial v_i}{\partial x_i} = 0$$
$$\rho_f \frac{\partial v_i}{\partial t} + \rho_f v_j \frac{\partial v_i}{\partial x_j} = -\frac{\partial P}{\partial x_i} + \mu \frac{\partial^2 v_i}{\partial x_i \partial x_j} \tag{2.1}$$

Where v is the flow velocity, μ is the dynamic viscosity, P is the fluid pressure and ρ_f is the density of the fluid. Computational fluid dynamics (CFD) employs numerical techniques to solve the NS equations for a given set of boundary conditions.

2.1.2 *Modeling Turbulence*

Flow regimes are classified as laminar, transitional or fully turbulent. The ratio of inertial forces to viscous forces is the Reynolds number (*Re*):

$$Re = \frac{\rho_f V L}{\mu} \tag{2.2}$$

Where V and L are the characteristic velocity and length scale respectively. Description of the flow regime as laminar or turbulent is expressed using the Reynolds number. Characteristics of

turbulent flows include irregularity, diffusivity, high *Re*, dissipation and three-dimensional fluctuating vorticity. The physical quantity describing the size of the large-energy containing eddies is referred to as the integral length scale. The Taylor and Kolgomorov scales correspond to the inertial sub-range and dissipation range respectively. Direct numerical simulations (DNS) resolve all length scales (i.e. integral, Taylor and Kolmogorov) and are associated with high computational costs. Large-eddy simulations (LES) are computationally less expensive than DNS and involve resolution of integral and Taylor length scales. Resolution of only the large-energy containing eddies can be achieved by obtaining solution to the Reynolds-Averaged Navier-Stokes (RANS) equations. The RANS equations for incompressible flow are expressed in Einstein notation as follows:

$$\begin{aligned}
&\frac{\partial \overline{v_i}}{\partial x_i} = 0 \\
&\rho_f \left(\frac{\partial \overline{v_i}}{\partial t} + \overline{v_i} \frac{\partial \overline{v_j}}{\partial x_i} \right) = -\frac{\partial \overline{P}}{\partial x_i} + \frac{\partial}{\partial x_i}\left(2\mu S_{ij} - R_{ij}\right) \\
&S_{ij} = \frac{1}{2}\left(\frac{\partial \overline{v_i}}{\partial x_j} + \frac{\partial \overline{v_j}}{\partial x_i} \right) \\
&R_{ij} = \rho_f \overline{v_i' v_j'}
\end{aligned} \tag{2.3}$$

where, S_{ij} is the mean rate of strain tensor, R_{ij} is the Reynold's stress tensor and the bar denotes time average. Turbulence models have been developed to close the RANS equations since the Reynolds-Stress tensor is a non-linear term that necessitates additional modeling. Equation 2.1 or 2.3 is discretized and solved using finite difference (FD), finite volume (FV) or finite element (FE) methods. In this dissertation, governing equations for fluid flow are solved using two commercial finite-volume solvers namely ANSYS Fluent and ANSYS CFX (Ansys Inc., Canonsburg, PA) [1]. It should be noted that ANSYS Fluent employs a cell-centered finite volume approach, where all flow variables are stored at the centroid of the control volume. On

the other hand, ANSYS CFX adopts a cell-vertex approach, where all flow variables are stored at the nodes of the control volumes.

2.2 *Computational Structural Mechanics (CSM)*

Computational structural mechanics (CSM) solves the discretized form of the governing equations for the deformable structure. For dynamic or static equilibrium of an elastic solid:

$$\begin{aligned} \sigma_{ij,j} + f_i - \rho_s a_i &= 0 \\ \sigma_{ij,j} + f_i &= 0 \end{aligned} \tag{2.4}$$

Where f is the body force, a is the acceleration (not applicable for statics), σ is the Cauchy stress tensor and ρ_s is the density of the solid. The governing equation for the tissue domain in dynamic equilibrium, is derived using the principal of virtual work,

$$\begin{aligned} &\int_V \sigma_{ij}\delta E_{ij} dV + \int_V \rho_s \frac{du_i}{dt}\delta u_i dV = \int_V f_i \delta u_i dV + \int_S \sigma_{ij} n_j \delta u_i dS \\ &\sigma_{ij} = \frac{1}{J_{el}} F \bullet \frac{\partial W}{\partial E} \bullet F^T \\ &E = \frac{1}{2}\left(F^T F - I\right) \end{aligned} \tag{2.5}$$

where, u is the displacement, F is the deformation gradient tensor, E_{ij} is the Green-Lagrangian strain tensor and W corresponds to the strain energy function. It should be noted that the small strain tensor is applicable only to linear elastic materials whereas the Green-Lagrangian strain tensor is applicable to hyperelastic materials such as elastomers and soft biological tissue, characterized using non-linear stress-strain curves. Solutions to Eqn 2.5 can be obtained by either referencing all variables with respect to the initial configuration or the last calculated configuration. The former approach is referred to as the total Lagrangian formulation and the latter is also known as the updated Lagrangian formulation. In this dissertation, the discretized updated Lagrangian formulation [69] of the governing equations are solved using either

commercial finite element codes namely ANSYS Mechanical (ANSYS Inc., Canonsburg, PA) and ABAQUS (Simulia, Dassault Systems, Providence, RI) or the publicly available FEBio (finite elements for biomechanics) code [70] developed by the Scientific Computing and Imaging Institute at University of Utah.

2.3 *Fluid-Structure Interaction (FSI)*

2.3.1 *Overview & Applications*

Fluid-structure, fluid-solid or flow-structure interaction (FSI) is the interaction between an internal or surrounding fluid flow and an elastic or rigidly moving solid body [71]. These interactions are either steady or unsteady. Unsteady or oscillatory interactions involve repetitive stressing of the solid body, followed by relaxation of the stresses when the flow-induced forces are reduced, over several cycles. Design of civil and aircraft structures often need to consider the effects of FSI. Oscillatory fluid-structure interactions in bridges, turbine blades and aircraft wings can lead to failure due to fatigue. Fluid-structure interactions are observed in several physiological scenarios [72] including blood flow in the heart [73], compliant vessels, arteries and aneurysms [74], cerebrospinal fluid flow [75] and airflow in the trachea [76].

2.3.2 *Computational FSI Modeling*

Computational fluid-structural interaction is a multi-physics problem that has been made possible through advances in the field of CFD and CSM. FSI modeling can be classified based on the treatment of the moving interface. Accordingly, conformal and non-conformal mesh methods have been developed. In conformal mesh methods, the computational grid for the flow domain adapts to the shape of the deforming structural domain. The most well-known example of the conformal grid method that has been implemented in commercial continuum mechanics codes is the Arbitrary Lagrangian Eulerian method (ALE) [77]. The ALE method permits the

arbitrary motion of mesh or grid points relative to the reference frame while accounting for convection of the points. The governing equations for the incompressible Navier-Stokes equations described in equation 2.1 are in the Eulerian frame of reference. In the ALE form, the material velocity v is replaced by the convective velocity c as follows:

$$c = v - \hat{v} \tag{2.6}$$

Where $\hat{v}$ is the mesh velocity. At the fluid-solid interface, the following boundary conditions are defined:

$$\begin{aligned} \sigma_{ij}^{s} \bullet \boldsymbol{n}_s + \sigma_{ij}^{f} \bullet \boldsymbol{n}_f &= 0 \\ v_i &= \frac{\partial u_i}{\partial t} \end{aligned} \tag{2.7}$$

where v is the flow velocity, u is the structural displacement, σ^s and σ^f correspond to the solid and fluid stress tensors, $\boldsymbol{n}_s$ and $\boldsymbol{n}_f$ denote the outward normal vectors corresponding to the structural and flow domains. The ALE method is easy to implement, has low computational costs and is accurate [78]. For the ANSYS Fluent flow solver, mesh motion is achieved either using a spring analogy [68], a diffusion based scheme [79] or by assuming the flow domain to behave as a linear elastic solid. The diffusion based scheme is the only available option in ANSYS CFX and the same was adopted for all FSI computations described using the two flow solvers. An appropriate remeshing strategy involving a section of or the entire computational domain is desirable since large rotations or translations of the solid or inhomogeneous motion of the grid points may cause the mesh to 'fold' or become ill-shaped. It should be noted that while the ANSYS Fluent solver provides the user the option to remesh the flow domain, this feature is currently unavailable in the ANSYS CFX code. Computational costs in the ALE method are

significantly higher for problems involving frequent remeshing. Besides, transfer of solutions from a degenerated mesh to the new mesh may result in some loss in accuracy.

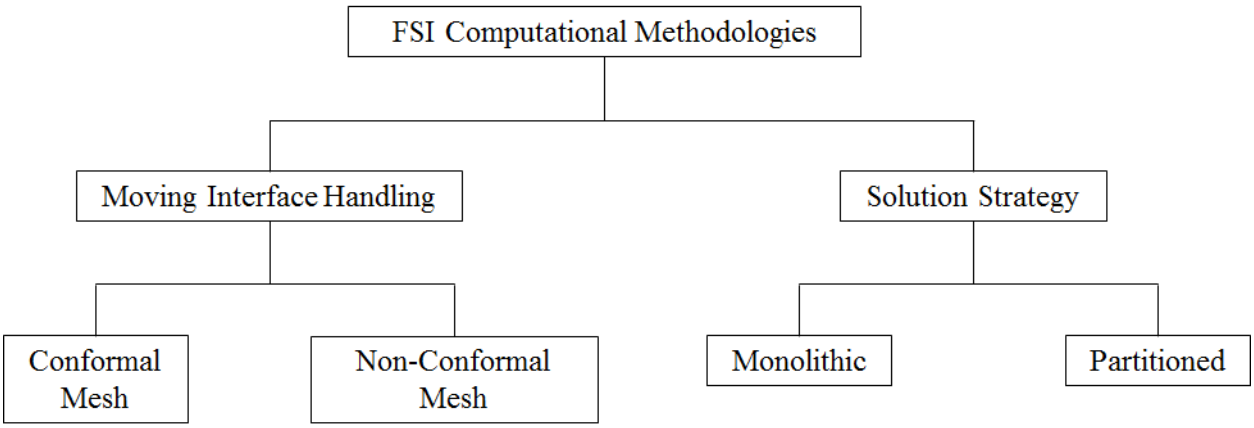

Figure 2.1: Classification of FSI modeling methods.

In non-conformal mesh methods, the grid for the flow domain is independent of the shape of the deforming structure. The immersed boundary method [80] is a widely employed non-conformal mesh method. The method consists of a fixed grid for the flow domain with an immersed set of non-conforming body boundary points, that are mutually interconnected by an elastic law [78]. Local body forces are defined using a Dirac delta function at these boundary points to achieve fluid-solid interaction. A kinematic constraint is imposed by these body forces so that the velocity of the solid point is coupled to that of the fluid point.

Classification of FSI modeling methods can also be based on the solution strategy. Monolithic and partitioned approaches have been proposed to solve FSI problems. The equations governing the flow and structure are solved simultaneously in the monolithic approach using a single solver. In the partitioned approach, equations governing flow and displacement of the solid are solved separately with two distinct solvers. Unlike the monolithic approach which necessitates a specialized code, the partitioned approach can couple existing flow and structural solvers. However, a stable coupling code is necessary in partitioned or segregated solvers. Figure

2.1 summarizes the classification of FSI methodologies based on the handling of the moving interface and solution strategy. The partitioned approach can be further categorized as loosely or strongly-coupled [81]. Loose coupling is often suitable for stiff structures where the motion of the solid domain in response to flow loads is relatively small. FSI simulations for aeroelasticity have been achieved previously using loosely-coupled procedures [82]. Loosely-coupled methods integrate the fluid and solid governing equations independently, once every coupling step. Low computational costs and simplicity are the advantages of this approach. However, special treatments are required to address numerical instability and temporal inaccuracies caused by spurious energy production. Convergence of interface properties at each coupling step is ensured using predictor-corrector sub-iterations for strongly coupled approaches. This increases the complexity and computational costs. Strong coupling is typically necessary for physiological problems where the density of the solid is comparable to the fluid [83] and the structures are extremely compliant.

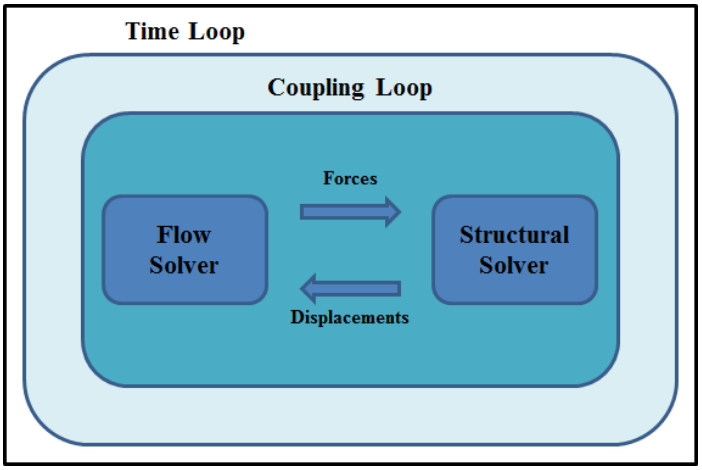

Figure 2.2: Flow-chart describing partitioned solution to FSI problem using ANSYS.

Fluid-structure interaction simulations can also be classified as one-way or two-way FSI analysis. The unidirectional analysis involves a CFD simulation followed by mapping of flow-induced forces to estimate deflections of the solid. The bidirectional method involves passing

forces from the flow solver to the structural solver to calculate displacements and relaying the displacements back to the flow-solver to update the flow variables [67]. Both coupled and uncoupled two-way analyses have been adopted in this dissertation. Bidirectional, fully-coupled FSI analysis is performed using the segregated approach where the ANSYS Mechanical solver is coupled either to ANSYS CFX using the MFX coupling code [84] or to ANSYS Fluent using the System Coupling code [46]. Figure 2.2 summarizes the segregated solution approach employed by the ANSYS Multiphysics software. Additional details regarding the two-way analysis are described in Chapters 5, 7-10.

2.3.3 *Segregated FSI Solver Validation*

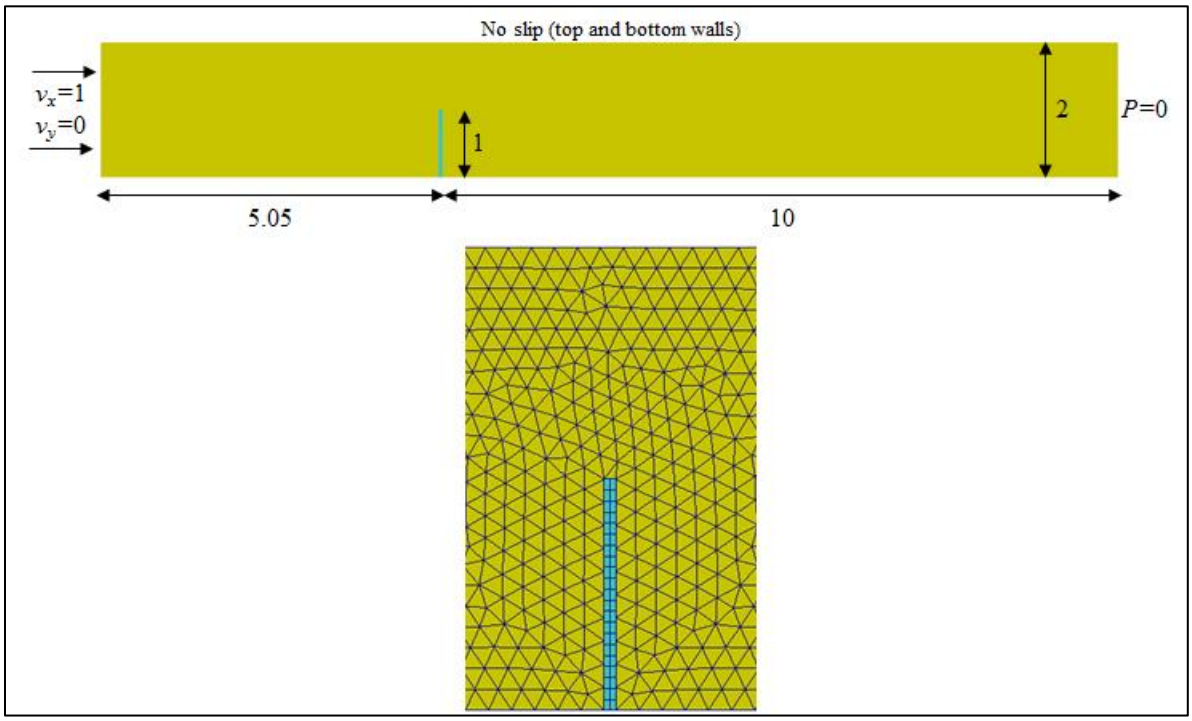

Figure 2.3: Definition of problem for validation of segregated solvers (Note: Flow domain – yellow, solid domain – blue, channel fixed at the bottom). Overview of mesh for flow (tri) and structural (quadrilateral) domains.

Validation of the segregated FSI solvers involving ANSYS Fluent and ANSYS CFX was performed by comparing the displacements and flow profiles for a numerical benchmark problem involving uniform channel flow over a slender obstacle [85]. Geometry for the flow and

structural domains were created using GAMBIT 2.4 (ANSYS Inc., Canonsburg, PA). The channel was meshed using triangular elements in GAMBIT and extruded by a single element to generate a prismatic mesh for the flow domain. It should be noted that this step was necessary since the ANSYS Multiphysics software is capable of solving FSI problems only in 3D. A quadrilateral mesh was adopted for the elastic flap and extruded by a single element to generate a hexahedral mesh for the structural domain. Figure 2.3 summarizes the details regarding the geometry, boundary conditions, fluid and solid meshes for the benchmark problem. A uniform flow corresponding to 1 m/s was prescribed at the inlet. A zero static pressure boundary condition was prescribed at the outlet. The fluid-solid interface, top and bottom walls were considered to be no-slip boundaries. Additionally, a symmetry boundary condition was imposed on the walls normal to viewing plane. Fluid density and viscosity were 1 kg/m^3 and 0.001 Pa-s respectively. The bottom face of the elastic obstacle was constrained in all directions and a FSI boundary condition was prescribed at the interface with the flow domain. The flap was modeled as a 50 cm thick, linear elastic solid capable of undergoing large deformations (i.e. geometric non-linearity was considered in the model). Elastic modulus, Poisson's ratio and density of the flap were 60000 Pa, 0.45 and 1000 kg/m^3 respectively. Constant velocity, bi-directional FSI simulations were performed for a time period of 4s, with a pseudo-time step of 0.1 s. Flow was assumed to be laminar since the maximum Reynolds number was less than 2000.

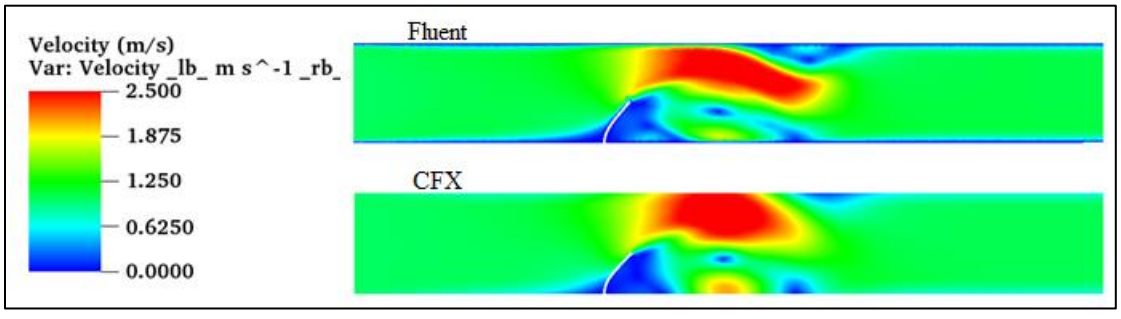

Figure 2.4: Comparison of flow patterns obtained using ANSYS Fluent and ANSYS CFX.

Figure 2.4 compares the flow patterns obtained using ANSYS Fluent and ANSYS CFX at the end of the simulation (i.e. t=4s). As can be seen, similar flow patterns were obtained downstream of the deformed flap for both solvers. A high velocity jet and a flow recirculation region were observed downstream of the obstacle in the proximity of the top and bottom walls respectively. The difference in the maximum magnitude of flow velocity was less than 5 percent. Differences were primarily observed in the size and strength of the recirculation region on the top wall and the length of the jet downstream of the obstacle. These differences could be attributed to multiple factors including variability in the control volume approach and mesh motion described in Sections 2.1 and 2.3.2. Figure 2.5 summarizes the displacements of the flap obtained using the two segregated solvers. The largest displacement was observed at the top surface of the flap. The difference in the maximum displacement obtained using ANSYS Fluent and ANSYS CFX was 7 percent. Differences in the simulated displacements could arise from variability in the interpolation of forces at the fluid-solid interface and mesh motion. Furthermore, the displacements obtained in this study were in excellent agreement with the same obtained in previous studies [85].

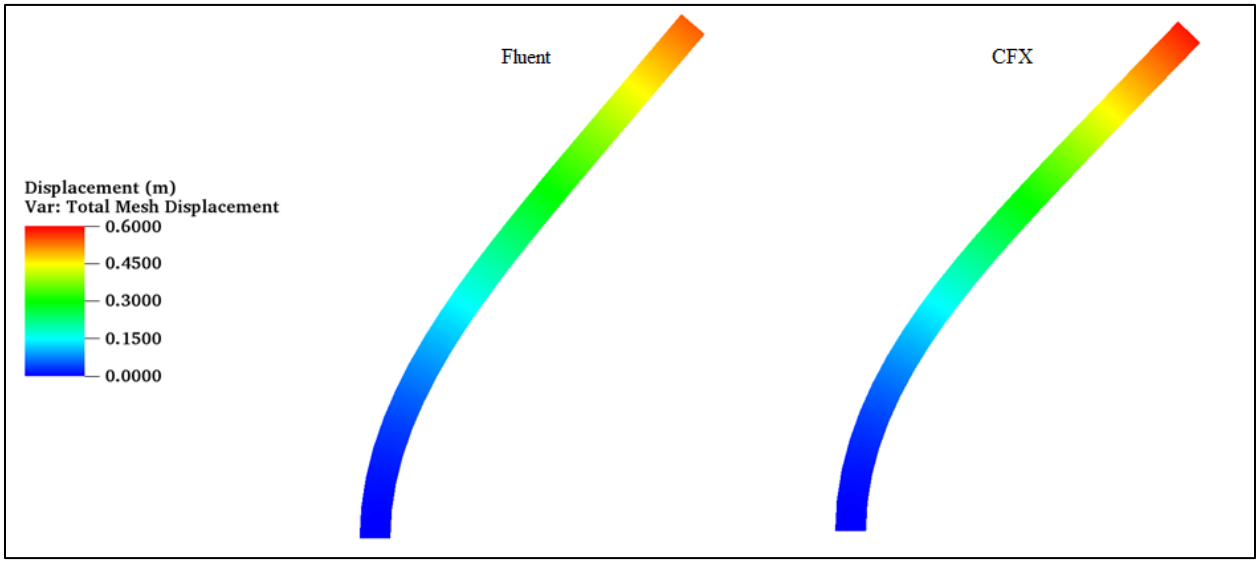

Figure 2.5: Comparison of displacement contours obtained using ANSYS Fluent and ANSYS CFX.

Chapter 3

Computational Flow Modeling for Sleep Apnea in DS

Results from this chapter were presented at the 2015 Triological Combined Sections Meeting Coronado, CA and subsequently resulted in a second author publication in the Otolaryngology – Head and Neck Surgery journal.

In this chapter, virtual surgery [45] is employed to evaluate surgical outcomes in 10 pediatric DS patients [86]. The following general steps were adopted for all subjects:

1.Anatomically accurate, 3D geometries of the pharyngeal airway geometry were reconstructed using magnetic resonance imaging (MRI).

2. The shape of the airway was virtually altered to replicate the actual surgery.

3.CFD simulations were performed to compute airflow resistance for the baseline (pre-operative) and virtually altered (post-operative) airways.

The following sections describe the methodology and results for two representative subjects.

3.1 *Methods*

3.1.1 *Airway Reconstruction and Virtual Surgery*

Respiratory gated MRI scans were obtained for a 21 year old male subject with severe OSA (AHI: 34, P_{crit}: -1.6 cm H_2O) and a 5 year old male patient with moderate OSA (AHI: 5.7, P_{crit}: -3.3 cm H_2O) following anesthesia. The study was approved by the Institutional Review Board (Cincinnati Children's Hospital Medical Center 2010-2332). 120 sagittal MR scans were imported into the Mimics (Materialise Inc., Plymouth, MI) image processing software for geometric reconstruction of the airway. 3D geometry of the airway including the nasal airway, pharynx and trachea was generated using a thresholding algorithm (Patient 1: lower threshold gray value (GV): 0, upper threshold gray value (GV): 100; Patient 2: lower threshold gray value

(GV): 0, upper threshold gray value (GV): 150). Coarse geometries of the airway were smoothed to remove surface artifacts. Outlets to the airway were identified at the nostrils and an inlet was created below the larynx in the trachea. Two ear/nose/throat (ENT) surgeons performed a 'virtual surgery' (VS) on each baseline airway model, to reflect changes in airway geometry and mirror those from the actual operations performed. Accordingly a midline posterior glossectomy (MPG) corresponding to 4.5 millimeters of tongue tissue and a palatoplasty corresponding to 8 mm of soft-palate tissue were 'virtually' removed to replicate the actual surgery in Patient 1 [45, 86]. Similarly, 5 mm of lingual tonsils and tongue were 'virtually' removed to reflect the surgery in patient 2. Pre and post-operative airways are indicated in Figure 3.1. It should be noted that the surface of the soft-palate was moved forward to make contact with the posterior surface of the tongue following MPG. Profiles of the virtually altered post-operative airways were confirmed with the ENT surgeons prior to CFD modeling.

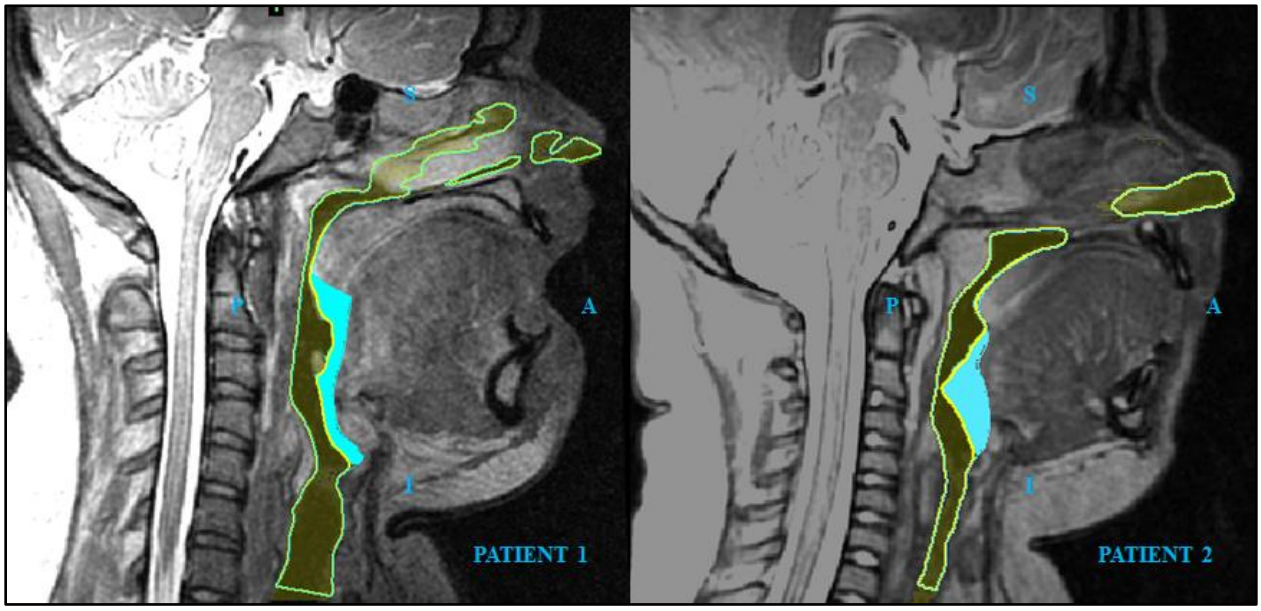

Figure 3.1: Mid-sagittal MR image indicating baseline airway (highlighted in yellow) and virtual surgery (highlighted in blue). (Note: Soft tissue excision increases the airway volume at the site of removal, A – Anterior, P – Posterior, I – Inferior, S – Superior).

3.1.2 *Mesh Generation and Boundary Conditions*

Geometries for the baseline and virtual surgery cases were then exported to 3-Matic (Materialise Inc., Plymouth, MI) to generate surface meshes. The airway surface was locally refined at the narrow cross-sections in the retropalatal airway for patient 1 and in the retroglossal airway for patient 2 using 3-Matic (Fig 3.2) to obtain better resolution of the flow in these regions. Surface meshes were then exported to the ANSYS T-Grid (ANSYS Inc., Canonsburg, PA) meshing software to generate volume meshes. Tetrahedral cells were generated for the airway and were recombined to create polyhedral cells. We adopted polyhedral cells for the flow domain to obtain homogenous distribution of wall quantities and increase the speed of solution convergence [87]. Figure 3.2 illustrates the local mesh refinement for the two patients analyzed in this study.

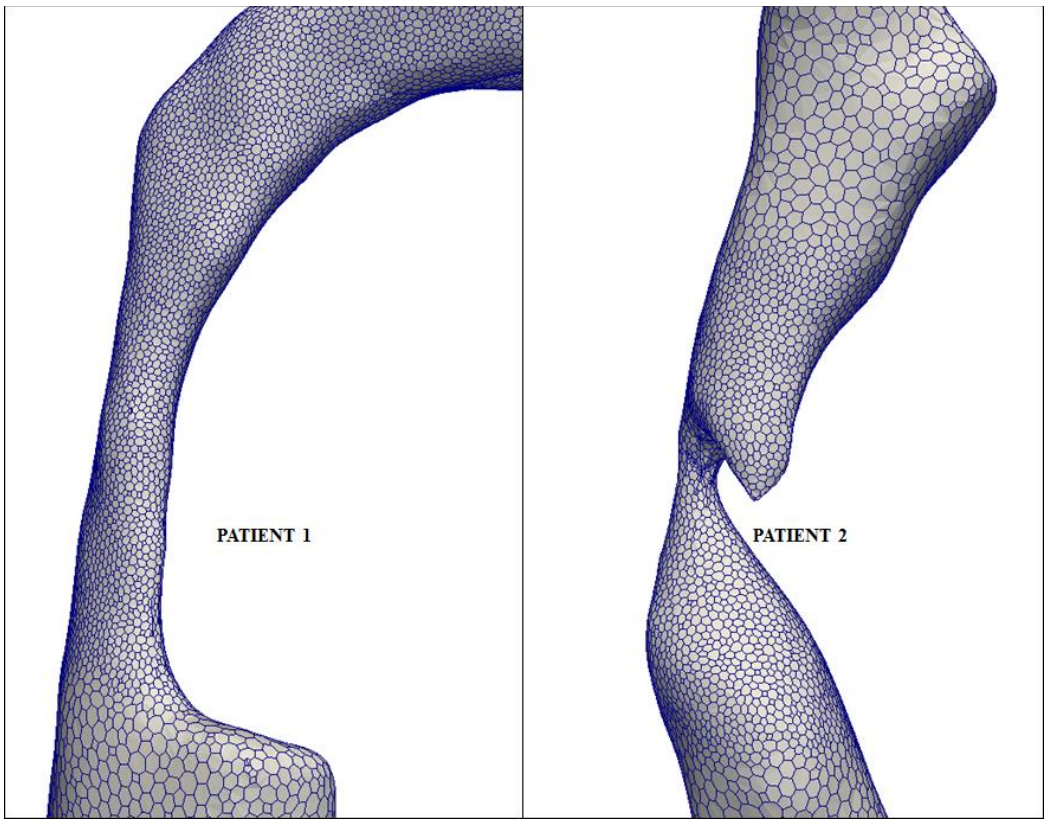

Figure 3.2: Local mesh refinement in the velopharynx (patient 1) and oropharynx (patient 2).

A mesh convergence study was performed until the change in airway resistance was negligible. Table 3.1 summarizes the optimum mesh resolutions employed in this study for the baseline and virtual surgery geometries corresponding to the two patients.

Table 3.1: Discretization (number of nodes) of pre and post-operative airways.

	Patient 1	**Patient 2**
Pre-Operative	849000	328000
Post-Operative	1010000	340000

The local Reynolds number of flow in the human upper airway has been reported to be approximately 6000 [45] for physiological flow rates and corresponds to a transitional or fully turbulent regime. CFD [40] and FSI simulations of airflow in the pharynx [49] have been performed previously using the incompressible Reynolds-Averaged Navier Stokes (RANS) (Eqn. 2.3). The k-ω model has been validated previously using pressure measurements in a mechanical model of the upper airway [40]. Besides, the k-ω SST model provides an improved description of flows involving curved boundary-layers and adverse pressure gradients [88]. The SST model was thereby employed for all pre and post-operative airflow simulations. The y+ value (i.e. height of the cell adjacent to the wall) was ensured to be ≤ 1 as indicated in Figure B in the Appendix for pre and post-operative airways. A no-slip boundary condition was set at the airway wall. Simulations were performed for an expiratory flow of 10 liters per minute [45]. A second-order upwind scheme was used to discretize the momentum and turbulence terms. Pressure-velocity coupling was achieved using a pressure-based coupled formulation [89]. An ambient pressure boundary condition (i.e. zero gauge pressure) was applied at the nostrils. A turbulence intensity corresponding to 5 percent and a 1 mm length scale was adopted in all simulations [86]. The resistance of the upper airway (UAR) was computed as follows:

$$\text{UAR} = \frac{\Delta P}{Q} \qquad (3.1)$$

where, ΔP is the pressure drop between the choanae and base of tongue and Q is the volumetric airflow. All simulations were performed using ANSYS Fluent and post-processing of flow variables was performed using Paraview (Kitware Inc., Clifton Park, NY).

3.2 *Results & Discussion*

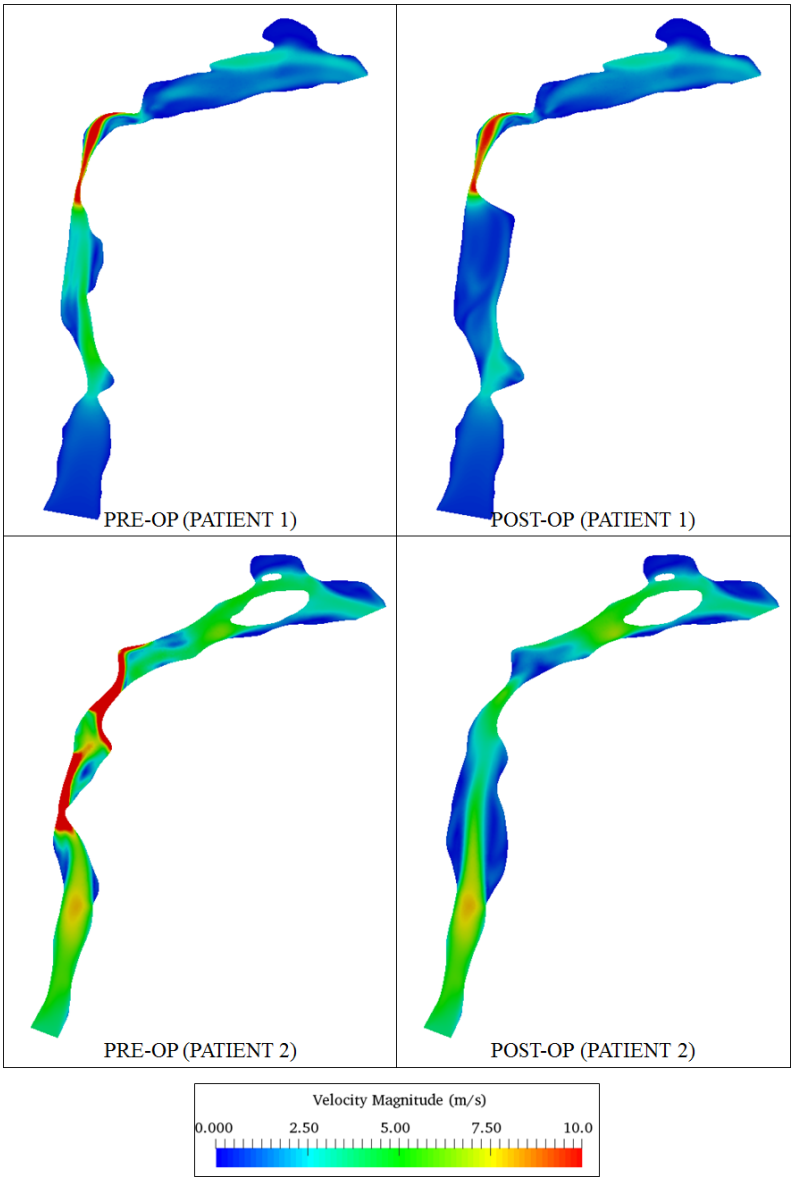

Figure 3.3: Velocity profiles in the mid-sagittal plane for the pre and post-operative airways.

Figure 3.3 summarizes the pre and post-operative flow patterns for the two patients analyzed here. As indicated for patient 1, a strong jet was formed in the velopharynx which was nearly unchanged between the pre and post-operative scenarios. A larger stagnation flow region was formed downstream of the laryngeal jet in the post-operative case. For patient 2, a strong jet was formed in the larynx, oropharynx and velopharynx for the baseline airway. The laryngeal jet velocity was similar for the virtual surgery case.

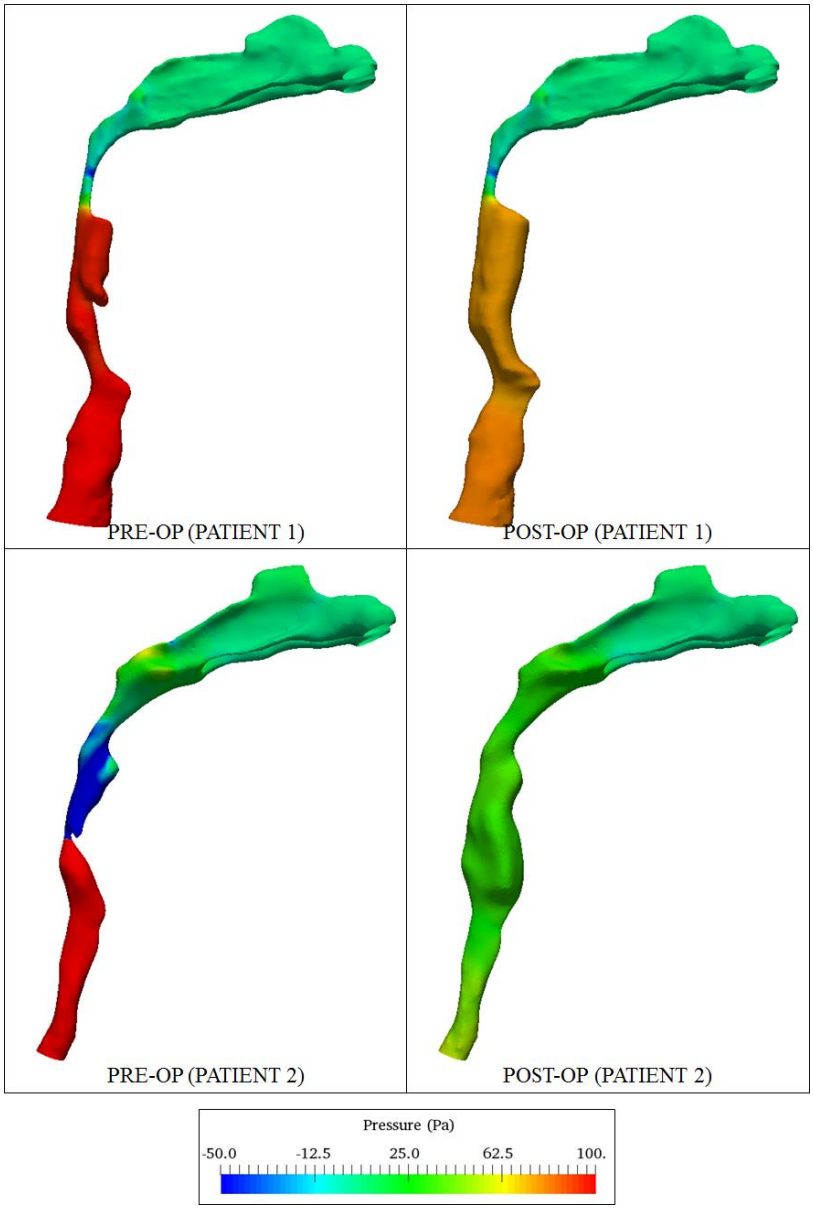

Figure 3.4: Airway wall pressure distribution for the pre and post-operative airways.

Stagnation flow regions were observed on the anterior and posterior wall of the retroglossal airway. Flow in the velopharynx was also relatively slower compared to the baseline case. The flow patterns in the nasal airway were nearly unchanged for both patients since the airways were not modified in this section. Surface maps of airway wall pressure for the baseline and virtual surgeries are indicated in Figure 3.4 These surface maps enable to visualize regions that are most likely to collapse during breathing.

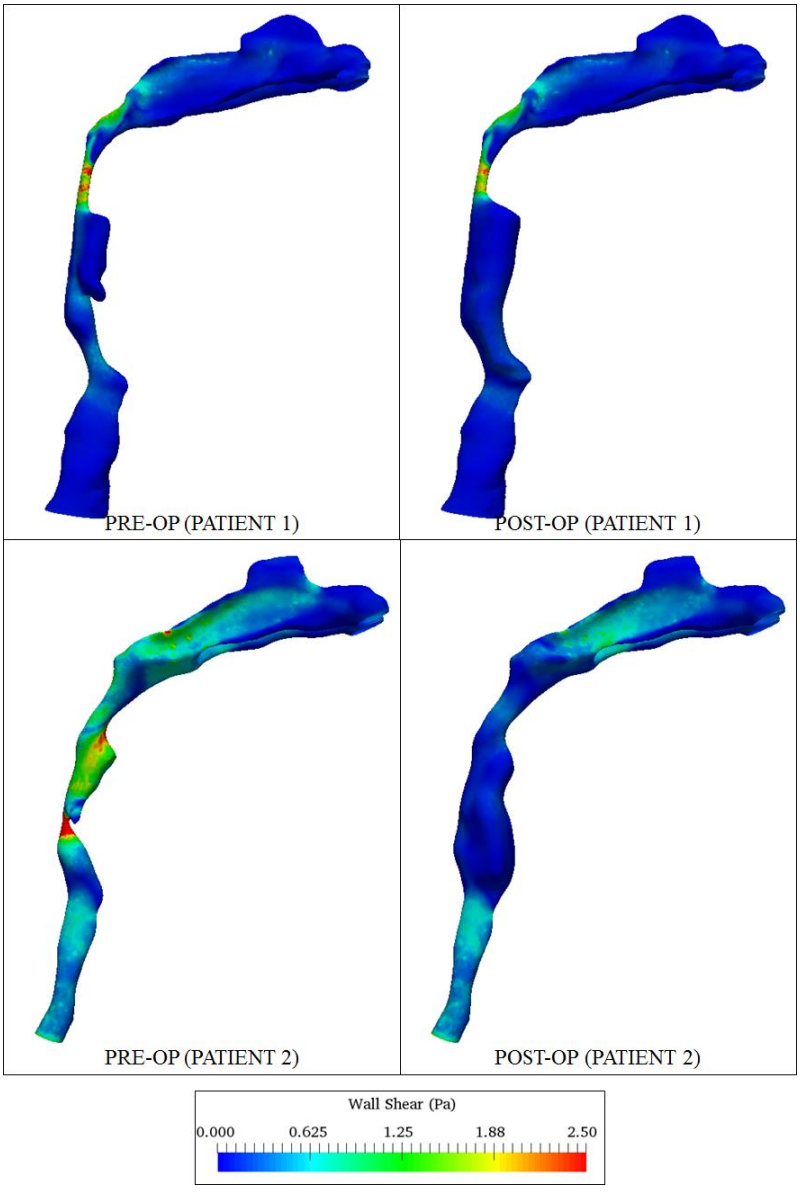

Figure 3.5: Shear stress distribution for the pre and post-operative airways.

For patient 1, airway wall pressure decreased to a minimum in the velopharynx following which the pressure recovered in the nasal airway. A similar pattern was observed for the virtual surgery case. However, the value of minimum pressure at the constriction in the velopharynx decreased by approximately 22 percent, indicating that the post-operative airway was less likely to collapse during expiration. The minimum pressure was distributed throughout the oropharynx (between the tip of the soft palate and epiglottis) in the baseline airway for patient 2. This value decreased by 99 percent following virtual lingual tonsillectomy. Figure 3.5 indicates maps of shear stress distribution for patient 1 and 2, before and after surgery.

The wall shear stress (WSS) was greatest in the velopharynx for patient 1 and at the tip of the epiglottis for patient 2. The magnitude of peak WSS was unchanged for patient 1. The same decreased by 99 percent for patient 2. WSS values were nearly an order of magnitude smaller than the values of airway wall pressure. This observation further emphasizes that flow-induced pressure forces are largely responsible for airway dilation and collapse as compared to shear induced forces. Besides, low WSS is beneficial in the upper airway since shear stresses can cause irritation to soft tissue as noted previously [45]. Table 3.2 summarizes the UAR values for the baseline and virtual surgery cases and the corresponding pre and post-operative oAHI (obstructive Apnea-Hypopnea Index).

Surgeries were defined as successful if the postoperative oAHI was less than or equal to 5 events per hour. The same was considered as a failure if the aforementioned criterion was not satisfied. Additionally, agreement between the modeled and actual surgeries was defined to be present when the direction of change in oAHI and UAR were similar [86]. The post-operative AHI following the actual surgery for patient 1 increased indicating that the surgery was unsuccessful. The CFD simulation on the other hand predicted a successful surgical outcome.

For patient 2, a successful outcome was predicted by CFD simulations and the actual operation. However, the change in the UAR was much larger (99 percent) as compared to the reduction in AHI (47 percent). One of the major factors contributing to the disagreement between the actual treatment outcome and virtual surgery could be attributed to the exclusion of airway tissue compliance in the numerical model. Less significant reasons contributing to these discrepancies include approximation of the post-operative airway shape, variability in the amount of tissue resected and smoothing of airway geometries. These observations emphasize the need to estimate the compliance of the upper airway and elasticity of supporting tissue in order to obtain better predictions from the numerical model.

Table 3.2: Summary of pre and post-operative airway resistance (All resistance values in Pa/lpm).

Patient No.	Pre-Op oAHI	Post-Op oAHI	Baseline UAR	VS UAR	Agreement
1	34	44	10.8	7.5	No
2	5.7	2.7	132.5	0.3	Yes

Chapter 4

Compliance Estimation and Modeling Airway Occlusion

Results from this chapter were presented at the 2014 American Thoracic Society Conference, San Diego, CA, 2014 BMES Annual Meeting, San Antonio, TX, 2015 BMES Annual Meeting, Tampa, FL and published in two first author manuscripts in the Annals of Biomedical Engineering journal and a third first author manuscript in the Journal of the Mechanical Behavior of Biomedical Materials.

Published quantification of pharyngeal soft tissue elasticity is based on in-vivo experiments in cadavers or computational studies of simplified anatomical models, using prior knowledge of the various forces, boundary conditions and resulting displacements. The major limitation of these studies is cadaver tissue properties are very different than live tissue and it varies significantly between individuals. Recently, a non-invasive method based on MR elastography has been developed to estimate material properties of the tongue and soft palate in control subjects [90] and OSA patients [91] during wakefulness. Elastography, which involves either ultrasound (US) or MR, is capable of quantifying small tissue displacements (1 μm or less) [92]. Airway wall stiffness has been characterized previously using the Starling resistor or 'tube law' model [93-96]. Localized estimates of change in airway elasticity at two arbitrary locations in the velopharynx and oropharynx have been described using patient-specific compliance curves [97, 98].

This chapter firstly models the interaction between the transmural pressure and the pharyngeal airway as a collapsible section [99]. The tube law is employed to evaluate the pharyngeal stiffness and non-linearity of airway elasticity in pediatric OSA patients with DS (Section 4.2). Section 4.4 describes a novel method to estimate variations in airway elasticity

along its periphery. The method involves upper airway segmentation of MR images, estimating radial displacements of the airway wall (interface between the airway lumen and soft tissue) in discrete angular sectors, and normalizing the computed displacements by the appropriate transmural pressure difference and radius of equivalent circle [100]. A novel methodology is then developed and validated to iteratively estimate the patient specific mechanical properties of airway tissue from numerical simulations of airway collapse (Section 4.6). The study tests the hypothesis that pharyngeal airway stiffness and Young's modulus of airway tissue in sedated patients, decreases with increasing severity of OSA. Section 4.7 describes a computational methodology to simulate narrowing of the pharynx in a pediatric DS patient with OSA using patient-specific 3D geometries of airway tissue and corresponding stiffness values, in response to airflow. Sensitivity of tissue displacement to flow parameters and selection of material models is described. The importance of this analysis in guiding surgical procedures is then discussed. Finally, the significance of including tissue elasticity to obtain an improved correlation between the simulated surgery and actual treatment outcome is illustrated.

4.1 *Sleep Study and MR Imaging*

The diagnostic sleep and MR imaging studies described in this section were approved by the Institutional Review Board (IRB). Overnight polysomnography was performed on volunteer patients using a computerized system (Grass-Telefactor, Astro Med Inc., West Warwick, RI) to record electroencephalogram (EEG), electrooculogram, electromyogram, electrocardiogram, desaturation index and AHI [15]. A light anesthesia was provided by an anesthesiologist using dexmedetomidine, a sedative that reduces pharyngeal muscle tone and simulates natural sleep with minimal respiratory depression [101]. The anesthetic dose was patient specific and dependent on the subject's BMI [102]. MR images of the pediatric DS sleep apnea patients, with

AHI≥5 were obtained using a 1.5-THDxt MRI scanner (software version 16; General Electric), once adequate depth of anesthesia was attained. The patients were in a supine position with head and neck placed in a vascular coil. An adhesive tape was used to secure the subject's head to the vascular coil and minimize patient head motion [103]. The imaging sequence was a 3-dimensional (3D) fast spin echo with proton density weighting (CUBE). Specific parameters included echotrain length, 64; acquisition matrix, 256 by 256; slice thickness, 1.60 mm and slice interval, 0.80 mm. The scans were obtained during the peak expiratory breathing phase at three pressures: zero pressure (baseline) and two positive pressures (CPAP1, CPAP2). A modified BiPAP device (Phillips Respironics Inc.) was used to record normalized inspiratory flow rate and administer CPAP using a face mask approved by the IRB. It should be noted that the choice of CPAP2 was patient specific and was based on the collapsibility or size of the airway. The highest CPAP level was below complete elimination of flow limitation. Narrow or extremely floppy airways needed a higher mask pressure to maintain airway patency [104]. CPAP1 was a value of mask pressure greater than zero and approximately midway between baseline and CPAP2.

Exclusion criteria included: collapsed airway during baseline, paradoxical breathing, open oral airways, patient movement, or awakening during scan, and low quality scans that were not suitable for automated computer analysis. Patients included in the study depicted a reduction in the airflow channel, only with slight phase shifts in the abdominal and thoracic movements. On the other hand, patients who exhibited paradoxical breathing had thoracic and abdominal movement signals that were completely out of phase. In patients who awoke, the arousal did not follow the apneic event and therefore was not clinically significant. The arousal was recorded by a sleep technician and based on examination of body movements. The protocol to calculate P_{crit} of a patient under anesthesia includes gradual reduction of the mask pressure approaching

conditions of total collapse. P_{crit} was calculated by extrapolating to zero flow the linear portion of the curve relating the negative pressure to flow [12].

4.2 *Pharyngeal Compliance Using Tube-Law Theory*

The tube law was adopted to evaluate the pharyngeal compliance for 22 DS pediatric patients with sleep apnea. It should be noted that the sleep studies and imaging protocol described in Section 4.1 was extended to include these 22 pediatric patients (see Appendix C, Table C.1 for clinical history) for stiffness measurements.

4.2.1 *Airway Segmentation*

Airway boundaries of the baseline, CPAP1 and CPAP2 were identified in MR scans, using an in-house MATLAB based thresholding algorithm [105]. The algorithm was designed to read in an image and increase the contrast by mapping the intensity values to new values such that 1% of data was saturated at low and high intensities. After cropping to the region of interest, the grayscale image was converted to a binary image using a normalized threshold level of around 0.05. The airway was identified in the output binary image where all pixels with luminance greater than 0.05 were replaced with the value 1 and the remaining pixels were assigned a value of 0. Segmentation was performed using the axial scans from the hard palate to the base of tongue (Fig. 4.1a). The airway boundaries in the mid sagittal and mid coronal planes are shown in Figs. 4.1b and 4.1c, respectively, for the three pressures. The pixel values of the airway approximated as a polygon were converted to Cartesian co-ordinates using spatial transformations. The high spatial resolution of the axial image slices (512x512 pixels) enabled computation of the airway cross-sectional area by counting the pixels and multiplying by pixel area. The process was repeated for each axial image slice that is part of the pharynx, to obtain the variation in the cross-sectional area of the baseline and dilated airways along the airway length

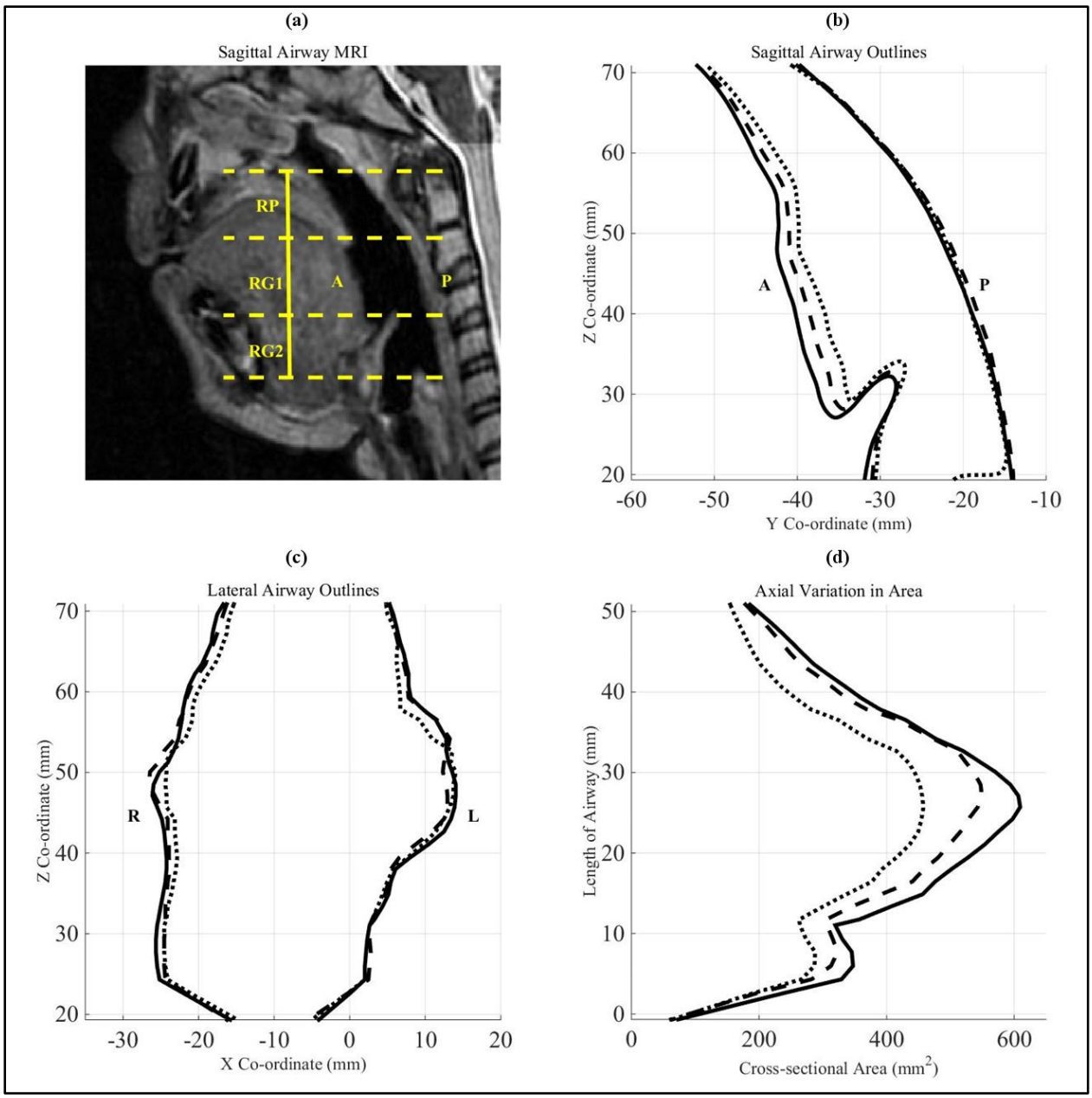

Figure 4.1: a) Extents of the pediatric pharyngeal airway and corresponding soft tissue domain (patient no. 13) in mid-sagittal MR image. Outline of the boundaries of the baseline (dotted) and dilated (dashed, solid) airways in b) mid-sagittal and c) coronal plane. d) Axial variation in cross-sectional areas in the pharyngeal airway corresponding to the baseline (dotted), CPAP1 (dashed) and CPAP2 (solid) (A – Anterior, P – Posterior, R – Right, L – Left, RP - Hard palate to soft palate, RG1 - Soft palate to epiglottis, RG2 - Epiglottis to base of tongue).

(Fig. 4.1d). Variation in position and angulation of the airway with respect to image slices may generate spurious values of airway area changes. Thereby, the slice orientation was used to correct the areas for angulation using simple trigonometric identities.

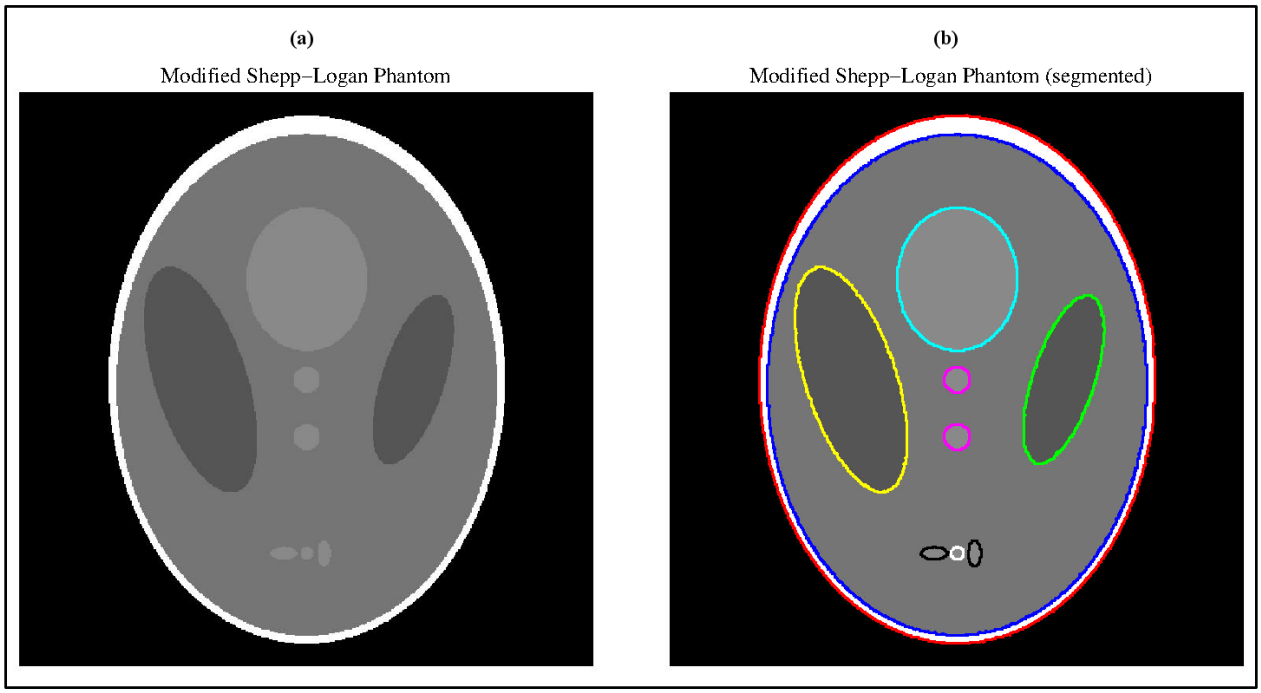

Figure 4.2: Modified Shepp-Logan phantom a) before segmentation b) after segmentation using the thresholding algorithm. The error between the theoretical and computed areas ranges from 0.2 to 6.3 %. (Note: Ellipse 1: red (outermost), Ellipse 2: blue, Ellipse 3: green, Ellipse 4: Yellow, Ellipse 5: Cyan, Ellipse 6, 7: Magenta, Ellipse 8, 10: black, Ellipse 9: white).

A modified two dimensional Shepp-Logan phantom [106] was employed to determine the accuracy of the segmentation algorithm (Fig. 4.2a). The gray levels depicted in the phantom are similar to those observed in MR or CT images of the human airway. Figure 4.2b indicates the phantom with outlines of the ten ellipses identified using the thresholding algorithm. As shown in table 4.1, numerically identified areas of the phantom were within 6 percent of the measured values. Besides, the error was higher for the smaller ellipses (6 – 10). Furthermore, the airways analyzed in this study were similar in size to ellipse nos. 1 – 5. Thereby, the largest error in the

calculation of their areas was approximately 2 percent. Boundaries of the patient's head and mandible for baseline, CPAP1 and CPAP2 configurations, were identified using the segmentation algorithm. The outlines were superposed to verify that lateral displacement of the mandible and change in head and neck position was negligible between pressures.

Table 4.1: Comparison between measured and computed areas (Note: Semi-major axis length, semi-minor axis length and corresponding ellipse areas are dimensionless).

Ellipse No.	Semi-major axis	Semi-minor axis	Measured Area	Computed Area	Percent Error (Absolute)
1	0.92	0.69	1.9942	2.0381	2.2
2	0.874	0.6624	1.8187	1.8557	2
3	0.31	0.11	0.1071	0.1061	0.9
4	0.41	0.16	0.206	0.2064	0.2
5	0.25	0.21	0.1649	0.1673	1.5
6	0.046	0.046	0.0066	0.0064	3
7	0.046	0.046	0.0066	0.0064	3
8	0.046	0.023	0.0033	0.0031	6.1
9	0.023	0.023	0.0016	0.0015	6.3
10	0.046	0.023	0.0033	0.0031	6.1

4.2.2 *Estimation of Airway Elasticity*

The index used to describe the local elasticity of the airway wall dilated by CPAP is the specific compliance [97]. The specific compliance is the normalized change in the cross-sectional area divided by the change in transmural pressure [94].

$$\frac{1}{A}\frac{\delta A}{\delta P} = \frac{1}{S} \qquad (4.1)$$

where δA is the absolute change in the cross-sectional area with respect to the reference configuration, A is the cross-sectional area of the reference airway, δP is the transmural pressure and S is the stiffness of the airway wall. Equation 4.1 can be rearranged to obtain an expression for the localized airway stiffness,

$$S = \frac{A\delta P}{\delta A} \qquad (4.2)$$

In the present study, δA and A are obtained from MRI measurements described in section 4.2.1, where A is the reference area corresponding to either the baseline pressure or pressure CPAP1 and δA is the difference between the reference area and the area corresponding to the final pressure. δP is the transmural pressure i.e., the difference between the reference pressure (baseline or CPAP1) and the final pressure (CPAP1 or CPAP2). Extraluminal tissue pressure (ETP) varies with changes in the position of the head [107, 108] and is greatest during the expiratory phase of the breathing cycle. The patient's head and neck position was found to be unchanged between CPAP levels in this study. The position being constant, the ETP distribution was assumed to remain the same for 2 values of mask pressure and baseline configuration. The transmural pressure was thereby affected only by changes in CPAP. The stiffness of the airway at each axial image slice is obtained from Equation 4.2. The average stiffness S_{avg} is obtained by evaluating the mean of the values obtained at every axial slice for the changes in transmural pressure described previously.

Axial variation in elasticity [98] was evaluated for three different conditions: from baseline to CPAP1, baseline to CPAP2 and CPAP1 to CPAP2. The softest cross-section

(location with smallest S i.e. more elastic or lowest stiffness) for each of the above conditions can be obtained using,

$$S'_{B-1} = \min(S_{B-1}) \qquad (4.3)$$

$$S'_{B-2} = \min(S_{B-2}) \qquad (4.4)$$

$$S'_{1-2} = \min(S_{1-2}) \qquad (4.5)$$

where $S_{B\text{-}1}$, $S_{B\text{-}2}$ and $S_{1\text{-}2}$ are arrays of stiffness values along the airway, corresponding to the CPAP levels indicated by the subscripts (B for baseline, 1 for CPAP1, and 2 for CPAP2). The softest location is then determined by using the lowest stiffness of the three values of δP tested (Eqn. 4.6).

$$S' = \min(S'_{B-1}, S'_{B-2}, S'_{1-2}) \qquad (4.6)$$

Stiffness values corresponding to the narrowest cross-section of the baseline airway were then determined for the three values of δP. The minimum of the three stiffness values was then evaluated to predict patient specific airway elasticity for the narrowest location.

4.2.3 *Results*

The variation in cross-sectional area along the airway length for six subjects (patient nos. 1, 5, 7, 9, 11, 15) is shown in Figure 4.3. The dotted curve represents the baseline airway, the dashed curve indicates the dilated airway corresponding to CPAP1 and the solid curve shows the dilated airway for CPAP2. Patients with larger differences between the three lines have more compliant airway. The narrowest cross-section in the baseline airway was located in the RP region (hard palate to soft palate) in patient 11 and 15, in the RG1 region (soft palate to epiglottis) in 2 patients (patient nos. 1, 9) and in the RG2 zone (epiglottis to base of tongue) in patient nos. 5 and 7. The site of narrowest cross-section is thus patient specific.

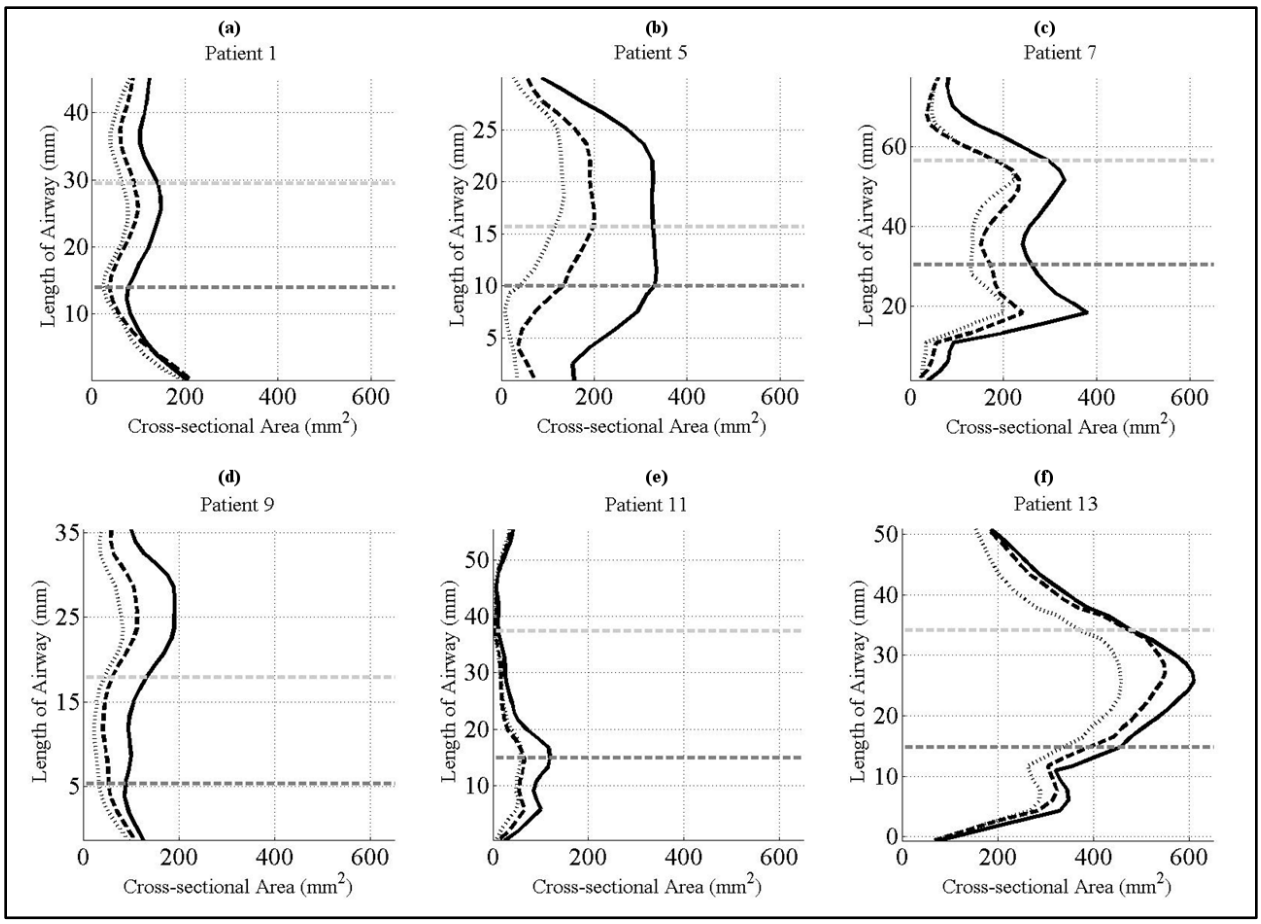

Figure 4.3: Variation in the cross-sectional area over the airway length for 6 patients (a - f). Variation in area corresponding to the baseline airway is indicated by a dotted curve, the same for CPAP1 and CPAP2 are represented using a dashed and solid line, respectively. Location of the tip of the soft palate is indicated by the dashed light gray line while the dashed dark gray line represents the tip of the epiglottis.

The average stiffness values (S_{avg}) corresponding to pressure change from baseline to CPAP1 (black bar) and CPAP1 to CPAP2 (gray bar) are then plotted as a bar-graph (Fig. 4.4a) to illustrate the nature and extent of non-linear behavior of individual airways. As can be seen, in GROUP D (patient nos. 5, 15, 16, 17, 18, 19) and GROUP B (patient nos. 6, 7, 11, 22), the stiffness is higher between baseline to CPAP1 and lower between CPAP1 to CPAP2, and indicates a 'strain-softening' behavior. Patients in GROUP D and GROUP B represent moderate and strongly ‘strain-softening’ behaviors, respectively. On the other hand, the stiffness was

higher between CPAP1 to CPAP2 than from baseline to CPAP1, for GROUP C (patient nos. 1, 8, 9, 10, 14) and GROUP A (patient nos. 2, 3, 4, 12, 13, 20, 21), and represents a 'strain-hardening' behavior.

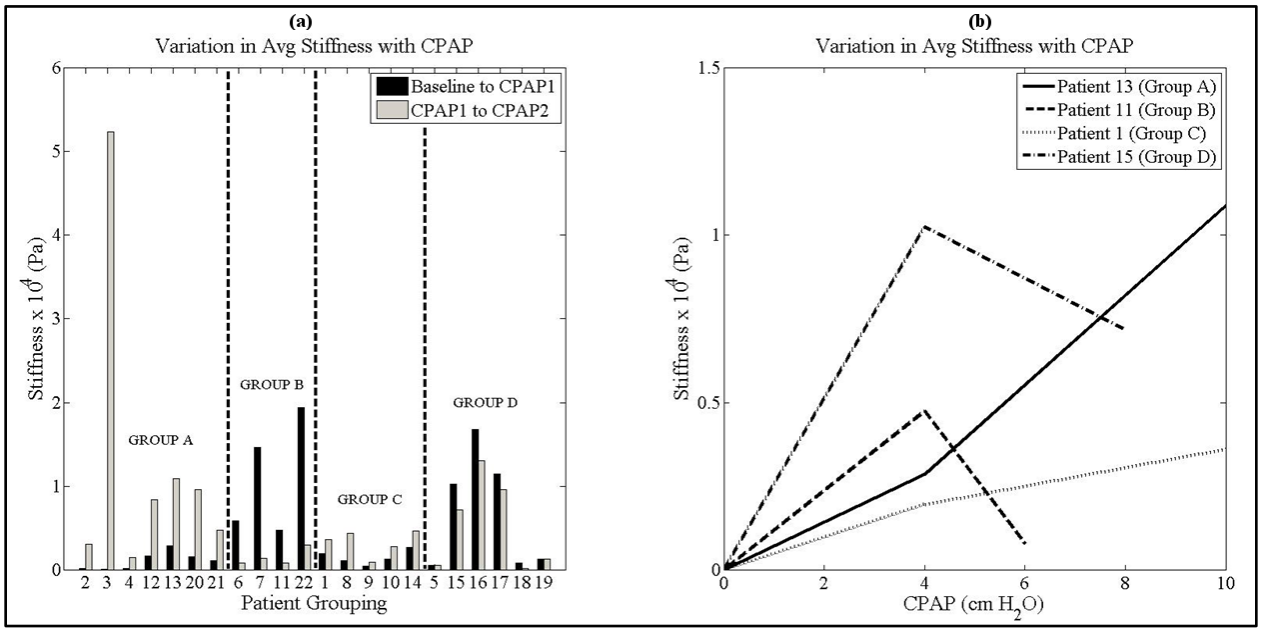

Figure 4.4: a) Overall response of individual airways indicated by plotting the variation in stiffness with CPAP as a bar graph, for the 22 patients considered in this study. Patients in GROUP D exhibit a moderately 'strain- softening' behavior and patients in GROUP B depict a strongly 'strain-softening' behavior. Patients in GROUP C indicate a moderately 'strain-hardening' behavior and patients in GROUP A represent a strongly 'strain-hardening' behavior. b) Representative line plots of variation in stiffness with CPAP for the four phenotypes identified in the study (Patient 13 – GROUP A, Patient 11 – GROUP B, Patient 1 – GROUP C, Patient 15 – GROUP D).

Patients in GROUP C and GROUP A represent moderate and strongly 'strain-hardening' behavior, respectively. The variation in stiffness with CPAP for four representative patients (1, 11, 13 and 15) is plotted as a curve (Fig. 4.4b) to explain the differences between the four phenotypes. The values of the estimated stiffness (S'_{soft} and S'_{narrow}) for the twenty-two subjects and their respective anatomical locations are summarized in Appendix C (Table C.2). The softest cross-section was located in the retropalatal airway, in 11 out of the 22 patients (patient nos. 6, 7, 8, 10, 11, 12, 13, 14, 17, 22). The softest and narrowest cross-sections were located in the same

anatomical region, in 16 patients (patient nos. 1, 2, 3, 4, 5, 6, 9, 10, 11, 12, 14, 16, 17, 18, 20, 21). The softest and narrowest locations were coincident in 5 patients (patient nos. 9, 10, 11, 18, 21).

The twenty-two patients were grouped according to the AHI or P_{crit} values and an average airway stiffness was estimated for each group. The three groups were identified based on the severity of OSA [13]. Variations in group averaged stiffness (S'_{soft} and S'_{narrow}) with AHI and P_{crit} are plotted as a bar-graph in Figure 4.5. Scatter plots of variation in stiffness with AHI and P_{crit}, at the softest and narrowest location are indicated in Fig. 4.5c and 4.5d. An exponential function of the form ae^{-bx} was employed to fit the data. The goodness of fit (R-value) for variation in stiffness with AHI was -0.41 and -0.76, corresponding to the softest and narrowest locations respectively. The corresponding values for variation in stiffness with P_{crit} were -0.08 and -0.24. Furthermore, the stiffness values for the female patients (patient nos. 1, 6, 11, 12 and 21) significantly influenced the correlation with P_{crit} (Fig. 4.5d). The airway stiffness at the softest and narrowest locations decreased with increasing AHI (Fig. 4.5a, c) and P_{crit} (Fig. 4.5b, d). This trend is especially clear at the narrowest locations.

4.2.4 *Discussion*

The change in airway elasticity between the two CPAP mask pressures is due to the non-linear response of the airway wall to positive pressures. The degree and nature of this non-linearity is patient specific as shown in Figure 4.4. Accordingly, 2 phenotypes were identified for the DS pediatric OSA patients considered in this study; airways that stiffen with increasing pressure (GROUP A and C) and ones that are floppier with increasing mask pressure (GROUP B and D). This implies that some OSA patients exhibited a decreasing change in compliance with increasing CPAP while others depicted an increasing change in compliance with CPAP. That is

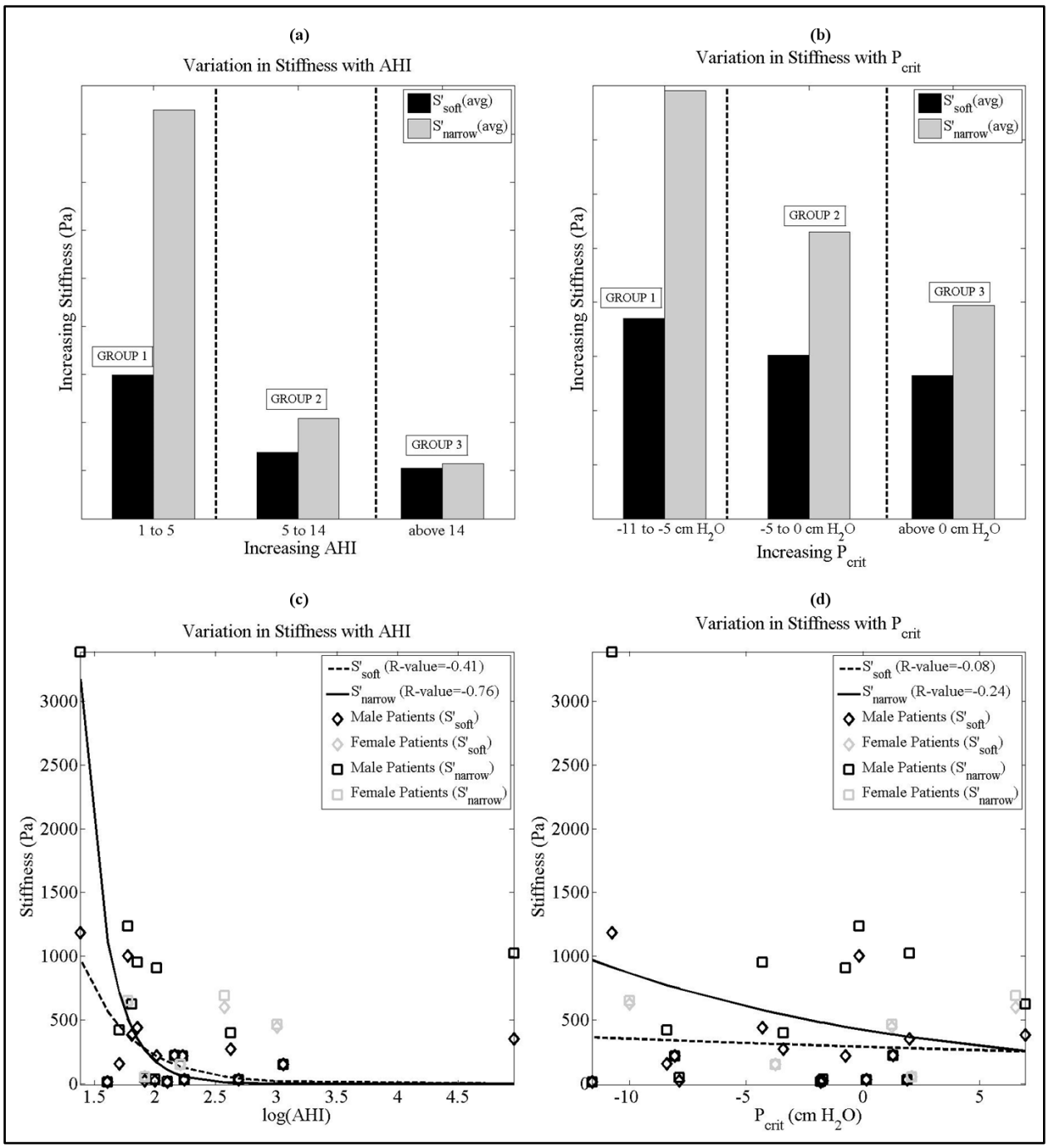

Figure 4.5: Variation in group averaged airway stiffness at softest (*S*'soft) and narrowest location (*S*'narrowest) location with a) AHI (GROUP 1 – Mild OSA (AHI values 0 to 5), GROUP 2 – Moderate OSA (AHI values 5 to 14), GROUP 3 – Severe OSA (AHI values above 14)) b) P_{crit} (GROUP 1 – Mild OSA (P_{crit} values from -11 to -5 cm), GROUP 2 – Moderate OSA (P_{crit} values from -5 to 0 cm), GROUP 3 – Severe OSA (P_{crit} values above 0 cm). Scatter plots depicting variation in individual airway stiffness at softest and narrowest location location with

c) AHI (semi-log plot) and d) P_{crit}. An exponential function of the form ae^{-bx} is used to fit the individual data sets. The trend lines indicate an inverse relationship of airway stiffness with AHI and P_{crit}.

to say, for phenotype 2 (GROUP B and D), the locus of the pressure-stiffness co-ordinates is a curve with an initially positive slope followed by a negative one. Conversely, for phenotype 1 (GROUP A and C), the locus is a curve with a positive slope that increases with pressure. The smallest and largest values of localized airway stiffness for the 22 subjects analyzed in our study differed by nearly two orders of magnitude (Appendix C: Table C.2). The large spread further emphasizes that the choice of CPAP needed to maintain airway patency is patient specific. Moreover, identification of the softest point in the airway was significant, since it did not necessarily coincide with the narrowest location (Appendix C: Table C.2). In other words, CPAP would potentially generate non-uniform mechanical ventilation of the pharynx. Furthermore, increased local airway compliance (i.e. decreased airway stiffness) would be associated with increasing severity of OSA in DS patients, as indicated in Fig. 4.5. Besides, a detailed statistical analysis would be performed in future studies that would include controls and OSA patients without DS.

4.3 *Upper Airway Compliance Mapping*

A major limitation of the tube law model described in Section 4.2 was its inability to account for variations in airway elasticity along its periphery. The objective of the study presented in this section is to describe a novel method to estimate three-dimensional variation in patient specific elasticity of the upper airway using medical image analysis. It should be noted that 10 out of the 22 patients analyzed in Section 4.2 were selected for the compliance computations presented in this section (See Appendix C, Table C.3 for patient clinical history).

4.3.1 *Quantifying Airway Wall Motion*

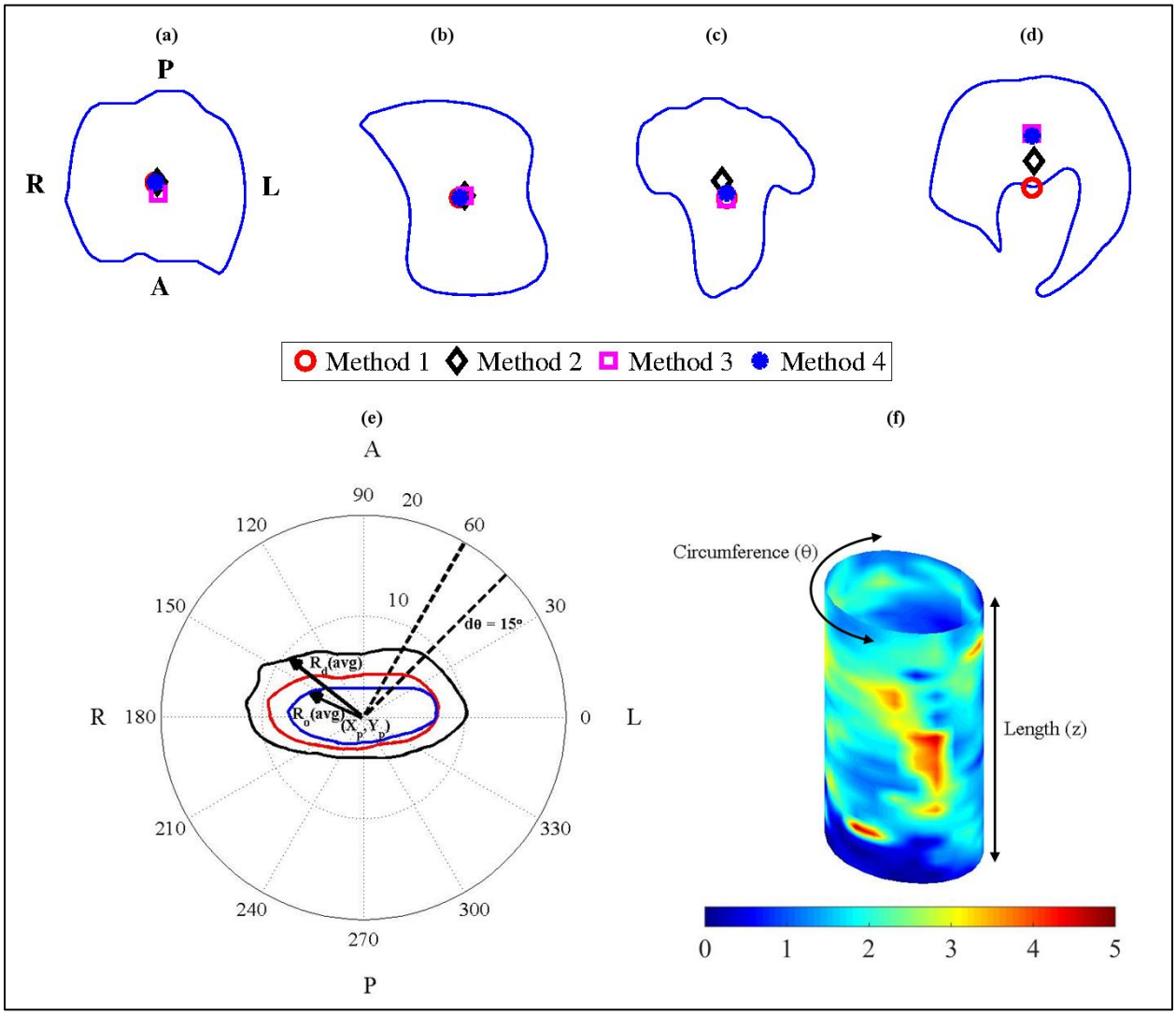

Figure 4.6: Representative outlines of upper airway a) Square shape b) Figure-eight Shape c) T shape d) Horseshoe shape. Reference point is determined by either the mean of extreme co-ordinates (Method 1), centroid (Method 2), center of inscribed circle (Method 3) or average of intersections (Method 4) e) Approximation of an angular segment of the airway as a cylindrical element subtending an angle dθ, arbitrarily chosen to be 15° f) Three-dimensional map of variation in radial displacement (patient 3, CPAP1 to CPAP2) along the airway periphery and length.

In order to compute the circumferential variation in the elasticity of the airway wall, the airway boundaries corresponding to the baseline (zero pressure) and dilated (CPAP level 1, 2) configurations are plotted in a polar co-ordinate system. In order to achieve this, a suitable

reference point was identified based on the shape of the baseline airway outline (Fig. 4.6a, b, c, d). The first method (mean) involves averaging the maximum co-ordinates in the anterior-posterior (Y) and lateral (X) directions.

$$\begin{aligned} X_p &= 0.5*(\max(X)+\min(X)) \\ Y_p &= 0.5*(\max(Y)+\min(Y)) \end{aligned} \qquad (4.7)$$

An alternative method is to identify the centroid of the airway, approximated as an n-sided, non-self-intersecting closed polygon.

$$\begin{aligned} X_p &= \frac{1}{6A_p}\sum_{i=0}^{n-1}(X_i + X_{i+1})(X_i Y_{i+1} - X_{i+1} Y_i) \\ Y_p &= \frac{1}{6A_p}\sum_{i=0}^{n-1}(Y_i + Y_{i+1})(X_i Y_{i+1} - X_{i+1} Y_i) \\ A_p &= \frac{1}{2}\sum_{i=0}^{n-1}(X_i Y_{i+1} - X_{i+1} Y_i) \end{aligned} \qquad (4.8)$$

where A_p is the area of the polygon. As can be seen from Figure 4.6 a, b and c, the first two methods are suitable for airways with a square, figure-8 or a 'T' shape. However for a horseshoe shape (Fig. 4.6d), the reference point computed using the aforementioned methods lies outside the airway outline. A third method estimates the center of the maximum inscribed circle and is suitable for most airway shapes. The fourth method involves identifying the X (or Y) co-ordinate based on the first method and computing the Y (or X) co-ordinate by evaluating the average of intersections between the airway outline and a constant X (or Y) line. For the purpose of the current study, we employed method 1 (average) and method 4 (average of intersections) to identify the reference point (X_p,Y_p). The reference point was then used to transfer the global Cartesian co-ordinates to local polar co-ordinates (R,θ) at every axial location along the airway length.

Figure 4.6e shows a polar plot of the baseline (blue) and airway shapes following deformation (CPAP level 1 - red, CPAP level 2 - black). We divide the airway boundary into discrete angular sectors subtending an angle dθ as shown in Figure 4.6e. The average radial distance within a sector with 'P' pixels or points is computed for the reference ($R_{o(avg)}$) or deformed configuration ($R_{d(avg)}$). It should be noted that the reference configuration can refer to either the baseline airway or the airway corresponding to CPAP level 1. The absolute radial displacement corresponding to each sector can be defined as,

$$\delta R = \left| R_{d(avg)} - R_{o(avg)} \right| \qquad (4.9)$$

The circumferential variation in radial displacements over the entire length of the airway is obtained by repeating the process outlined earlier at each axial location. The airway wall was discretized into 24 angular sectors and the procedure was repeated for the three patients analyzed in this study, for CPAP level 1 and 2. The resulting three-dimensional color map indicating the peripheral and axial variations in displacement is given in Figure 4.6f.

A cutting plane is now chosen on the posterior wall to unfold the 3D map and project it onto a 2D plane (Fig. 4.7a). The projected map enhances visual clarity of the most relevant regions of interest, namely the anterior and lateral walls. The circumferential locations namely anterior (A), right (R), posterior (P) and left (L) are labelled on the abscissa in Fig. 4.7a. These maps account for the airway wall displacements in three significant anatomical regions (Fig. 4.7b), namely the hard palate to soft palate (RP - retropalatal airway), soft palate to the tip of epiglottis (RG1 - retroglossal airway) and tip of epiglottis to base of tongue (RG2 - retroglossal airway). Three sets of displacement maps (baseline to CPAP level 1, baseline to CPAP level 2 and CPAP level 1 to level 2) are generated for the ten patients included in this study. Displacement maps corresponding to patient no. 3 and patient no. 10 are shown in Fig. 4.8b, c, d

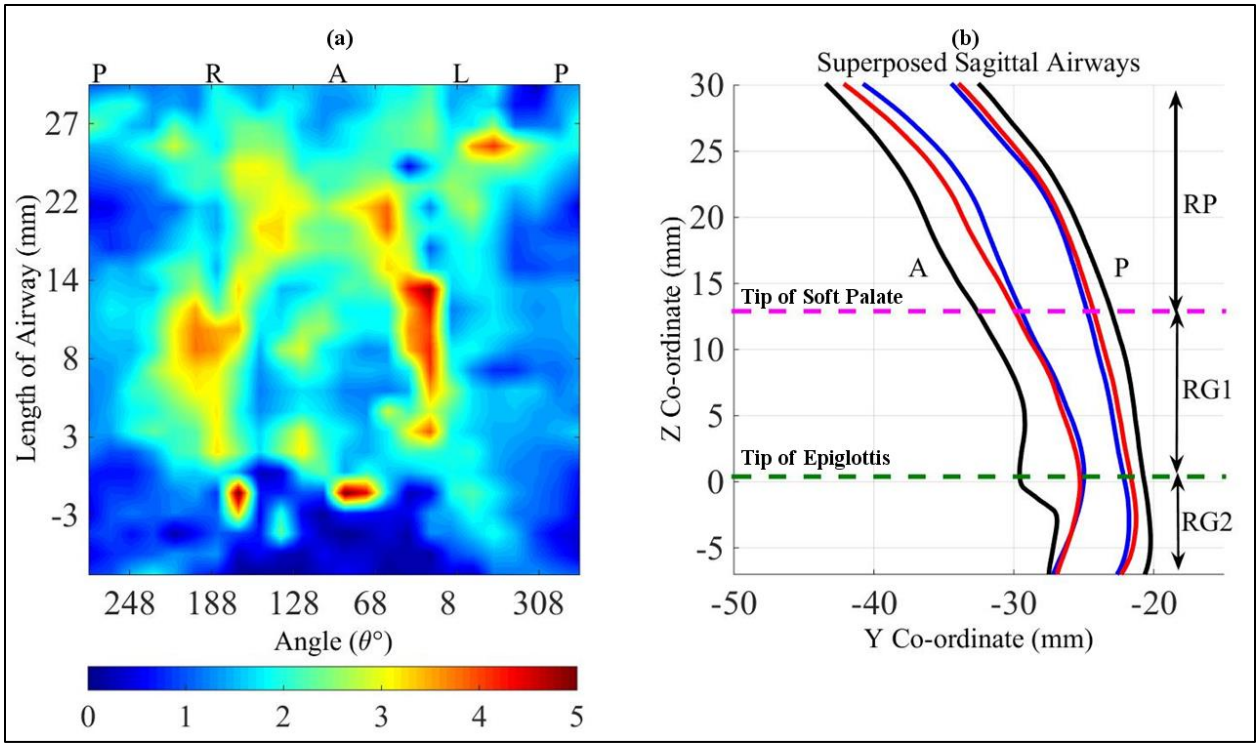

Figure 4.7: a) Unwrapped displacement map (patient 3, CPAP1 to CPAP2) quantifying airway wall displacements circumferentially (A,R,P,L) and axially (RP,RG1,RG2) b) Mid-sagittal airway profiles for patient 3 (blue – Baseline, red – CPAP1, black – CPAP2) indicating axial extents of relevant anatomical regions. (Note: A-Anterior, R-Right, P-Posterior, L-Left, RP-Retropalatal Airway (Hard palate to tip of soft palate), RG1-Retroglossal Airway (Tip of soft palate to tip of epiglottis), RG2-Retroglossal Airway (Tip of epiglottis to base of tongue)).

and Fig. 4.8f, g, h respectively. These two patients were chosen based on the observations of airway wall elasticity (as described in the following section). Three-dimensional geometries of the baseline, CPAP1 and CPAP2 airways were generated using the MIMICS (Materlialise NV, Belgium) image processing software. Figure 4.8a and 4.8e indicate the superposed baseline, CPAP1 and CPAP2 airway geometries for patient nos. 3 and 10 respectively (green-baseline, yellow-CPAP1 and blue-CPAP2). In patient 3, significant airway wall movement was observed only on the right wall, upon application of CPAP level 1 (Fig. 4.8b). The anterior, right and left walls of the airway displaced following an increase in mask pressure to CPAP level 2 (Fig. 4.8c, d). For patient 10, application of CPAP level 1 resulted in lateral wall displacements in the RG1

airway (Fig. 4.8f). Furthermore, the increased pressure caused the lateral walls to dilate further in the same anatomical region (Fig. 4.8g, h). It should be noted that superimposed models of the airways and corresponding displacement maps are aligned with the patient's anterior direction.

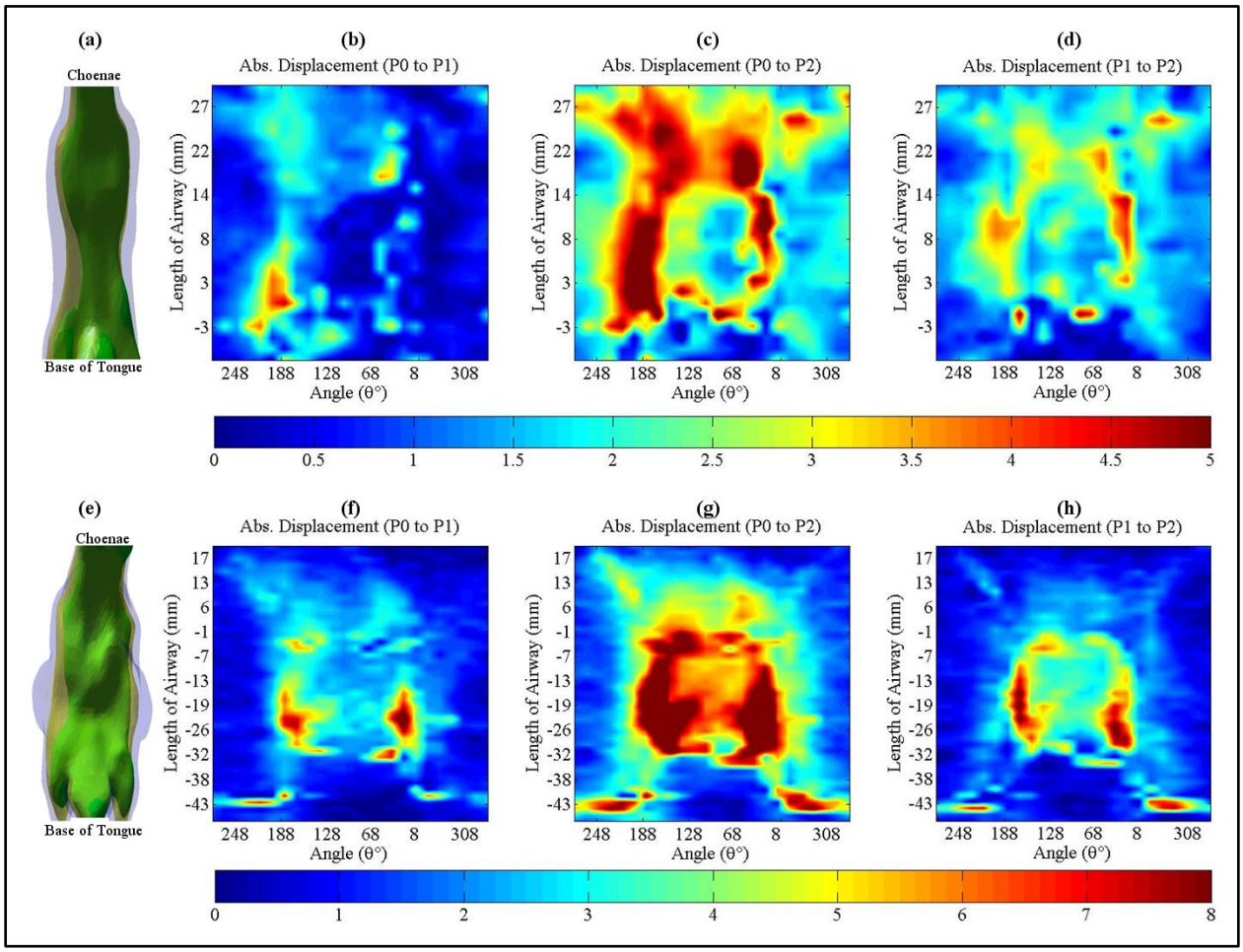

Figure 4.8: Unwrapped displacement maps for patient 3 (b, c, d) and patient 10 (f, g, h) corresponding to changes in CPAP levels (0 (baseline) to pressure 1, 0 (baseline) to pressure 2, pressure 1 to pressure 2). Superposed three-dimensional geometric models of the baseline (green), CPAP1 (yellow) and CPAP2 (blue) also indicated for reference (a – patient 3, e – patient 10). (Note: All displacements are in mm).

4.3.2 *Evaluating Airway Wall Elasticity*

The compliance and the elasticity was evaluated in a manner analogous to the tube law (Eqn. 4.1 and 4.2). The equivalent radius of circle R_c at a given axial location in the pharynx is defined by,

$$R_c = \sqrt{\frac{A}{\pi}} \qquad (4.10)$$

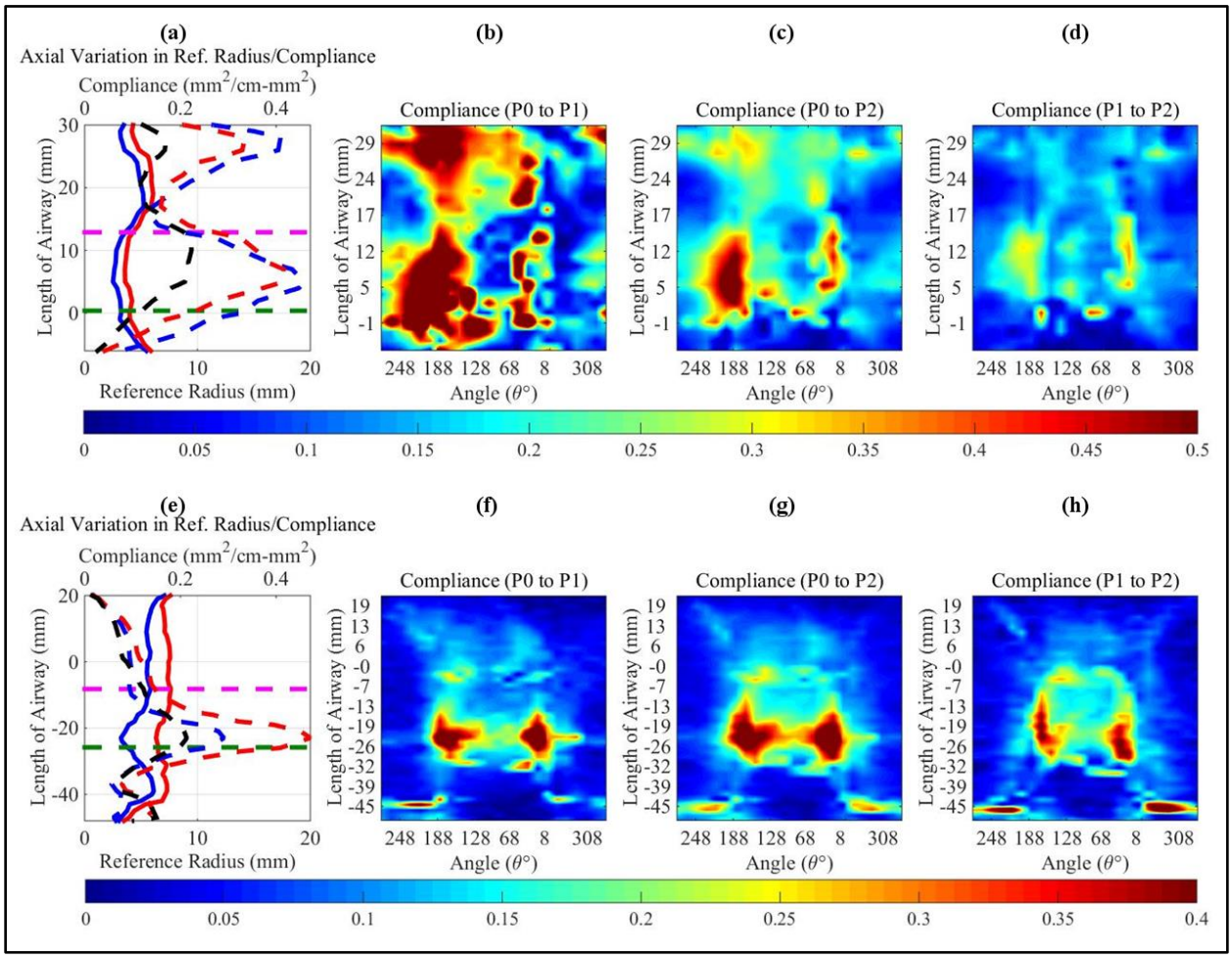

Figure 4.9: Compliance maps obtained by normalizing radial displacements by CPAP pressure difference (δP) and axially varying equivalent radius of circle (R_c) (a, e (baseline – solid blue line, CPAP1 – solid red line)) for patient 3 (b, c, d) and patient 10 (f, g, h), corresponding to changes in CPAP levels (0 to pressure 1, 0 to pressure 2, pressure 1 to pressure 2). Axial variations in compliance (blue dashed line – 0 to pressure1, red dashed line – 0 to pressure 2, black dashed line – pressure 1 to pressure 2) computed using the tube law (Eqn. 4) are also indicated in Fig. 4a, e. (Note: Units for compliance are mm/cm-mm (compliance maps) or $mm^2/cm\text{-}mm^2$ (tube law). For 0 to pressure 1 and 0 to pressure 2, the displacements are normalized by the equivalent circle radius corresponding to baseline airway. For pressure 1 to 2, the corresponding displacements are normalized by the equivalent circle radius corresponding to the airway dilated by pressure 1).

where A is the axially varying airway cross-sectional area. The area strain term (δA/A) in equations 4.1 and 4.2 can be expressed in terms of the area of a circle,

$$\frac{\delta A}{A} = \frac{\delta(\pi R_c^{\,2})}{\pi R_c^{\,2}} \qquad (4.11)$$

Replacing the differential term 'δ' by a derivative,

$$\frac{\delta A}{A} \approx \frac{d(\pi R_c^{\,2})}{\pi R_c^{\,2}} \qquad (4.12a)$$

$$\text{i.e.} \quad \frac{\delta A}{A} \approx \frac{2\pi R_c dR_c}{\pi R_c^{\,2}} \qquad (4.12b)$$

$$\text{i.e.} \quad \frac{\delta A}{A} \approx \frac{2dR_c}{R_c} \qquad (4.12c)$$

The term dR_c in equation 4.12c is replaced by the differential radius δR (equation 4.9), that varies along the airway periphery and length. Accordingly, the specific compliance (C) is defined as follows,

$$C = \frac{1}{S} = \frac{2\delta R}{R_c \delta P} \qquad (4.13)$$

Using equation 4.13, the displacements at every circumferential and axial location (Fig. 4.8b, c, d, f, g, h) are normalized by the appropriate circle radius of the reference airway at the respective axial location (Fig. 4.9 a, e) and by the CPAP pressure differences relevant to each map, in order to generate a compliance map (Fig. 4.9b, c, d, f, g, h). Since the change in head and neck position was negligible between CPAP levels, extraluminal tissue pressure (ETP) distribution [107] was assumed to remain the same for baseline, CPAP1 and CPAP2 configurations. Variations in transmural pressure were influenced only by changes in CPAP.

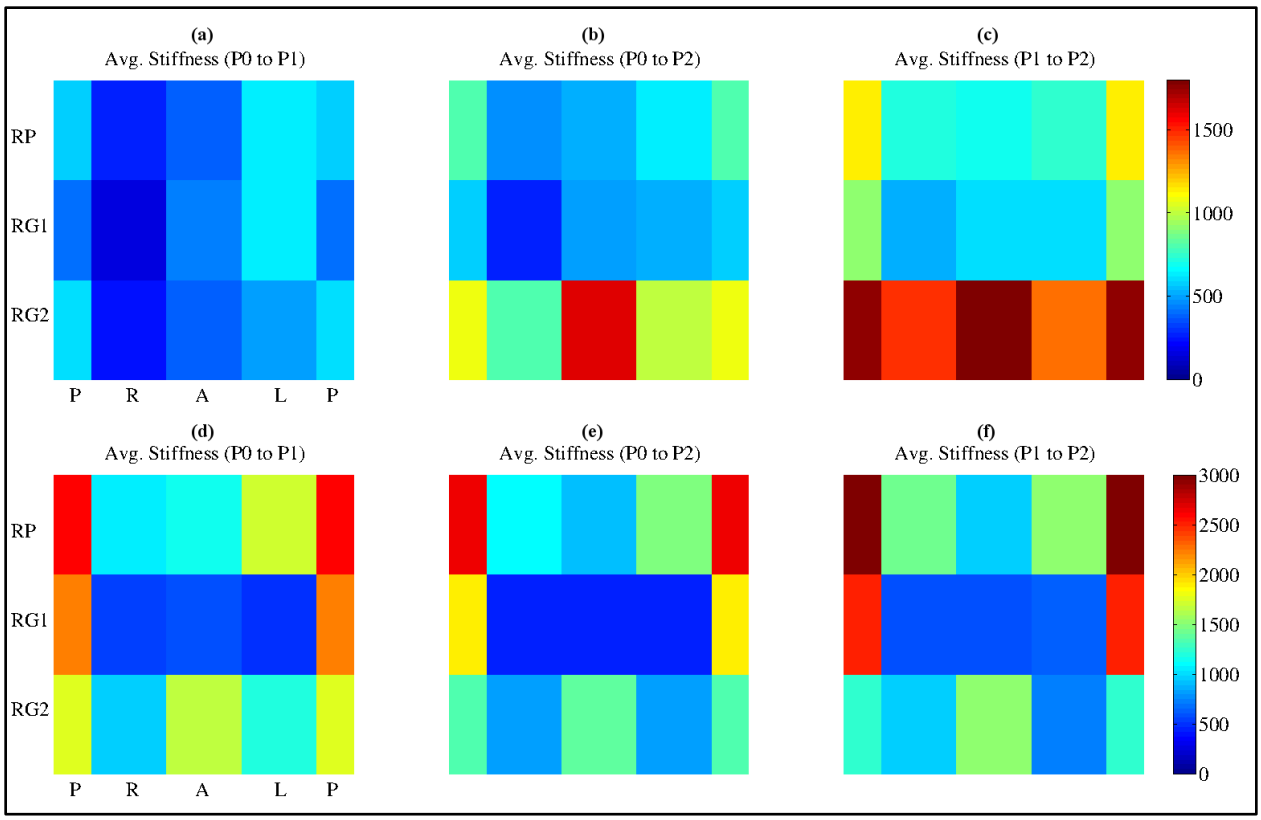

Figure 4.10: 4x3 maps of average stiffness for patient 3 (a, b, c) and patient 10 (d, e, f). (Note: Units of stiffness is Pa. A-Anterior, R-Right, P-Posterior, L-Left, RP-Retropalatal Airway (Hard palate to tip of soft palate), RG1-Retroglossal Airway (Tip of soft palate to tip of epiglottis), RG2-Retroglossal Airway (Tip of epiglottis to base of tongue)).

It should be noted that the unit of compliance employed in this study is mm/cm-mm or 1/cm. A higher value indicates that the airway wall is more flexible and the surrounding tissue is softer. For patient 3, the compliance of the right wall was higher for δP=CPAP1-CPAP0 (Fig. 4.9b) than for CPAP2-CPAP1 (Fig. 4.9d). Conversely, for patient 10, the compliance of the lateral walls in the RG1 airway is comparable for changes in CPAP levels corresponding to CPAP1-CPAP0 and CPAP2-CPAP1 (Fig. 4.9f, h). The axial variation in compliance computed using the tube law (Eqn. 4.2) is also plotted (Fig. 4.9a, e) to illustrate the novelty of the proposed method. As can be seen, the proposed mapping method captures circumferential and axial changes in compliance compared to the tube law. An overall value of patient specific stiffness

can be obtained for each of the three maps, by computing the average of compliance values at every location and inverting the resulting value. It should be noted that the stiffness was expressed in terms of Pa (1 cm of water ~ 100 Pa). The compliance maps are also simplified by evaluating the average compliance in the anterior, posterior, right and left walls corresponding to the RP, RG1 and RG2 anatomical regions. For the purpose of this analysis, it was assumed that the anterior, posterior and lateral walls subtend equal angles of 90° each, at every axial location. The resulting 4x3 maps of average compliance for patient nos. 3 and 10 are inverted to generate 4x3 maps of average elasticity as indicated in Figure 4.10. The simplified maps indicate that although the posterior wall is most likely much stiffer than the other sections of the airway, there are some instances where the posterior wall stiffness is comparable or smaller than that of the anterior and lateral walls (Fig. 4.10a, b). The maps also indicate that the lateral walls could be significantly softer than the anterior wall in some patients, particularly in the RG1 airway (Fig. 4.10a, b, d, e, f). The compliance of the anterior wall in the RP airway is found to be greater than the compliance of the lateral walls for patients 3 and 10.

4.3.3 *Results*

4.3.3.1 *Elasticity based Patient Phenotyping*

The overall airway stiffness corresponding to pressure changes from baseline to CPAP level 1 (blue bar) and CPAP level 1 to level 2 (red bar) are then plotted as a bar graph (Fig. 4.11) to illustrate the nature of non-linear behavior of the individual airways. As can be seen in GROUP 1 (patient nos. 5, 8, 9, 10), the stiffness is higher between baseline and CPAP1 and lower between CPAP1 to CPAP2, and indicates a ‘strain-softening’ behavior. On the other hand, the stiffness is higher between CPAP1 and CPAP2 than from baseline to CPAP1 for GROUP 2 (patient nos. 1, 2, 3, 4, 6, 7) and represents a ‘strain-hardening’ behavior.

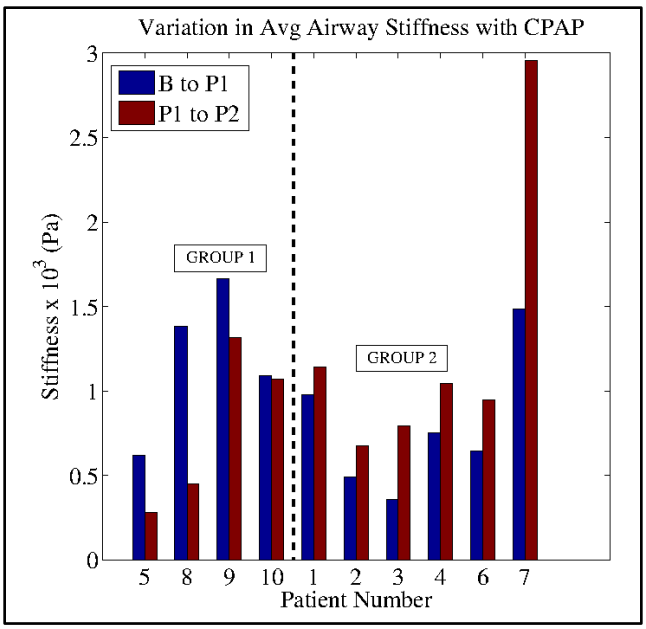

Figure 4.11: Variation in overall stiffness with CPAP, for patients considered in this study. Patients in GROUP 1 (patient nos. 5, 8, 9, 10) exhibit a 'strain- softening' behavior and patients in GROUP 2 (patient nos. 1, 2, 3, 4, 6, 7) depict a 'strain-hardening' response. Patients within each group are arranged in the order of increasing AHI.

Patient phenotyping based on circumferential and axial variations in elasticity with CPAP (i.e. change in airway wall stiffness in the anterior, posterior and lateral section corresponding to the RP (hard palate to tip of soft palate), RG1 (tip of soft palate to tip of epiglottis) and RG2 (tip to base of epiglottis) airways), was achieved using the simplified 4x3 maps of average elasticity. The elasticity phenotypes (overall, circumferential and axially varying) for patients analyzed in the study are summarized in Table 4.2.

Retro-palatal (RP) Airway:

For the anterior section, the airway stiffness decreases with CPAP for patient nos. 4, 5, 7, 8, 9, 10 and increases with CPAP for patients 1, 2, 3 and 6. Patient nos. 5, 6, 8 and 9 exhibit a strain-softening behavior (GROUP 1) and patients 1, 2, 3, 4, 7 and 10 depict a strain-hardening response in the lateral right section (GROUP 2). For the posterior section, airway stiffness decreases with CPAP for patients 5, 8 and increases with CPAP for patients 1, 2, 3, 4, 6, 7, 9 and

10. Patient nos. 1, 4, 5, 8 and 10 exhibit a strain-softening behavior (GROUP 1) and patients 2, 3, 6, 7 and 9 depict a strain-hardening response in the lateral left section (GROUP 2). The elasticity phenotypes for patient nos. 2, 3, 5 and 8 were unchanged along the airway periphery within the RP airway.

Table 4.2: Summary of elasticity phenotypes (Note: 1 indicates softening, 0 depicts hardening).

		Anterior			**Right**			**Posterior**			**Left**		
Patient	**Overall**	**RP**	**RG1**	**RG2**	**RP**	**RG1**	**RG2**	**RP**	**RG1**	**RG2**	**RP**	**RG1**	**RG2**
1	0	0	1	1	0	0	0	0	0	0	1	1	0
2	0	0	1	0	0	1	0	0	0	0	0	0	1
3	0	0	0	0	0	0	0	0	0	0	0	1	0
4	0	1	1	0	0	0	0	0	0	0	1	1	0
5	1	1	1	1	1	1	1	1	1	0	1	1	1
6	0	0	1	0	1	1	0	0	0	0	0	0	0
7	0	1	0	1	0	0	0	0	0	0	0	0	0
8	1	1	1	0	1	1	1	1	1	1	1	1	0
9	1	1	1	1	1	1	1	0	0	0	0	1	1
10	1	1	1	1	0	0	0	0	0	1	1	0	1

Retro-glossal (RG1) Airway:

For the anterior section, the airway stiffness decreases with CPAP for patient nos. 1, 2, 4, 5, 6, 8, 9, 10 and increases with CPAP for patients 3 and 7. Patient nos. 2, 5, 6, 8 and 9 exhibit a strain-softening behavior (GROUP 1) and patients 1, 3, 4, 7 and 10 depict a strain-hardening response in the lateral right section (GROUP 2). For the posterior section, airway stiffness decreases with

CPAP for patients 5, 8 and increases with CPAP for patients 1, 2, 3, 4, 6, 7, 9 and 10. Patient nos. 1, 3, 4, 5, 8 and 9 exhibit a strain-softening behavior (GROUP 1) and patients 2, 6, 7 and 10 depict a strain-hardening response in the lateral left section (GROUP 2). The elasticity phenotype of patient nos. 5 and 8 did not change with the circumferential location in the RG1 airway.

Retro-glossal (RG2) Airway:

For the anterior section, the airway stiffness decreases with CPAP for patient nos. 1, 5, 7, 9, 10 and increases with CPAP for patients 2, 3, 4, 6 and 8. Patient nos. 5, 8 and 9 exhibit a strain-softening behavior (GROUP 1) and patients 1, 2, 3, 4, 6, 7 and 10 depict a strain-hardening response in the lateral right section (GROUP 2). For the posterior section, airway stiffness decreases with CPAP for patients 8, 10 and increases with CPAP for patients 1, 2, 3, 4, 5, 6, 7 and 9. Patient nos. 2, 5, 9 and 10 exhibit a strain-softening behavior (GROUP 1) and patients 1, 3, 4, 6, 7 and 8 depict a strain-hardening response in the lateral left section (GROUP 2). The elasticity based phenotypes for all 10 patients varied along the airway circumference within the RG2 airway.

Moreover, no patient exhibited the same phenotype across all circumferential and axial locations. Patients 3, 5 and 8 exhibited a different phenotype at only one location.

4.3.3.2 *Correlations with Clinical Parameters*

The softest section in the 4x3 simplified maps of elasticity (Fig. 4.10) is obtained by evaluating the minimum of the 12 airway stiffness values. The 'representative' softest section of a patient's airway is then obtained by computing the least of the three minimum values obtained from the 4x3 maps of stiffness (i.e. baseline to CPAP1, baseline to CPAP2 and CPAP1 to CPAP2). The ten patients were grouped according to the severity of OSA (Fig. 4.11) and average airway stiffness was estimated for each group, corresponding to the softest section. As indicated in

Figure 4.11, the group averaged airway stiffness values decreased with increasing severity of OSA. Table 4.3 summarizes the locations of the representative softest sections for each airway and the corresponding values of localized airway wall stiffness.

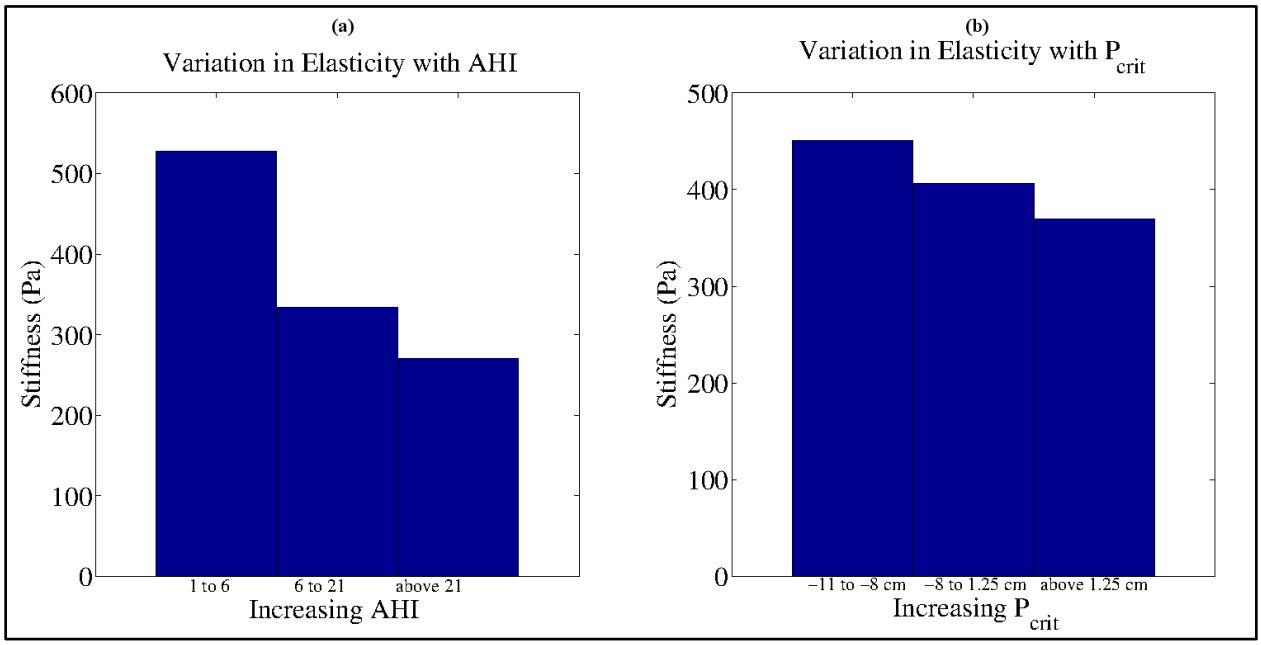

Figure 4.12: Variation in group averaged airway stiffness at softest location with a) AHI (GROUP 1 – Mild OSA (AHI values 1 to 6), GROUP 2 – Moderate OSA (AHI values 6 to 21), GROUP 3 – Severe OSA (AHI values above 21)) b) P_{crit} (GROUP 1 – Mild OSA (P_{crit} values from -11 to -8 cm), GROUP 2 – Moderate OSA (P_{crit} values from -8 to +1.25 cm), GROUP 3 – Severe OSA (P_{crit} values above +1.25 cm). The trend indicates an inverse relationship of group averaged airway stiffness with AHI and P_{crit}.

4.3.4 *Discussion*

The nature of non-linearity in the airway wall response to CPAP for the ten patients analyzed in this study was found to be patient specific and varies along the periphery and length of the airway (Table 4.2). This highlights the anisotropy in elasticity of the airway and tissue supporting the pharynx. Two types of non-linearity were observed in a manner similar to the tube law approach. The elasticity phenotypes based on the overall stiffness corresponded well with those obtained from the 4x3 maps of elasticity for patient nos. 3, 5, 7 and 8 (as indicated in Table

2). Although the proposed method is derived from a tube law model (i.e. pressure-area relationships), it provides an improvement over the simplified Starling resistor theory. It accounts for circumferential changes in localized airway elasticity in addition to changes in pharyngeal stiffness along the airway length. With the exception of patients 1, 2, 6 and 7, the lateral walls were observed to be more elastic than the anterior and posterior walls. This observation confirms the importance of assessing lateral tissue stiffness in apneic patients [109].

Table 4.3: Summary of softest sections in the pharyngeal airway.

Patient No.	Axial Location	Peripheral Section	Airway Stiffness (Pa)
1	RG1	Anterior	545
2	RG2	Posterior	335
3	RG1	Right	145
4	RP	Right	370
5	RG1	Right	165
6	RG2	Posterior	375
7	RP	Posterior	835
8	RP	Right	270
9	RG2	Right	540
10	RG1	Right	445

The methodology was demonstrated on ten pediatric OSA patients with DS. Exclusion criteria described in section 4.1 resulted in several patient scans being not usable for the analysis. The group-averaged stiffness at the softest location was found to decrease with increasing severity of OSA. The inverse relationship between airway stiffness and OSA severity suggests

that localized airway compliance can supplement clinical measures such as AHI and P_{crit}. Conclusive evidence of this inverse relationship would be obtained in future studies by performing multivariate analysis, with adjustments for gender and BMI. Furthermore, a larger sample size and incorporation of controls would significantly enhance this study. The static MRIs employed in this study are acquired during the peak expiratory phase of the breathing cycle. The shapes of the airways and subsequently the elasticity values computed in this study are averaged over multiple breathing cycles. Elasticity calculation during the inspiratory phase is challenging since the baseline airway may be partially or fully occluded [104]. Besides, imaging of the airway during natural sleep would necessitate acoustic scanner noise attenuation and real time imaging that does not induce signal image artifacts [110].

Although the segmentation algorithm was demonstrated to be fairly accurate, coarse angular discretization of the airway boundary and averaging reduce the accuracy of the elasticity computations. The present study discretizes the airway cross-section into 24 angular segments, each subtending an angle of 15 degrees. Finer discretization, although possible, are limited by the number of pixels per sector. A non-uniform angular discretization is also relatively simple to implement in the current algorithm. The simplified compliance maps (Fig. 4.10) assume that the anterior, posterior and lateral walls subtend equal angles of 90 degrees over the entire length of the pharyngeal airway. Although patient-specific, non-uniform, axially varying angular extents of the circumferential sections would improve the accuracy of the 4x3 maps of stiffness, identifying the extents of individual tissue from MR images is quite challenging. The presented methodology assumes a uniform airway wall pressure distribution along the airway length and periphery. This assumption was validated using computational fluid dynamics (CFD) [44, 45] of the upper airway. Results from the CFD simulations indicated that with application of CPAP, the

intraluminal pressure was uniformly distributed circumferentially and axially. A combination of ETP measurements with specialized IRB approved catheters and CFD or the use of IRB approved cannula and pressure transducers [97] is proposed, in order to accurately estimate the transmural pressure difference.

The overall and local compliance estimates reported in this study are within the range of values evaluated previously. Phenotyping of patients based on localized variations in airway stiffness can potentially influence the treatment needed to reduce the severity of the disorder. The present approach is suitable to estimate the static or passive compliance of the airway wall, a quantity that can significantly vary from the dynamic or active compliance. The active compliance stems from muscle activity and temporal variations in pressure during breathing [3]. The same can be estimated from cine MRIs that also serve to improve the patient specific aspects of sleep disordered breathing including neck movement, jaw thrusting, independent and coupled behavior of soft-tissue components such as the tongue, soft palate, etc.

4.4 *Computational Method to Estimate Mechanical Properties In-vivo*

This section describes the procedure to iteratively determine the non-linear mechanical properties of airway tissue using finite element (FE) simulations of airway collapse.

4.4.1 *Numerical Simulations of Airway Collapse*

The methodology is illustrated for 3 patients (patient nos. 1, 9, 11). The patients were chosen based on the observations of P_{crit} (Patient 1 – positive P_{crit}, Patient 9 – largely negative P_{crit}, Patient 11 – moderately negative P_{crit}).

Figure 4.13a indicates an axial slice midway of the RG1 airway (between the tip of the soft palate and tip of the epiglottis). The structures surrounding the airway consist of the tongue (or palate in the RP airway), lateral fat-pads, spine, blood vessels and mandible. Due to the

extremely complicated nature of these anatomical features, certain simplifying assumptions were made. Firstly, the tissue at an axial location was considered to be homogenous. Coupled or

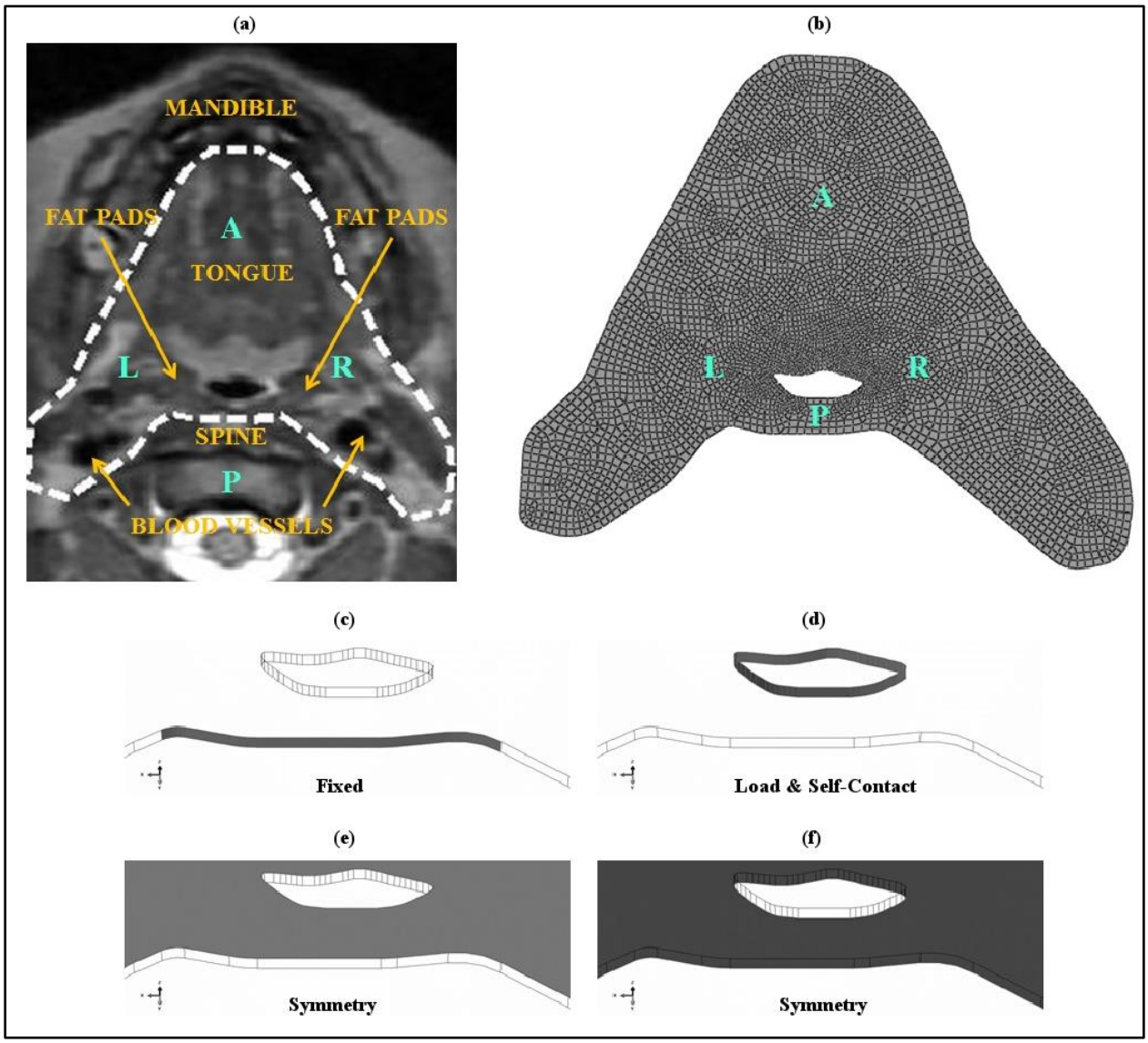

Figure 4.13: a) Axial MR image (patient no. 9) indicating the anatomical structures (tongue, lateral walls and blood vessels) that constitute upper airway tissue (indicated by dashed white outline). b) CAD geometry and unstructured hexahedral mesh of the computational domain for FE simulations. c) No displacement boundary conditions applied on the posterior wall tissue d) Pressure load corresponding to P_{crit}-CPAP and self-contact applied on airway wall. Symmetry bondary conditions in the Z direction applied on the e) top and f) bottom faces of the domain. (Note: The CAD geometry has been extruded by 1 mm in the Z direction. A – Anterior, R – Right, P – Posterior, L – Left).

independent behavior of soft tissue structures was not considered in this study. Based on recommendations from the radiologist, the outline of the tissue structure was identified manually to include anterior soft tissue, thin mucosa overlying the spine, fat pads (to the right and left of the airway) and blood vessels (outline indicated by white dashed line in Fig. 4.13a). The resulting shape of the structural domain in the RG1 airway is shown in Fig. 4.13b. The process was repeated for the narrowest cross-section in the RP airway and a computational domain was suitably identified. The profile of the baseline airway or airway dilated by CPAP was chosen as the starting point for the numerical simulation. The choice was based on the starting value of mask pressure which was gradually reduced resulting in airway collapse. For example, in case of patient 1 and 11, the starting mask pressure was 4 cm of H_2O and for patient 9, the same was 0 cm of H_2O (i.e. no mask pressure).

Co-ordinates of the tissue outline and airway were imported into GAMBIT 2.4 (ANSYS Inc., Canonsburg, PA, USA) to generate planar CAD geometries. The planar geometry was then extruded by 1 mm in the Z-direction and the resulting volume was exported to the ABAQUS 6.12 (Simulia, Dassault Systems, Providence, RI, USA) finite element solver. Simulations of velopharyngeal collapse under gravitational loads in two dimensions [111] and tracheal collapse subject to negative transmural pressure loads at select axial locations [112] have been performed previously using the ABAQUS software. The procedure outlined in these aforementioned studies was employed for the simulations presented in this section. The geometric models were meshed using 8-node, linear hexahedral elements (C3D8R) [113] in ABAQUS. Reduced integration alleviates the volumetric locking phenomenon associated with full integration (C3D8) elements employed to model nearly incompressible solids. Hourglassing which results from the excitation of zero energy modes is a potential drawback of reduced integration elements. The hourglass

control was thereby activated to minimize spurious deformations [114]. 3 mesh resolutions corresponding to element sizes of 3, 2 and 1 mm (i.e. coarse, medium and fine) were tested. Accordingly the number of hexahedral cells for patient 1, 9 and 11 varied from 2000 to 7500, 1000 to 4500 and 800 to 4000 respectively. An element size of 1 mm was found to be optimum for all cases and generated grid independent solutions without excessive element distortion. The corresponding number of elements for patient 1, 9 and 11 were 7500, 4500 and 4000 cells respectively. Further reduction in the element size resulted in less than 1 per cent change in the measure of airway area following pharyngeal collapse. A neo-Hookean material model described by the following strain energy function (W) was used to approximate the non-linear behavior of airway tissue [111, 115],

$$W = C_{10}(I_1 - 3) + \frac{1}{D_1}(J_{el} - 1)^2$$

$$C_{10} = \frac{\mu_0}{2} \qquad (4.14)$$

$$D_1 = \frac{2}{\kappa_0}$$

where, μ_0 is the shear modulus, κ_0 is the bulk modulus, I_1 is the first strain invariant and J_{el} is the elastic volume strain. The neo-Hookean material is the simplest hyperelastic model and can be used in the absence of accurate material data. Similar hyperelastic materials such as Mooney-Rivlin [116] and Yeoh [117] have been employed to model airway tissue. The initial guess for the shear modulus (μ_{0ini} = 2530 Pa) was obtained from previous MR elastography studies of the tongue and soft palate [90]. A Poisson's ratio (ν) of 0.475 has been reported for airway smooth muscle previously [112] and was adopted here.

Figure 4.13 c-f summarizes the boundary conditions employed in the simulations. The interface between the spine and posterior wall mucosa was fixed (Fig. 4.13c). A linearly

increasing load corresponding to the negative transmural static pressure difference $\delta P_{collapse}=P_{crit}$ – CPAP was applied on the airway wall (Fig. 4.13d). Frictionless, hard contact was defined for the airway wall to model self-contact [112]. A symmetry boundary condition in the Z direction was assigned to the top and bottom faces (Fig. 4.13 e, f). Displacements and rotations about the vertical axis were thereby constrained. The surfaces bounding the anterior, lateral walls and blood vessels were free to displace as observed in dynamic MR images of alternate airway dilation and contraction. Furthermore, since the MR images were acquired in supine position, gravitational forces were equilibrated and not considered in the governing equations [47]. Airway collapse was assumed to be quasi-static and the updated lagrangian formulation of the continuum equations of motion for large strains [118] were solved using the ABAQUS Explicit module. All simulations were performed on a workstation computer with a single Intel i7-3770 Quad-core processor and 32 GB RAM. Finite element simulations of pharyngeal airway collapse at a given axial location required approximately 20 minutes of CPU time. The shear modulus was iteratively changed until the airway collapsed for the prescribed transmural pressure $\delta P_{collapse}$ and the difference between the slope of the experimental and numerical pressure-flow curves (described in Section 4.4.2) was minimized. In the present study, an area reduction of 97 percent or more was chosen as the criterion for airway collapse.

4.4.2 *Results*

At each load step, deformed configurations were exported from ABAQUS as an input file. Surface meshes of the deformed airway and surrounding tissue were reconstructed from the input files, to process the co-ordinates of the airway lumen surface (Fig. 4.13d) using FLUENT 6.3 (ANSYS Inc., Canonsburg, PA, USA). Lumen area prior to deformation and after each pressure load step was estimated from the surface meshes in GAMBIT, by summarizing the airway face

information. A linear fit was employed to construct a pressure-area curve [119]. The theoretical maximum inspiratory flow rate $\dot{V}_{\mathrm{i,max}}$ was then determined using the following equation [95, 119],

$$\dot{V}_{\mathrm{i,max}} = \sqrt{A_{\mathrm{num}}^3 / \rho C_{\mathrm{num}}} \qquad (4.15)$$

where A_{num} is the airway cross-sectional area obtained from numerical simulations, ρ is the density of air (1.2754 kg/m^3) and C_{num} is the slope of the numerical pressure-area curve.

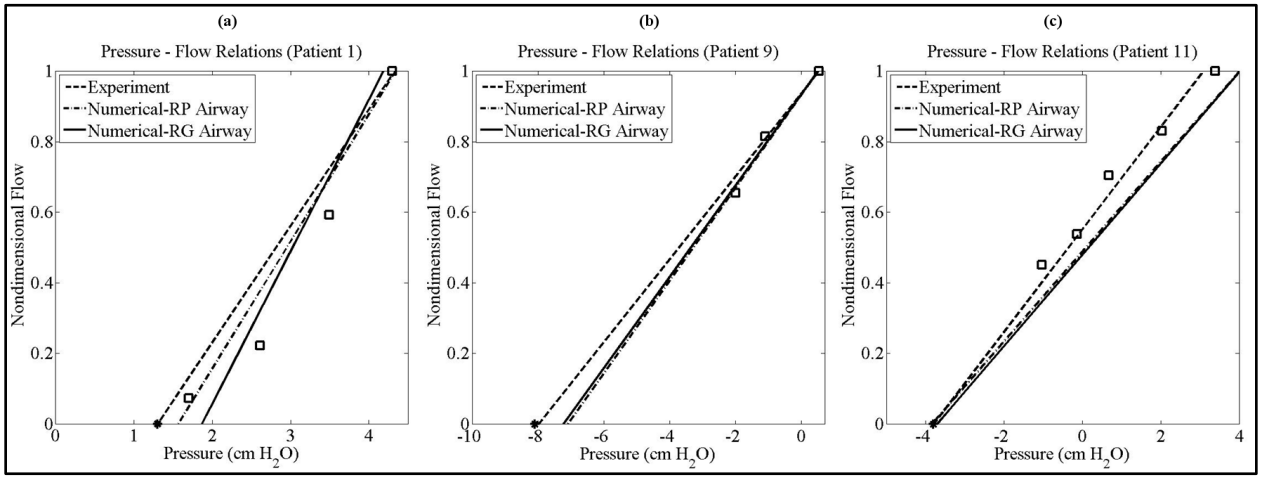

Figure 4.14: Comparison between the pressure-flow curves obtained from numerical simulations of airway collapse (dot-dashed line – RP airway, solid line – RG airway) and pressure-flow curves obtained from experimental estimation of P_{crit} (dashed line), for a) patient 1 b) patient 9 c) patient 11. A linear fit has been used to describe the pressure-flow curves. (Note: Black square markers indicate experimental data points. Black asterisk indicates P_{crit}. The flow values (experimental) and numerical) have been normalized by the respective peak values).

Maximum inspiratory flow rates were computed for the areas obtained at the end of each load step using equation 8 and normalized by the flow rate corresponding to the lumen area prior to deformation. Numerical pressure-flow curves corresponding to the RP and RG1 airways were then generated using linear regression [12]. The FE methodology was validated by comparing the pressure-flow curves obtained from numerical simulations of collapse in RP and RG1 airways to the pressure-flow curve obtained from experiments. As indicated in Fig. 4.14, a good

match was achieved between the experimental data (dashed line) and simulation results (dash-dotted line – RP airway, solid line – RG1 airway) thereby validating the computational methodology. The optimized elastic or Young's modulus is obtained from the optimized shear modulus using the following relation,

$$E_{\text{corrected}} = 2\mu_{0\text{corrected}}(1+\nu) \qquad (4.16)$$

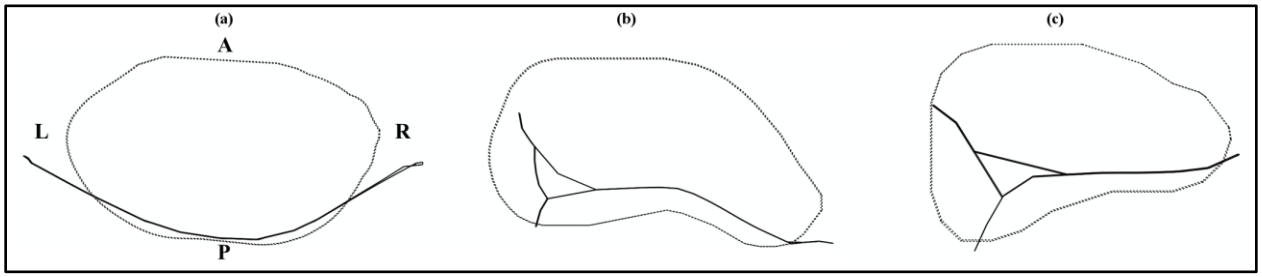

Figure 4.15: Superposed axial cross-sectional shapes of the airway lumen prior to deformation (dotted line) and after collapse (solid line), predicted from FE simulations a) Patient no. 1 (RP Airway - U shaped collapse) b) Patient no. 9 (RP Airway – Y shaped collapse) c) Patient no. 11 (RP Airway – Y shaped collapse).

Where, $\mu_{0\text{corrected}}$ is the optimized shear modulus and ν is the Poisson's ratio. Figure 4.15 indicates the lumen profile of the airway prior to deformation (dotted outline) and the airway shape corresponding to the final load step (i.e. collapsed) (solid outline). Two distinct collapse modes were observed namely, U-shape (Fig. 4.15a, patient 1) and Y-shape (Fig. 4.15b, c, patient 9, 11).

Table 4.4: Summary of results from FE simulations.

Patient No.	$\delta P_{\text{collapse}}$ (Pa)	RP - $E_{\text{corrected}}$ (Pa)	RG1 - $E_{\text{corrected}}$ (Pa)	Collapse Mode (RP)	Collapse Mode (RG)
1	-275	1700	5000	U shape	U shape
9	-810	21500	37500	Y shape	U shape
11	-780	15000	14000	Y shape	Y shape

The optimized Young's modulus ($E_{corrected}$) for the 3 patients and their respective collapse modes is summarized in table 4.4.

4.4.3 *Discussion*

The airway static pressure employed in the numerical simulations has been described as an important indicator of airway collapsibility [39, 120]. Moreover, similar studies involving finite element simulations of airway tissue collapse in animal models have been performed by applying static pressure boundary conditions at the airway tissue interface [51]. Besides, the CPAP values employed in this study are nearly an order of magnitude greater than the airway wall pressure obtained from computational fluid dynamics (CFD) of open [39] and constricted [45] upper airways. Shear stresses arising from airflow [44, 47] that stretch the airway tissue in the streamwise direction was not included in this study (Chapter 3). Moreover, the symmetry boundary conditions imposed on the top and bottom faces of the computational domain (described in Section 4.4.1) constrains tissue motion in the vertical direction. The computational model would be significantly enhanced by accounting for flow induced pressure and shear forces.

The lowest and highest moduli of elasticity ($E_{corrected}$) determined from FE simulations of airway collapse differed by an order of magnitude. Besides, the Young's modulus of tissue in the RP airway was lower than that in the RG1 airway for the 3 patients examined in this study (table 4.4). These observations suggest that the RP airway is more floppy and susceptible to collapse. Moreover, the moduli were found to decrease with increasing P_{crit} (i.e. increasing severity of OSA). Estimated mechanical properties of soft tissue are extremely sensitive to the adopted methodology [90]. For instance, the Young's modulus of the soft palate determined from FE simulations [115] was found to vary from 500 to 97500 Pa. The corresponding value obtained

from MR elastography was 7465 Pa [90]. Similarly, the elastic modulus of the tongue varied from 1100 Pa (obtained from ex-vivo compression [117]) to 250000 Pa (obtained from FE simulations [121]). The material properties reported in this study were within the aforementioned range of values. Differences between live tissue properties estimated in the current study and MR elastography could be attributed to several factors including differences in the patient population being studied and conditions under which the imaging was performed. Moreover, the inverse relationship between tissue stiffness and OSA severity established using MR elastography [91], was also identified using the proposed method. Imaging static airway collapse in human subjects during inspiration can be extremely challenging. In the absence of MR images or endoscopic views of the collapsed airway [76], the experimental inspiratory pressure-flow curve was compared to the pressure-flow curve obtained from computer simulations, to validate the numerical procedure (Fig. 4.14). Besides, the expiratory and inspiratory compliance contours are not coincident due to significant hysteresis in the pressure-flow curves for sleep disordered breathing [122]. The proposed numerical methodology can be employed to non-invasively estimate the Young's modulus of upper airway tissue in OSA patients during sleep. Furthermore, the estimated values of tissue elasticity would serve as input to a virtual computational tool, to assess the success or failure of different surgeries prior to application.

The mode of airway collapse was found to be either U (2 fold) or Y-shaped (3 fold). The fold number was smaller for the patient with greater severity of OSA [123] (i.e. with positive P_{crit}). The pattern of airway collapse was found to strongly depend on the profile of the airway lumen prior to deformation. This emphasizes the need to accurately image and segment the airway dilated by CPAP. The current study assumed that the airway collapsed at the same closing pressure in the RP and RG1 airways. However, previous studies have shown that P_{crit} for

the velopharynx is less negative compared to that in the oropharynx [98]. Furthermore, this study assumed that airway collapse would occur midway in the RG1 airway or at the narrowest point in the RP airway. It should be noted that this assumption was made to assess the regional differences in tissue properties along the airway length. The study assumed that mechanical properties at an axial location were homogenous and isotropic. However, tissue properties of the upper airway are not only non-linear but also anisotropic or heterogeneous [90, 124]. This observation emphasizes the need to calculate a more comprehensive 3D map of tissue elasticity accounting also for circumferentially varying mechanical properties.

4.5 *Computational Modeling of Airway Obstruction in DS*

The patient analyzed in the study is a 3 year old male with DS and moderate OSA (AHI: 6.8, P_{crit}: -790 Pa) [125, 126]. The sleep study and MR imaging protocols for this patient have been previously described in section 4.1. A statistical analysis was performed to evaluate the association between airway collapsibility and measures of OSA severity for a group of 31 pediatric OSA patients with DS [127]. Linear regression plots indicated a strong correlation between apnea-hypopnea index and fractional collapse of the airway. The pre to post-operative change in AHI was thereby employed to estimate the effectiveness of the adenoidectomy recommended for the patient described in this study.

4.5.1 *Estimation of Tissue Stiffness*

Patient-specific stiffness of soft tissue was estimated iteratively using the previously developed computational method involving finite element simulations of airway collapse [126] and is briefly described in this section. Outline of the tissue domain was identified manually using two-dimensional axial scans of the patient's airway. An in-house MATLAB (Mathworks Inc., Natick, MA) code [125] was employed to automatically identify the airway outline. The profile of the

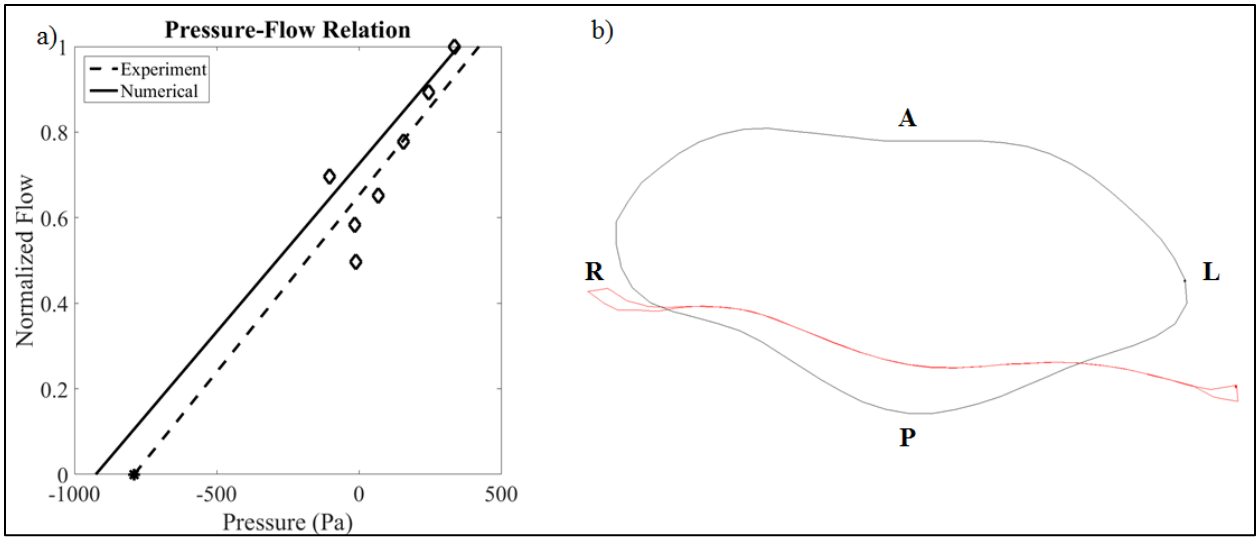

Figure 4.16: a) Comparison between the pressure-flow curves obtained from numerical simulations of airway collapse (solid line) and pressure-flow curves obtained from experimental estimation of P_{crit} (dashed line), for the patient analyzed in this study. A linear fit was used to describe the pressure-flow curves. (Note: Black diamond markers indicate experimental data points. Black asterisk indicates P_{crit}). b) Superposed axial cross-sectional shapes of the airway lumen prior to deformation (black solid line) and after collapse (red solid line), predicted from FE simulations (Note: A – Anterior, P – Posterior, R – Right, L – Left).

airway corresponding to a CPAP value of 350 Pa was used as the starting point of the simulation. The geometric model was meshed using GAMBIT v2.4 (ANSYS Inc., Canonsburg, PA) and exported in the Gmsh format [128] using the mesh conversion utility available in the Elmer finite element software [129]. Grid independent solutions without excessive mesh distortion was obtained using an optimum element size of 0.5 mm. Non-linear behavior of the airway tissue was modeled using a nearly incompressible Neo-Hookean hyperelastic material [126]. The negative transmural static pressure difference $\delta P_{collapse} = P_{crit} - \text{CPAP}$ was applied as a linearly increasing load on the airway wall. Self-contact of the airway wall was modeled as a sliding contact and the posterior wall adjacent to the spine was constrained in all directions. Symmetry boundary conditions were applied in the axial direction to constrain the motion to two-dimensions.

Gravitational forces were equilibrated and not considered in the governing equations since the images were acquired in supine position. Finite element simulations of airway collapse were performed using the FEBio v2.5 [70] implicit finite element solver (Chapter 2). The shear modulus was iteratively changed from an initial guess value of 2420 Pa obtained using MR elastography [91] until the airway collapsed completely and the difference between the slope of the experimental (linear regression co-efficient: 0.96) and numerical (linear regression co-efficient: 0.99) pressure-flow curves (Fig. 4.16a) was minimized. Accordingly, the value of shear modulus obtained using the iterative method was equivalent to 5800 Pa (~ 140 percent higher than the starting value). For the patient analyzed, the difference between the slopes was 4 percent. As can be seen in Figure 4.16b, a U-shaped collapse pattern was observed for this patient. A detailed description of the slope matching procedure and airway collapse patterns in pediatric OSA patients with DS is described elsewhere [126] (Section 4.4).

4.5.2 *Geometric Reconstruction & Mesh Generation*

120 sagittal MR scans corresponding to no mask pressure were imported into the Mimics (Materialise Inc., Plymouth, MI) image processing software for geometric reconstruction of the airway and tissue structures. 3D geometry of the airway including the nasal airway, pharynx and trachea was generated using a thresholding algorithm (lower threshold gray value (GV): 0, upper threshold gray value (GV): 200). 3D geometries of the tongue, soft-palate and adenoid were reconstructed to model the structural domain. It should be noted that the lateral extents of these structures were similar to previous studies involving computational [130] and imaging analysis [131] of upper airway tissue motion. The lower and upper threshold GV for the palate and tongue were 200 and 590 respectively. The corresponding values for the adenoid were 360 and 590 GV. Coarse geometries of the airway and tissue structures were smoothed to remove surface

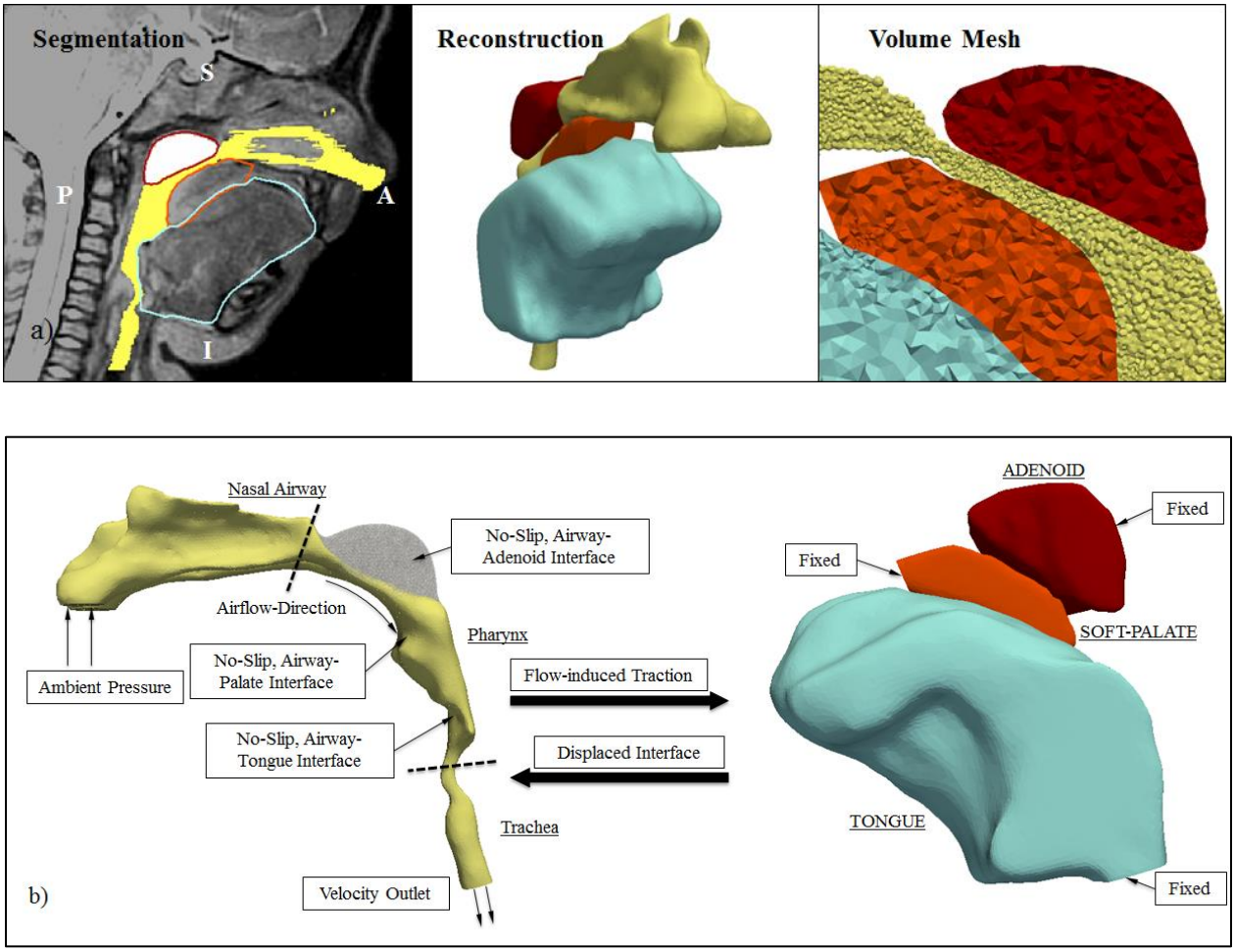

Figure 4.17: a) Mid-sagittal MR image indicating segmentation of airway (highlighted in yellow), adenoid (red outline), tongue (blue outline) and soft palate (orange outline). Location and amount of adenoid tissue (6 mm) removed virtually is highlighted in white (Note: Soft tissue excision increases the airway volume at the site of removal, A – Anterior, P – Posterior, I – Inferior, S – Superior). Reconstructed pharynx and tissue indicated in three-dimensions. Mid-sagittal cross-section indicating volume mesh for flow (polyhedral cells) and structural domain (tetrahedral cells). b) Superposed anatomically accurate 3D models of baseline airway (yellow color) and surgically altered airway (gray color) with flow boundary conditions. Anatomically accurate 3D models of adenoid (red color), tongue (blue color), soft-palate (orange color) with structural boundary conditions. (Note: Contact conditions defined between soft-palate, tongue and adenoid. Tracheal extension added to avoid boundary artifacts resulting from backflow, resulted in minimal changes in airway wall pressure distribution for the outlet boundary condition chosen in this study).

artifacts. Inlets to the airway were identified at the nostrils and an outlet was created below the glottis (i.e. vocal folds). Fixation surfaces for the tongue at the base of the epiglottis, soft-palate at the level of the hard palate and adenoid at the interface with the spinal column were also generated using Mimics. 6 millimeters of adenoid tissue was 'virtually' removed to replicate the actual surgery [45, 86] and modified geometries of the adenoid and upper airway were generated accordingly. Pre and post-operative airway and tissue structures are indicated in Figure 4.17a. Geometries for the baseline and virtual surgery case were then exported to 3-Matic (Materialise Inc., Plymouth, MI) to identify common interfaces between the airway and soft structures. The airway surface mesh was locally refined at the narrow cross-sections in the velopharynx (i.e. retropalatal airway) and trachea using 3-Matic to obtain better resolution of the flow. Surface meshes were then exported to the ANSYS T-Grid (ANSYS Inc., Canonsburg, PA) meshing software to generate volume meshes. Tetrahedral elements were generated for the tissue [46, 47, 50]. Although hexahedra are preferred for modeling nearly incompressible materials, tetrahedrons were employed due to the complicated morphology of individual tissue components. The discretization (i.e. number of nodes) for the structural domain was of the same order of magnitude adopted in previous computational models of the tongue [116] and soft palate [47]. Tetrahedral cells were also generated for the airway and were recombined to create polyhedral cells. Polyhedral cells were adopted for the flow domain to obtain homogenous distribution of wall quantities and increase the speed of solution convergence [87], as described previously in Chapter 3. It should be noted that the grid resolution for the flow domain was of the same order (10^5) as that employed in a previous study involving flow in a pediatric pharynx [40]. Table 4.5 summarizes the mesh resolutions employed in this study for the baseline and virtual surgery case. A grid sensitivity analysis was performed to ensure that the mesh

resolutions indicated in Table 4.5 were optimum. For the flow domain, the error in the airway wall pressure distribution was 0.8 percent when the number of nodes was increased by a factor of 3. Similarly, for the structural domain the error in peak displacements was 0.5 percent when twice the number of nodes was employed.

Table 4.5: Discretization (number of nodes) of pre and post-operative tissue and airway.

	Airway	**Soft-Palate**	**Tongue**	**Adenoid**
Pre-Operative	360000	15000	52000	21000
Post-Operative	390000	15000	52000	12000

4.5.3 *Computational Modeling of Tissue Motion in response to Airflow*

The SST model was employed for pre and post-operative inspiratory airflow simulations as described in Chapter 3. Additionally, the k-ε realizable model [132] was tested to assess the sensitivity of tissue displacement to the choice of turbulence model for a known inspiratory flow rate. A no-slip boundary condition was set at the airway wall and airway-tissue interface. Maximum inspiratory airflow ranging from 20 to 25 liters per minute has been employed previously in CFD [45] and FSI simulations [46, 47] of pharyngeal airflow and are representative of physiologically relevant flow rates in the pediatric upper airway [43]. Furthermore, inspiratory and expiratory flow rates can vary between breaths in apneic patients [6]. The sensitivity of tissue displacement to variation in inspiratory flow rates was thereby evaluated as described in the following section. An ambient pressure boundary condition (i.e. zero gauge pressure) was applied at the nostrils. Inspiratory airflow in the pharynx has been simulated previously by prescribing either a velocity boundary condition [43] or outflow boundary condition [133] at the trachea. Recent computational studies describing pharyngeal airflow in obese adolescent girls with OSA [133] have described the importance of extending the

trachea by 10 diameters to avoid boundary artifacts resulting from backflow. A velocity boundary condition was prescribed at the trachea in the present study. Inclusion of the tracheal extension to avoid flow recirculation at the outlet resulted in minimal changes (less than 1 percent change) in the airway pressure distribution, for the boundary condition chosen in this study. Previous computational studies of airflow in the pharynx also employed truncated geometries of the upper airway [39, 119]. The influence of excluding the nasal cavity on tissue displacements was tested for a known flow rate. A turbulence intensity of 5 percent and a 1 mm length scale was assumed in all simulations. The governing equations describing the flow were solved using ANSYS Fluent finite volume software (Chapter 2). A second-order upwind scheme was used to discretize the pressure, momentum and turbulence terms. Pressure-velocity coupling was achieved using a pressure-based coupled formulation [89]. Gradients were evaluated using a least-squares cell-based scheme to obtain a more accurate solution compared to the same obtained using a Green-Gauss cell based gradient evaluation method. Peak inspiratory airflow in the pharynx has been simulated previously using steady [45] and unsteady [43] RANS solvers available in ANSYS Fluent. The steady state solver and associated stopping criterion described in previous publications [39, 40] was employed in the present study.

Wall shear stresses resulting from airflow were nearly 100 times smaller than the corresponding values of airway wall pressure. Besides, previous studies involving fully-coupled FSI simulations of soft-palate motion have indicated that the influence of forces arising from shear stresses on tissue displacement is much lower compared to pressure forces [47]. Flow-induced traction arising from airway wall pressure was applied as a load at the tissue-airway interfaces of the tongue, soft-palate and adenoid. It should be noted that the traction varies three-dimensionally along the airway periphery and length and depends on the inspiratory flow rate.

Similar computational strategies have been employed to simulate the displacement of human cornea caused by air-puff applanation [134], acoustic simulations of stridor in a patient's obstructed airway [135] and pharyngeal collapse in adult OSA subjects modeled as a thin walled structure [136]. Displacements and rotations were constrained at the fixation surfaces defined in Section 4.5.2. A bonded or no separation contact condition was applied at the interface between the tongue and soft-palate [137] and a sliding contact was defined between the soft-palate and adenoid as described in Section 4.5.1. Body forces arising from gravity were again not considered as described in Section 4.5.1. The discretized updated Lagrangian formulation [138] of the governing equation was solved using ANSYS Mechanical finite element software (Chapter 2). It should be noted that the FEBio solver was employed for patient-specific calculation of shear modulus described in Section 4.5.1, due to its relative simplicity in modeling airway self-contact. However, for flow induced tissue displacement, the ANSYS Mechanical solver was preferred for its ability to interface with the ANSYS Fluent flow solver. Although the Neo-Hookean model was employed for material parameter optimization, the sensitivity of flow-induced tissue displacement was also determined with respect to variability in the choice of material model. Three hyperelastic materials were tested in this analysis including: a) Yeoh [137] b) Mooney-Rivlin [116] (both materials adopted previously to model the biomechanics of airway structures such as the tongue and soft palate) c) Gent [139] (proposed to model soft tissue). The second-order Yeoh model can be described using the following strain-energy function:

$$W = C_{10}(I_1 - 3) + C_{20}(I_1 - 3)^2 + \frac{1}{d_{10}}(J_{el} - 1)^2 + \frac{1}{d_{20}}(J_{el} - 1)^4 \qquad (4.15)$$

where, C_{10}, C_{20} are material constants and d_{10}, d_{20} are compressibility parameters. The strain energy function corresponding to the Gent model is given by:

$$W = -\frac{G_0 J_m}{2}\ln\left(1 - \frac{I_1 - 3}{J_m}\right) + \frac{2}{K_0}\left(\frac{J_{el}^{\,2} - 1}{2} - \ln J_{el}\right) \qquad (4.16)$$

where, ln is the natural logarithm and J_m is a dimensionless parameter. The fifth-order Mooney-Rivlin model can be described using the following strain energy function:

$$W = \sum_{i+j=1}^{2} C_{ij}(I_1 - 3)^i (I_2 - 3)^j + \frac{2}{K_0}(J_{el} - 1)^2 \qquad (4.17)$$

where, C_{ij} are material constants and I_2 is the second invariant of the right Cauchy-Green strain tensor. For the estimated shear modulus of 5800 Pa, the material constants for the Yeoh and Mooney-Rivlin model were adjusted to correspond to the parameter ratios presented by Amatoury et al and Stavness et al respectively. For the Gent model, a value corresponding to 6.56 was assumed for the dimensionless parameter [139].

In order to evaluate the influence of tissue displacement on the airflow patterns for the pre and post-operative airways, the displaced airway-tissue interfaces for the baseline and virtual-surgery cases were combined with the respective pharyngeal geometries to generate the corresponding narrowed airways. This approach involving the use of CSM simulations to estimate the deformed lumen geometry for subsequent CFD analysis has been employed previously for hemodynamic simulations in the inferior vena cava [140] virtually altered to accommodate filters. It should be noted this approach was adopted to minimize the possibility of negative cell volumes in the flow domain resulting from opposite wall contact between the soft-palate and adenoid. Inspiratory flow simulations were repeated on the constricted geometries and resistances were computed for the retropalatal, pharyngeal and complete airway. Figure 4.17b summarizes the boundary conditions and computational methodology employed in this study. All simulations were performed on a workstation computer running Windows 7 Enterprise. Post-processing was performed using Paraview (Kitware Inc., Clifton Park, NY).

4.5.4 *Results & Discussion*

4.5.4.1 *Sensitivity Analysis*

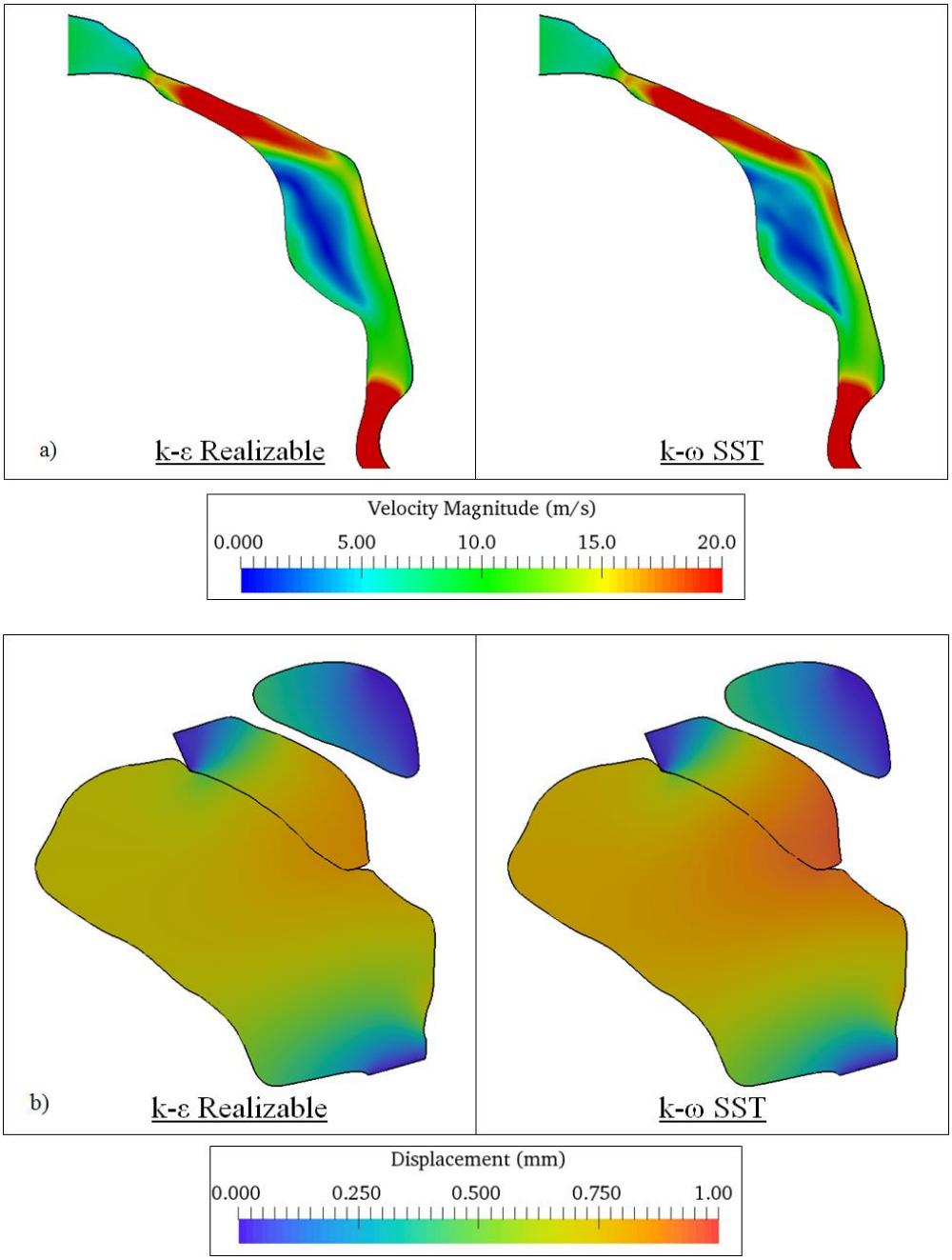

Figure 4.18: a) Contours of inspiratory airflow velocity in the mid-sagittal plane for k-ε realizable and k-ω SST turbulence models (Note: The turbulence models are compared for a known flow rate of 22 lpm. Airflow patterns indicated for the pharyngeal airway). b) Contours of airway tissue displacement in the mid-sagittal plane for k-ε realizable and k-ω SST turbulence models.

The flow-parameter sensitivity analysis for pre-operative tissue displacements was performed using a peak inspiratory flow rate of 22 lpm. The corresponding value of maximum displacement of soft-tissue structures was 1 mm. Mid-sagittal cross-sectional planes were defined to compare flow and displacement patterns. The greatest displacement was observed at the uvula (i.e. tip of the soft palate) as obtained previously using fully coupled FSI simulations [47, 48]. Large displacements were also observed in the proximity of the transversalis and verticalis tongue muscle groups. Figure 4.18 describes the sensitivity of the displacement to the choice of turbulence model. As indicated in Fig. 4.18a, differences between the k-ε realizable and k-ω SST models were primarily observed downstream of the constriction in the velopharyngeal airway. An increase in the cross-sectional area of the airway resulted in deceleration of airflow following the initial acceleration. Furthermore, this region was characterized by flow separation and formation of recirculation regions for both models. However, a faster decay in the flow velocity was observed for simulations involving the k-ε realizable model [39]. Differences were also observed in the flow patterns downstream of the constriction in the glottis. The velocity magnitude corresponding to 20 m/s is comparable to the inspiratory flow velocities (~ 16 m/s) reported in previous computational studies of pharyngeal airflow in pediatric OSA patients [119]. Additionally, the k-ε model predicted less negative values of airway wall pressure [40] and subsequently resulted in displacements of the tongue and soft-palate that were lower by approximately 10% (Fig. 4.18b) compared to the SST model.

Figure 4.19 describes the sensitivity of tissue displacement to variability in flow rate for a known turbulence model. Since flow in the airway is driven by the streamwise pressure gradient, a higher pressure drop between the nostrils and trachea would be necessary to obtain a greater volume airflow rate. Subsequently, airflow velocity, shear stress and wall pressure distribution

would also increase with increasing flow rate. As can be seen in Fig. 4.19a, 11 percent change in the peak inspiratory flow rate (22 lpm to 24.5 lpm) increased the negative pressure values by 24

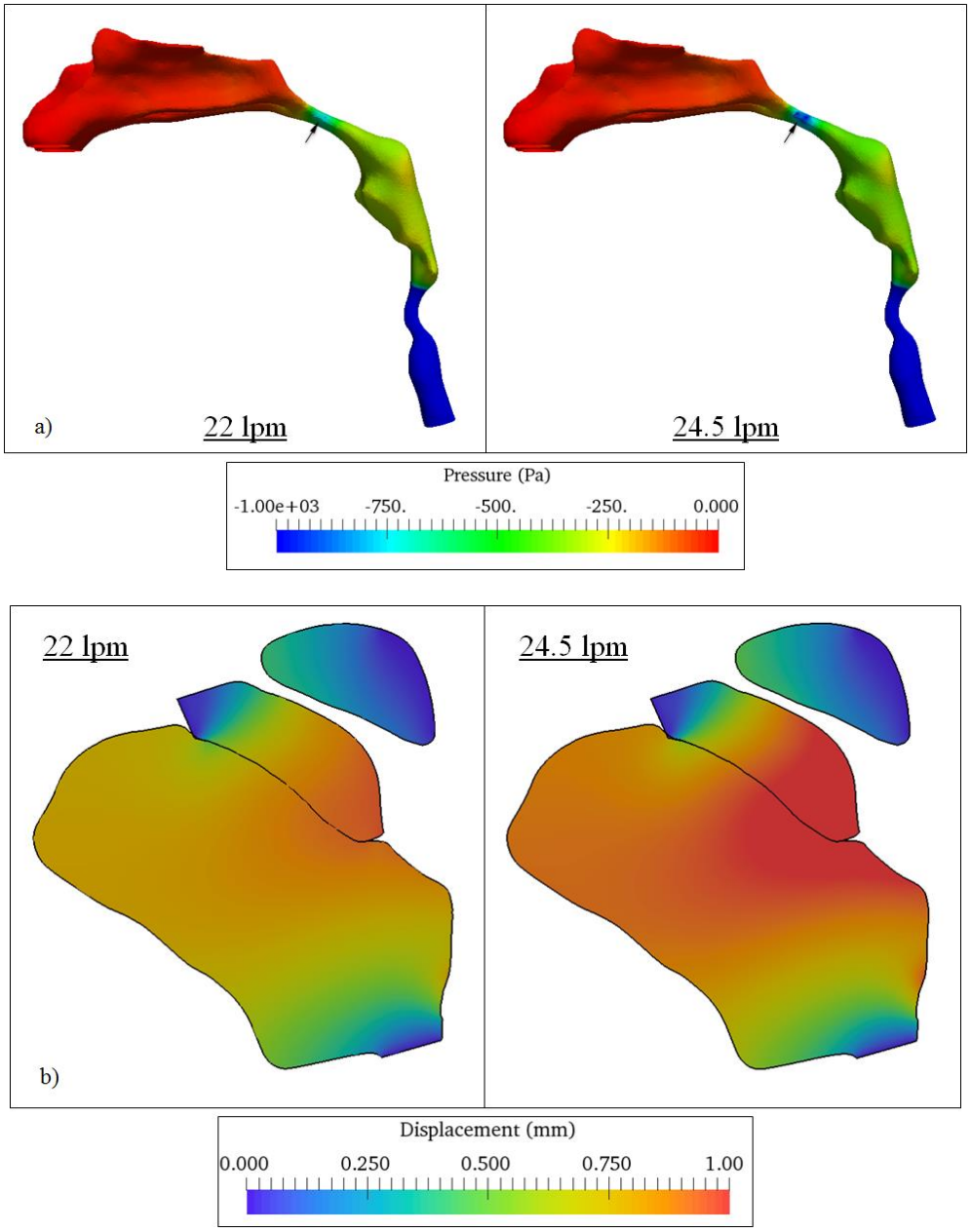

Figure 4.19: a) Distribution of wall pressure for airflow corresponding to 22 and 24.5 lpm (Note: The two flow rates are compared for the identical turbulence model (k-ω SST). Arrows indicate location of minimum pressure in the velopharynx. Inclusion of a tracheal flow extension resulted in minimal changes in airway pressure distribution in the regions of interest, for the outlet boundary condition chosen in the study). b) Contours of airway tissue displacement in the mid-sagittal plane for inspiratory airflow corresponding to 22 and 24.5 lpm.

percent at the narrowest cross-section in the velopharynx (location indicated by arrow). This resulted in 20 percent increase in displacement (Fig. 4.19b) of the tongue and soft palate. The minimum airway wall pressure corresponding to -1000 Pa is comparable to the same (~ -800 Pa) reported in previous computational studies of pharyngeal airflow in obese children prior to and following adenoidectomy [43]. Negative pressures corresponding to -6000 Pa have been reported in computational studies of flow induced pharyngeal collapse in adult OSA patients [136]. Figure 4.20 indicates the variability in tissue displacement for the full and truncated airways for a known inspiratory flow and turbulence model. It should be noted that the truncated model extends from the choanae (i.e. posterior end of the nasopharynx) to the trachea [45, 119]. The nasal resistance for the truncated airway was calculated using the following clinical correlation developed previously [119],

$$R_{\mathrm{N}} = (1\mathrm{kPa}\cdot\mathrm{l}^{-1}\cdot\mathrm{s})\mathrm{e}^{[-0.663-0.328\ln(y)]}$$
$$P_{\mathrm{C}} = -R_{\mathrm{N}}V_{ins} \qquad (4.18)$$

where, R_{N} is the nasal airway resistance, y is the patient age in years, P_{C} is the gauge pressure at the choanae, V_{ins} is the maximum inspiratory flow rate. For a flow rate of 22 lpm, the pressure at the choanae corresponds to -130 Pa. The average pressure distribution in the retropalatal airway increased by 36 percent (Fig. 4.20a) and a 30 percent increase was observed in the displacement magnitude (Fig. 4.20b). The magnitude of tissue displacement predicted by the second-order Yeoh, fifth-order Mooney-Rivlin and Gent models was within 1% of the value predicted by the Neo-Hookean model. The location of maximum displacement was also unchanged between the four material models. However, the maximum equivalent strain decreased by 15% for the Mooney-Rivlin and Yeoh models. For the Gent model, the strain was lower by 20% (Fig 4.21a). As indicated in Figure 4.21a, the peak Von-Mises stress increased by 20% for the Yeoh and Mooney-Rivlin models and 30% for the Gent model. The peak mechanical stress and

corresponding strain were located at the interface between the tongue and soft palate, approximately 2.3 mm below the soft palate fixation surface as indicated in Figure 4.21b.

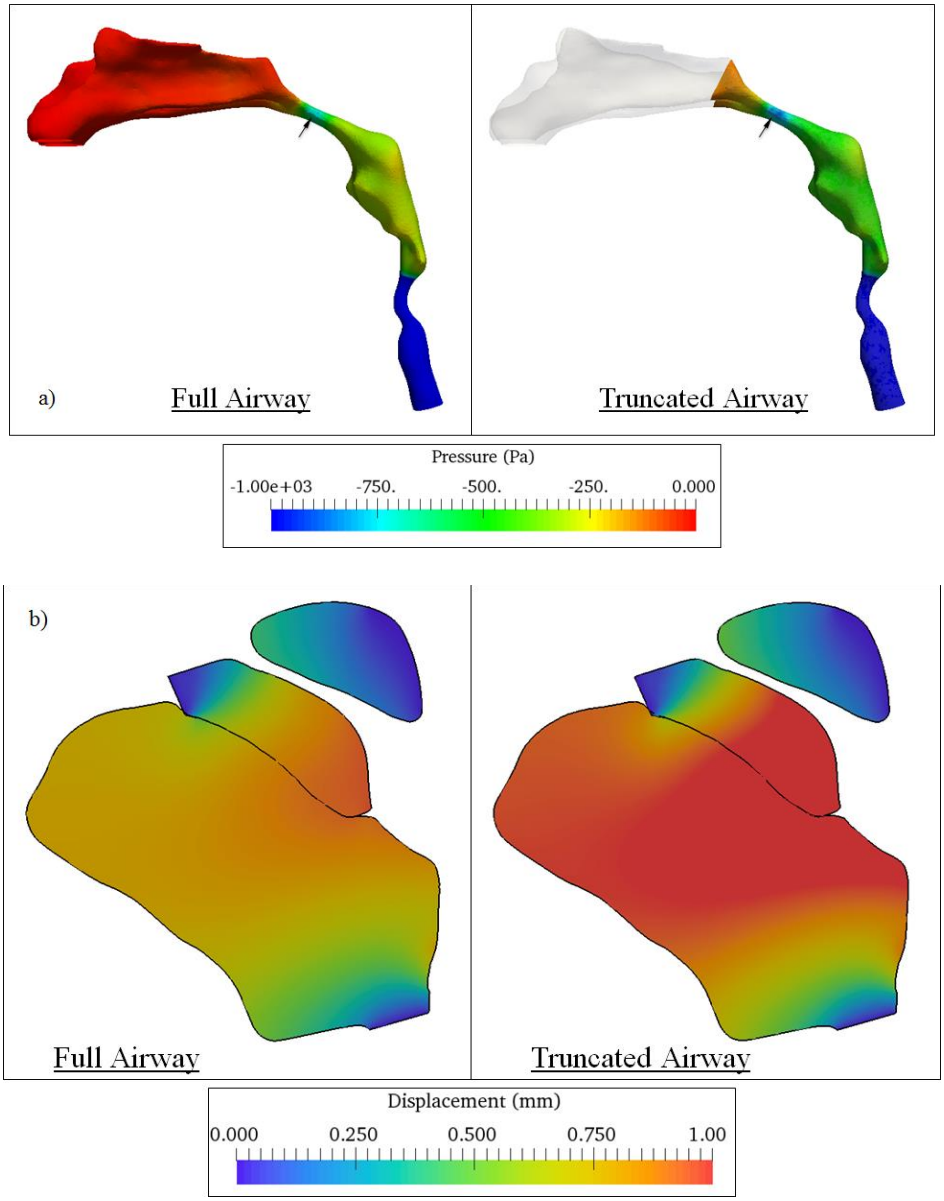

Figure 4.20: a) Distribution of airway wall pressure for the complete and truncated airway models (Note: Full airway model superposed on truncated model for reference. The two geometries are compared for the identical turbulence model (k-ω SST) and flow rate (22 lpm). Arrows indicate location of minimum pressure in the velopharynx. Inclusion of a tracheal flow extension resulted in minimal changes in airway pressure distribution in the regions of interest, for the outlet boundary condition chosen in the study). b) Contours of airway tissue displacement in the mid-sagittal plane corresponding to complete and truncated airway models.

This location was unchanged between the four material models and was in good agreement with results reported in previous CSM studies involving mandibular advancement in animal models [137].

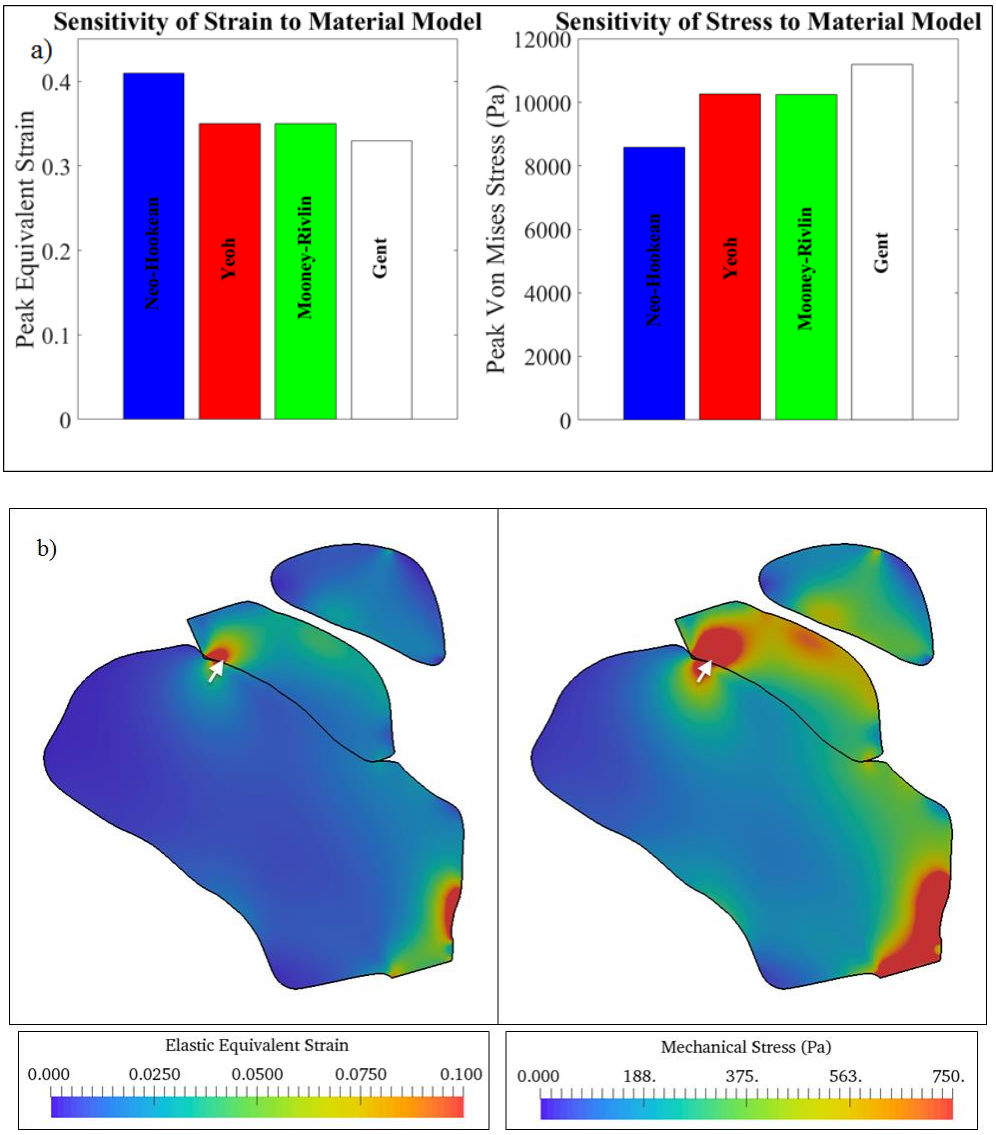

Figure 4.21: a) Comparison between peak elastic equivalent strain and Von-Mises stress for the Neo-Hookean, Yeoh, Mooney-Rivlin and Gent models (Note: The stresses and strains are compared for the complete baseline airway geometry, known turbulence model (k-ω SST) and maximum inspiratory airflow rate (24.5 lpm)). b) Contours of elastic equivalent strain and Von-Mises stress of airway tissue in the mid-sagittal plane (Note: Strains and stress distribution indicated for the Neo-Hookean material model. White arrows indicate location of peak strain/stress for all material models).

Shear modulus of upper airway tissue computed using the method presented in this study is within the range of values reported in literature. Neuromuscular activity has been observed to considerably alter the stiffness of upper airway tissue [91]. CPAP and changes in patient head position [90] also produce variability in the estimated elasticity. P_{crit} measurements have been observed to vary significantly between conditions of natural and sedation induced sleep for OSA patients [141]. Variations in critical closing pressure would subsequently alter the estimated values of tissue compliance (Section 4.5.1). The maximum inspiratory flow rate that causes tissue to deform by a known magnitude would in turn be affected by these variations in stiffness estimates. Recognizing the significance of the aforementioned sources of uncertainty in stiffness measurement and breath-to-breath variation in airflow volume, a patient-specific family of curves was created to describe the variation between tissue elasticity and maximum inspiratory flow rate for known values of maximum displacement (Fig. 4.22). This was achieved by repeating computational simulations described in the study for the complete range of elasticity values available in the literature [91, 142-144] to iteratively compute the corresponding maximum inspiratory airflow that produced peak displacements of 1 and 1.2 mm. It should be noted that the Neo-Hookean material model and k-ω SST turbulence model was employed for these simulations performed on the complete pre-operative airway geometry. An exponential function of the form ae^{bx} (regression coefficient: 0.98) was fitted to both sets of data points as indicated by the red (peak displacement: 1.2 mm) and black (peak displacement: 1 mm) regression lines in Fig. 4.22. An exponential function was chosen to ensure a non-zero, positive stiffness value for zero inspiratory airflow. This process can be repeated for additional values of known displacement to obtain a more comprehensive ‘operating map’. The regression lines can be potentially used to obtain an estimate of breath-to-breath variation in tissue stiffness using

prior knowledge of flow and displacements measured using MR imaging. For instance, a shear modulus of 975 Pa would be necessary to generate 1.2 mm displacement of the uvula for 3.6 lpm maximum inspiratory airflow measured previously in a pediatric OSA patient [119].

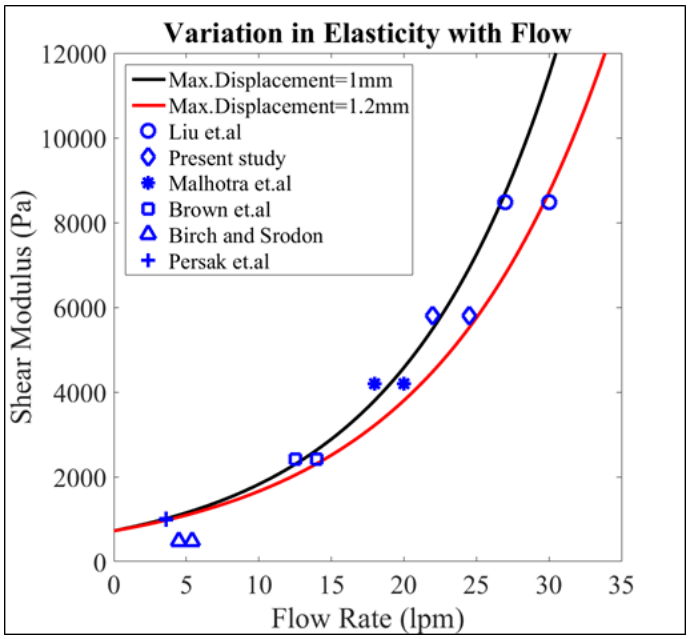

Figure 4.22: Variation in tissue stiffness with maximum inspiratory flow for known displacement values: black solid line – 1 mm, red solid-line – 1.2 mm, blue circle, diamond, asterisk, square and triangle marker – elasticity values from Liu et al (2007), present study, Malhotra et al (2002), Brown et al (2015) and Birch and Srodon (2009) respectively, blue plus marker – elasticity estimates corresponding to 3.6 lpm inspiratory flow rate measured in pediatric OSA patients by Persak et al (2011) (Note: Exponential function of the form ae^{bx} employed for regression plots).

4.5.4.2 *Virtual Surgery*

The influence of tissue compliance on the effectiveness of the virtual adenoidectomy was evaluated using a peak inspiratory flow rate of 24.5 lpm. Figure 4.23 compares the mid-plane velocity profiles for the pre and post-operative cases, including (collapsible model) and excluding (rigid model) tissue compliance. For the pre-operative case, the flow downstream of the constriction in the velopharyngeal airway was characterized by a smaller recirculation region

and slower flow velocity decay for the collapsible case. For the post-operative case, a jet was observed in the expansion region downstream of the choanae for the rigid and collapsible cases.

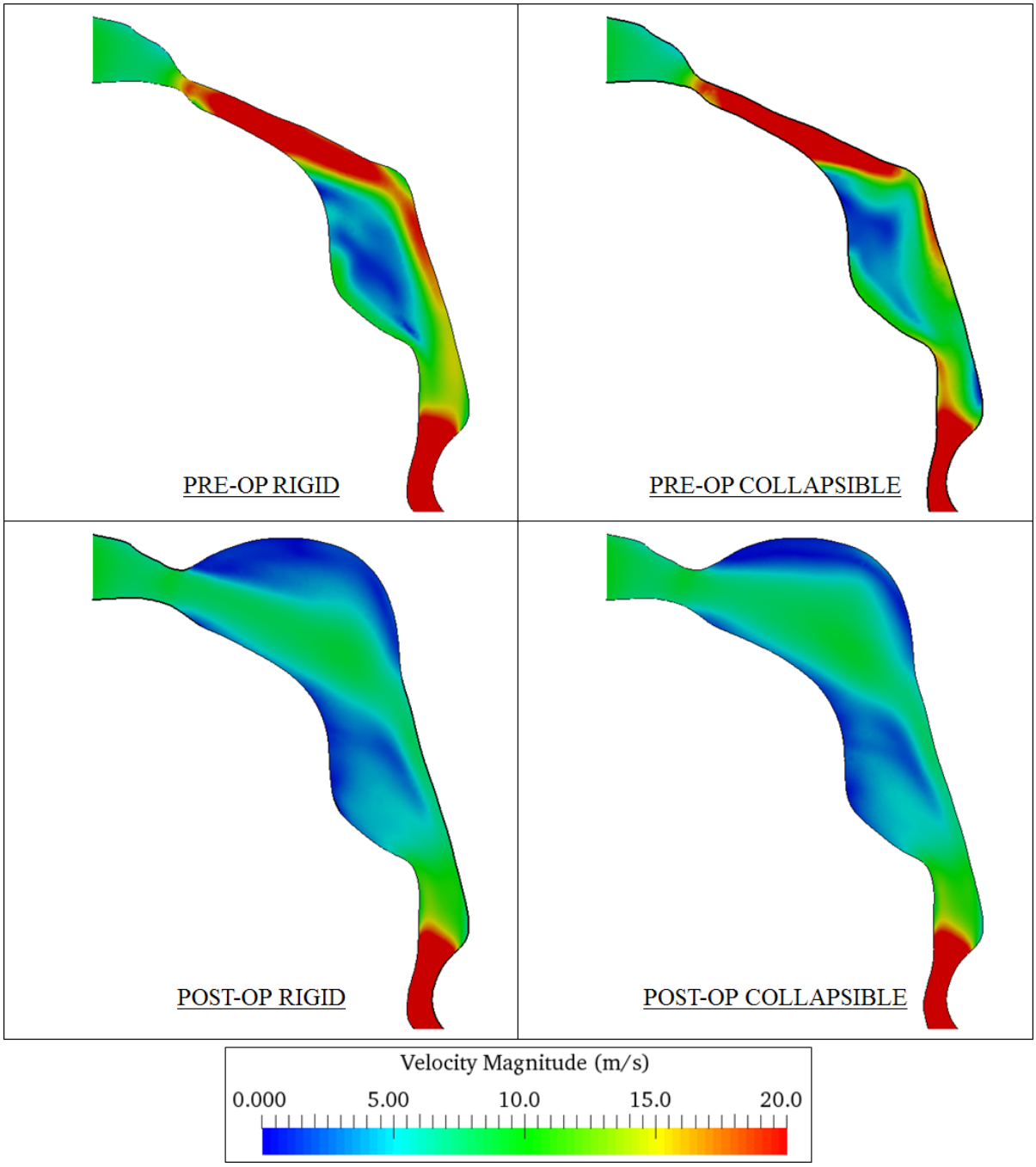

Figure 4.23: Contours of inspiratory airflow velocity in the mid-sagittal plane for pre and post-operative pharyngeal airways including (collapsible model) and excluding (rigid model) tissue compliance (Note: Airflow patterns are compared for the identical turbulence model (k-ω SST) and flow rate (24.5 lpm)).

However, the size of the recirculation region observed posteriorly slightly reduced (i.e. jet width slightly increased) for the collapsible case. The maximum displacement magnitude decreased by nearly 35 percent between the pre and post-operative cases. Furthermore, the displacements were greatest in the weakened section of the post-operative adenoid tissue. Plots comparing variation in airway cross-sectional area and area-averaged pressure distribution along the pharynx are indicated in Figure 4.24. As can be seen, the negative pressure at the narrowest location was approximately 50 percent higher for the pre-operative collapsible case. The pressure distribution was nearly unchanged between the rigid and collapsible cases for the post-operative airway.

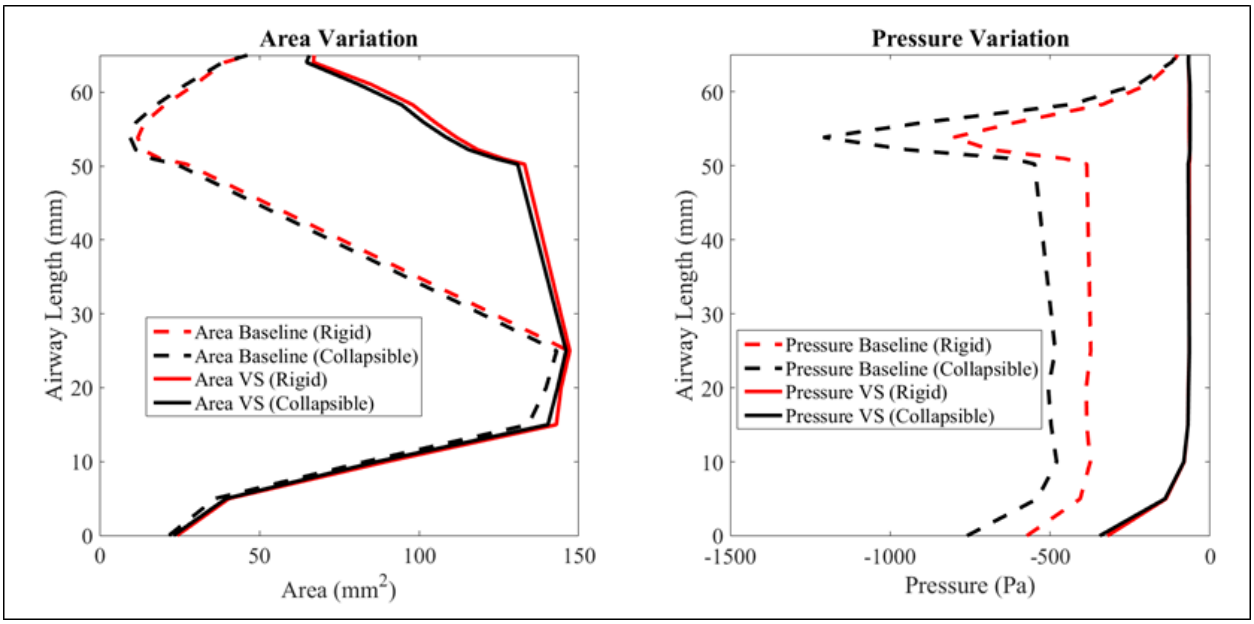

Figure 4.24: Variation in cross-sectional area and pressure along the pharynx for pre and post-operative airways (Note: red solid/dashed line – rigid model, black solid/dashed line – collapsible model).

Table 4.6 indicates the change in airway resistance between baseline and virtual surgery including and excluding tissue compliance. The pharyngeal resistance of the airway computed from flow simulations has been previously correlated with AHI [145]. The AHI decreased by nearly 94 percent following adenoidectomy and correlated well with the velopharyngeal resistance obtained using the rigid (99.2 percent) and collapsible (98.9 percent) models.

However, better concordance between the change in pharyngeal resistance and AHI was achieved with the latter. The distribution of equivalent strain for the pre and post-operative cases is indicated in Figure 4.25. The largest strain (16%) for the virtual surgery was observed at the base of the tongue. The strain at the site of obstruction in the velopharynx was lower by approximately 84 percent than the corresponding baseline case. Tissue strain resulting from contact of the soft palate with the adenoid (Section Y-Y') was also not observed following virtual surgery (Section Z-Z').

Table 4.6: Summary of pharyngeal and overall airway resistance before and after surgery (Note: Units for resistance and AHI employed in this study is Pa/lpm and Events/hr respectively).

Case	**Overall**		**Velopharynx**		**Pharynx**		
	Rigid	Collapsible	Rigid	Collapsible	Rigid	Collapsible	**AHI**
Pre-Operative Airway	93.2	159.5	13.1	18	20.56	28.22	6.3
Post-Operative Airway	80.3	104.4	0.1	0.2	10.37	11.4	0.4
Percent Change (Pre-op to Post-op)	13.8	34.5	99.2	98.9	49.5	59.6	93.7

4.5.4.3 *Discussion*

For the virtual surgery, choosing the k-ε model would have overestimated the surgical outcome for the same amount of tissue removed. Conversely, selection of this model would have guided the surgeon to remove less tissue to achieve the same airway patency. Large eddy simulations (LES) [44] and direct numerical simulations (DNS) of flow in the upper airway [146] have been performed previously to demonstrate the unsteadiness in pharyngeal airflow. High computational

costs resulting from resolving all flow scales makes these aforementioned methods less suited for clinical applications. Besides, flow velocities and pressure distribution predicted using the k-ω SST model has been observed to correlate well with those obtained using LES [40].

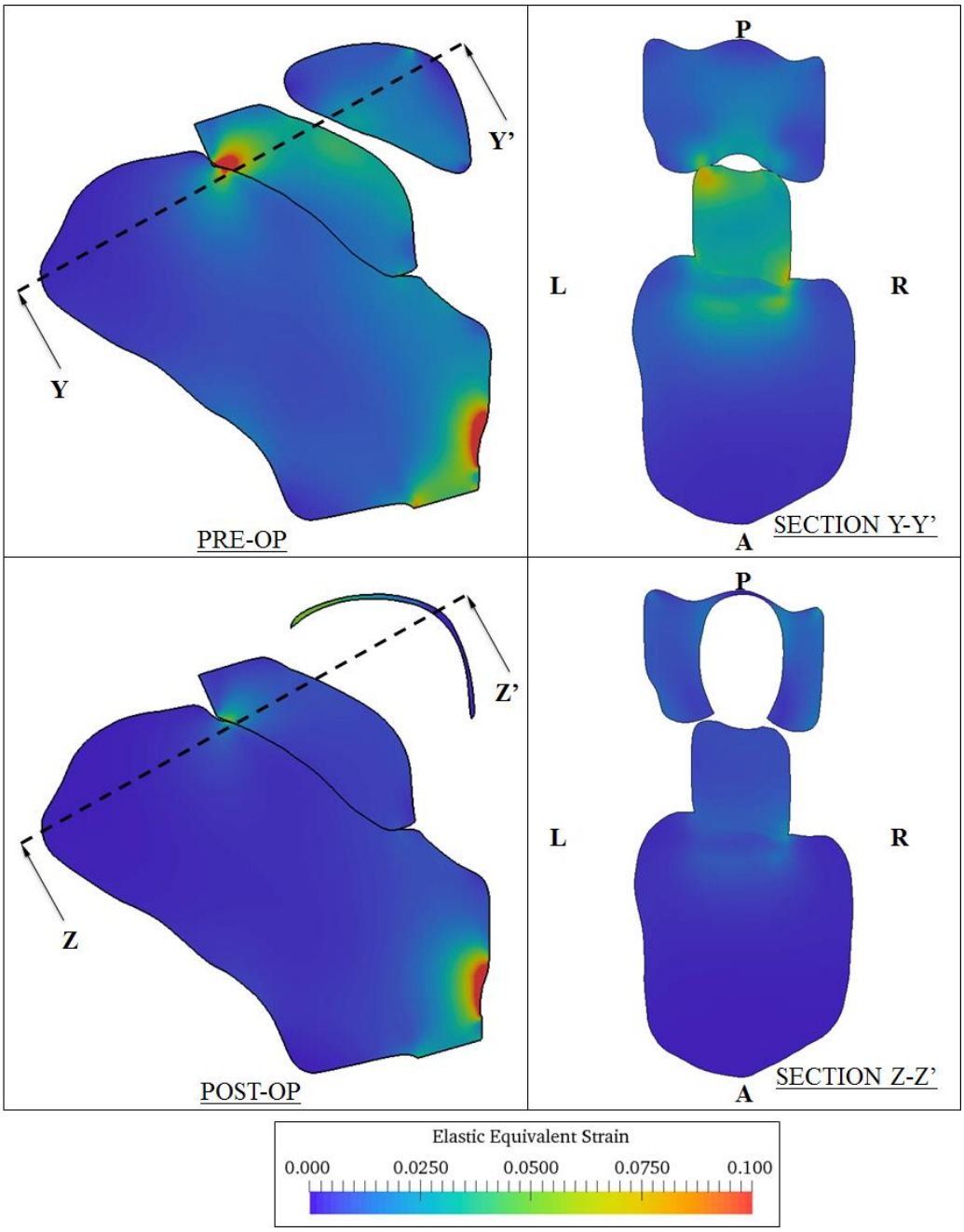

Figure 4.25: Contours of elastic equivalent strain of airway tissue in the mid-sagittal plane for baseline and virtual surgery (Note: Section Y-Y' and Z-Z' have the same spatial location and angular orientation, A – Anterior, P – Posterior, R – Right, L – Left).

Selection of a higher flow rate would have potentially underestimated the effectiveness of the surgery. Conversely, selecting a higher flow rate would have guided the surgeon to remove more tissue to achieve the same airway patency. It is thereby necessary to accurately measure volumetric airflow rates and corresponding variability between breaths in patients with OSA, during sleep. For the virtual surgery, truncation of the airway would have potentially underestimated the surgical outcome for the same amount of tissue removed. Conversely, excluding the nasal cavity would have guided the surgeon to remove more tissue to achieve the desired airway patency. The geometry of the nasal cavity influences the nasopharyngeal pressure drop and flow entering the choanae [119]. However, pressure at the posterior end of the nasopharynx can be estimated physiologically using IRB approved pressure catheters [97] to potentially minimize the need to model the complete airway and produce results similar to those obtained from the full model [133].

Selection of the Yeoh, Mooney-Rivlin or Gent models would have potentially estimated an identical surgical outcome as that predicted by the Neo-Hookean model, for the same amount of tissue removed and flow conditions. The surgeon would have removed the same amount of tissue for all material models analyzed, to ensure that the airway remains open during inspiration. It should be noted that the Gent model was tested since pharyngeal tissue could potentially exhibit a strain-stiffening behavior [125, 126]. Response of upper airway tissue to compressive loads [117] has been described previously using the Yeoh material model. Although, mechanical testing could potentially assist in improved characterization of the mechanical behavior of pharyngeal tissue on a subject-specific basis, it is currently limited to tests involving tissue specimens from cadavers and animal models. The choice of a bonded contact between the tongue and soft-palate was primarily based on MR images (Fig. 4.17a). Since human saliva has a high

viscosity [147], it was assumed that flow induced forces were not sufficient to overcome the strength of the adhesive bond between the two tissue structures. It is hypothesized that large strains at the interface between the tongue and soft-palate for the pre and post-operative case could be attributed to flow induced forces and the bonded contact. This boundary condition would not be applicable for open oral airways since the velum would be freely suspended in the oral cavity.

Contour plots of velocity magnitude for the baseline and virtual surgery (Fig. 4.23) indicate that deformation of tissue supporting the pharynx would result in flow acceleration [46] and a larger jet spreading angle for the same value of maximum inspiratory flow rate. Narrowing of the pharynx in the collapsible case increased the velopharyngeal pressure drop as compared to the rigid case (Fig. 4.24). Airflow velocity would subsequently increase to maintain the continuity criterion and the negative pressure drop would increase further eventually resulting in airway occlusion. For the virtual surgery, minimal airway narrowing resulting from small post-operative tissue displacements would lower the probability of velopharyngeal collapse. The present study employed a quasi-steady assumption of pharyngeal narrowing and illustrated the interaction between airflow and surrounding tissue at a fixed time point in the breathing cycle. An enhanced description of the same could be potentially obtained using transient simulations. Wall shear stresses excluded from the present study, can potentially cause discomfort to upper airway tissue [45]. Although the decoupled CFD-CSM-CFD method presented in this study is easy to implement and suitable for clinical applications involving small tissue displacements of the order of 1 – 1.5mm [140], the aforementioned observations emphasize the necessity to perform fully-coupled FSI simulations of pharyngeal airflow [49]. The inspiratory flow patterns and magnitude of tissue displacements described using the presented CFD-CSM-CFD method

were in good agreement with previous computational studies of pharyngeal airflow using fully-coupled FSI modeling [46]. Fully-coupled FSI modeling of opposite wall contact could be achieved using non-body conformal grid methods such as the immersed boundary method [148]. Parapharyngeal fat pads and ptergyoid muscles to the right and left of the airway [109] were excluded from 3D simulations due to challenges in accurately identifying their extents in MR scans. Lateral airway wall tissue can significantly influence pharyngeal compliance, as observed in a previous study [125]. Pediatric DS patients with severe OSA exhibit large variations in tissue stiffness along the airway length [126]. The present study modeled the passive response of tissue to airflow. Neuromuscular activity or additional airway muscles currently incorporated into CSM models [121, 137, 149] would have to be extended to FSI simulations. Improved validation of the presented computational model could be potentially achieved using post-operative tissue elasticity measurements and MR imaging. It would also be necessary to analyze control subjects and additional patients with surgeries such as glossectomy or lingual tonsillectomy to correlate the virtual surgery outcome with known measures of OSA severity using detailed statistical analysis.

Chapter 5

Modeling Velopharyngeal Obstruction in PCOS

Computational fluid dynamics (CFD) has been employed to describe airflow patterns in adult [150] and pediatric female subjects [42, 151] with PCOS. In this chapter, the necessity to model flow induced obstruction in PCOS subjects with sleep apnea is illustrated by mapping flow-induced strain of velopharyngeal tissue using a deformable image registration algorithm. A method that combines medical image analysis and simulations of flow-induced airway tissue motion to non-invasively determine subject-specific biomechanical properties of the soft palate in PCOS is then described. The estimated mechanical properties are then employed in the FSI model to evaluate the effectiveness of different surgical procedures in minimizing the possibility of airway occlusion.

5.1 *Strain Mapping of Pharyngeal Tissue during Quiescent Breathing*

5.1.1 *MR Imaging, Flow Waveform Acquisition & 2D Segmentation of Soft Tissue*

Two subjects namely a female OSA patient and a gender matched control were recruited at the Montefiore Medical Center for Polycystic Ovarian Syndrome [152]. Magnetic resonance (MR) image acquisition was performed during wakefulness without any sedation. Informed consent was obtained from the subjects and the study was approved by the Institutional Review Board at the Albert Einstein College of Medicine. Breathing airflow waveforms were collected from a nasal cannula coupled to a pressure transducer (TSD-160B, Biopac Systems Inc., Goleta, CA). A National Instruments data acquisition board (DAQCard-6036E coupled to a SCB-68 board) was used to digitize the signal and was displayed on a custom graphical user interface written for Labview (National Instruments, Austin, TX). The MR images were collected on a 3T Philips

Achieva scanner (Phillips Medical System, Best, Netherlands). The patient was positioned in the radiofrequency (RF) coil and head and neck motion were constrained using padding on both sides of the head. The dynamic study used a 3D, retrospectively-gated, turbo gradient echo sequence. Images were acquired over the complete respiratory cycle in 10 equal phase increments [151]. Additional details regarding the gating system and imaging protocol have been described elsewhere [152].

The image dataset was processed using Matlab (Mathworks Inc., Natick, MA) to extract the mid-sagittal image for each point in the breathing cycle. Accordingly, a set of 10 images were available for each patient. An in-house Matlab-based image processing algorithm was written to manually identify the outline of the soft-palate for each time point, with the help of a radiologist. A binary mask was created and was then embedded on the original image to extract the pixels corresponding to soft-tissue only. This procedure enabled to narrow the region of interest to the soft-tissue and subsequently minimize the artifacts in the image-registration process described in the following section. Figure 5.1 summarizes the procedure adopted in the study to identify velopharyngeal tissue from MR images.

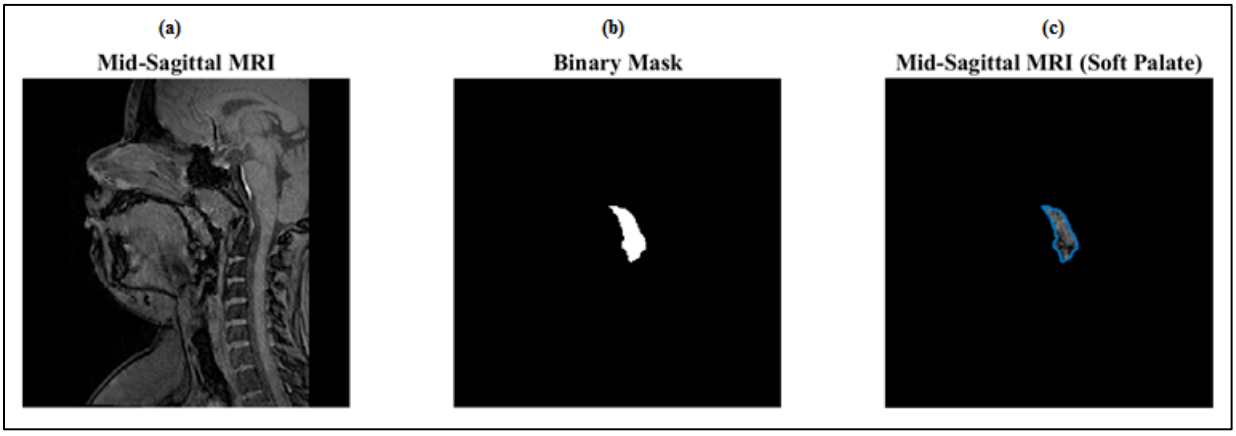

Figure 5.1: a) Mid-sagittal MR image (sequence 1) of the pharyngeal airway and surrounding anatomy (OSA subject) b) Binary image of the ROI (Tongue and Soft Palate) c) Mid-sagittal MR image of the tongue and soft palate obtained by embedding the binary mask.

5.1.2 *Deformable Image Registration and Displacement Mapping*

An open-source demons deformable registration scheme written in Matlab was employed to estimate the temporal variations in strain [153]. This diffusion-based registration method simulates an image-based force to align gradients in the images. Neighboring points are restricted to move alongside each other to model the image elasticity. The algorithm defines the displacement of every pixel in the fixed image x_f such that it translates the pixel to the corresponding position in the moving image (x_m):

$$x_m = x_f + u(x_f) \tag{5.1}$$

The deformation field $u_n(x_f)$ was computed successively in n iterations using the following updating rule:

$$\begin{aligned} u_{n+1}(x_f) &= u(x_f) + \Delta u_n(x_f) \\ \Delta u_n(x_f) &= -\frac{2(I_m - I_f)(\nabla I_m + \nabla I_f)}{(\nabla I_m + \nabla I_f)^2 + (I_m - I_f)^2} \end{aligned} \tag{5.2}$$

where I_f is the intensity value in the fixed image at position x_f, I_m is the intensity value in the moving image at location x_m, ∇I_f and ∇I_m are gradients of the respective intensity values. A total of 500 iterations were computed for each image pair and additional iterations did not significantly affect the accuracy of the resulting displacement field. The deformation gradient and Green-Lagrangian strain tensor defined in eqn. 2.5 were then computed for the displacement field. Principal strains were then computed from the Green-Lagrangian strain tensor assuming a state of plane strain [154]. The octahedral shear strain was then calculated from these values of principal strain [153]. The code adopted in this study was initially validated for a phantom image pair shown in Figure 5.2. The displacements and shear strains obtained using diffusion-based registration were compared to the same obtained using an alternative hyperelastic warping

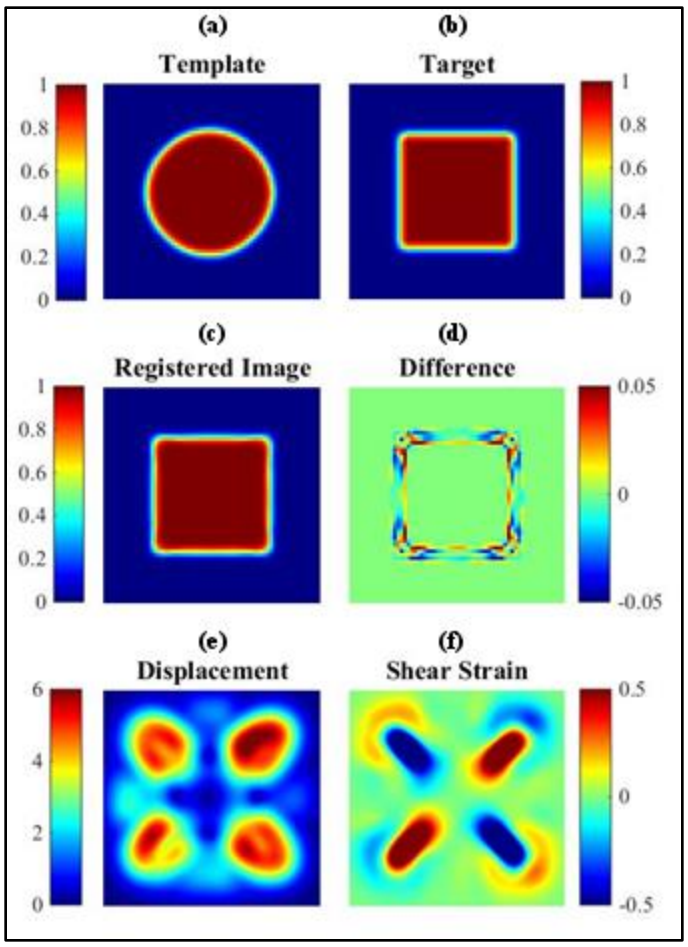

Figure 5.2: Validation of the diffusion based registration algorithm for a phantom image pair a) template (moving) image b) target (stationary) image c) registered image d) difference between target and registered image e) contours of displacement resulting from the fluid matching f) contours of Green-Lagrange shear strain (E_{xy}).

registration [155] algorithm implemented in FEBio [70]. The displacement and strain values were interpolated on a finer grid to obtain a smooth and continuous displacement and strain field. The magnitude and range of displacements and shear strains were in good agreement with those obtained using hyper-elastic warping. For octahedral shear strain mapping of velopharyngeal tissue, the first image corresponding to the start of the inspiratory breathing phase was used as the template or moving image. The remaining 9 images were set as the target or fixed image. Maximum and mean strains for the apneic and control subjects were computed at each time point in the breathing cycle.

5.1.3 *Results & Discussion*

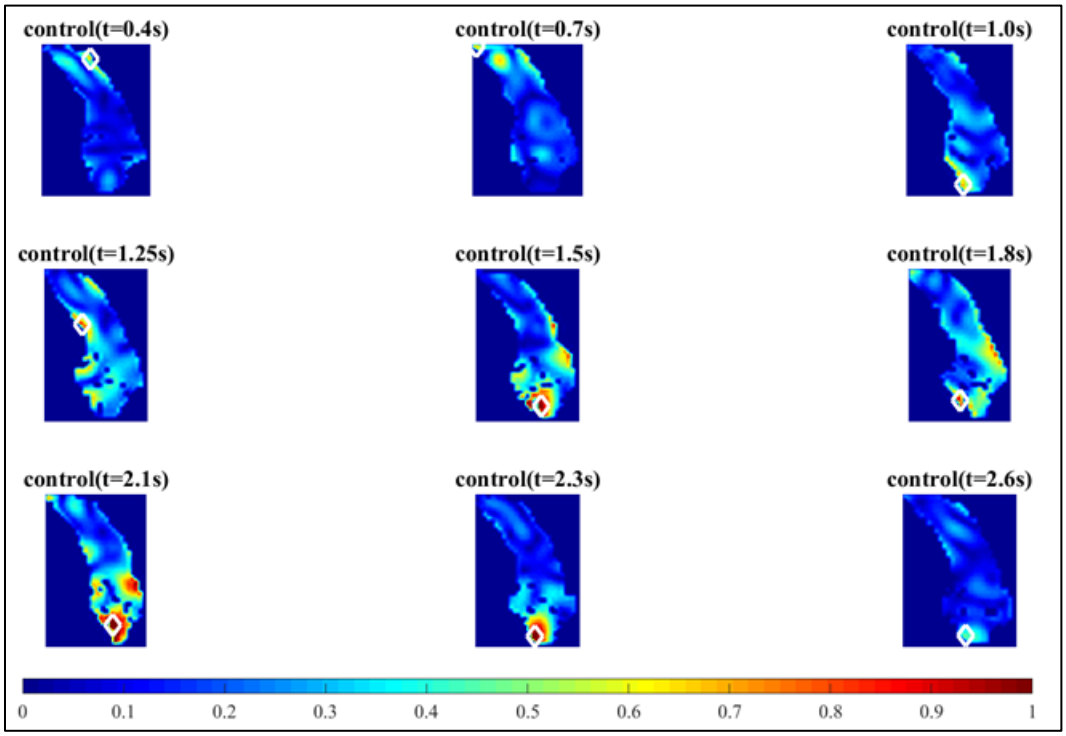

Figure 5.3: Temporal variation of shear strain in the soft palate of the control subject at successive time points 0.4s, 0.7s, 1.0s, 1.25s, 1.5s, 1.8s, 2.1s, 2.3s, 2.6s. White diamond markers indicate location of maximum strain.

Temporal variation in octahedral shear strains of the soft palate at individual time-points in the breathing cycle is indicated in Figure 5.3 for the control subjects. As can be seen, the location (indicated by white diamond markers) and magnitude of the peak displacement varied throughout the breathing cycle. At peak inspiration (t=0.4s), the strain was greatest on the posterior wall in the proximity of the adenoid and hard palate. With decreased inspiratory flow volume (t=0.7s), peak strain was located on the anterior edge of the soft palate. High strain concentration was also observed inferior to the hard palate and at the velum with further reduction in the flow volume (t=1s). At end inspiration (i.e. t=1.25s), strain was concentrated on the anterior face of the soft palate in the oral airway. Peak strains were observed in the velum during the entire expiratory phase of the breathing cycle (t=1.5-2.6s). Figure 5.4 indicates the

temporal variation in peak and average strains in the soft palate for the healthy individual. As can be seen, temporal variation in maximum and mean strains were similar over the breathing cycle, with the maximum value occurring prior to the peak expiratory phase (i.e. t=2.3s). For the control, greatest magnitude of peak and average strains were 108 and 30 percent respectively.

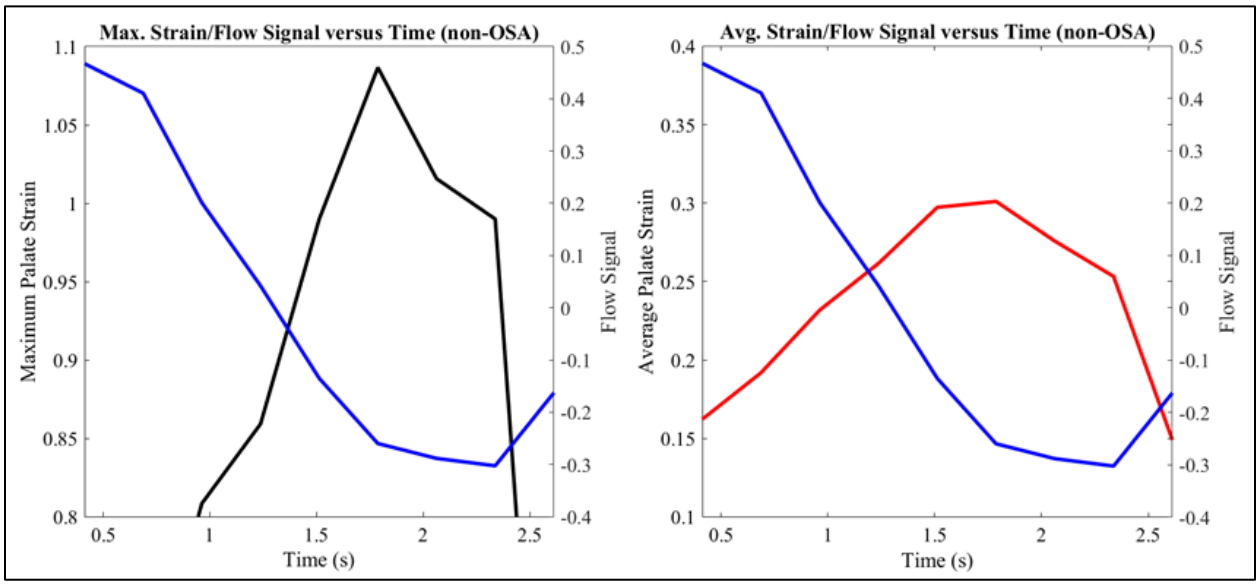

Figure 5.4: Temporal variation in peak (black line) and mean strain (red line) in upper airway tissue for the control. The flow signal (blue line) is also superposed for reference (Note: Positive voltage refers to inspiration and negative voltage corresponds to expiration).

Temporal variation in strain at the individual time-points in the breathing cycle for the OSA subject is indicated in Figure 5.5. The maximum magnitude of strain prior to the peak inspiratory flow (t=0.5s) was observed on the posterior wall approximately 50 percent of the length of the uvula. The value increased with increasing inspiratory flow volume between 0.5 and 0.8s. Unlike the control case, maximum strain during peak inspiration was observed at the tip of the soft palate. With decrease in inspiratory flow volume and increase in expiratory flow, the strains increased (t=1s to t=1.7s). During this period strains were highest at the velum. Figure 5.6 indicates the temporal variation in peak and average strains of the soft palate for the apneic subject. Trends describing the temporal variation of the maximum and mean values were similar

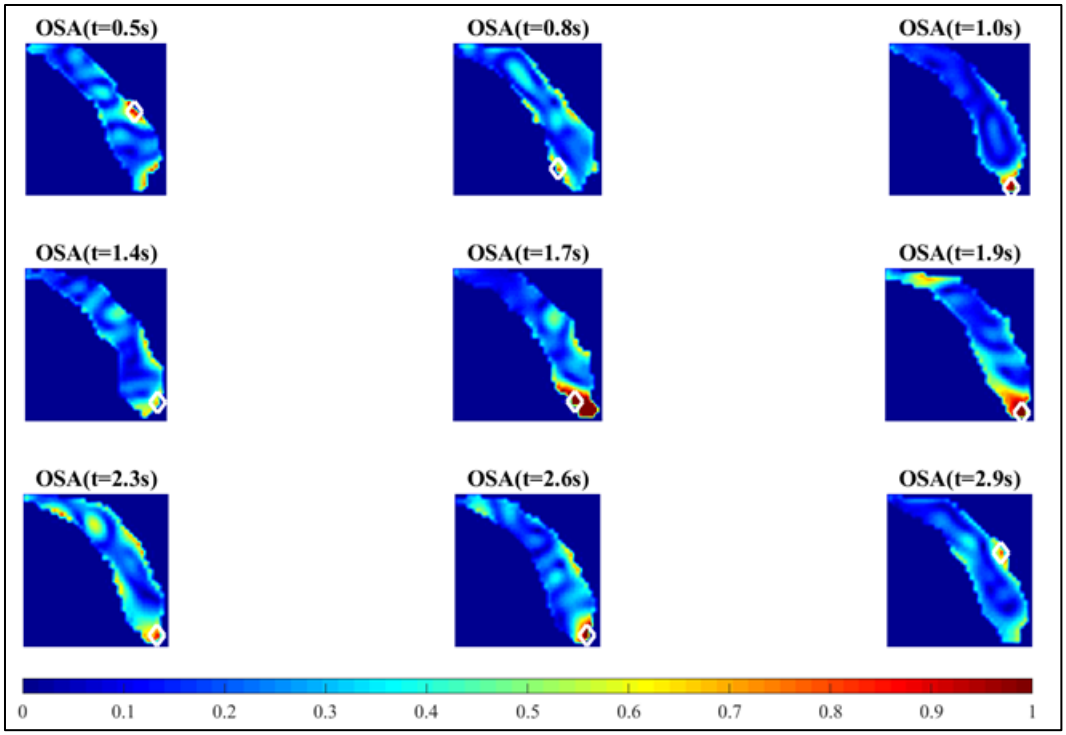

Figure 5.5: Temporal variation of shear strain in the soft palate of the OSA subject at successive time points 0.5s, 0.8s, 1.0s, 1.4s, 1.7s, 1.9s, 2.3s, 2.6s, 2.9s. White diamond markers indicate location of maximum strain.

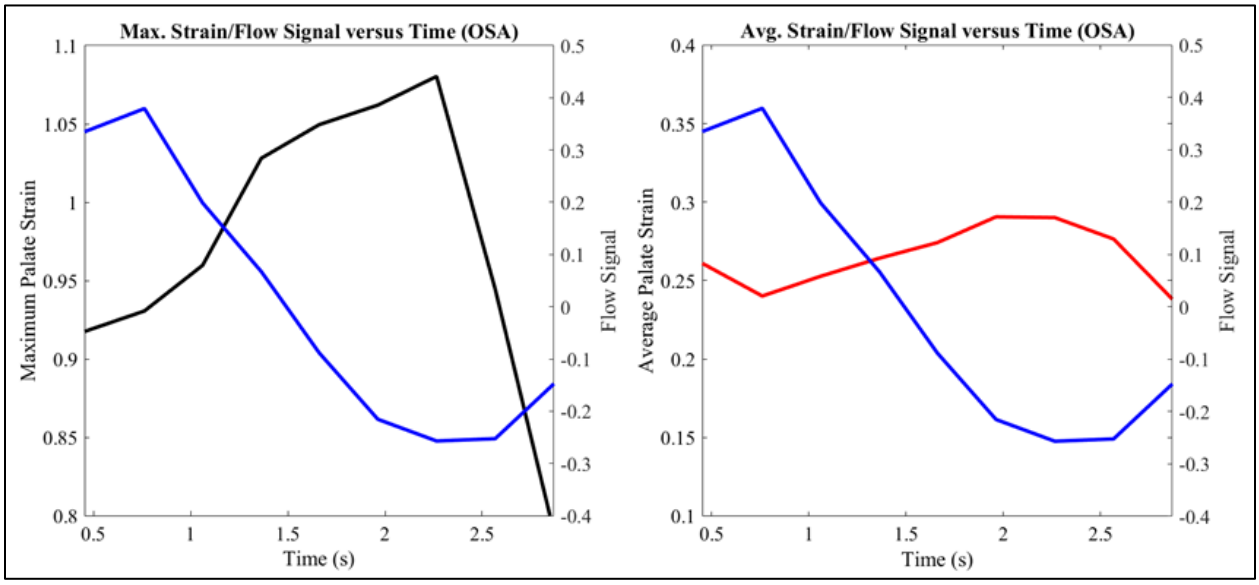

Figure 5.6: Temporal variation in peak (black line) and mean strain (red line) in upper airway tissue for the OSA subject. The flow signal (blue line) is also superposed for reference (Note: Positive voltage refers to inspiration and negative voltage corresponds to expiration).

as observed for the control. The maximum value was observed at peak exhalation unlike the healthy case. Besides, the greatest magnitude of peak and average strains was similar to the control. However, the time averaged maximum and mean strains were 11 percent and 8 percent higher than the corresponding values for the healthy case.

These results indicate that greatest magnitude of tissue strain was observed at the tip of the soft palate for the OSA patient and the healthy subject. Strain maps obtained in this study were relatively coarse due to the low spatial resolution of the MR images analyzed. Besides, changes in brightness levels and differences in soft-tissue segmentation between time-points could generate inaccuracies in the strain measures. Moreover, the presented methodology gives an estimate of airway tissue elasticity that cannot be directly incorporated into a computational model of airway obstruction since flow-induced loads and a suitable hyperelastic constitutive model were not considered in the analysis. This method was potentially useful in recognizing the most compliant sections of upper airway tissue and the phase in the breathing cycle that corresponded to the greatest tissue deformation.

5.2. *Biomechanics of the Soft-Palate in PCOS*

5.2.1 *Reconstruction and Discretization of Fluid and Solid Domains*

36 sagittal MR images (1.1 mm thick) corresponding to the end of the inspiratory phase (i.e. beginning of exhalation) and the peak expiratory phase of the breathing cycle were employed in this study. The images were imported into the Mimics (Materialise Inc., Plymouth, MI) image processing software for reconstruction of anatomically accurate geometries of the upper airway and soft-palate. Three-dimensional (3D) models of the airway comprising of the pharynx, oral airway, trachea and nasal airway were segmented using a thresholding algorithm (lower threshold gray value (GV): 0, upper threshold GV: 40) for the control and apneic subjects.

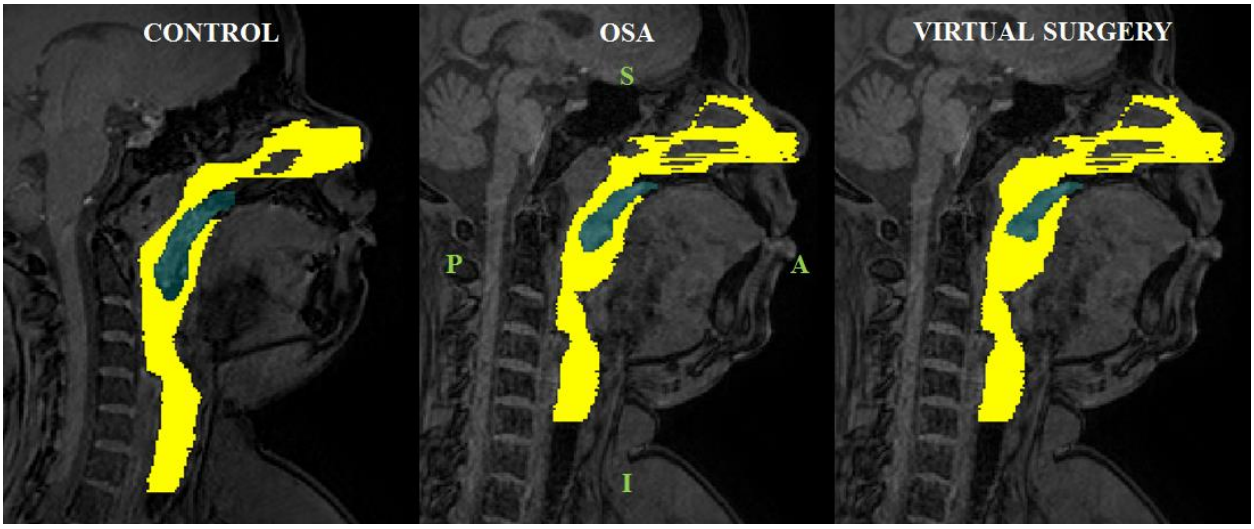

Figure 5.7: Mid-sagittal MR image (end inspiratory phase) corresponding to the control, OSA patient and virtual surgery (Note: yellow – pharynx, blue – soft-palate, S – Superior, I – Inferior, A – Anterior, P – Posterior, Virtual surgery – palatoplasty: 6 mm, adenoidectomy: 10 mm, genioglossus advancement – 2 mm, Removal of soft tissue increases airway caliber locally).

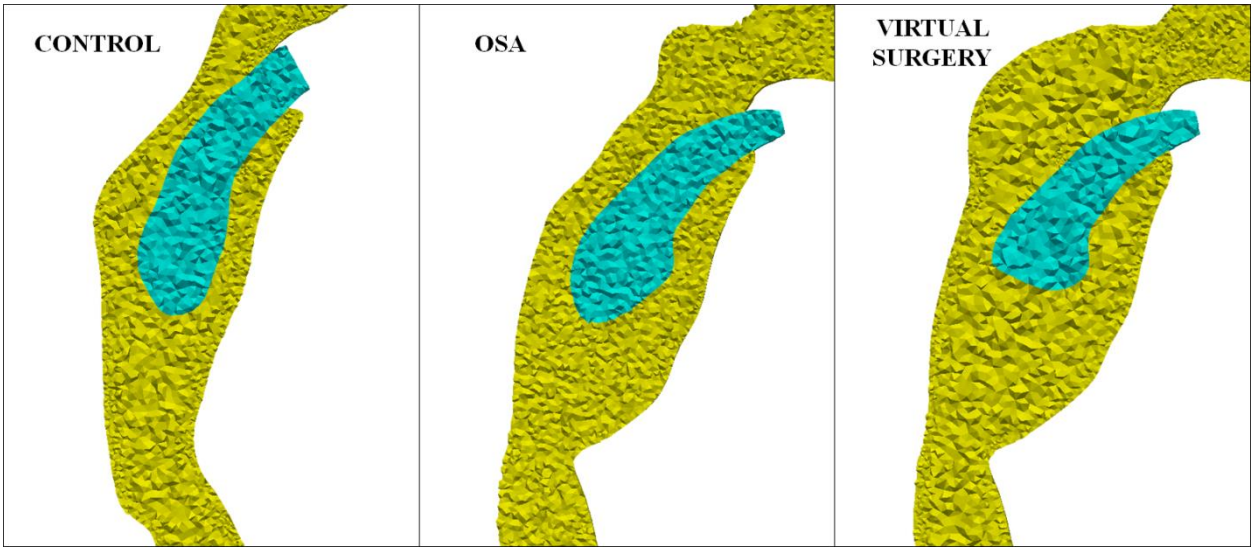

Figure 5.8: Discretization of the flow (yellow) and structural (blue) domains corresponding to the control, OSA and virtual surgery cases.

3D geometries of the soft-palate were reconstructed for the 2 subjects using a lower threshold GV corresponding to 50 and upper threshold GV corresponding to 150. It should be noted that lateral extents of the soft-palate were similar to previous computational studies involving flow-

induced motion of upper airway structures in pediatric OSA patients with Down syndrome [156]. Previous studies involving computational modeling of soft-palate movement in response to airflow assumed that the tissue was completely 'immersed' in the pharynx [47, 48] and a similar approach was adopted in this study (Fig. 5.7). Additionally, 10 mm of adenoid tissue, 6 mm of palate tissue and 2 mm of tongue tissue were 'virtually' removed [156] for the OSA case (Fig. 5.7), to replicate a surgical scenario comprising of adenoidectomy, palatoplasty and genioglossus advancement.

Surface artifacts were then removed by smoothing the coarse geometric models. A fixation surface was created for the soft-palate at the hard palate. Inlet and outlets for the airway were generated at the trachea and nostrils respectively using Mimics. Common interfaces between the soft-palate and airway were then identified by exporting the pre and post-operative geometries to 3-Matic (Materialise Inc., Plymouth, MI). Surface meshes of the airway for the control, OSA and virtual surgery (VS) cases were refined at the fluid-solid interface and at narrow cross-sections using 3-Matic, to obtain better resolution of flow variables. Volume meshes for the airway and soft-palate (Fig. 5.8) were then generated using ANSYS T-Grid (ANSYS Inc., Canonsburg, PA). We employed tetrahedral cells for the flow [42, 133] and structural domain [156]. Although polyhedral cells potentially enhance the rate of solution convergence and ensure homogenous distribution of wall variables [156], tetrahedral elements were preferred for the flow domain (control: 800000 elements, OSA: 700000 elements, virtual surgery (VS): 900000 elements) due to flow solver element constraints for computations involving dynamic meshes. Linear tetrahedral elements generated for the tissue (control: 90000 elements, OSA: 60000 elements, VS: 50000 elements) were converted into quadratic tetrahedrons [50] using ANSYS ICEM-CFD (ANSYS Inc., Canonsburg, PA) since the latter are

preferable for modeling nearly incompressible materials. It should be noted that the mesh resolution of the flow and solid domains were of the same order of magnitude (10^5 and 10^4) as that employed in a previous study [156].

5.2.2 *Computational Modeling of Flow-induced Tissue Motion*

Transitional or fully turbulent flow in the pediatric upper airway corresponding to physiological flow rates has been modeled previously using the incompressible Reynolds Averaged Navier Stokes (RANS) [156] and the same was employed for this study. The present study employed the k-ω shear stress transport (SST) model as described previously in Chapters 3 and 4. A no-slip boundary condition was prescribed on the airway wall. Flow waveforms for 10 normal tidal breaths were averaged for the control and apneic subject [42] to compute the peak expiratory flow rate. Accordingly a flow rate corresponding to 10 liters per minute was prescribed at the inlet in the trachea and an ambient pressure boundary condition was applied at the nostrils. Simulations of soft tissue movement in response to airflow at peak inspiratory and expiratory flows have been performed previously using a transient flow solver [48, 49] and the same was utilized in the present study. Pressure, momentum and turbulence terms were discretized using a second-order upwind scheme. A coupled formulation was adopted to achieve pressure-velocity coupling [156]. A least-squares cell-based scheme was employed to evaluate gradients. Time integration was performed using a second-order implicit scheme that enabled selection of larger time steps since the scheme is unconditionally stable [48].

The governing equations of tissue motion in dynamic equilibrium (Chapter 2) were discretized and solved to evaluate the displacements and stresses in soft-palate. It should be noted that a neo-Hookean model was employed in this study, since the study involving DS apneic patients (Chapter 4) showed that tissue displacements were predicted accurately by this

relatively simple constitutive law for identical flow conditions [156]. Body forces arising from gravity were not considered since the MR images were acquired in supine position [42]. A zero displacement boundary condition was prescribed at the fixation surface. The density and Poisson's ratio of the soft palate was assumed to be 1100 kg/m^3 and 0.475 respectively. An FSI boundary condition was applied at the interface between the airway and tissue [48] (Chapter 2). The grid for the flow domain was remeshed at every time step and smoothed using a diffusion based scheme [46] to maintain mesh quality and minimize the possibility of negative cell volumes. Governing equations for the flow and structural domain were solved using ANSYS multi-physics software (ANSYS Inc., Canonsburg, PA). The ANSYS System Coupling code was employed to communicate forces from the flow solver to the structural solver and relay the resulting displacements to the flow solver to update the mesh and flow variables [46]. A stagger loop was employed to ensure that flow, structural and data transfer variables converged at the end of each step. 20 iterations were observed to be sufficient for each stagger loop. A time step corresponding to 0.0025 s was employed in this study and 70 coupling steps were simulated to fulfill the convergence criteria defined in previous studies [46, 156]. The time required to increase the magnitude of flow-induced forces on the soft-palate from zero to the maximum value (~ 170 ms), was similar to the same employed previously [48]. Post-processing was performed using Paraview (Kitware Inc., Clifton Park, NY).

5.2.3 *Results & Discussion*

5.2.3.1 *Inverse Estimation of Biomechanical Properties*

FSI simulations have been employed previously to noninvasively compute viscoelastic material parameters of adherent osteocytes in fluid flow [157]. Mechanical properties of the soft-palate for the control and apneic subjects were not known a-priori and the same were estimated using

the inverse FSI methodology described in this section. An initial guess value of the shear modulus corresponding to 2420 Pa obtained previously using MR elastography [158] was employed in this study. FSI computations of soft-palate movement were performed for the flow boundary conditions described in the previous section and the shear modulus was iteratively changed to match peak expiratory tissue displacements obtained using MR imaging. At the end of each iteration, mid-sagittal profiles of the soft-palate obtained from simulations (Figure 5.9: solid red line) were compared with the same obtained from imaging (Figure 5.9: solid black line) until the error was minimized [157]. Accordingly, the optimized shear modulus for the control and apneic subjects was 10000 Pa and 7250 Pa respectively. Mechanical properties of the soft-palate for the two subjects evaluated using the proposed method were within the range of values estimated previously [156] (Chapter 4).

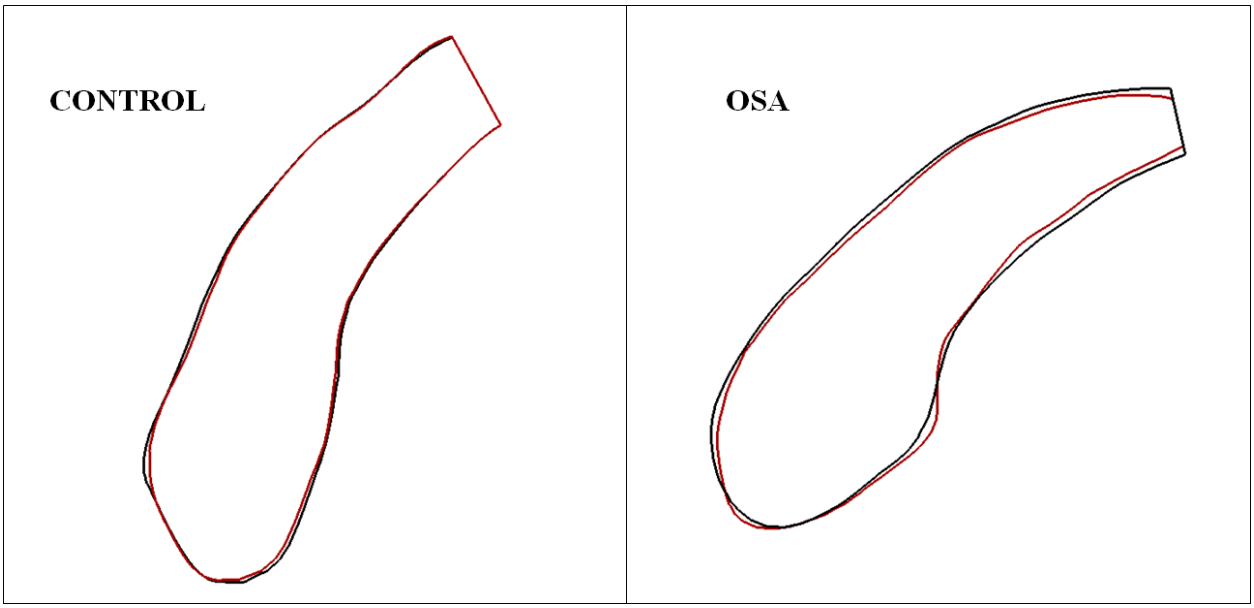

Figure 5.9: Mid-sagittal outlines of the soft palate at peak exhalation obtained from MR imaging (solid black line) and computational modeling (solid red line) for the control and OSA patients considered in the study.

As described in Chapter 4, shear modulus of pharyngeal tissue varies exponentially with the flow rate [156]. Recognizing the sensitivity of the material property to the choice of

volumetric airflow and breath-to-breath variations in airflow volume, it would be necessary to repeat the optimization process for the highest and lowest values of expiratory airflow and determine the range of tissue elasticity for each subject. Secondly, passive mechanical properties of the soft-palate were estimated in this study. Neuromuscular control resulting from activation of the levator veli palatini and musclus uvulae fiber groups [159] would have to be considered in a future study to model flow-induced palate movement during wakefulness. The present study described estimation of material properties for one of several upper airway structures, to minimize the number of unknowns. Additionally the sagittal MR images employed in this study did not include the complete geometry of the tongue and lateral wall tissue [152]. Inclusion of these aforementioned airway structures, the adenoid and posterior wall mucosa could significantly increase the complexity of the optimization problem. Besides, the biomechanical response of pharyngeal tissue has been characterized previously as viscoelastic [142, 160]. The neo-Hookean constitutive model would have to be suitably modified in a future study to incorporate relaxation of mechanical stresses with increasing strain. Estimation of the anisotropy in material properties of the soft-palate would also be necessary since previous studies involving MR elastography have indicated variations in tissue stiffness along the length of the uvula [158]. The presented methodology would have to be repeated for the same subjects under conditions of sedation-induced or natural sleep to evaluate possible variations in tissue elasticity resulting from reduced neuromuscular control. Although significant out-of-plane movements of the uvula stemming from additional bending or twisting modes were not observed in the dynamic MR images, the same could potentially increase the complexity of the profile matching technique presented in this section. Besides, a higher spatial resolution of the MR images would significantly enhance the shape registration technique employed in this study.

5.2.3.2 *Virtual Surgery*

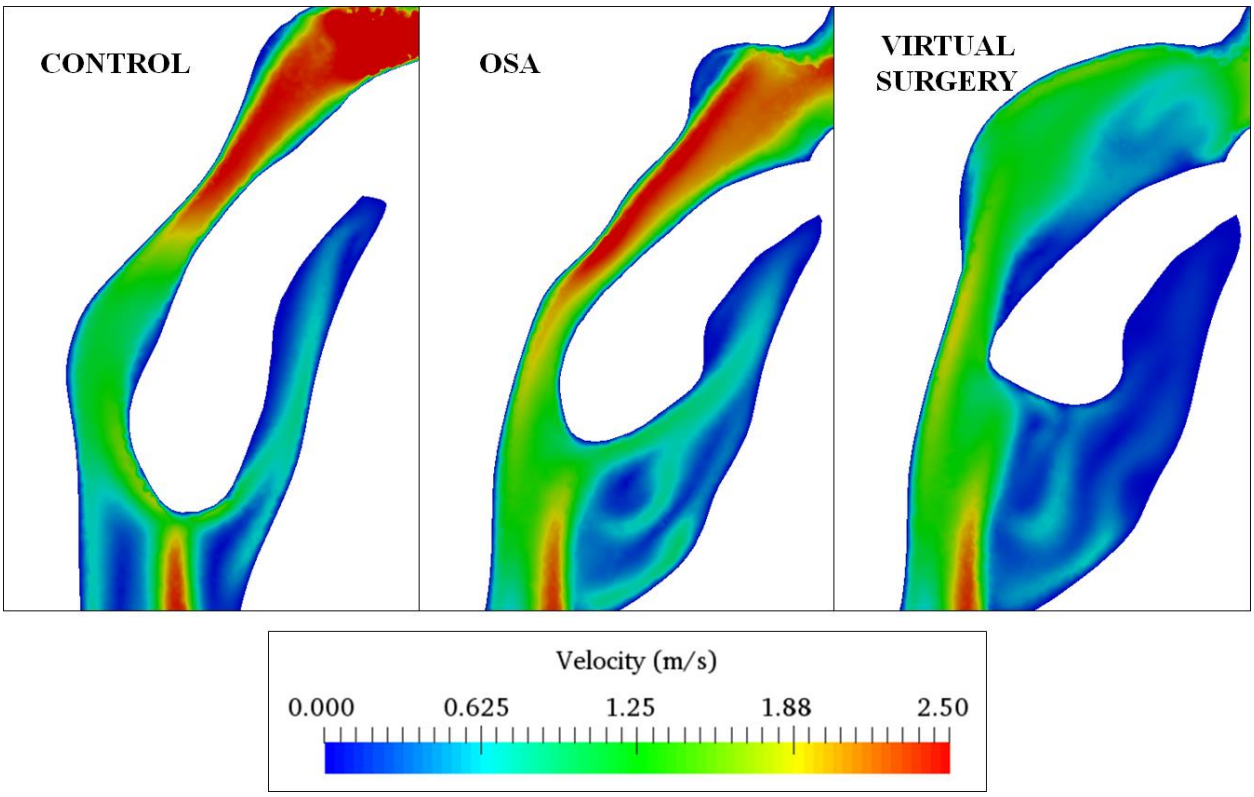

Figure 5.10: Contour plots describing velopharyngeal airflow patterns in the mid-sagittal plane for the control, apneic and virtual surgery cases at peak exhalation.

Figure 5.10 describes contour plots of flow velocity magnitude in the velopharynx for the control, OSA and virtual surgery cases at peak exhalation. As can be seen for the control and pre-operative OSA case, the flow accelerated at the narrowest cross-section. The magnitude of flow velocity, size and strength of the separation region in the oral airway were comparable for the healthy and apneic subjects. The flow remained attached to the posterior surface of the soft-palate and velum. For the post-operative case, magnitude of flow velocity decreased by nearly 100 percent in sections of the airway virtually altered by the adenoidectomy. Moreover, palatoplasty resulted in separation of flow on the posterior surface of the soft-palate. We recognized that the absence of the flow separation for the pre-operative case could be attributed to the streamline shape of the soft-palate prior to the palatoplasty surgery. Additionally, the

genioglossus advancement increased the stagnation region in the oral airway. The resistance of the retropalatal airway was computed as the ratio of the velopharyngeal pressure drop to the peak expiratory flow rate. The velopharyngeal resistance for the control (0.48 Pa/lpm) was 70 percent higher than the apneic subject (0.28 Pa/lpm). Following surgery, the resistance decreased by 60 percent. The higher resistance for the normal subject resulted from a smaller airway cross-sectional area in the choanae. Besides, higher airway resistance in controls compared to OSA has been documented in previous computational studies involving a rigid pharynx [42].

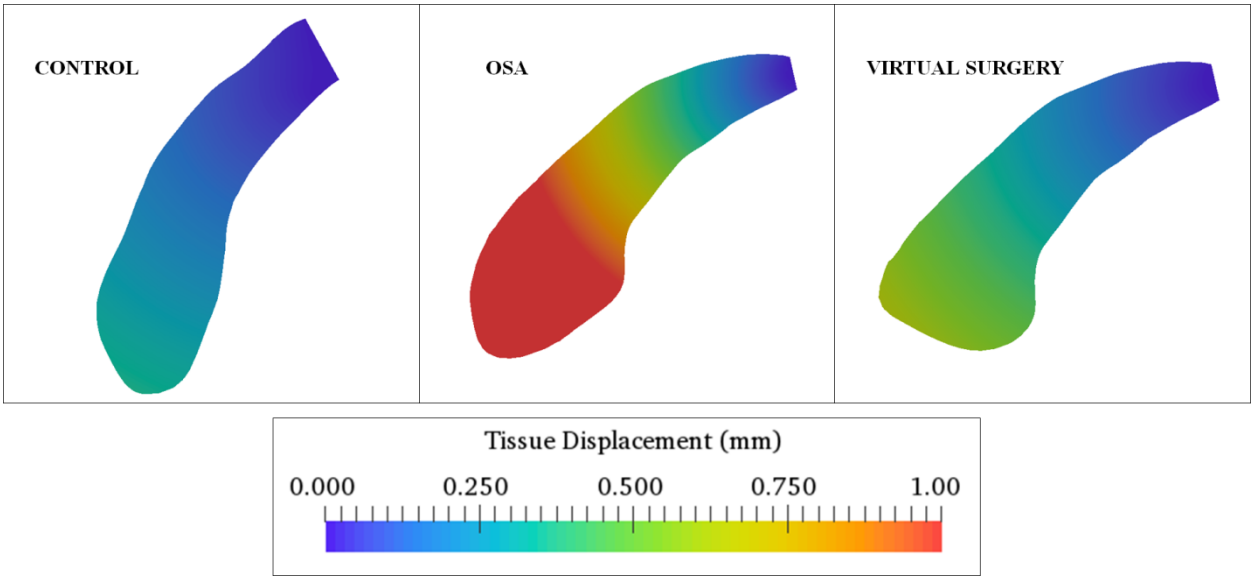

Figure 5.11: Tissue displacement contours in the mid-sagittal plane for the control, apneic and virtual surgery cases at peak expiratory airflow.

Figure 5.11 and 5.12 summarize the mid-sagittal contour plots of peak expiratory palate displacement and mechanical stress for the three cases. As indicated in Fig. 5.11, maximum tissue displacement was observed in the velum for the control, apneic and virtual surgery cases. However, the magnitude of displacement for the pre-operative case was nearly 350 percent higher than the control. The displacement decreased by 63 percent following surgery. The location and magnitude of displacements were in good agreement with previous FSI studies involving the soft palate [47, 48]. Maximum mechanical stresses were observed in the proximity

of the hard palate for all the cases (Fig. 5.12). Stresses for the OSA case were greater than the control by 62 percent. Higher stresses in the apneic subject resulted from a smaller tissue cross-sectional area at the fixation. The stresses for the virtual surgery were lower than the control by 35 percent.

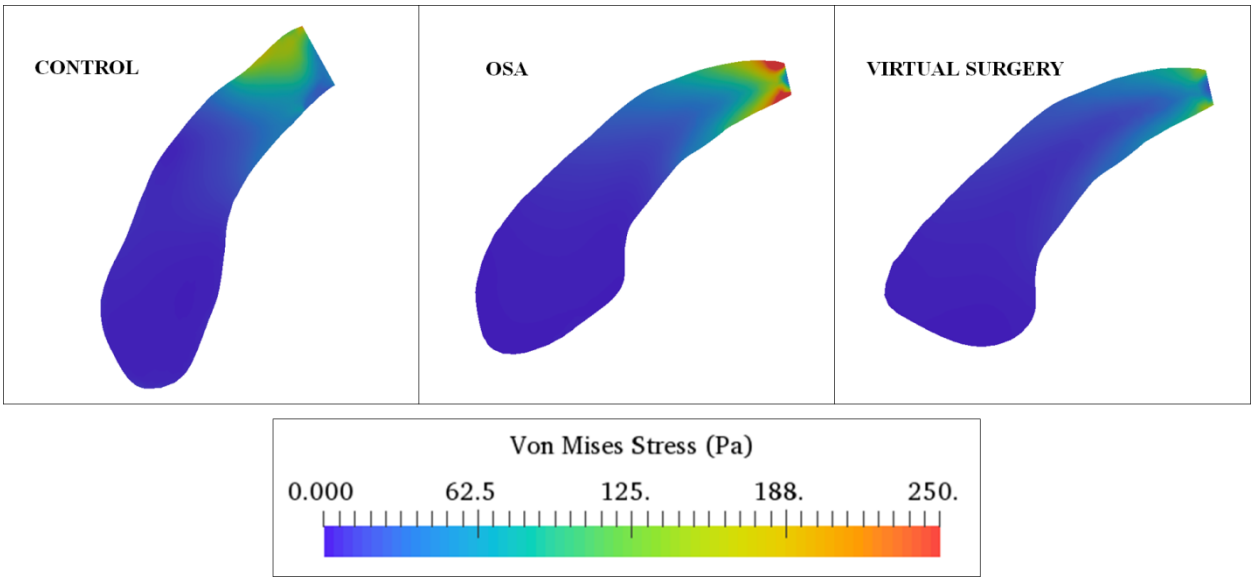

Figure 5.12: Mechanical stress variation in the mid-sagittal plane for the control, apneic and virtual surgery cases at peak expiratory airflow.

It should be noted that a virtual surgery was performed to demonstrate the effect of increasing the airway caliber on flow-induced motion and stresses of supporting tissue. Although the virtual adenoidectomy and palatoplasty resulted in increased airway caliber, changes in tissue displacement resulting from these surgeries were small, as also observed in a previous computational study [161]. The genioglossus advancement resulted in greater damping of tissue motion since the magnitude of flow-induced forces acting on the anterior surface of the palate decreased following the tongue surgery. Although occlusion of the velopharyngeal airway was observed and modeled during the expiratory phase, inspiratory airway collapse could potentially occur when the oral airway is closed. Removal of the adenoids and shortening the palate would significantly decrease the airway resistance and tissue stresses in the latter scenario as observed

in a recent study [156]. The conformal mesh FSI method adopted in this study is suitable for moderate displacements of the soft-palate (~1 to 2 mm) and scenarios involving partial airway occlusion. Modeling complete airway closure could be potentially achieved using non-conformal grid methods such as the immersed boundary technique [162] as discussed previously (Chapter 4). The methodology presented in this pilot study would have to be extended to model the complete respiratory cycle and estimate the effectiveness of additional invasive and non-invasive treatments for sleep disordered breathing. Future studies would also include more subjects to define endpoints based on tissue elasticity and aid clinicians in obtaining an improved description of sleep apnea in patients with polycystic ovarian syndrome.

5.3 *Summary*

- The necessity of incorporating airway compliance for virtual surgery was described using CFD modeling.
- Airway compliance was computed for DS using tube law and 3D compliance mapping methods. Strain mapping of velopharyngeal tissue was performed for PCOS. Two iterative approaches namely 2D CSM and 3D FSI methods were proposed to inversely compute biomechanical properties of upper airway tissue. Advantages and limitations of each of the aforementioned methods were discussed.
- Sensitivity of flow parameters and selection of material models to guide upper airway surgery was described for DS.
- Mechanical properties evaluated using the iterative method was applied to computational models of airway obstruction during inhalation and exhalation to emphasize the role of pharyngeal tissue elasticity on airflow characteristics for planning surgical treatment in OSA.

Chapter 6

Characterization of Aorta Morphology in TS

Results from this chapter were presented at the Biomedical Engineering Society (BMES) 2015 Annual Meeting Tampa, FL, 2016 ENDO Annual Meeting, Boston, MA and published in one first author manuscript in the Journal of Cardiovascular Magnetic Resonance.

The present study sets out to devise a novel continuous measurement tool to improve the ability to, in a highly detailed fashion, characterize aortic size and geometry with the aim to improve the ability to diagnose and monitor thoracic aortic disease in TS. To then assess the clinical validity of the novel approach, measurements obtained from the continuous methodology were compared using the same methodology but different algorithms and with the existing manual measurements. The preciseness of the approach is discussed and results are presented for the various clinical phenotypes in TS. To further provide insight into thoracic aortic disease in TS, geometric asymmetry and local dimensions of normal and diseased aortae were assessed by introducing a geometric quantity that varies along the aorta length and circumference. To lastly provide basis for future measurement of aortic size in TS a novel registration method was devised to estimate 3D visit-to-visit change in aortic geometry.

6.1 *Methods*

Fifteen patients, with karyotypically proven TS, were recruited through the Danish National Society of Turner Syndrome contact group and a tertiary endocrine outpatient clinic [32]. Exclusion criteria included malignancy, liver disease, and mechanical aortic valve prosthesis. The TS subjects were examined at baseline (Visit 1) and two subsequent follow-up visits (Visit 2 and 3) over a 10 year period using CMR and transthoracic echocardiography (for aortic valve

morphology) [34]. Ten healthy subjects were recruited as baseline controls, and examined once. Table D.1 (Appendix D) summarizes the age and structural morphologies encountered according to definitions described elsewhere [21, 24].

6.1.1 *MR Imaging*

CMR was performed using a 1.5 T whole-body scanner (Philips Medical System- Best, The Netherlands). A contrast-free, fat-saturated, nearly isotropic, 3D steady-state-free-precession and electrocardiogram (ECG) triggered gradient echo sequence with a respiratory navigator was adopted in this study [32, 35]. The 3D image stack was acquired during the diastolic phase of the cardiac cycle (stack dimensions: 27 cm (anterior-posterior) x 20 cm (feet-head) x 36 cm (left-right)). Spatial resolution was 256 x 256 pixels (pixel spacing: 1.41 x 1.41 mm).

6.1.2 *Manual Measurements*

Dedicated software (Systematic Software Engineering, Aarhus, Denmark) that allowed multiplanar reformatting of the 3D image stack, was used by two CMR experienced readers to manually measure maximum aortic diameter at eight discrete locations and guided by aortic and extra-aortic landmarks [35]. These locations were: 1) the sinotubular junction 2) the ascending aorta, midway between the sinotubular junction and the innominate artery, 3) the ascending aorta, immediately proximal to innominate artery, 4) the proximal transverse arch, midway between innominate and left carotid artery, 5) the distal transverse arch, just proximal to left subclavian artery, 6) Aortic isthmus, immediately distal to the left subclavian artery, 7) the descending aorta, between left pulmonary artery and top of left atrium, 8) the descending aorta, at the caudal border of the left atrium [34]. For the aforementioned measurement stations, inter-observer variability was: (i) -0.3 (−2.3;1.8) mm; (ii) -0.1 (−1.9;1.4) mm; (iii) 0.1 (−1.6;1.7) mm; (iv) -0.2 (−1.4;1.9) mm; (v) -0.01 (−1.6;1.4) mm; (vi) -0.1 (−1.4;1.9) mm; (vii) 0.08 (−1.1;1.9)

mm; and (viii) 0.1 (−1.2;1.5) mm [32]. The corresponding intra-observer measurement variability was: (i) 0.02 (−1.8;1.9) mm; (ii) -0.1 (−1.9;1.8) mm; (iii) -0.1 (−1.9;2.1) mm; (iv) 0.20 (−1.6;2.0) mm; (v) 0.01 (−1.7;1.7) mm; (vi) 0.1 (−1.6;1.4) mm; (vii) 0.08 (−1.5;1.4) mm; and (viii) -0.06 (−1.6;1.7) mm [32].

6.1.3 *Aortic Segmentation*

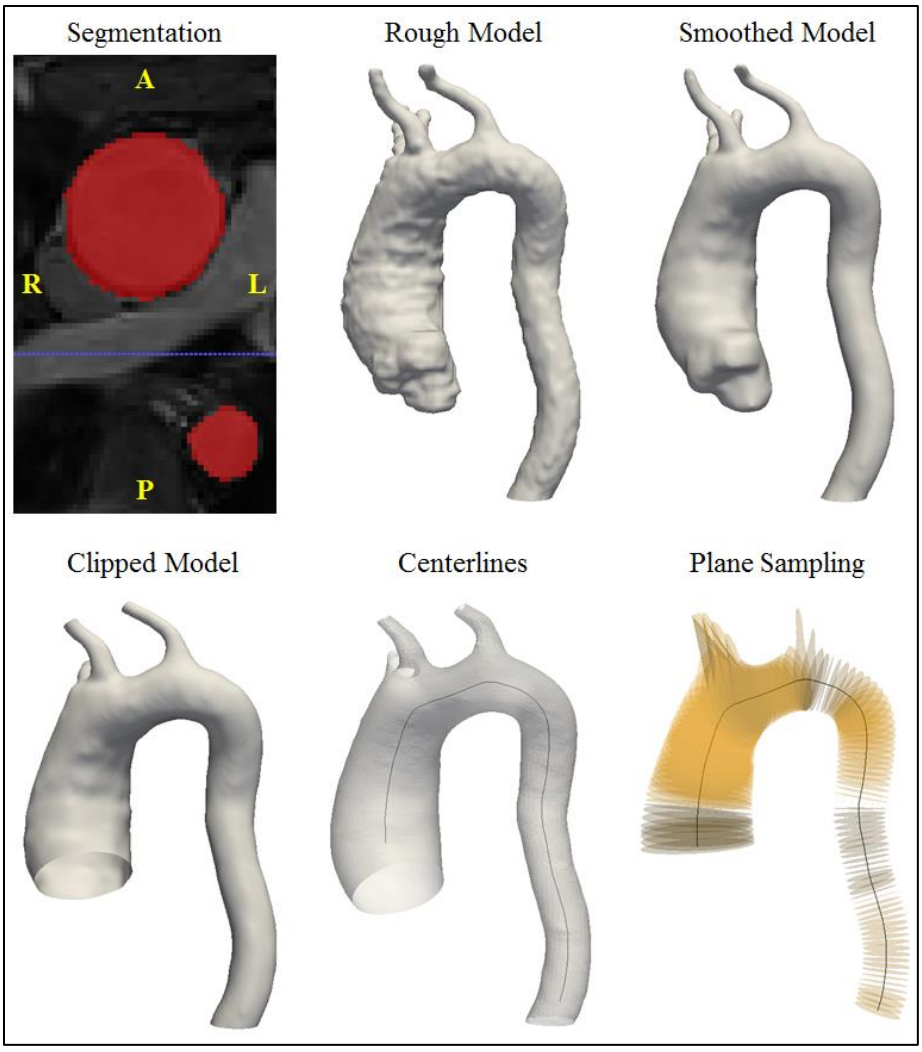

Figure 6.1: Procedure to generate 3D patient-specific geometries of the thoracic aorta, exemplied for a subject with Turner sydrome (Subject 6). The CMR images were segmented to identify a rough geometry which is subsequently smoothed and clipped for analysis. Centerlines were then identified using VMTK (highlighted in black, overlayed on corresponding aorta geometry) and planes could be sampled normal to the centerline (highlighted in yellow, centerline also shown for reference).

In order to accurately estimate aorta dimensions without multiplanar reformatting, the thoracic aortae were reconstructed in 3D. Each CMR data set was then imported into a specialized image-processing software (Mimics, Materialise Inc., Plymouth, MI) to segment the aorta using a thresholding algorithm, as described elsewhere [53] (Fig. 6.1). Exclusion criteria for segmentation included noisy datasets that exhibited random brightness variations in the aorta lumen and image stacks that did not encompass the entire thoracic aorta (3 out of 45 datasets). The lower and upper threshold values for segmentation of the thoracic aorta ranged from 310 to 640 Grey Values (GV). Geometries of the thoracic aorta were then generated to include the innominate, left common carotid and left subclavian arteries. As shown in Fig. 6.1, the coarse geometries were smoothed in Mimics to minimize surface artifacts prior to geometric analysis. Smoothed geometries were clipped to identify inlets and outlets of the aorta (Fig. 6.1) using the Paraview software (Kitware Inc., Clifton Park, NY). The truncated geometries were triangulated using 3-Matic (Materialise Inc., Plymouth, MI) and the lumen surface was exported in stereolithography (STL) format for geometric measurements.

6.1.4 *Centerline Extraction and Geometric Parameter Estimation*

In order to ensure that maximum diameter measurements were truly perpendicular to the aorta axis [32], centerline of the reconstructed aortas were identified [53]. The Vascular Modeling Toolkit software (VMTK) [163] has been employed previously to identify centerlines for geometric measurements of the thoracic and abdominal aortae [54, 164]. The open-source version of this software was adopted here. VMTK estimates the centerlines as the weighted, shortest paths traced between two extremal points. The lines are ensured to be central, since they run on the Voronoi diagram (i.e. the location where centers of maximal inscribed spheres are defined) of the vessel geometry. A detailed description of the methodology used to estimate

centerlines can be found elsewhere [165]. The centerlines for continuous measurements were identified between the inlet in the ascending aorta and outlet in the descending aorta (i.e. excluding branches) and smoothed using VMTK (Fig. 6.1). Planes (highlighted in yellow in Fig. 6.1) spaced 2 mm apart were then sampled normal to the smoothed centerlines using VMTK. Geometric variables including maximum aortic diameter and cross-sectional area were estimated at the individual cross-sections. Centerlines were also employed to calculate tortuosity of the aorta [165] and curvature at the highest point in the aortic arch [53]. The procedure outlined was performed for the 15 TS subjects, including baseline and subsequent follow-up visits, in order to quantify change in aortic dimensions over time. Growth or shrinkage was defined as visit-to-visit change in the maximum diameter above inter-observer variability [32]. It should be noted that a sensitivity analysis was performed to test for inter-user variability in aorta diameter measures obtained using the presented approach. Variability in aorta diameter measures was also tested with respect to choice of smoothing algorithm, segmentation and smoothing software. The details of this sensitivity analysis are presented in Appendix E.

6.1.5 *Evaluation of Localized Dimensions and Asymmetric Change*

In order to obtain 3D markers of thoracic aortic morphology, methods are described to estimate localized dimensions and regional changes between visits. A size field was proposed on the aortic surface that was quantified by evaluating the distance from the centerline to each point of the lumen. This geometric variable, known as the Euclidean distance, varies circumferentially (along the vessel periphery) and axially (along the aortic length). This parameter has been employed to quantify diameter growth of the abdominal aorta [54]. The Euclidean distance was measured using VMTK for controls and TS subjects in order to: a) assess the dimensional differences between normal and diseased aorta, and b) quantify the anisotropy (asymmetry) in

the aortae dimensions between visits in TS. To measure this variable, a new smoothed centerline was computed for the thoracic aorta and its branches. A new method was also proposed to estimate the asymmetric change between visits (Visit 1 to 2, Visit 2 to 3 and Visit 1 to 3) using an iterative closest point (ICP) registration algorithm, that minimizes the difference between a pair of point clouds [166]. Aortic geometries to be compared were initially registered using the ICP registration available in VMTK [167-169]. The CloudCompare open-source mesh processing software (www.cloudcompare.org) was then employed to further align the two aortic surfaces by picking point-pairs. Fine alignment of the aortic surfaces was subsequently achieved by employing the ICP implementation available in CloudCompare. The difference between the aortae (i.e. change between visits) was afterwards assessed using the surface distance module available in VMTK, which computes the minimum point to point distance of the target (i.e. registered) aorta surface (Visit 2 or 3) from the reference (Visit 1 or 2) [170].

6.1.6 *Statistical Methods and Data Analysis*

A least-squares linear regression analysis was performed to assess the correlation between manual and continuous measures, Bland-Altman plots were generated to estimate the agreement between these two methods, with the reproducibility co-efficient or limit of agreement computed as ± 1.96SD. In these plots, the difference between the methods was plotted on the ordinate and the average of the continuous and manual techniques was plotted on the abscissa. Horizontal lines were drawn to indicate the mean difference and the upper and lower limits of agreement [171]. In order to test for presence of constant and proportional bias, Passing-Bablok regression analysis was performed. As compared to the least-squares regression method described earlier, the Passing-Bablok regression involves no special assumptions regarding the distribution of samples or measurement methods [172]. These analyses were performed using MATLAB

(MathWorks Inc., Natick, MA). An F-test was performed using Microsoft Excel 2010 to estimate the concordance between visit-to-visit change in maximum diameter for the measurement positions, obtained manually and continuously. It should be noted that the F-value and corresponding critical value were compared in order to determine equivalence of the variances of change between visits obtained manually and continuously [173]. All continuous variables were indicated as means ± standard deviations. A p-value of < 0.05 was considered statistically significant and R-values were employed to describe coefficient of correlation.

6.2 *Results*

6.2.1 *Comparison between Methods*

Values of maximum aortic diameter and cross-sectional area obtained from continuous measurements were presented as one-dimensional line plots. Geometric measures at the innominate (IA), left common carotid artery (LCCA) and left subclavian artery (LSCA) were excluded from the analysis, with their locations indicated using black bands [164]. Fig. 6.2 indicates three cases, including one subject with regurgitant tri-leaflet aortic valve (Subject 1), a second subject with elongated transverse aorta (ETA) (Subject 9) and a third subject with aortic coarctation (Subject 7), used to demonstrate the ability of the continuous method to quantify visit-by-visit dimensions of the thoracic aorta with manual measures of maximum diameter superimposed. It may be seen, that for instance for the subject with aortic valve regurgitation, maximum diameter predicted using the manual and continuous methods were in concordance throughout the thoracic aorta. Furthermore, aortic diameter measures were consistent over time in the ascending, transverse and descending aorta. For the subject with ETA (Subject 9), both methods depicted reduction in descending aorta diameter with each visit. Descending aorta dimensions were nearly equivalent for the two methods. The continuous method predicted

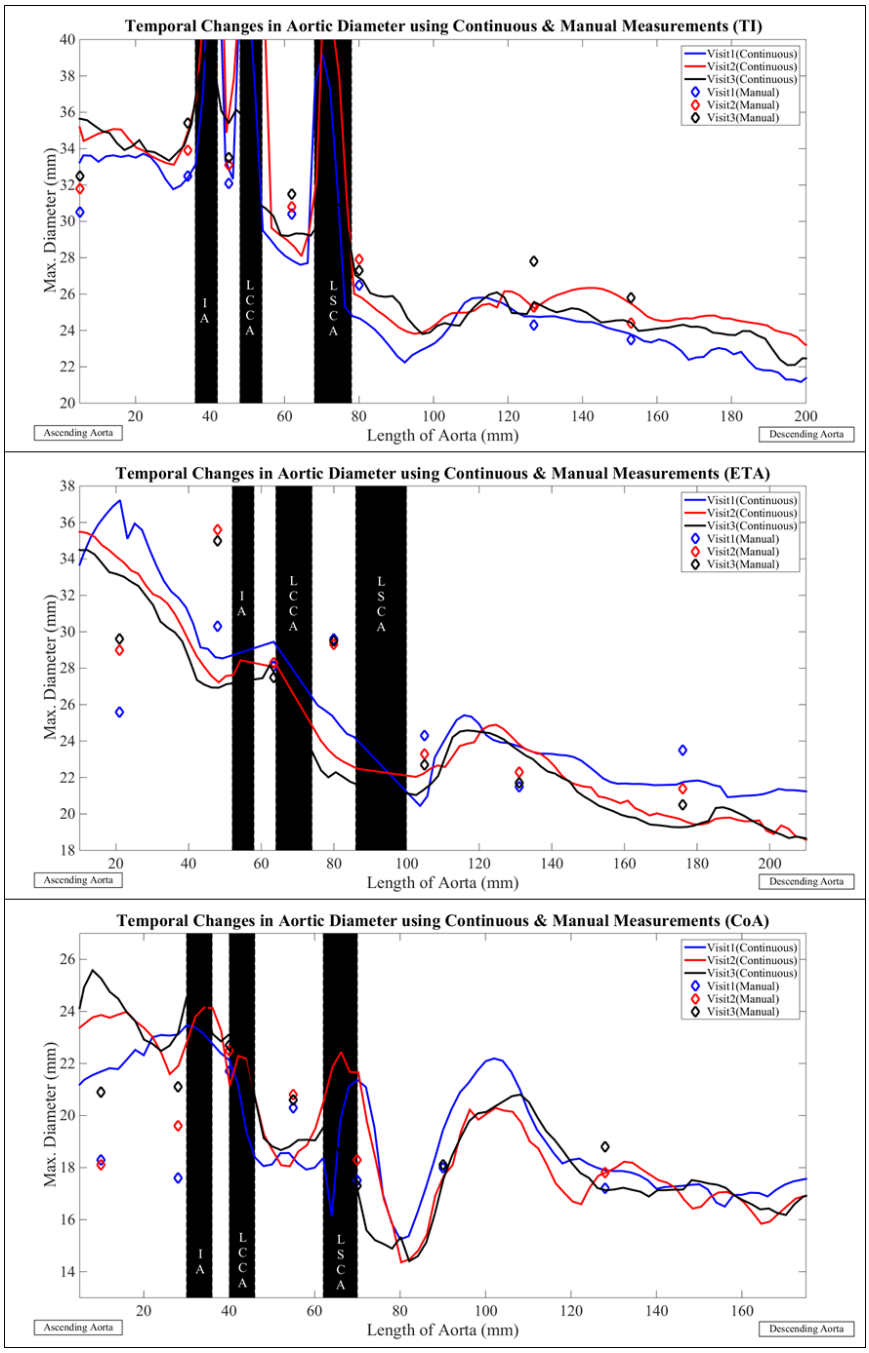

Figure 6.2: Visit based variation in maximum aortic diameter for three aortic phenotypes in TS comprised of aortic valve regurgitation (Subject 1), elongation of the transverse aortic arch (Subject 9) and aortic coarctation (Subject 7). Visit 1 – solid blue line, Visit 2 – solid red line, Visit 3 – solid black line. Diamond markers indicate corresponding manual measures. Data at locations of the inominate artery (IA), left common carotid artery (LCCA), left subclavian artery (LSCA) (shaded in black) excluded from analysis. All values are in mm. Aortas for the three visits aligned at the branches.

smaller registered diameters in the ascending and transverse aorta. The manual method predicted growth in the ascending segment and stable dimensions in the transverse aorta.

Both methods predicted growth in the ascending aorta and stable dimensions in the transverse section, for the subject with aortic coarctation (Subject 7) (Fig. 6.2). The continuous method predicted smaller registered diameters in the descending aorta and the manual method indicated stable dimensions over time. The continuous method predicted larger values of maximum diameter in the ascending aorta for all visits considered in this study. Maximum diameter values obtained from the two methods were similar in sections of the transverse and descending aorta. The coarctation and its location (immediately following the LSCA), was expressed more accurately by the continuous method. The visit-by-visit variation in lumen cross-sectional area for the three subjects is indicated in Fig. 6.3. As can be seen, the trends for variation in area were nor surprisingly similar to the variation in maximum diameter (Fig. 6.2). For TS, curvature at the highest point in the aortic arch was greater for all visits (Visit 1: 0.3±0.2 (1/mm), Visit 2: 0.6±1.1 (1/mm), Visit 3: 0.4±0.3 (1/mm)) as compared to controls (0.2 ± 0.1 (1/mm)). Similar trends in aortic arch curvatures were observed between patients with post-coarctation repair, patients with post-arterial switch operation and healthy subjects [53]. Aorta tortuosity was also lower for the healthy individuals (1.3±0.2) as compared to the TS patients for all visits considered in this study (Visit 1 and 3: 1.5±0.3, Visit 2: 1.6±0.3).

Scatter plots and least-squares based linear regression lines comparing maximum diameter obtained manually and continuously, at the discrete measurement positions, for all cases and visits are indicated in Fig. 6.4. The overall least-squares regression coefficient was 0.77 (p-value<0.01) and was equivalent to the correlation coefficient reported in a previous study [52]. Similar correlation coefficients were obtained for the individual visits (Visit 1: R-

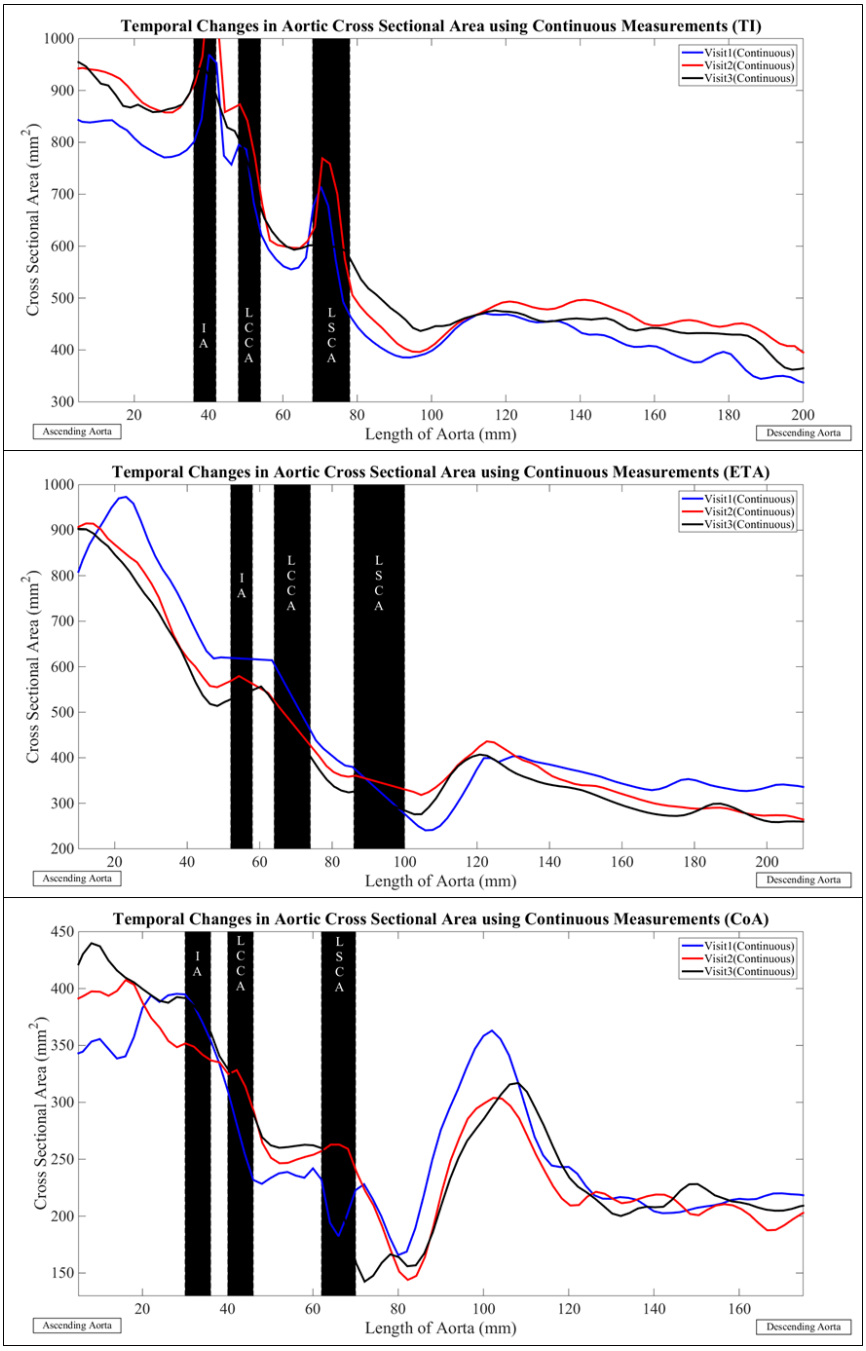

Figure 6.3: Visit based variation in cross-sectional area for three aortic phenotypes in TS comprised of aortic valve regurgitation (Subject 1), elongation of the transverse aortic arch (Subject 9) and aortic coarctation (Subject7).Visit 1 – solid blue line, Visit 2 – solid red line, Visit 3 – solid black line. Diamond markers indicate corresponding manual measures. Data at locations of the inominate artery (IA), left common carotid artery (LCCA), left subclavian artery (LSCA) (shaded in black) excluded from analysis. All values are in mm^2. Aortas for the three visits aligned at the branches.

value=0.72, Visit 2: R-value=0.75, Visit 3: R-value=0.71, all P<0.005). The Bland-Altman plots (Fig. 6.5) showed a slight negative bias of -0.78 mm between the manual and continuous methods for all visits considered together. The reproducibility coefficient was 8.6 mm. For the baseline (Visit 1) and second follow-up (Visit 3) visits, a negative bias was observed between the two methods (Visit 1:-0.96 mm, Visit 3:-1.1 mm) as compared to Visit 2 (-0.29 mm). The

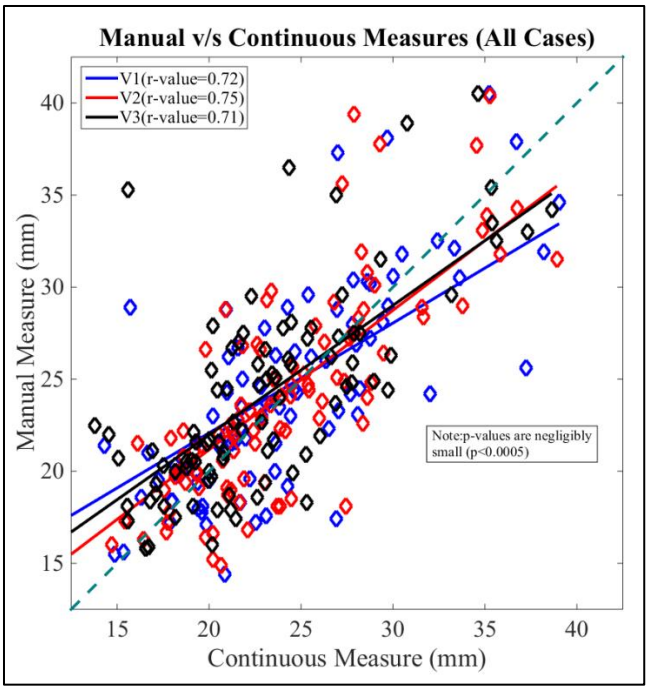

Figure 6.4: Scatter plot and linear regression lines for maximum diameter at select locations along the thoracic aorta for all cases and visits. Visit 1 - blue diamond markers and solid line, Visit 2 - red diamond markers and solid line, Visit 3 - black diamond markers and solid line. 45° dashed green line also shown to indicate deviation of manual measures relative to the corresponding continuous values.

corresponding limits of agreement were also smaller for Visit 2 (±7.9 mm) compared to Visit 1 (±9.4 mm) and Visit 3 (±8.4 mm). Analysis of the Passing-Bablok regression (Fig. 6.6) parameters indicated significant constant bias between the manual and continuous methods overall and for the individual visits considered in this study (Appendix D: Table D.2). The bias was least significant for the first follow-up (Visit 2) and greatest for the baseline visit (Visit 1).

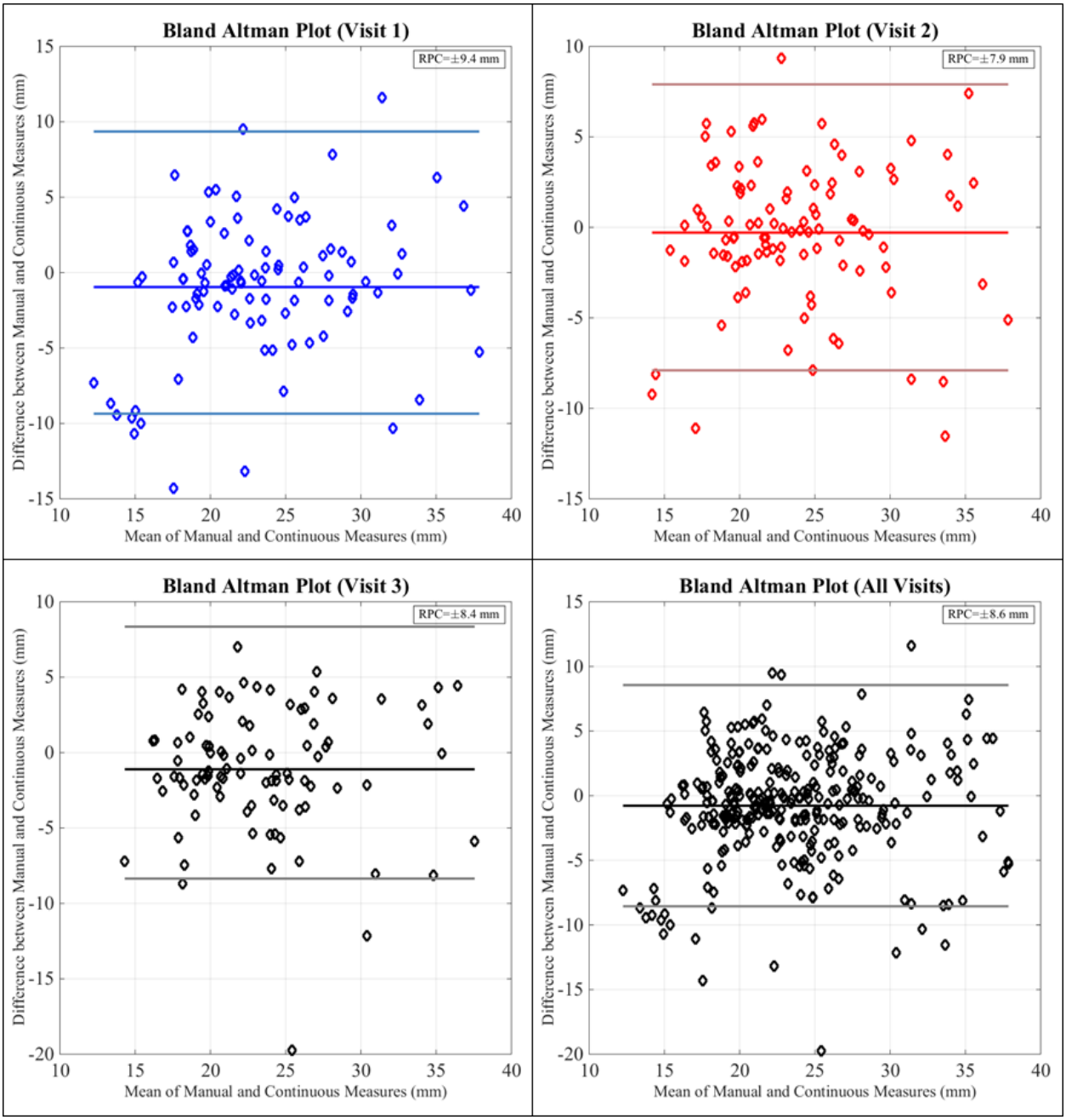

Figure 6.5: Bland-Altman analysis comparing maximum aortic diameter obtained using manual and continuous methods for individual visits and all visits considered. Visit 1 - blue diamond markers, solid blue line – mean, light blue lines - ±1.96SD, Visit 2 – red diamond markers, solid red line – mean, light red lines - ±1.96SD, Visit 3, All Visits - black diamond markers, solid black line – mean, gray lines - ±1.96SD.

In addition, the slopes were lower than one and indicated the presence of proportional bias between the two methods. The proportional bias was observed to be most significant for aorta

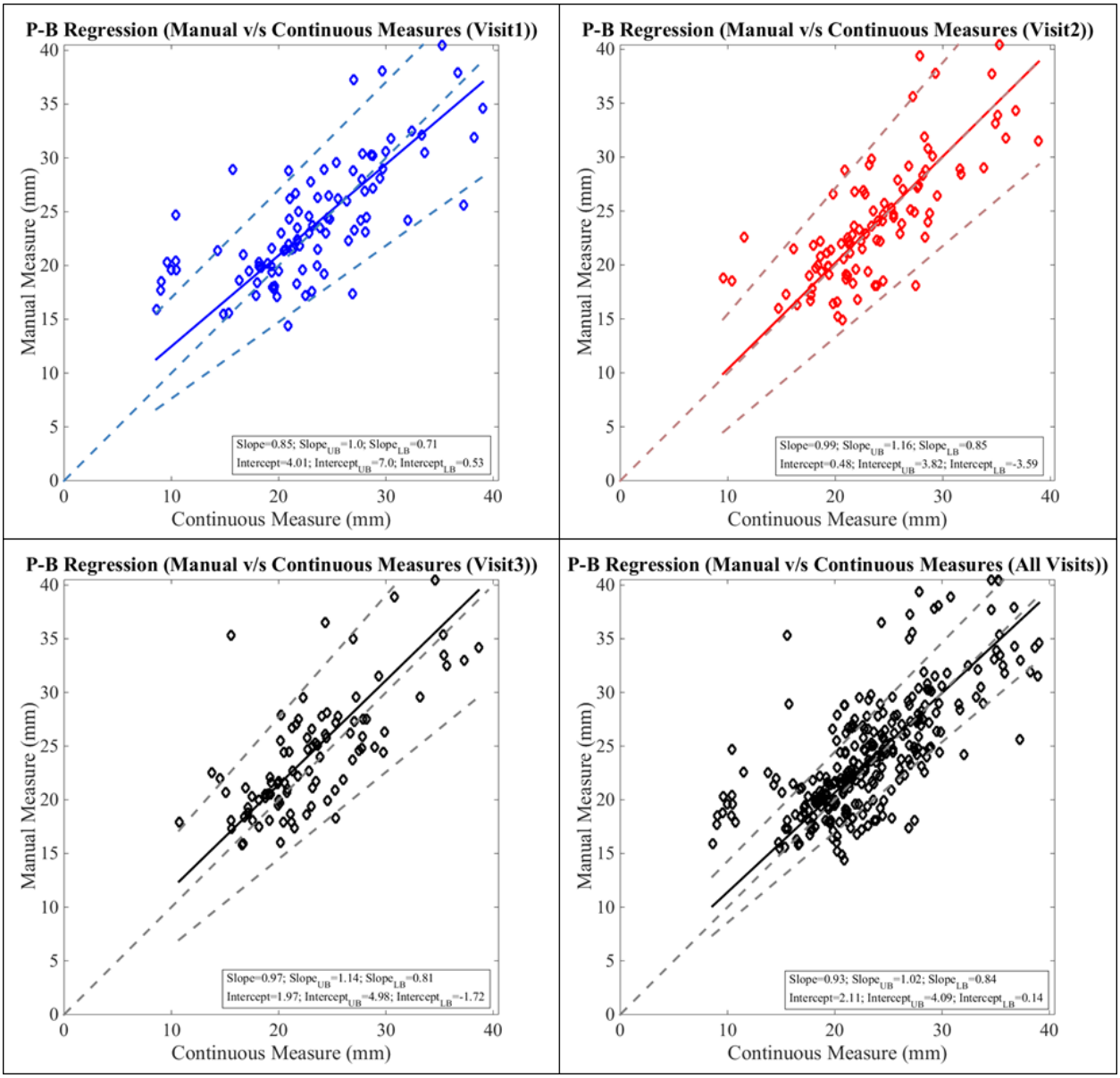

Figure 6.6: Passing-Bablok regression plots comparing manual and continuous methods for individual visits and all visits considered. Visit 1 - blue diamond markers, solid blue line – regression line, light blue dashed lines – upper and lower bounds, Visit 2 – red diamond markers, solid red line – regression line, light red lines – upper and lower bounds, Visit 3, All Visits - black diamond markers, solid black line – regression line, gray lines – upper and lower bounds.

maximum diameter measurements at Visit 1. Table D.3 (Appendix D) summarizes the F-test correlations for different sections of the thoracic aorta. As can be seen, the visit-by-visit changes for the complete thoracic aorta and the individual segments correlated well ($F<F_{crit}$).

6.2.2 *Variation in Localized Change*

Figure 6.7: Color plots indicating circumferential and axial variation in Euclidean distance from centerlines for controls included in this study. All dimensions are in mm. Anterior and posterior views of the aorta are shown for each case.

Figure 6.8: Color plots indicating circumferential and axial variation in Euclidean distance from centerlines for 10 TS patients (patient nos. 1, 4, 5, 6, 8, 9, 10, 11, 13 and 15). All dimensions are in mm. Anterior and posterior views of the aorta are shown for each subject.

Among the 10 controls, the ascending aorta was larger (12.6 ± 1 mm (mean Euclidean distance ± standard deviation)) than the descending aorta (9.5 ± 0.9 mm) and transverse aortic arch (Figure 6.7). Likewise for the TS subjects, the ascending aorta was larger (13.4 ± 2.1 mm) than the descending segment (10.2 ± 1.3 mm). Figure 6.8 summarizes distance maps for 10 subjects (baseline visit: case no. 1, 4, 5, 6, 8, 9, 10, 11, 13 and 15), who represent the various aorta phenotypes in TS. The maximum Euclidean distance in the ascending aorta for TS, averaged over all visits, was greater than the corresponding values for controls ($F>F_{crit}$), and similar for the descending aorta segments ($F<F_{crit}$). Greater asymmetry (anisotropy) in the Euclidean distance was observed throughout the thoracic aorta in TS compared to controls. It should be noted that for a circular (i.e. symmetric) cross-section, the color (value of Euclidean distance) would be unchanged along the aortic circumference. The visit-by-visit Euclidean distance was nearly unchanged throughout the aorta. Table D.4 summarizes the maximum and mean distances for the ascending and descending aorta.

The visit-by-visit asymmetry in the aorta cross-section is illustrated for Subject 9 in Fig. 6.9a. The anisotropy in the ascending aorta (proximal to the aortic root) was larger for Visit 1 compared to Visit 2 and 3, as observed in the anterior view. At the aortic isthmus distal to the LSCA, the out-of-circularity was similar for Visit 1 and 2 and more pronounced than Visit 3. The 3D change in aorta geometry between visits for patient 9, obtained using the iterative closest point registration is presented in Fig. 6.9b. The reference surface indicated in blue (Visit 1 or 2) and target surface to be compared (either Visit 2 or 3) indicated in white are shown for clarity; positive and negative values implies growth and decrease, respectively. As shown in Fig. 6.9b, growth resulted anteriorly from Visit 1 to 2 and 1 to 3 in the ascending aorta and in the descending aorta. Apparently progressive aortic coarctation (CoA) was observed to occur in the

A)

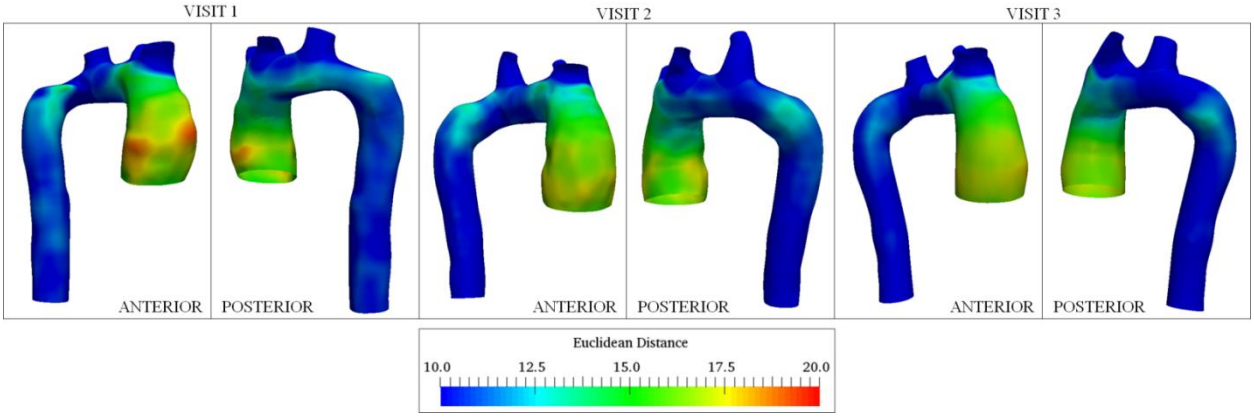

B)

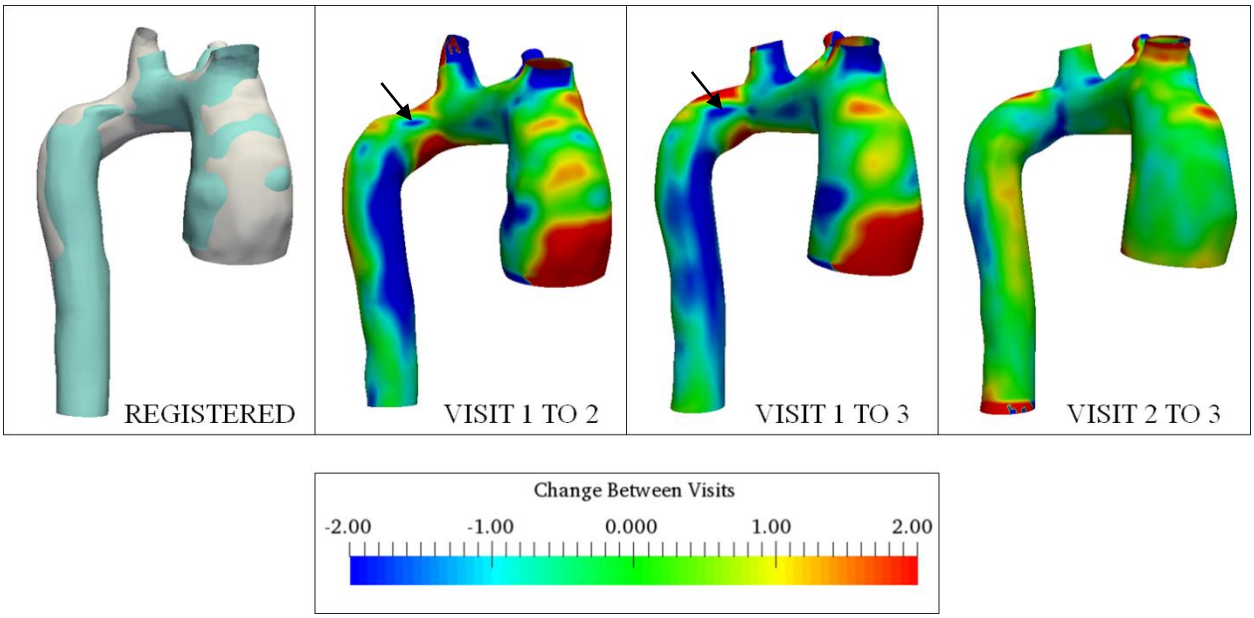

Figure 6.9: Three dimensional visit-to-visit variation in aorta geometry (Subject 9). Figure 9A: Color plots indicating circumferential and axial variation in Euclidean distance from centerlines. All dimensions are in mm. Anterior and posterior views of the aorta are shown for each visit. Figure 9B: Color plots indicating circumferential and axial variation in visit-by-visit change, obtained using point registration. Positive indicates increasing and negative indicates decreasing dimension of Visit 2 / Visit 3 relative to Visit 1 / Visit 2. Reference aortic surface (Visit 1 or 2) and registered aorta (Visit 2 or 3) are shown in blue and white, respectively. All values in mm. Anterior views shown for the three cases. Arrows shown to indicate location of progressive coarctation.

follow-up visits anteriorly in the descending aorta, downstream of position 7. The 3D plots of geometry change and Euclidean distance maps for this subject correlated well with the corresponding line plots of variation in maximum diameter indicated in Fig. 6.2.

6.3 *Discussion*

A novel continuous method for assessment of thoracic aortic diameter and geometry was presented in this Chapter. The continuous method has several advantages over the manual approach. Firstly, the continuous method eliminates the need for measurement at both identical locations and cross-sectional angles. Secondly, the continuous measurement method provides complete anatomical information about the entire thoracic aorta. Thereby, the new method is capable of highlighting features, such as the extent and location of any aortic abnormalities and localized increment or decrement, including out-of-circularity changes, unlike manual single-point measurements. It also produces optimum measurements near steep gradients (i.e. at CoA or near branch points), where manual overestimation may occur. Least-squares and Passing-Bablok regression analysis indicated good concordance between values of maximum diameter at the discrete measurement positions obtained using manual and continuous methods. The continuous method was observed to generally predict a higher diameter at different stations along the aorta as indicated by slope values less than one for the least-squares and Passing-Bablok regression lines. The negative bias obtained using the Bland-Altman plots also provided evidence of this trend. Differences in positioning of the discrete measurement stations for the manual or continuous measurement methodology would potentially increase the bias obtained from the Passing-Bablok regression analysis. The outliers indicated in the Bland-Altman plots (Fig. 6.5) corresponded to aorta scans that concluded at station 8 (i.e. at the caudal border of the left atrium). Improved concordance between the methods could be potentially obtained by extending

the scans below the diaphragm level (i.e. inclusion of the abdominal aorta). In addition to the statistical approach presented in this study, validation of aorta lumen segmentation would have to be performed using probabilistic models to minimize under or over-estimation of aortic diameter and enhance the agreement between the continuous and manual methods. The same can be achieved by considering a set of segmentations of the aorta lumen performed manually and automatically and computing a probabilistic estimate of the true segmentation and performance level represented by each segmentation [174]. The presented method estimated stable aortic dimensions over time for most cases as compared to the manual method, which predicted larger changes. The need for unnecessary intervention based on overestimation of growth may thus be potentially minimized with the continuous approach. This approach prevents missing changes between manual locations and neighboring points and establishes continuity and validation. A previously proposed automated method involved fitting of an elliptic cross-section to identify the minimum and maximum aorta diameters [52]. The presented method could potentially provide a better estimate of the true maximum diameter given the full circumferential cross-sectional information. Moreover, the plots describing the variation in cross-sectional area (Figure 6.3) could be used to obtain measures of localized aortic compliance and the corresponding change over time [53]. The Euclidean distance maps enabled to not only elucidate dimensional differences between TS and controls, but also to recognize regions that exhibited the greatest asymmetry, and may also provide a better understanding of the aortic pathophysiology in Turner syndrome, especially the localized changes that seem to take place over time. The presented approach to estimate 3D growth or shrinkage is a multi-step registration process that requires low computational effort. Statistical shape atlas techniques based on deformable registration have been demonstrated to precisely reconstruct complex aorta shapes for several cardiovascular

disorders [168, 169], by employing suitable values of transformation resolution and stiffness parameters to capture small features [167]. These computational template methods would be considered in a future study to quantify visit-to-visit change in aorta morphology for TS patients.

The continuous measurement method was observed to be more sensitive to the choice of segmentation software and smoothing algorithm as compared to the inter-user variability or choice of smoothing software. Recognizing this large variability, surface area measurements using the different segmentation software were compared with the corresponding analytical values for a modified 3D Shepp-Logan phantom. The errors in surface area measurements were: a) Mimics: 0.8±4.6%, b) ITK-Snap: 1.5±4.5%, c) 3D Slicer: 1.1±4.7%. The absolute error in surface area values was greater for 3D Slicer (~1.5%) as compared to Mimics (~0.2%) and ITK-Snap (~0.4%), for ellipsoids with gray values similar to that of the aorta. Although these aforementioned observations imply that Mimics is potentially more suitable for reconstruction of the aorta geometry using CMR, further validation of the same would be performed in a future study using cardiac phantoms [175]. The average inter-user variability was evaluated to be approximately one pixel (~1.5 mm) and was similar to the values reported previously [32]. Errors in measurement of the aorta diameter using the presented method stem from a variety of sources. Firstly, segmentation of the thoracic aorta was achieved by setting the upper and lower threshold values. Variation in the threshold could potentially result in over or under prediction of the aorta lumen, prior to surface smoothing. Noisy images and low spatial resolution significantly influence the choice of threshold levels needed to segment the vessel lumen. Secondly, smoothing of the aortic geometries was achieved using a fixed number of iterations and smoothing factor. Few iterations or a low smoothing factor could result in more surface artifacts. Smoothing of the centerline prior to sampling of planes could lead to variations in the

reference point needed to evaluate the maximum aortic diameter. Thirdly, visit-to-visit changes in the orientation of the branch arteries from the transverse arch present challenges in accurately aligning the aortae necessary to compare geometry changes over time, especially in the transverse section. Correlation with manual measurements is also subsequently influenced by the preciseness of this alignment. This study assumes no variations in the ECG triggering between visits (i.e., all scans are acquired during the same time point in the diastolic phase of the cardiac cycle). The TS subjects examined were prescribed anti-hypertensive treatment during the first follow-up visit. Changes in diastolic pressure influenced by the treatment and variations in hemodynamic flow variables such as wall shear stress with time [176] could potentially alter the aortic geometry between visits. Additionally, increasing aortic stiffness with age [177] could generate changes in aortic morphology for a fixed aortic pressure. Dilatation of the aortic root may be observed in TS [26, 178]. The methods presented here have been enhanced to include aorta sinuses for 3D measurements of aorta morphology in controls and TS, the details of which would be presented in a future study. The methodology and descriptive statistics reported in this study were performed for a relatively small sample size of 15 subjects, and future studies would include additional diseased subjects and longitudinal scans for healthy individuals. However, the validity of the novel approach was demonstrated with the present sample size. Hierarchical clustering has been employed previously to detect patterns of aortic dilatation in patients with BAV disease [179]. A similar cluster analysis will be performed in a future study to define growth or shrinkage patterns of the aorta in TS.

Evaluating hemodynamic parameters and aortic flow patterns in patient-specific deformed aortae is one of the further necessary steps to improve risk stratification of aortic disease in TS [58, 59]. The one-dimensional continuous measurement method proposed in this

study has been previously utilized to explain changes in aortic flow patterns over time, in animal models [164] and the same approach may prove valuable in a future research into associations of variation in flow patterns and wall shear stress with changes in aortic geometry in TS. Spiraling nature of blood flow in the aortic arch has also been observed to correlate with aortic arch curvature [180] and tortuosity [181]. Furthermore, correspondence between mechanical stresses and Euclidean distance maps has been reported previously for dilated aortae [63, 182]. In addition to the statistical model based on manual measurements developed previously [32], a mathematical model based on continuum mechanics has also been described to predict vessel growth [183, 184]. The changes between visits obtained using one-dimensional line plots and 3D surface change maps could be utilized to validate and advance models of growth prediction and disease progression such as the aforementioned. Surgical planning for interventions on diseased thoracic aortae or aortic valves [185] requires precise dimensional information prior to surgical intervention [52]. The measurement approaches proposed in the study can be used for such pre-operative surgical planning. The described methodology improved to include the aortic sinus, can be applied to cardiovascular disorders such as Marfan syndrome and comparative studies between conditions such as TS and other aortopathies would potentially be of value in delineating differences in pathophysiology and how this manifests in different geometries and changes over time.

Chapter 7

Modeling Blood Flow in a Compliant Aorta

Results from this chapter were presented at the 2016 AIAA DCASS, Dayton, OH and 2016 BMES Annual Meeting, Minneapolis, MN

This chapter describes a quasi-steady FSI methodology (Section 7.1) to simulate aortic blood flow in a compliant vessel and introduces functional measures that could potentially serve as risk markers of aortic dissection. Flow and biomechanical functional variables are compared for healthy and diseased subjects. The described methodology is then extended to study the progression of aortic disease in TS.

7.1 *Quasi-steady FSI Modeling in Healthy and Diseased Aortas*

2 subjects, including a healthy individual and a patient with elongated transverse aorta (ETA) and coarctation (CoA), were chosen for this study. Reconstruction of aorta geometries from CMR has been described previously in Chapter 6.

7.1.1 *Flow Model*

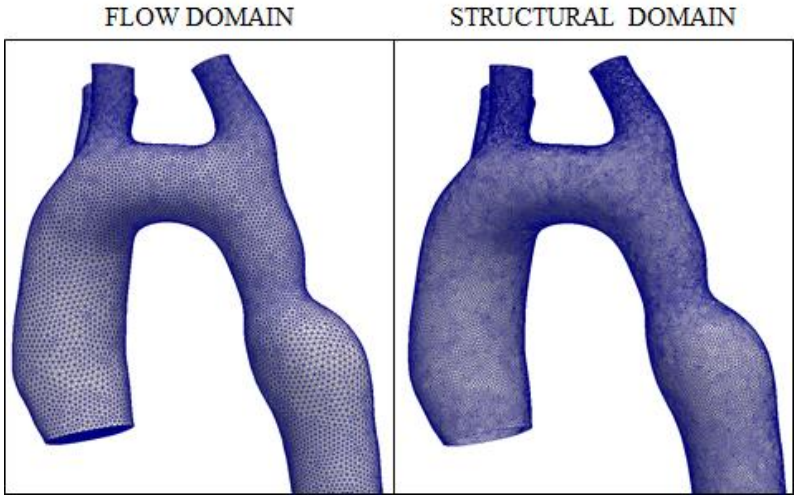

Figure 7.1: Discretization of flow and structural domains.

Blood flow in the thoracic aorta has been modeled previously by assuming either a laminar or transitional flow regime for steady [58, 186] and transient simulations [187, 188]. Aortic flow was described using the continuity and Reynolds-Averaged Navier Stokes (RANS) equations [186] (Chapter 2) since the critical Reynolds number for transition from laminar to the turbulent flow regime is lower for constricted vessels [189]. To model flow turbulence, Menter's Shear Stress Transport (SST) model [187] was employed, which assumes that the turbulent viscosity μ_t is related to the fluid density ρ, turbulent kinetic energy (TKE) k and specific-dissipation rate (SDR) ω as follows:

$$\mu_t = \rho \frac{k}{\omega} \tag{7.1}$$

The SST model solves transport equations for TKE and SDR using two blending functions F_1 and F_2 described previously [88]. The model incorporates a production-limiter into the kinematic viscosity as described below:

$$\nu_t = \frac{0.31k}{\max(0.31\omega, \Omega F_2)} \tag{7.2}$$

Where Ω is the absolute vorticity. The blending function F_1 is so chosen such that its value is zero and unity close to and away from the wall respectively. The second blending function restricts the production-limiter to the boundary layer adjacent to the wall. The SST model was chosen due to its ability to provide a better description of the flow in situations involving adverse pressure gradients and curved boundary-layers [45]. The aortic lumen was discretized using unstructured tetrahedral elements. The centerlines-based mesh generator adapts to changes in aortic geometry [20] and ensures a smooth transition in mesh density, such as would be required at the sites of CoA in order to obtain an improved estimation of flow variables (Fig. 7.1). Blood was assumed to behave as an incompressible, Newtonian fluid [181] with a density of 1060

kg/m^3 and a viscosity of 0.0035 Pa-s. Constant velocity flow computations [186, 190] were performed for a mean cardiac output corresponding to 5 liters per minute [191]. A flow boundary condition was defined at the inlet assuming a flat velocity profile and 85 percent of the flow was assumed to exit from the descending aorta [58]. The turbulence intensity was set to 2 percent and a 1 mm length scale was assumed. Static pressure corresponding to the pulse pressure was prescribed at the branch outlets [59]. These values were based on cardiac pressure measurements performed previously in adult female subjects [192]. Accordingly, pressures equivalent to 55 and 72 mmHg was employed for the TAV and BAV subjects respectively. Combination of pressure and outflow boundary conditions have been adopted previously to model aortic blood flow in thoraco-abdominal aortic aneurysms [188] and in the thoracic aorta in Marfan syndrome [187]. Uniformity in flow boundary conditions enabled a comparison of hemodynamic variables between the subjects analyzed in this study. A no-slip boundary condition was assigned to the lumen wall. A high resolution advection scheme and turbulence numerics were chosen [187].

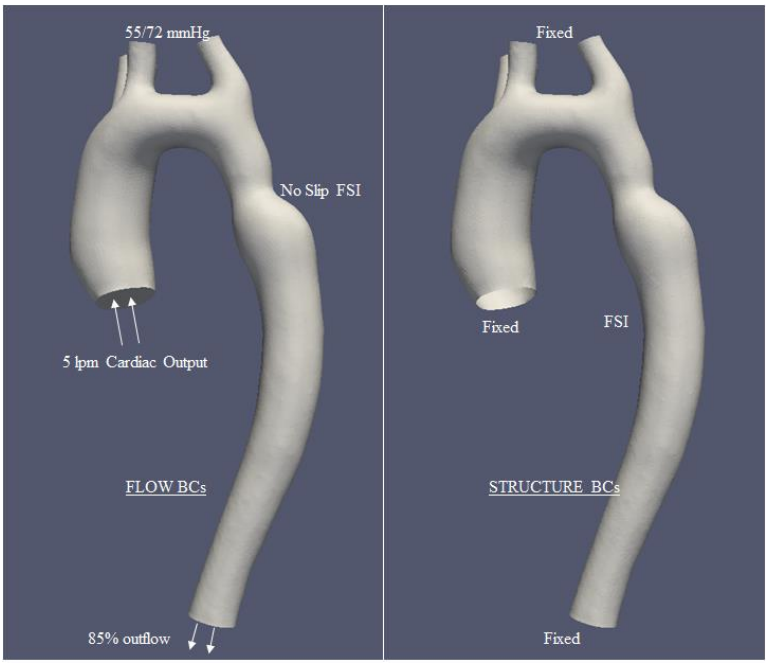

Figure 7.2: Summary of boundary conditions for flow and structural domains.

7.1.2 *Structural Model and Flow-Structure Interaction Coupling*

Limiting chain extensibility models, such as the Gent constitutive law, have been proposed previously to describe arterial wall mechanics [193]. This is based on good agreement with experimental data and the ability of these material models to predict a stress-strain response similar to that estimated by exponential models, including the Fung [194] and Holzapfel-Gasser-Ogden [195] constitutive laws. The molecular-based limiting chain extensibility Arruda-Boyce material model has been recently proposed to simulate the biomechanical response of the aorta [68] and the same was adopted in the present study. This material model is described using the following strain energy function W:

$$W = \mu \sum_{i=1}^{5} \frac{C_i}{\lambda_L^{2i-2}} (I_1^i - 3^i) + \frac{1}{d}\left(\frac{J_{el}^2 - 1}{2} - \ln J_{el} \right) \qquad (7.3)$$

Where μ is the initial shear modulus, λ_L is the limiting network-stretch, I_1 is the first invariant of the right Cauchy-Green strain tensor, d is the incompressibility parameter and J_{el} is the elastic volume strain. The limiting network stretch was set to 1.01 [68]. The constants C_i are defined as follows:

$$C_1 = \frac{1}{2}, C_2 = \frac{1}{20}, C_3 = \frac{11}{1050}, C_4 = \frac{19}{7050}, C_5 = \frac{519}{673750} \qquad (7.4)$$

The initial shear modulus for the diseased case (0.225 MPa) was determined using material constants of the Raghavan-Vorp model [64] obtained previously from mechanical testing of ascending aortic aneurysms for patients with BAV [190]. The initial shear modulus for the healthy control was 0.1 MPa [196]. The aortic wall was discretized using 4-node shell elements [55] in ICEM CFD (Ansys Inc., Canonsburg, PA). The density of the arterial wall was equal to 1120 kg/m^3 and a constant wall thickness equivalent to 1.25 mm was adopted in this study. The inlet and outlets were constrained in all directions [65, 66] to ensure that the resulting aortic

displacements are physiological [190]. Mesh resolutions for the healthy and diseased cases are indicated in Table 7.1. The boundary conditions for the flow and structural domain are summarized in Figure 7.2.

Table 7.1: Summary of mesh resolutions employed in the study.

Case	Mesh Size (Flow)	Mesh Size (Structure)
Normal	0.5 million tetrahedral cells	0.06 million quadrilateral shells
Diseased	1.45 million tetrahedral cells	0.1 million quadrilateral shells

Parallel, 2-way FSI simulations were performed using the ANSYS multiphysics software (Ansys Inc., Canonsburg, PA) [84, 197]. The FSI solution was obtained using a partitioned approach where nodal displacements from the structural solver are received by the flow solver, and the flow solver, in turn, sends the updated nodal force (resulting from normal and shear stresses) to the structural solver. An FSI boundary condition (Chapter 2) was applied at the interface between the flow and structural domains [79]. In order to maintain this aforementioned condition throughout the simulation, the lumen mesh was moved using the Arbitrary-Lagrangian Eulerian (Chapter 2) approach [67]. The mesh for the flow domain was updated using a displacement diffusion scheme [79]. The coupling data transfer control was set at 0.01 with an under relaxation factor equal to unity. Interpolation of flow-induced forces was not required during data exchange for each coupling step since the nodes for the fluid and solid domain were aligned at the FSI interface. Blood flow in the compliant aorta was modeled as quasi-steady [190] with data-exchange between the ANSYS CFX flow and ANSYS Mechanical structural solvers occurring for a total simulation time of 1s, which is approximately the length of a cardiac cycle. Additional details regarding the FSI coupling method have been described elsewhere [197].

7.1.3 *Post-Processing of Solution Variables*

Post-processing of all data was performed using Paraview. Stations were chosen normal to the ascending, transverse and descending aortas to describe the effect of elasticity on flow patterns in controls and TS. Swirling motion of blood in the aorta was quantified using the area-weighted average helicity density H_a [181] as given below:

$$H_a = \frac{1}{S}\int H_d dS \qquad (7.5)$$
$$H_d = v \cdot (\nabla \times v)$$

Where v is the flow velocity, H_d is the helicity density (i.e. scalar product of velocity and vorticity), S is the cross-sectional area. 3D distribution of shear stress was compared for the 2 subjects. 3D maps of vessel wall motion were generated to identify regions that displaced the most in response to flow-induced forces. The potential risk and corresponding location of wall rupture was quantified using 3D distribution of von Mises (VM) stress as described previously for AAAs [198].

7.1.4 *Results*

As indicated in Figure 7.3, deformations were observed throughout the thoracic aorta. The greatest displacements were concentrated in the transverse segment and outer wall of the descending aorta. Flow for the rigid wall case was observed to accelerate from the inlet in the ascending aorta to the outlet in the descending section due to the aortic taper. Although this pattern was unchanged for the FSI model, magnitude of flow velocity decreased in the locations of large, non-uniform radial expansion of the arterial wall.

For the diseased case, the flow was observed to accelerate in the elongated transverse aorta up until the site of coarctation (Fig 7.4). The jet of fluid issuing from the coarctation eventually reattached downstream of the constriction for the CFD and FSI cases. Aortic taper in

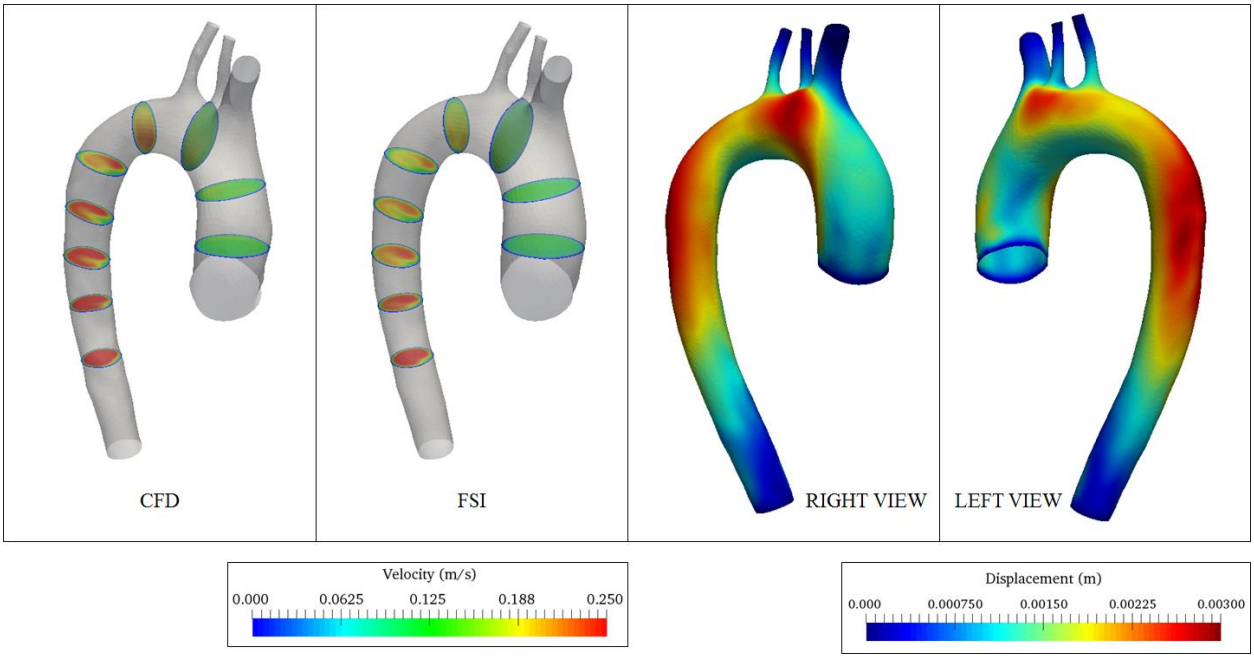

Figure 7.3: Comparison between flow patterns for the healthy control excluding (CFD) and including vessel elasticity (FSI). Displacements of arterial wall for FSI case shown for reference.

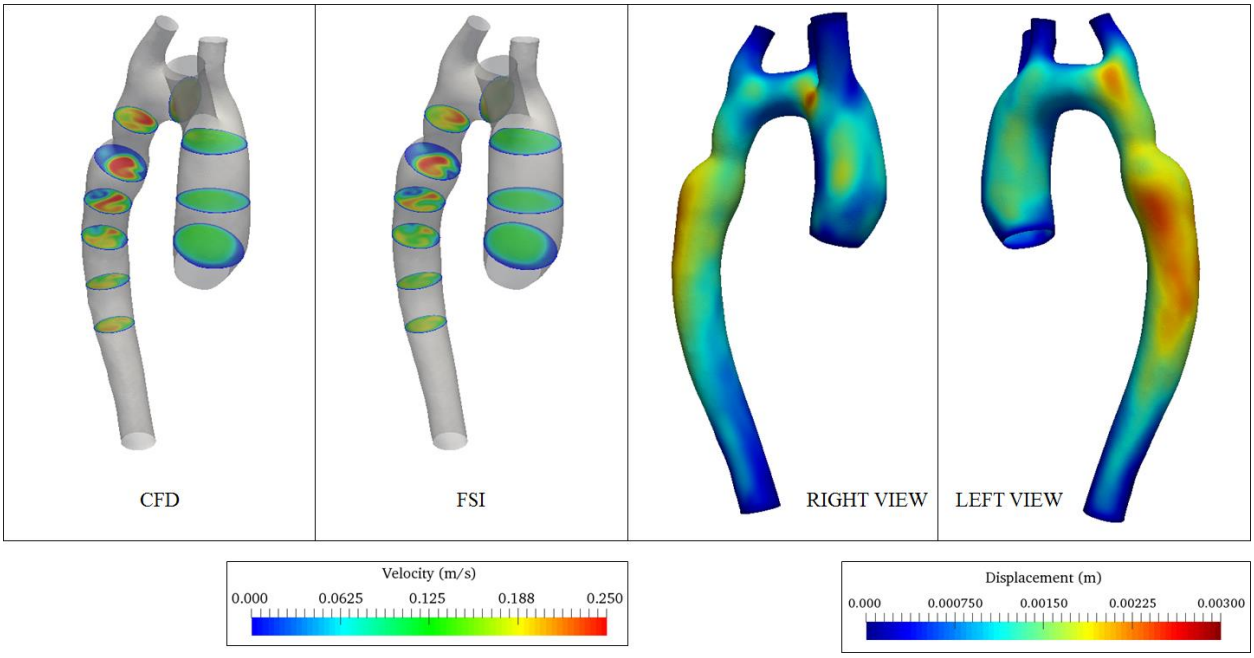

Figure 7.4: Comparison between flow patterns for the TS patient excluding (CFD) and including vessel elasticity (FSI). Displacements of arterial wall for FSI case shown for reference.

the descending aorta resulted in subsequent acceleration of the flow. Although the stiffness of the wall was nearly twice that of the healthy subject, hypertension resulted in large displacements of

the transverse and descending sections that were comparable in magnitude to the healthy case and resulted in flow deceleration. Furthermore, displacements in the descending aorta were greater in the lateral direction. The flow patterns reported in this study were in good agreement with the same reported previously for healthy [199] and diseased aortae [58], for the same flow conditions tested in this study.

Shear stresses minimize plaque deposition in blood vessels. Figure 7.5 indicates the wall shear stresses arising from gradients in flow velocity for the healthy subject.

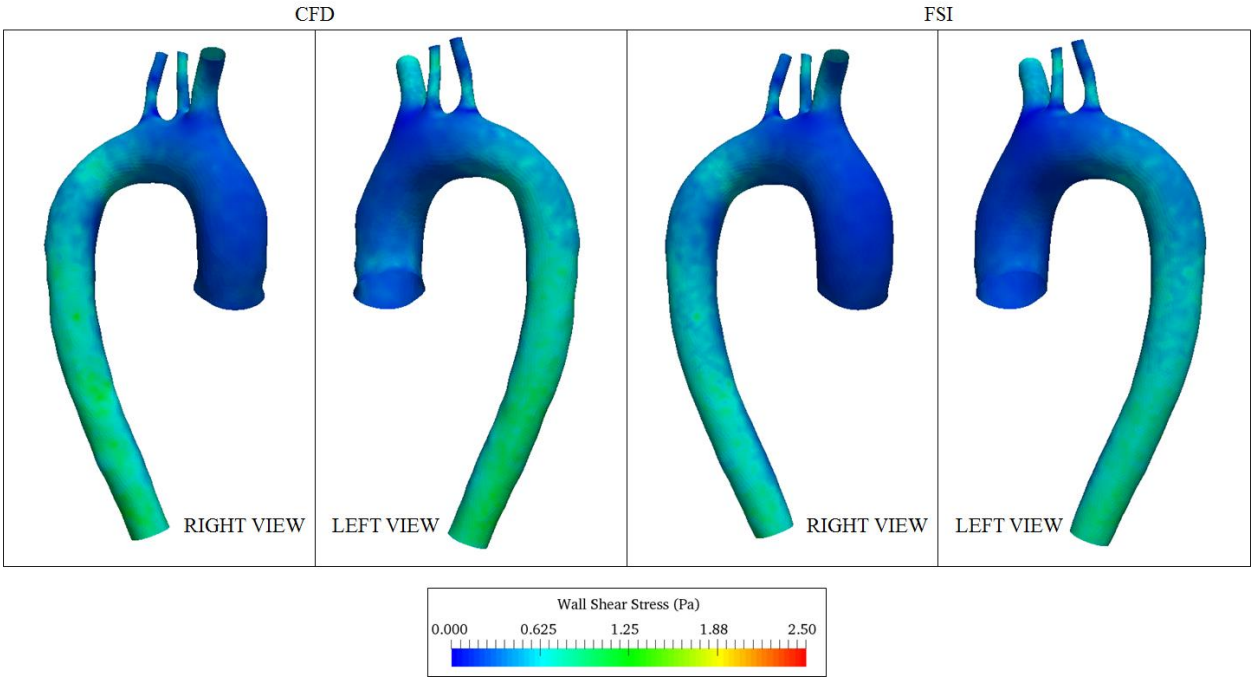

Figure 7.5: Comparison between WSS patterns for the healthy subject including and excluding arterial compliance.

As can be seen, low shear was observed in the ascending aorta for the CFD and FSI cases. The reduced flow velocity for the FSI case enhanced the stagnation regions on the inner and outer walls of the ascending aorta. The wall shear stress was uniformly distributed along the aorta circumference in the descending section. Inclusion of vessel elasticity decreased the mean WSS in this segment by 17 percent. High WSS in TS is undesirable as described previously and can lead to localized thinning of the stiff and brittle vessel wall. Figure 7.6 describes the shear stress

maps for the TS patient. As can be seen, stagnation regions were observed in the ascending aorta similar to the normal subject. Regions of high shear were observed in the transverse aorta and

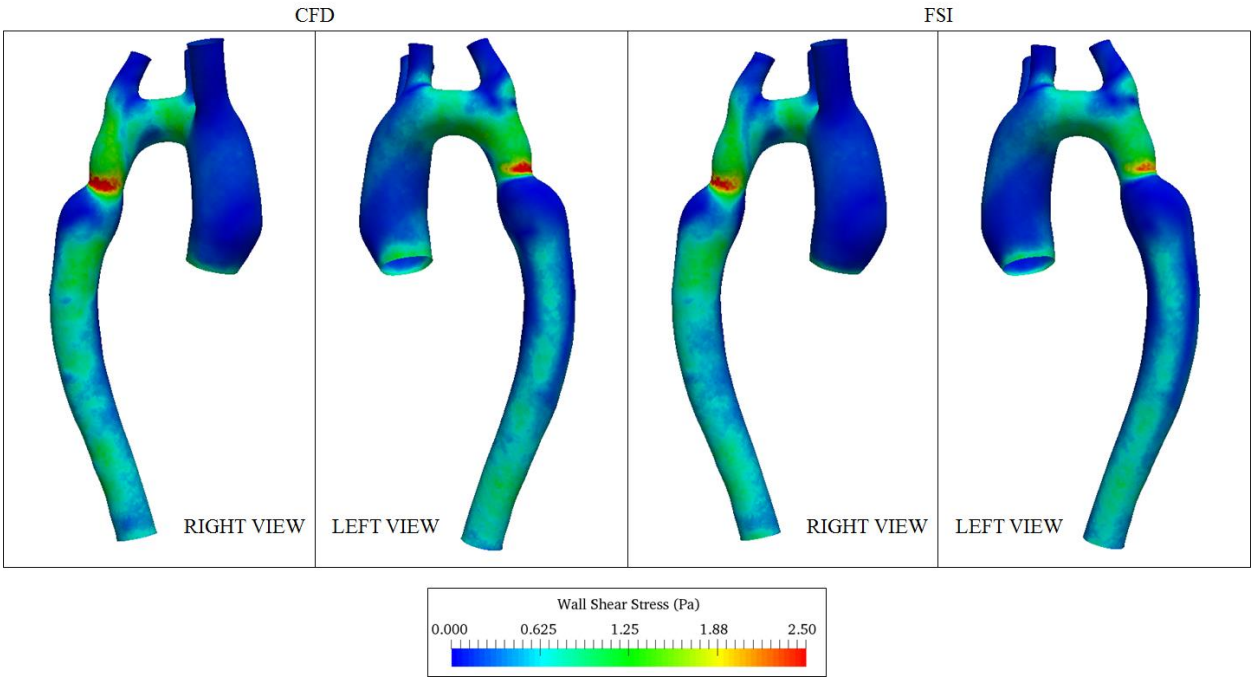

Figure 7.6: Comparison between WSS patterns for the TS patient including and excluding arterial compliance.

reached a maximum at the constriction. Inclusion of vessel elasticity decreased the maximum shear stress by 15 percent in the proximity of the coarctation. Good concordance was obtained between the regions of high and low shear identified in this study, with prior studies [58, 200]. Furthermore, reduced magnitude of peak WSS resulting from the inclusion of vessel elasticity has also been reported previously [68, 201].

Doppler ultrasound studies have indicated that flow patterns in the normal aortic arch are helical and the same was observed in the simulations. The spiral flow is believed to have a beneficial effect on mechanisms of endothelial damage repair. Furthermore, the swirl minimizes stagnation flow regions, flushes the inner wall or intima more evenly and minimizes atherosclerosis. Helicity distribution was described qualitatively in Figure 7.7 (healthy case) and 7.8 (TS patient) using isosurfaces of helicity density H_a [187]. It should be noted that the red and

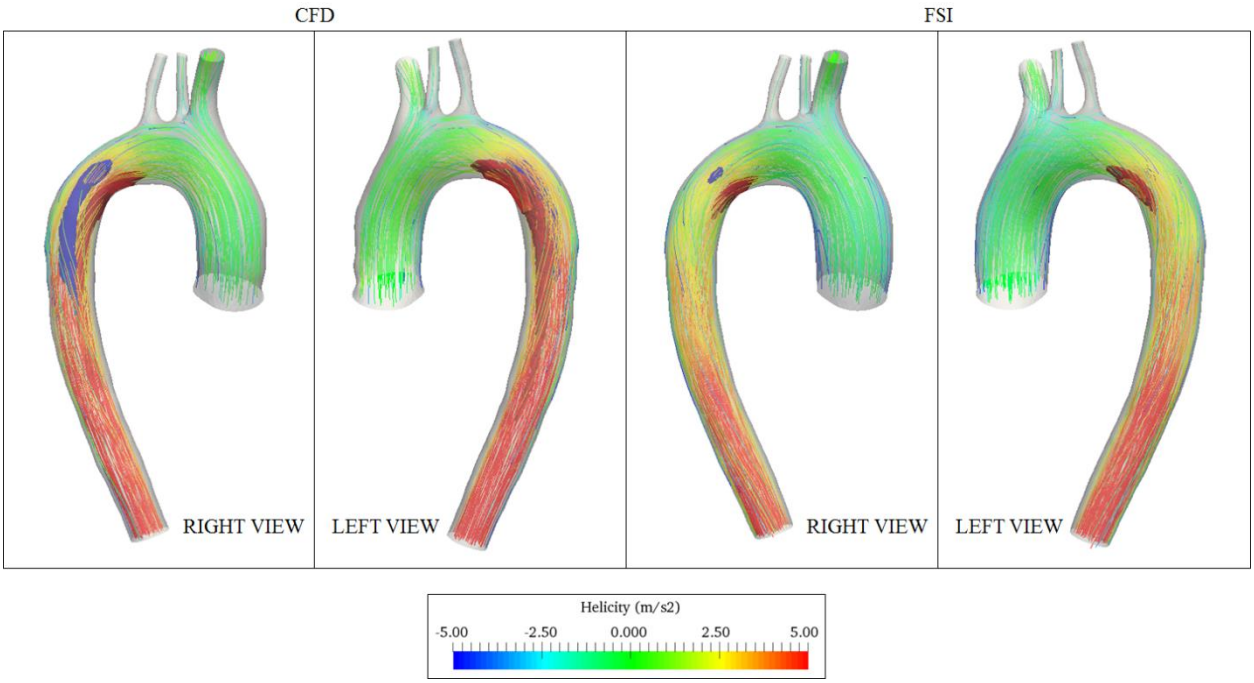

Figure 7.7: Helicity comparison for the control case including and excluding arterial compliance. Streamlines superposed to indicate directionality of the helix.

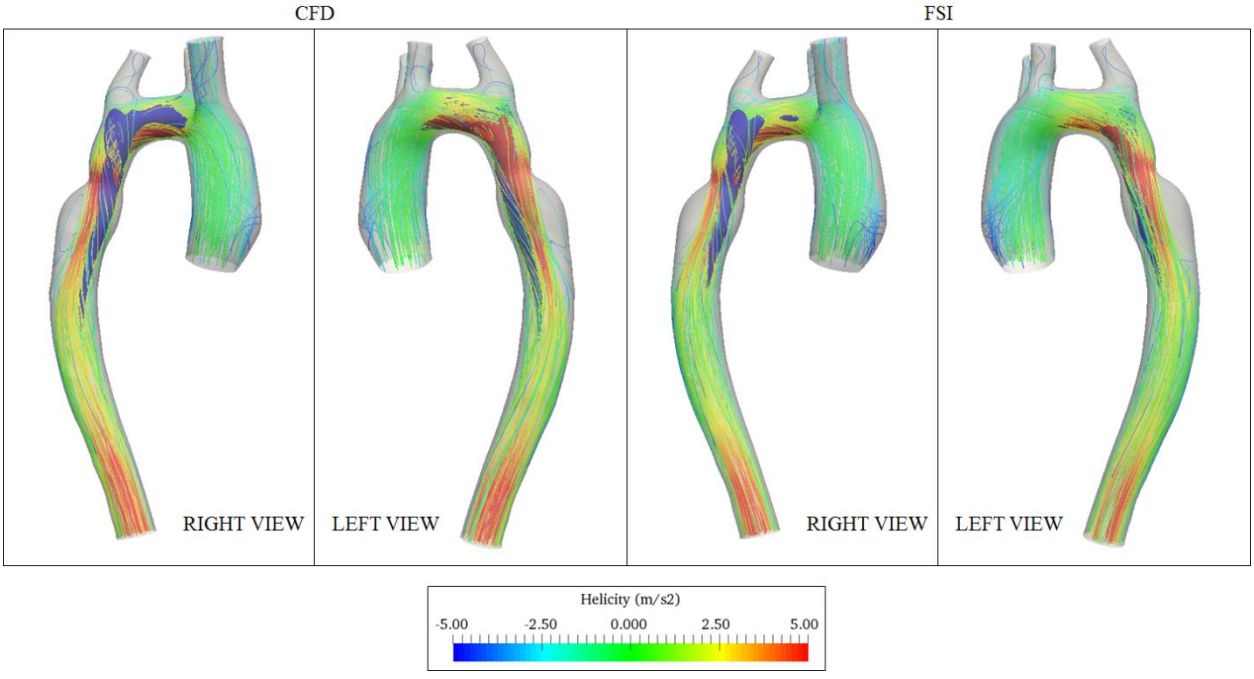

Figure 7.8: Helicity comparison for the TS patient including and excluding arterial compliance. Streamlines superposed to indicate directionality of the helix.

blue surfaces represent a clockwise and counterclockwise spiral respectively. Streamlines were superposed on these surfaces to elucidate the direction of the helix. Line plots describing variation in area-weighted average helicity density (H_a) for all models are summarized in Figure 7.9. Markers indicating values of H_a at 7 stations for the healthy case and 6 stations for the diseased case are superposed on these plots. For the healthy subject, the swirl increased gradually in the ascending aorta and steeply in the aortic arch. The helicity density was greatest at the end of the aortic arch [181] and the swirl steeply decreased in the descending segment. Inclusion of arterial compliance resulted in a slightly reduced helicity and similar station-to-station variation until the exit of the aortic arch. Cancellation of the double helix (also indicated in Fig 7.7)

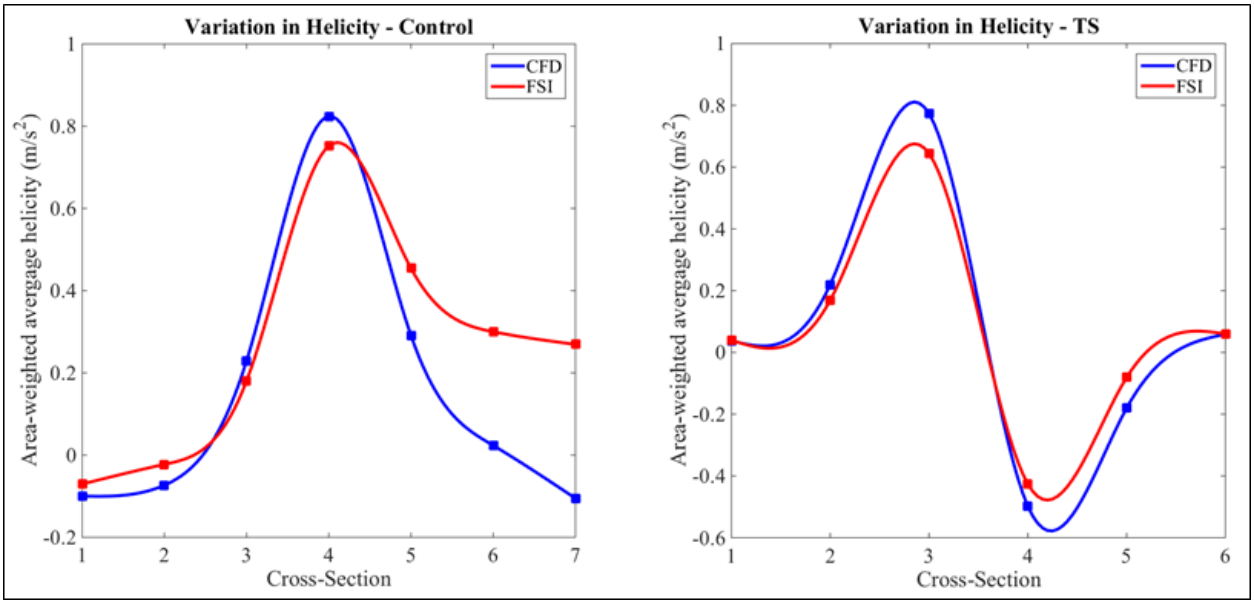

Figure 7.9: Variation in H_a along the thoracic aorta for the control and TS subject (All values in m/s^2. Blue solid line – CFD, Red solid line – FSI, Helicity values at 7 stations indicated using square markers).

resulted in higher helicity density in the descending section for the FSI case. For the TS patient, variation in helicity was similar for the CFD and FSI models. As compared to the healthy subject, the helicity increased steeply in the ascending aorta and reached a maximum value in the transverse aorta. Furthermore, direction of the swirl apparently reversed, in the proximity of the

coarctation due to cancellation of the helix, following which the direction of the swirl recovered and eventually reduced to zero in the descending aorta.

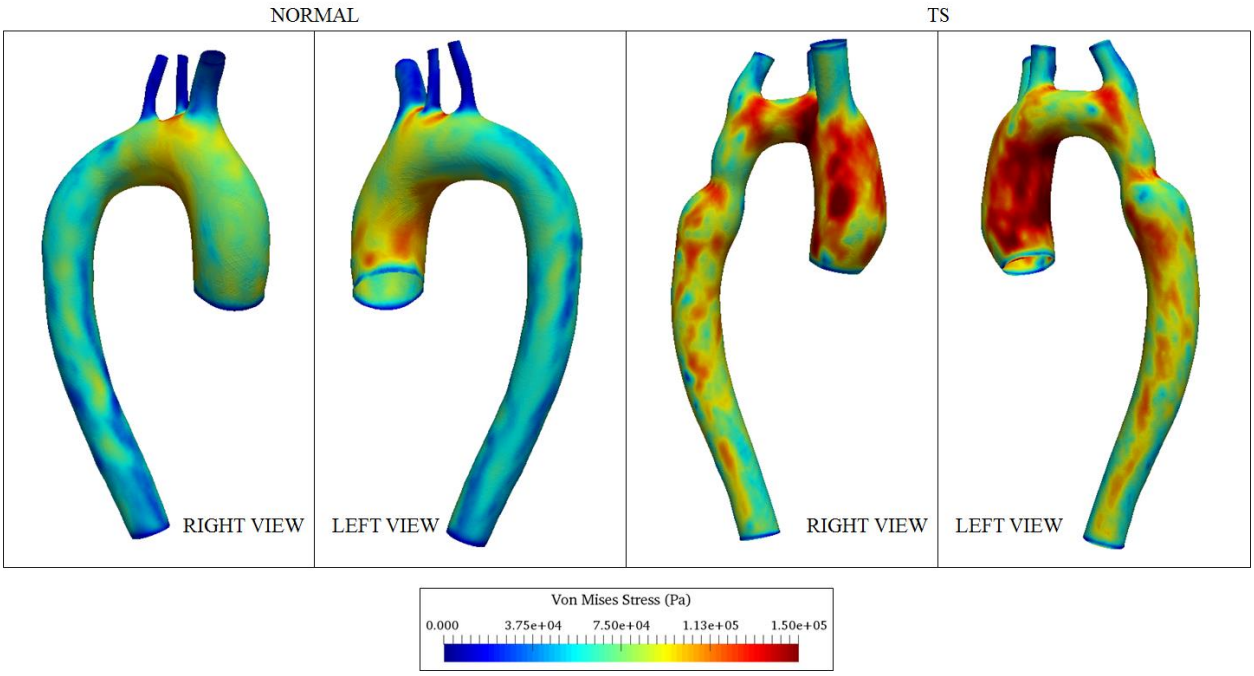

Figure 7.10: Maps of Von-Mises stress distribution for healthy and diseased aortae.

Figure 7.10 indicates patterns of mechanical stresses in the control and TS patients. As can be seen for the normal case, high mechanical stresses were observed on the inner wall of the ascending aorta. The stress concentration was greatest at the junction between the daughter vessels and the transverse aorta. For the TS patient, high stress concentration was observed throughout the ascending aorta and in sections of the transverse aorta. Moreover, the stresses in the descending section were more significant as compared to the normal case. Although the simulation results indicated high rupture potential of the ascending section, the probability of weakening of the vessel wall at the site of coarctation was also increased due to the high shear stresses and concentration of mechanical stresses. Higher mechanical stresses in the diseased case could be attributed to higher arterial stiffness and greater aortic wall pressure compared to the control.

7.2 *Longitudinal Comparison of Hemodynamic and Mechanical Variables in Turner syndrome*

7.2.1 *Methods*

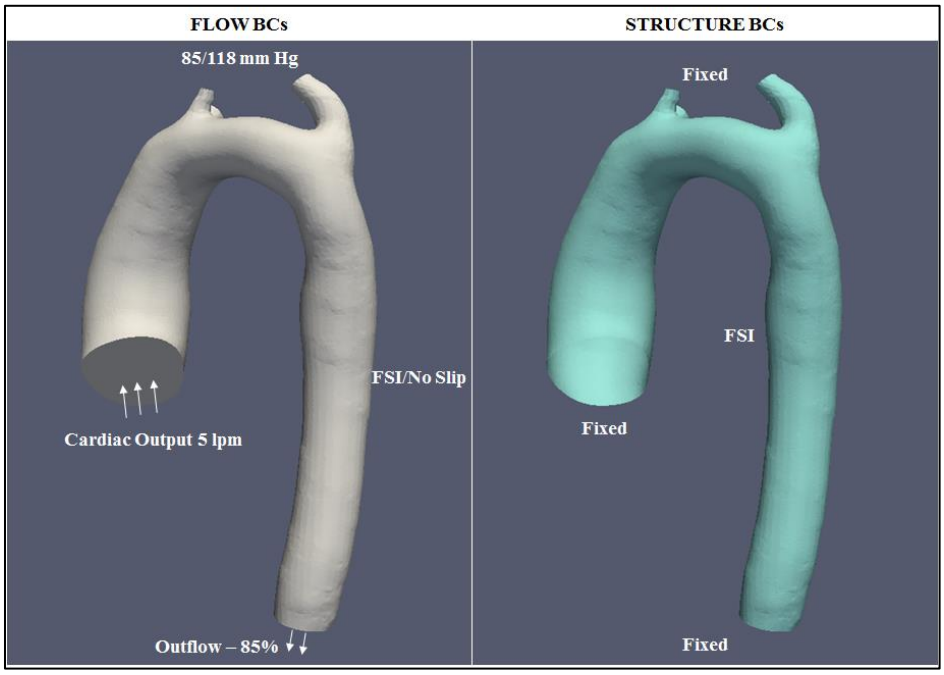

Figure 7.11: Summary of FSI boundary conditions for longitudinal comparison study.

Progression of cardiovascular disease in TS was quantified previously using the Euclidean distance maps described in Chapter 6. Quasi-steady FSI modeling described in section 7.1 was applied to the present study. 3 adult TS patients (Two patients with BAV, ETA, HTN (Patient 1, 2) and one patient with BAV, ETA, CoA and HTN (Patient 3)) were selected for this analysis. 3 healthy adult female volunteers were also analyzed in this study. Longitudinal scans corresponding to the first (i.e. baseline) visit and the fourth visit (10 years following the baseline visit) were considered in this analysis. Subject-specific geometries of the aorta lumen and vessel wall were reconstructed and discretized as described earlier. Figure 7.11 summarizes the boundary conditions employed for the simulations. It should be noted that the static pressure at the outlet (Fig. 7.11) corresponded to a mean aortic pressure (MAP) of 85 mmHg for the healthy subjects and 118mmHg for the diseased cases [192]. Additionally, an initial shear modulus corresponding to 0.145 MPa [190] was assigned for the controls.

7.2.2 *Results and Discussion*

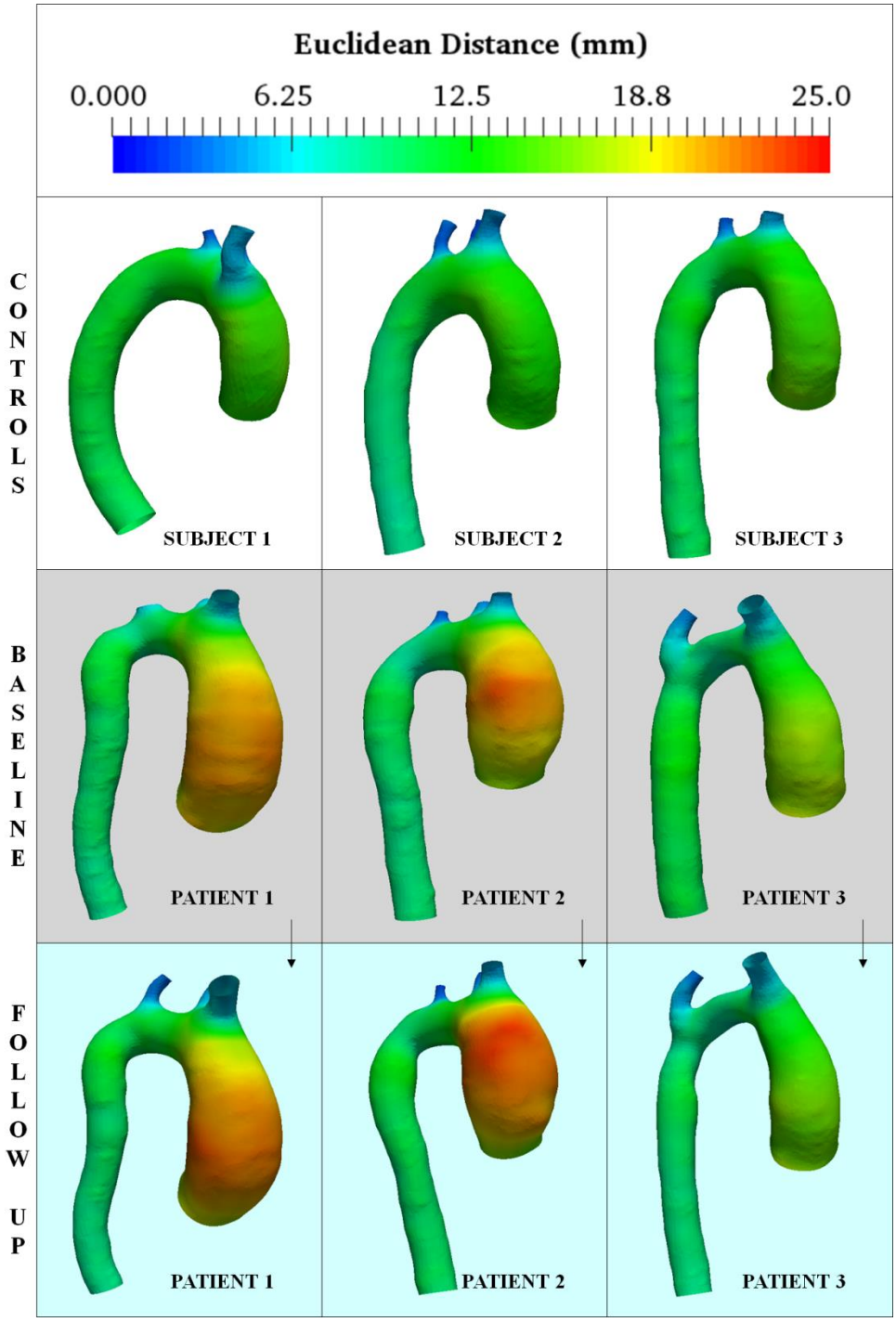

Figure 7.12: Variation in aorta dimensions for controls and visit-to-visit variation in aorta dimensions for TS. (Note: Baseline: First visit, Follow-up: Visit after 10 years, Arrows indicate disease progression with age, For circular cross-section, color (value) is identical circumferentially).

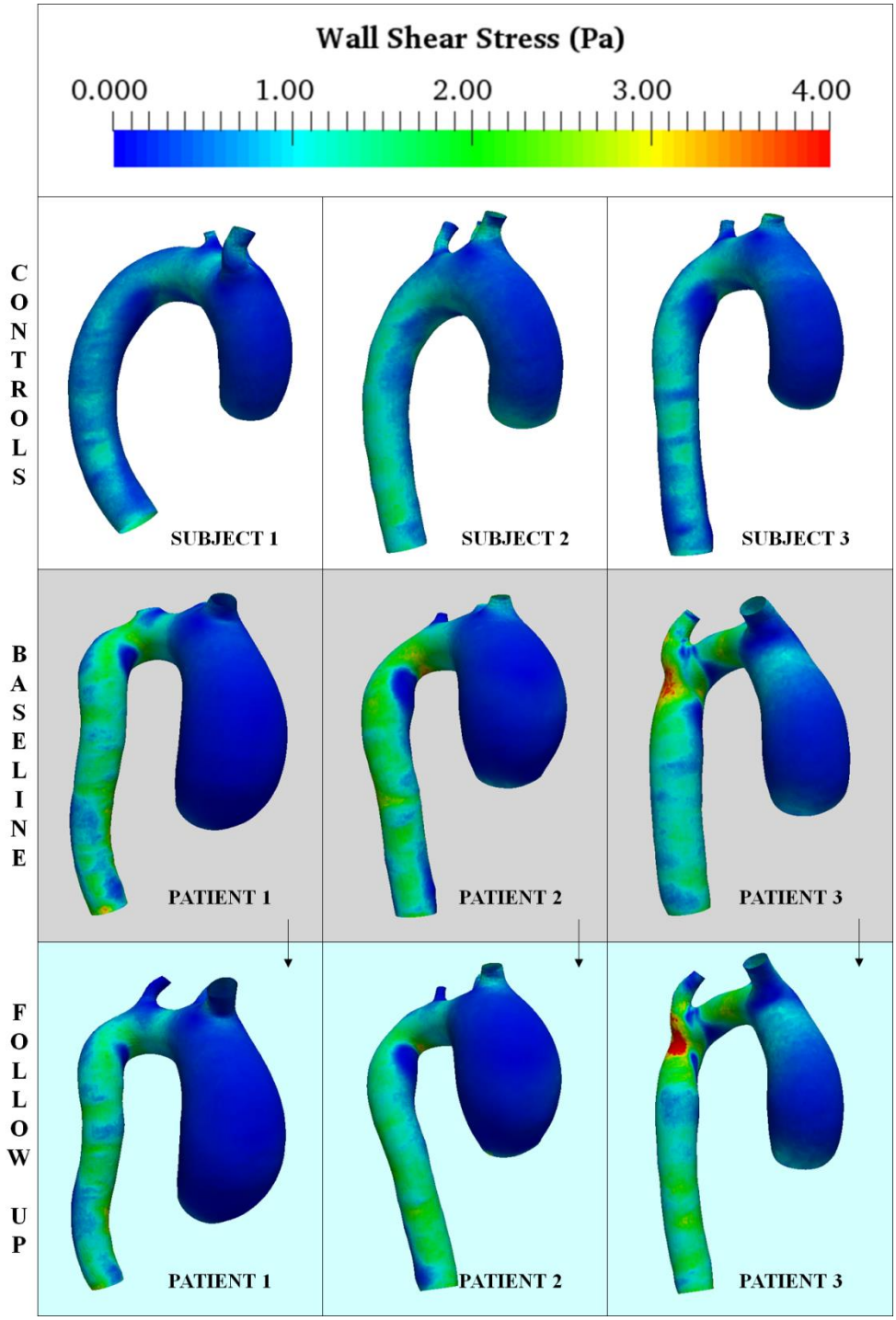

Figure 7.13: Variation in wall shear stress for controls and visit-to-visit variation in WSS for TS (Note: Baseline: First visit, Follow-up: Visit after 10 years, Arrows indicate disease progression with age).

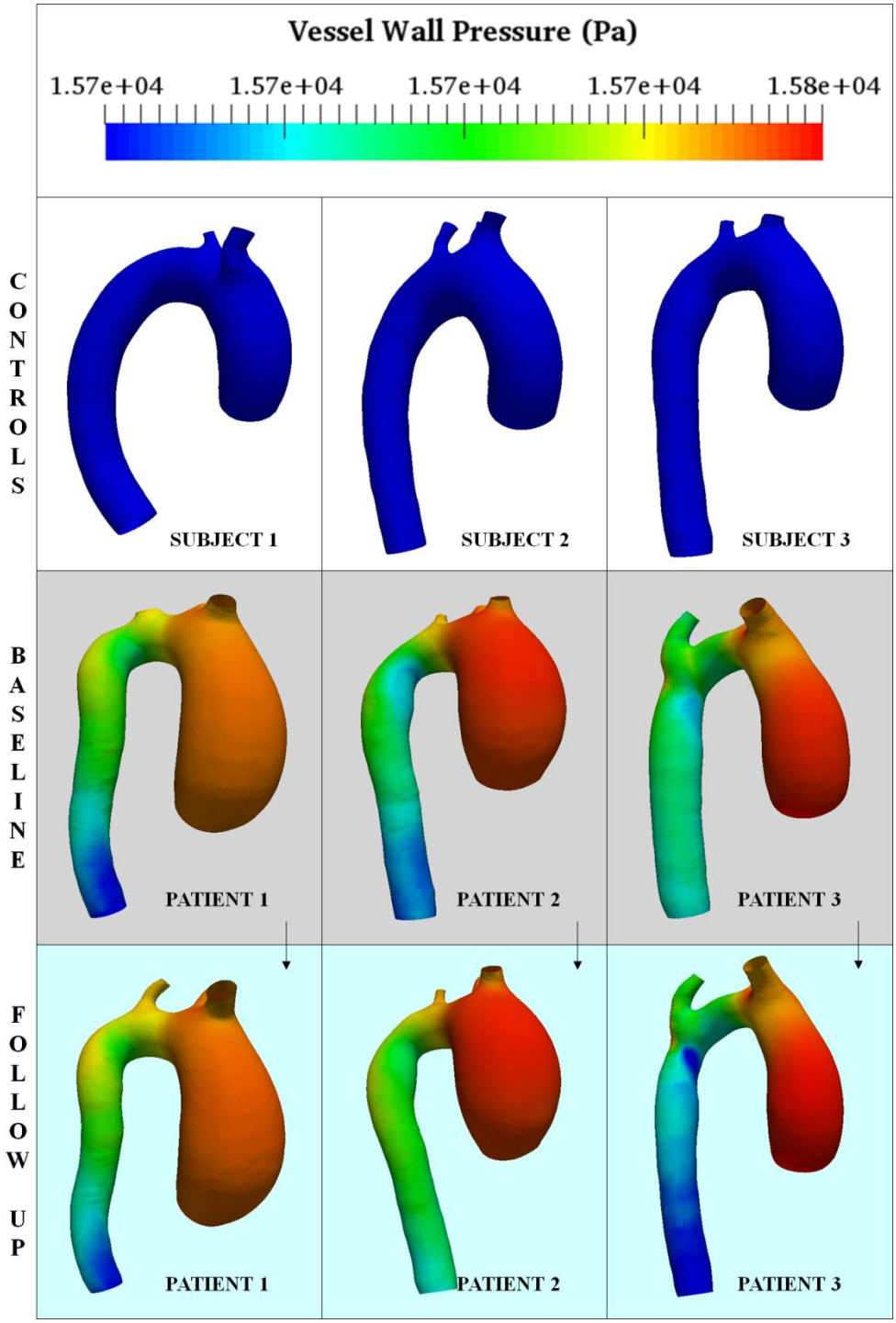

Figure 7.14: Variation in aorta wall pressure for controls and visit-to-visit variation in vessel wall pressure for TS. (Note: Baseline: First visit, Follow-up: Visit after 10 years, Arrows indicate disease progression with age, Color scale adjusted to highlight variation in vessel wall pressure for TS).

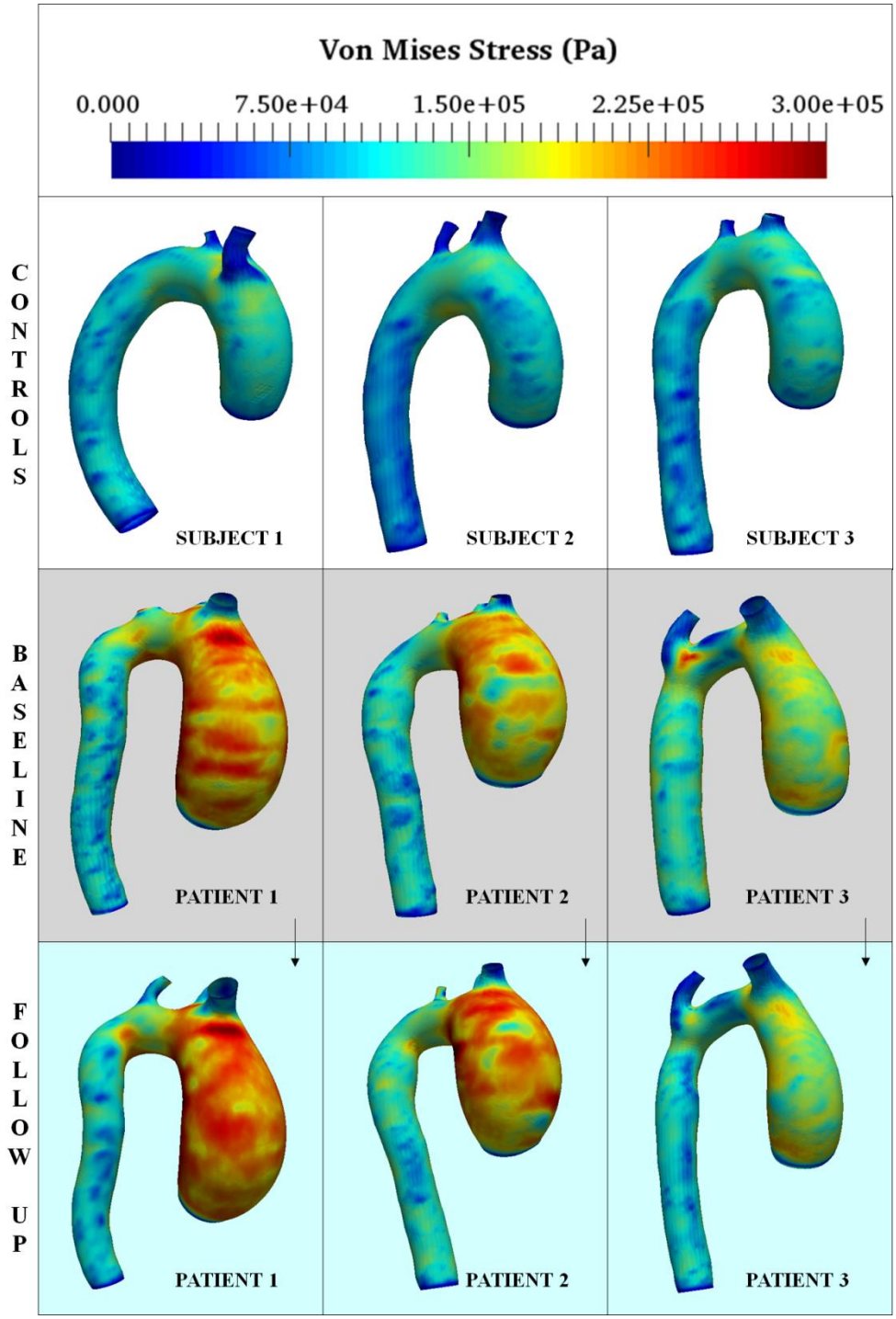

Figure 7.15: Variation in mechanical stress for controls and visit-to-visit variation in Von-Mises stress for TS.

(Note: Baseline: First visit, Follow-up: Visit after 10 years, Arrows indicate disease progression with age).

Variation in aorta geometry for the 3 TS subjects and 3 controls analyzed in this study are described in Fig. F.1 (Appendix) and Fig. 7.12. The largest aorta caliber was observed in the ascending aorta for the TS and control subjects, as described in Chapter 6. Aortic dimensions for patient 1 were stable in the transverse and descending sections and moderate dilatation was observed between the baseline and follow-up visit (<10 percent change with time). Patient 2 exhibited progressive dilatation over the entire length of the thoracic aorta and larger changes were observed in the ascending section (>10 percent visit-to-visit change). A reduction in lumen radius was observed throughout the aorta for patient 3. The decrease in dimensions could be potentially attributed to anti-hypertensive treatment. Furthermore, the distance maps indicated that TS patients exhibited larger ascending aorta dimensions compared to controls. Asymmetry was also greater in the ascending aorta for TS and controls. The healthy and diseased descending and transverse sections were nearly circular.

Figure F.2 (Appendix) and 7.13 summarizes the 3D distribution of WSS for the controls and TS patients analyzed in this study. For the controls, the shear was uniformly distributed in the descending aorta. Low shear was observed throughout the ascending aorta. Average WSS for healthy control 1 was lower as compared to control subjects 2 and 3. A stagnation (i.e. low WSS) region was observed at the end of the aortic arch on the inner wall of the descending aorta. The stagnation region was observed in the ascending aorta for the 3 TS subjects. The average WSS in the descending aorta was ~50 percent higher than the corresponding value for controls. Patient 3 (i.e. the subject with CoA) exhibited the highest shear stress (~4 Pa) for all the TS subjects considered in this study. Stagnation regions on the inner wall of the descending aorta at the end of the aortic arch were observed for patients 1 and 2. WSS distribution was stable for patient 1 over time. Besides, the stagnation region at the end of the aortic arch decreased between visits.

For TS patient 2, WSS concentration at the end of the aortic arch decreased moderately over time and the stagnation region downstream was unchanged between visits. For TS patient 3, higher shear stresses were observed in the ETA as compared to patients 1 and 2. The distribution of shear stresses in the transverse aorta was unchanged between visits. Maximum magnitudes of shear stress at the coarctation increased by 30 percent over time. Subsequently, higher WSS was observed downstream of the CoA for the follow-up visit.

Distribution of aorta wall pressure for the controls is described in Figure F.3 (Appendix). The wall pressure was observed to decrease distally (i.e. from the inlet in the ascending aorta to the outlet in the descending section). The decrease in the aorta wall pressure was greater for controls 2 and 3 as compared to healthy subject 1. Figure 7.14 summarizes the distribution of aorta wall pressure for the 3 TS subjects. Higher wall pressures were observed throughout the thoracic aorta for the diseased subjects due to hypertension. Larger magnitudes of wall pressure were observed in the ascending aorta in a manner similar to the control subjects. For TS patient 1, the wall pressure distribution was stable between visits. For TS patient 2, lower wall pressure was observed in the proximity of the outlet in the descending segment for the baseline visit. The region of low pressure at the end of the aortic arch was also not observed in the follow-up visit. For the follow-up visit corresponding to TS patient 3, a low pressure region was observed at the site of the CoA that recovered downstream of the constriction. Recovery in the wall pressure was followed by further decrement due to the aortic taper.

Figure F.4 (Appendix) summarizes the distribution of von-Mises stresses for the controls. Mechanical stresses were distributed distally in the ascending aorta (i.e. in the proximity of the IA). High stresses were observed at the junction between the transverse aorta and the daughter vessels. Stresses were also distributed at the end of the aortic arch on the inner wall of the

descending section. The mean value of the peak stress for controls was 0.19 MPa. Figure 7.15 summarizes the mechanical stress distribution for the TS subjects considered in this study.

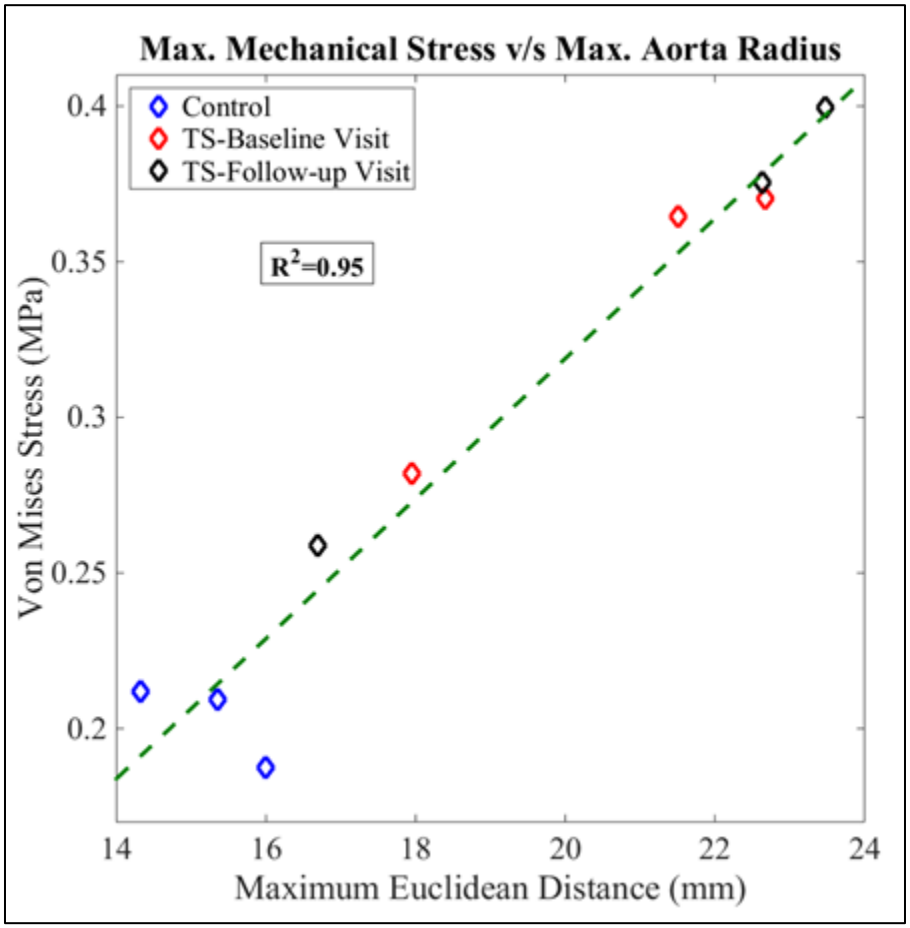

Figure 7.16: Correlation between peak mechanical stress and maximum aorta radius.

Average value of the peak mechanical stresses in TS were 74 percent higher than the corresponding values for controls primarily due to hypertension and lower vascular compliance (Section 7.1). For all TS subjects, high mechanical stresses were concentrated on the inner wall of the ascending aorta. For patient 1, the distribution of von-Mises stress on the outer wall of the ascending aorta was unchanged between visits. Concentration of mechanical stresses distally on the outer wall (i.e. proximity of IA) increased from the baseline to the follow-up visit. The peak values of mechanical stress increased by 3 percent over time. For patient 2 with progressive ascending aortic dilatation, the maximum stresses increased by 6 percent between visits. For the

baseline visit, high stresses were observed distally on the outer wall of the ascending aorta. The stresses were distributed both proximally and distally for the follow-up visit. As indicated in Figure 7.16, peak values of VM stress correlated highly with the maximum value of Euclidean distance (R^2=0.95). High correlation obtained between Von-Mises stress and aorta radius provided evidence of high rupture potential in TS patients with ascending aortic dilatation. The distribution of Von-Mises stress could be potentially employed by clinicians and radiologists to predict the probability and location of vessel wall tear. It should be noted that the computational studies described in this chapter did not consider the influence of including the aortic sinus on flow patterns and distribution of biomechanical variables. Furthermore, the study presented in this section did not consider TS subjects with tricuspid aortic valve. It is hypothesized that inclusion of the aortic sinus would provide an enhanced description of cardiovascular risk markers in TS. Additionally, the FSI modeling presented in this study would have to be extended to additional aortic phenotypes to provide more evidence of the correlation between geometric and functional variables.

Chapter 8

Role of the Sinus in Characterization of Aortic Disease

Results from this chapter are included in a manuscript currently in preparation for submission to a peer-reviewed biomedical engineering journal.

The present study aims to describe the importance of including the aortic root geometry in the computational FSI model of aortic blood flow described in Chapter 7. This study also compares hemodynamic and mechanical risk markers of aortic disease for several aortic phenotypes observed in TS and healthy individuals.

8.1 *Methods*

8.1.1 *Aortic Reconstruction and Geometric Characteristics*

Six adult patients with karyotypically proven TS (two with tricuspid aortic valve (TAV); four with BAV) were recruited through the Danish National Society of Turner Syndrome contact group as part of a larger ongoing study. Additionally, four healthy adult female volunteers were recruited to serve as control subjects. All subjects with TAV were normotensive (including the controls), while patients with BAV were hypertensive. Among patients with TAV, the first patient (TAV-1) had aortic valve regurgitation (mild), ETA and CoA while the second subject (TAV-2) had ascending aortic dilation only. All 4 subjects with BAV had ETA, and CoA was observed in two subjects (BAV-1 and BAV-3). Table G.1 (Appendix) summarizes the clinical history for the TS patients. All subjects provided informed consent to participate in this study following approval by the ethical committee of The Central Denmark Region (#201250012); the study was registered at ClinicalTrials.gov (#NCT01678274). All subjects were examined using cardiovascular magnetic resonance (CMR) on a 1.5 T whole body-scanner (Philips Medical

System – Best, The Netherlands). The CMR protocol has been described elsewhere [32]. The CMR data was imported into Mimics (Materialise Inc., Plymouth, MI) to reconstruct control and patient-specific geometries of the thoracic aorta as described previously in Chapter 6.

Three-dimensional (3D) geometries of the thoracic aorta, including the aortic sinuses, innominate (IA), left common carotid (LCCA) and left subclavian arteries (LSCA) were reconstructed and smoothed using Mimics. The geometries were then clipped in the descending aorta at the diaphragm and below the aortic sinuses using Paraview (Kitware Inc., Clifton Park, NY). The Vascular Modeling Toolkit (VMTK) was then employed to compute centerlines [165] of the clipped aortas, between the aortic root and descending aorta. A short tubular extension normal to the aorta and directed into the left ventricle was then constructed using the centerline generated in the previous step. This ensured that the flow inlet was located below the aortic root [202]. The extensions were merged with the reconstructed aortic models, smoothed in Mimics and exported in stereolithography (STL) format for geometric measurements and computational modeling. Inlet and outlets of the computational domain were identified for the resulting aortic surfaces. Euclidean distance maps were generated to quantify asymmetry in the morphology of the thoracic aorta using VMTK [203]. In order to compare flow and mechanical variables for complete and truncated aortic geometries, the ascending aorta was clipped at the sinotubular junction to generate a second set of aortic models for 2 randomly chosen subjects – healthy control 4 and BAV-3.

8.1.2 *Computational FSI Modeling*

The flow model described in Chapter 7.1.1 was also employed in the present study. The flow domain was discretized using unstructured tetrahedral elements (Chapter 7.1.1) using the centerlines-based mesh generator which adapts to changes in aortic geometry [204] and ensures a

smooth transition in mesh density, such as would be required at the STJ and constrictions in the thoracic aorta. Table G.2 (Appendix) summarizes the mesh resolutions. Mesh resolutions adopted for the flow domain were of the same order of magnitude (10^6) employed in a previous study involving steady CFD simulations of aortic blood flow in TS [58]. Constant velocity flow computations were performed using thermo-physical properties of blood outlined earlier, for boundary conditions defined in Chapter 7.1.1. It should be noted that the static pressure at the branch outlets corresponded to the mean aortic pressure [205] for normotensive and hypertensive subjects defined in Chapter 7.2.1. For the vessel wall, the hyperelastic material model defined in Chapter 7.1.2 was also employed in the current study. Shear moduli corresponding to 0.145 MPa and 0.225 MPa were assigned for the normotensive (the 4 healthy controls, TAV-1, TAV-2) and hypertensive (BAV-1, BAV-2, BAV-3, BAV-4) subjects, respectively (Chapter 7.2.1). The aortic wall was discretized using 4-node shell elements [55]. Table G.2 summarizes the vessel wall mesh resolutions. The number of elements was an order of magnitude (10^5) higher than the same reported previously (10^4) [56, 205]. A constant wall thickness corresponding to 1.5 mm [206] was adopted. The inlet (corresponding to the aortic root (complete model) or the STJ (truncated model)) and outlets were constrained in all directions [65, 66] to ensure that the resulting aortic displacements were physiological [190]. Parallel, 2-way FSI simulations were performed using the ANSYS multiphysics software as described previously in Chapter 7.1.2.

8.1.3 *Post-processing of Solution Variables*

Post-processing of the solution variables for the flow and structural domains was performed using Paraview and VisIt [207]. 3D streamline plots were generated to describe flow patterns in TAV and BAV aortas. Flow velocity magnitudes corresponding to healthy subject 4 and BAV 3 were compared for the full and truncated computational models at seven stations (Appendix G)

[58]: Station 1 – Ascending aorta midway between the sinotubular junction and IA, Station 2 – Ascending aorta proximal to the IA, Station 3 – Transverse aortic arch midway between LCCA and LSCA, Station 4 – Aortic isthmus distal to the LSCA (upstream of any CoA), Station 5, 6, 7 – Descending aorta between left pulmonary artery and left atrium (downstream of any CoA). Swirling motion of blood in the aorta was quantified using the area-averaged helicity density H_a (Chapter 7.1.3, Equation 7.5) and absolute area-averaged helicity density H_{abs} (Appendix G). 3D distribution of WSS and aorta wall pressure was compared for the 10 subjects. 3D maps of vessel wall motion were generated to identify regions that displaced the most in response to flow-induced forces. The potential risk and corresponding location of wall rupture was quantified using 3D distribution of von Mises (VM) stress as described previously in Chapter 7.1.3. Linear regression analysis was performed using MATLAB (MathWorks Inc., Natick, MA) to describe correlations between the mechanical stress and aorta geometry (Chapter 7.2).

8.2 *Results*

8.2.1 *Comparison of Aortic Geometries*

The maximum aortic radius was in the sinus for all the controls (19.8±0.9 mm (mean radius±SD)) and the change in radius from the root to the ascending aorta was 25 percent (Figure 8.1a). In BAV-4 the largest Euclidean distance was in the ascending aorta, with the largest aortic dimensions observed in the aortic sinus for the remaining patients (Figure 8.1b). The maximum aortic radius for all TS patients (21.6±1.9 mm) was 10 percent higher than the corresponding value for healthy volunteers. Moreover, the change in lumen dimensions for patients with aortic root dilatation was higher compared to controls (50 percent). Truncation of the aortic geometries above the sinotubular junction would both miss the true location of the largest aortic radius and fail to depict the geometric changes across the proximal thoracic aorta.

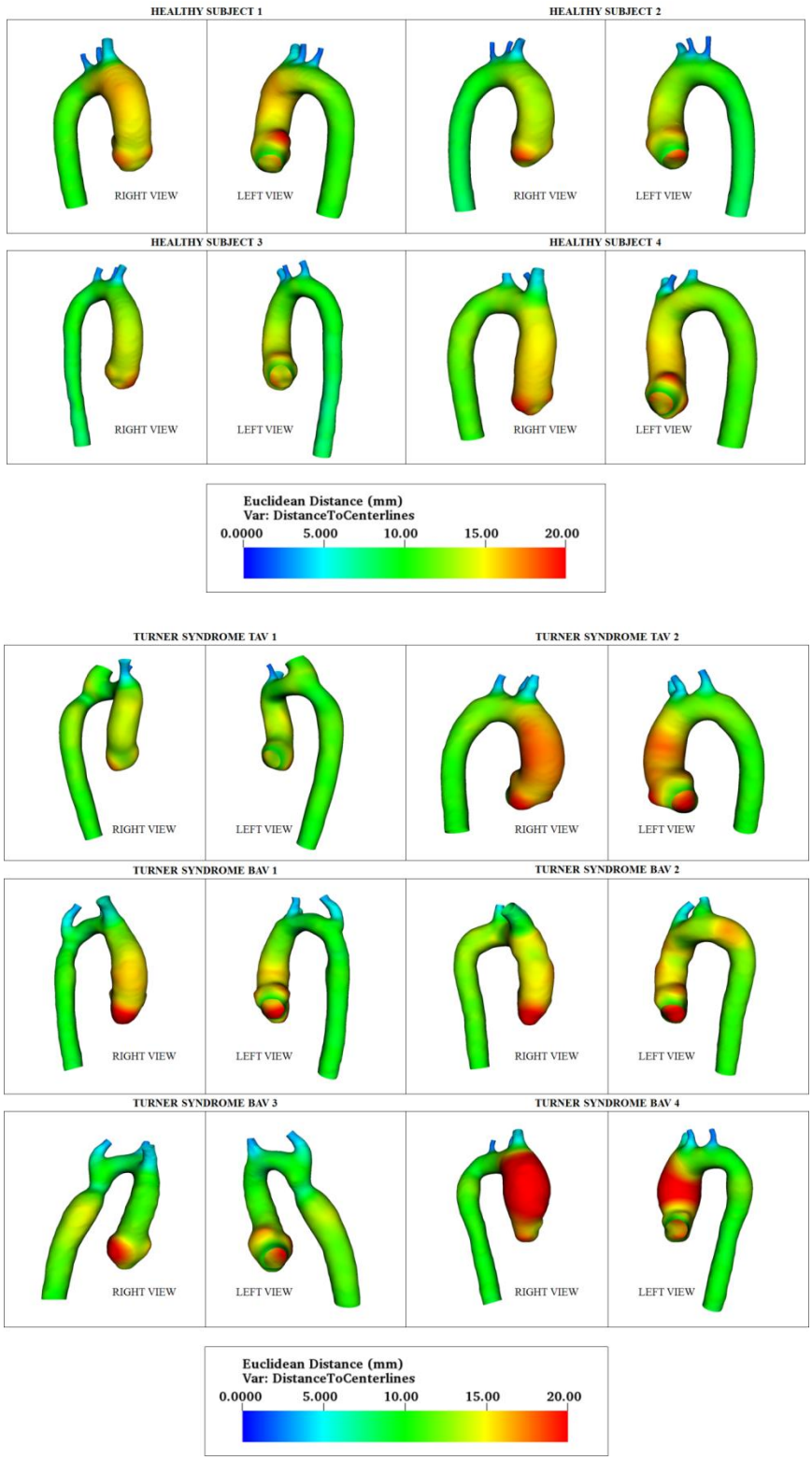

Figure 8.1: Contour plots describing the three-dimensional variation in Euclidean distance from centerlines for the four healthy controls and the six Turner syndrome patients analyzed in the study.

8.2.2 *Comparison of Hemodynamic Variables*

Flow was skewed towards the convexity (i.e. outer curvature) of the ascending aorta for all the subjects (Figure 8.2), occuring as left-handed spiral flows on the outer wall of the ascending aorta. Higher ascending aortic flow velocities were observed for healthy control 2, TAV-1 and BAV-3. Flow accelerated in the descending aorta for all subjects in relation to luminal tapering (Fig. 8.2), but the peak descending aortic flow velocity was higher for TS subjects with CoA (TAV-1, BAV-1 and BAV-3). These subjects also exhibited increased flow velocities in the elongated transverse segment. Descending aortic flow velocities for healthy controls 2, 3 and BAV-4 were comparable, and greater than the same for healthy controls 1, 4, TAV-2 and BAV-2. Flow recirculation was observed in the sinus for controls and TS. Low flow velocity regions observed on the inner curvature of the ascending aorta were higher in TAV-2 and BAV-4. As randomly chosen illustrations, variability in aortic flow patterns and helicity following exclusion of the aortic root are described for healthy control 4 and BAV-3 in Appendix G.

The distribution of WSS in the descending aorta was similar for healthy controls 2 and 3, and for healthy controls 1 and 4 (Figure 8.3). The magnitude of shear stresses was lower for the latter pair. The distribution of WSS in the ascending aorta was similar for healthy controls 2 and 4, and for healthy controls 1 and 3. Shear stresses on the outer wall of the ascending aorta were higher for the former pair (Figure 8.3). Moreover, the segment with maximum WSS was observed in the transverse aorta for 3 controls (healthy control 1, 2 and 4) and in the descending aorta for the last control (healthy control 3). Similar patterns of WSS were observed in TS with a CoA and ETA (Figure 8.3, TAV-1, BAV-1 and BAV-3). Moreover, similarities were observed between the ascending aortic WSS distribution for TAV-1 and healthy control 2 and BAV-1 and

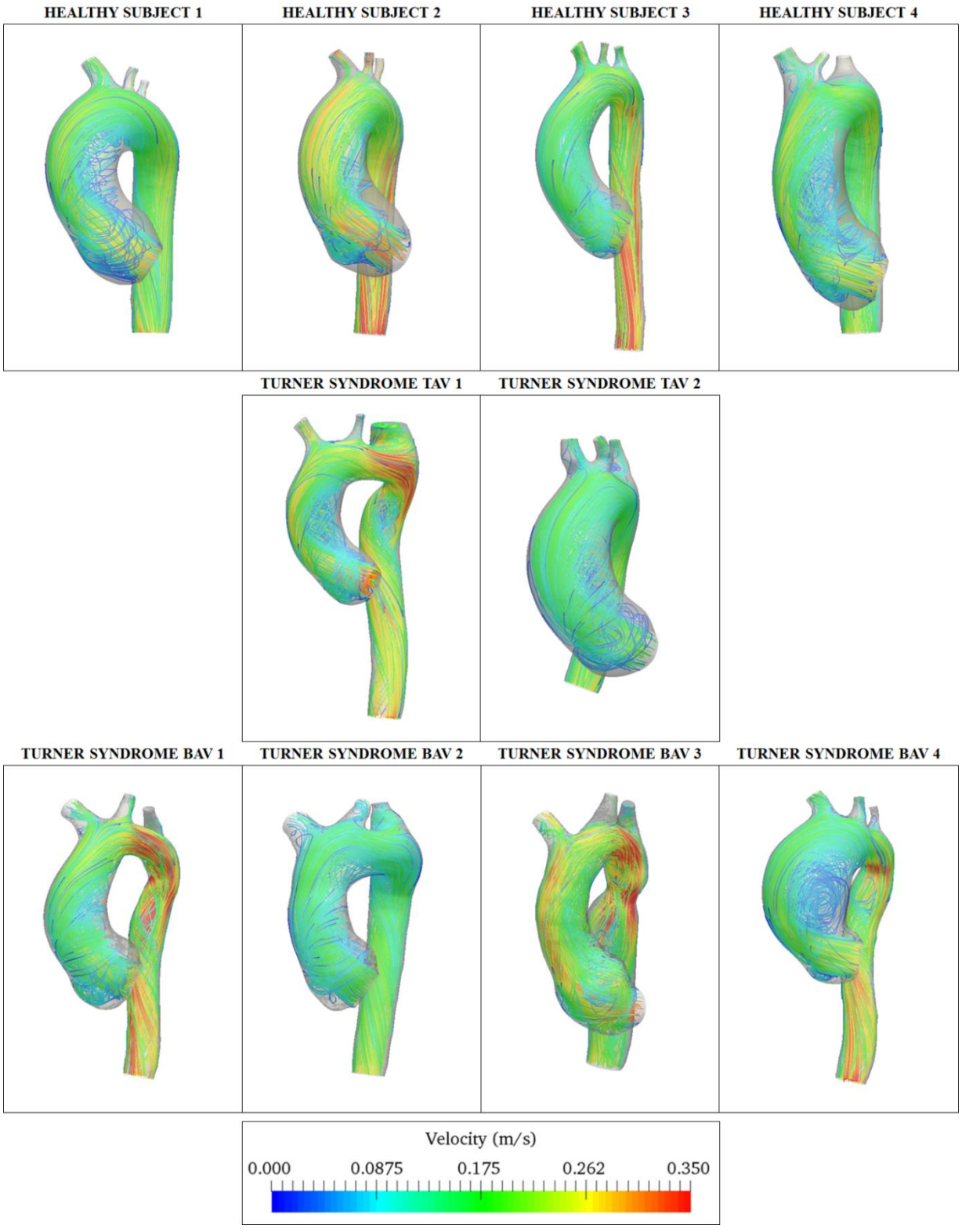

Figure 8.2: Streamlines (colored by velocity magnitude) comparing flow patterns for the control subjects (top row), TAV TS patients (middle row) and BAV TS patients (bottom row).

healthy control 4. The distribution of WSS for TAV-2 and BAV-2 (Figure 8.3b) resembled that for healthy control 1 over the entire aortic length. For subject BAV-4, the distribution of WSS in the ascending aorta resembled that of TAV-2 and was similar to healthy control 3 in the descending segment. The highest WSS was located in the transverse segment for 3 subjects (TAV-2, BAV-1, BAV-2), at the site of CoA for 2 patients (TAV-1, BAV-3) and at the end of the aortic arch for the patient with a dilated ascending aorta (BAV-4). The peak magnitude of WSS for TS (5.2±2.4 Pa) was 22 percent higher than the corresponding value for the controls (4.3±1.4 Pa).

Exclusion of the aortic sinus impacted not only mapping of the maximum radii but also the computational models. This is exemplified by: 1) a different anatomical location and significant reduction in WSS for healthy control 4, and: 2) a moderate reduction in maximum WSS for TS BAV-3 (Appendix: Figure G.4). The anatomical location of WSS concentration was unchanged. Table G.3 (Appendix) summarizes the locations of the maximum WSS for the controls and TS. Additionally, the average WSS for the sinus, ascending, transverse and descending aortic segments in the normotensive (i.e. controls and TS-TAV) and hypertensive (i.e. TS-BAV) subjects was computed. The variation of the group-averaged mean WSS is illustrated in Figure 8.7. The section-averaged WSS increased sharply from the sinus to the transverse aorta for the normotensive patients. Similarly, the section-averaged WSS increased gradually for the hypertensive subjects. The magnitude of average shear stresses corresponding to the sinus, ascending and descending aorta were greater for patients with BAV as compared to subjects with TAV. The three-dimensional vessel wall pressure for the normotensive and hypertensive subjects decreased from the sinus to the descending aorta (Figure 8.4). For patients with CoA (TAV-1, BAV-1, BAV-3), the pressure decreased to a minimum value at the CoA

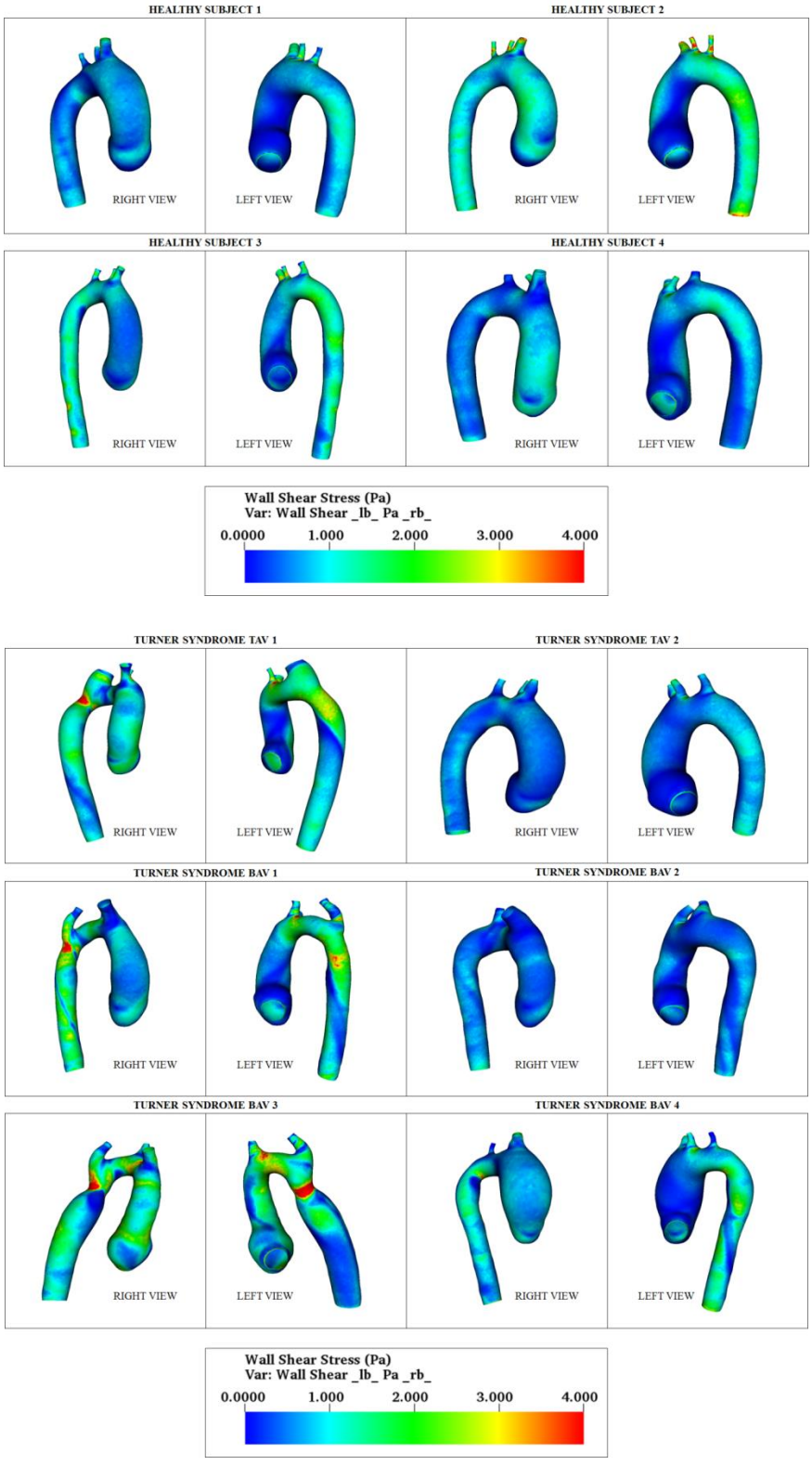

Figure 8.3: Comparison of WSS contour plots corresponding to the 4 healthy controls and for the 6 TS patients analyzed in this study.

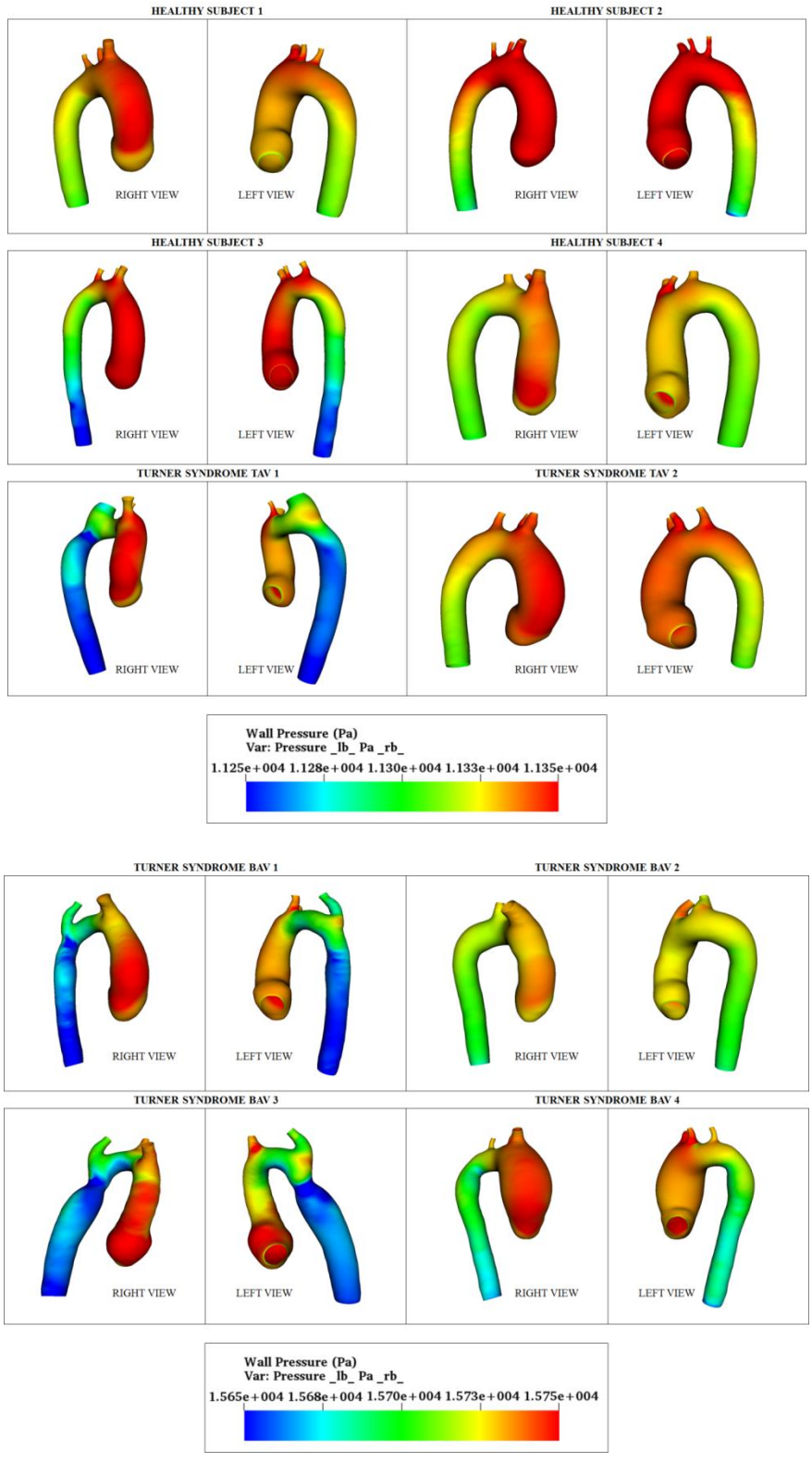

Figure 8.4: Surface maps indicating circumferential and axial variation in aorta wall pressure for the normotensive (healthy control 1, 2, 3, 4, TS-TAV 1, 2) and the hypertensive subjects (TS-BAV 1, 2, 3, 4).

and recovered downstream of the constriction. The wall pressure reached maximum at the sinotubular junction for 6 subjects (TAV-1, BAV-2, BAV-3, BAV-4, healthy controls 3, 4), in the ascending aorta proximal to the sinotubular junction (TAV-2, healthy controls 1, 2) and in the sinus for the patient with aortic root dilatation (BAV-3). Table G.3 summarizes the location of the maximum wall pressure.

8.2.3 *Comparison of Mechanical Variables*

The maximum vessel wall displacement in TS with BAV (3.1±0.3 mm) was comparable to subjects with TAV (2.9±0.2 mm) (Figure 8.5). The greatest vessel wall displacements were observed at sinus level for 5 subjects (TAV-2, BAV-1, BAV-3, healthy control 3, healthy control 4), at the sinotubular junction for the TS patient with aortic regurgitation, ETA and CoA (TAV-1), in the ascending aorta for 2 TS patients with hypertension (BAV-2, BAV-4) and in the transverse aorta for 2 healthy subjects (healthy control 1 and 2) (Figure 8.5). The distribution of vessel wall displacements for TAV-1 resembled that of healthy control 3, throughout the aorta. Significant displacements of the descending aorta were observed for 2 normotensive subjects (TAV-1, healthy control 3) and 1 hypertensive patient (BAV-2). Large displacements in the ascending aorta were observed for 3 subjects with TAV (healthy control 1, healthy control 4, TAV-2) and for a single patient with BAV (BAV-4). Furthermore, the largest displacement was located between the left-posterior sinus and anterior sinus in four aortas (healthy control 3, healthy control 4, TAV-2, BAV-3) from the group of subjects that exhibited the maximum displacement in the sinus or sinotubular junction.

The peak von-Mises stress for the hypertensive aortas (284000±35500 Pa) was 61 percent higher than for the normotensive subjects (176000±16250 Pa) (Figure 8.6). For the normotensive subjects, the distribution of mechanical stress over the entire aortic length was similar for healthy

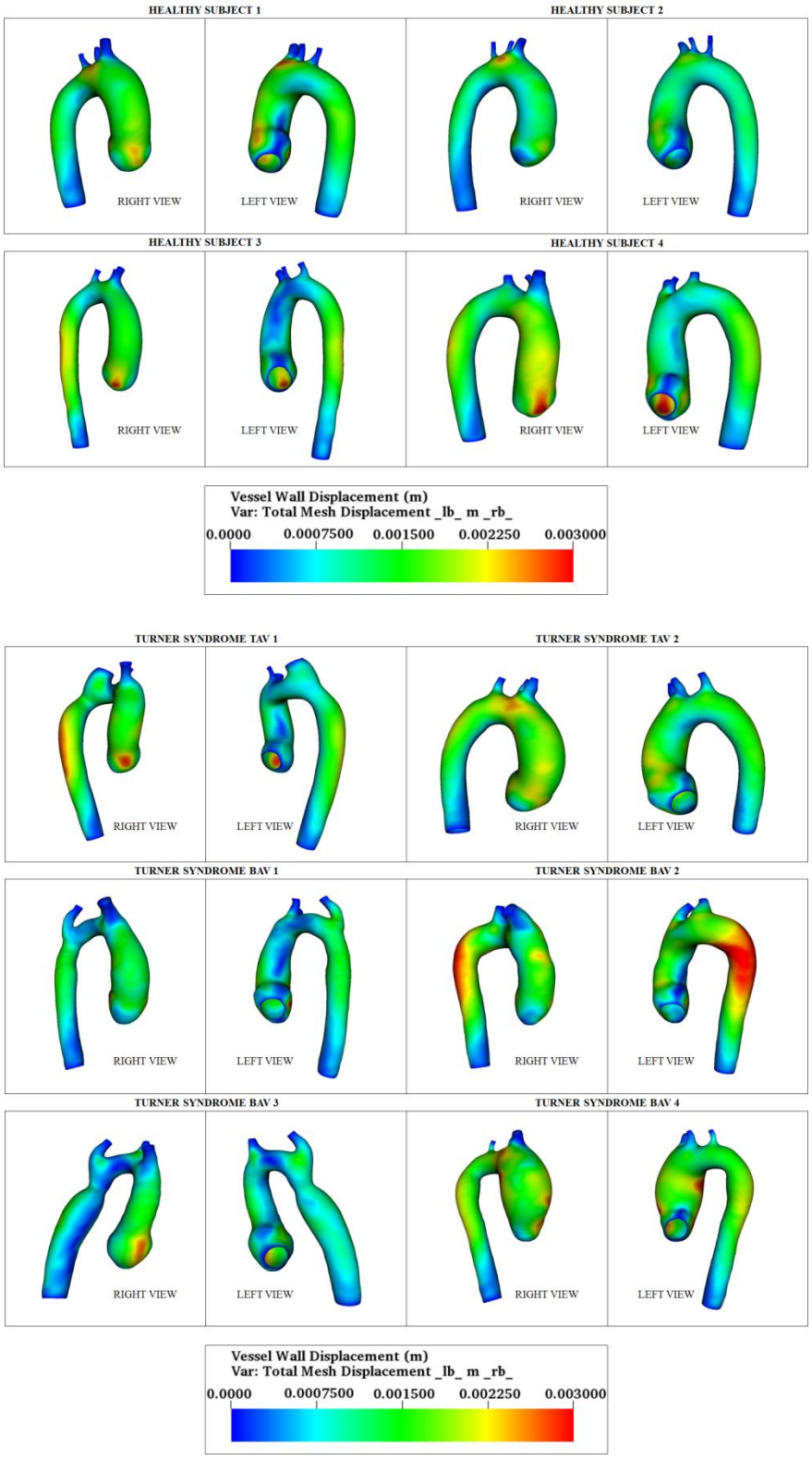

Figure 8.5: Comparison of vessel wall displacement contours corresponding to the 4 healthy controls and the 6 TS patients analyzed in this study.

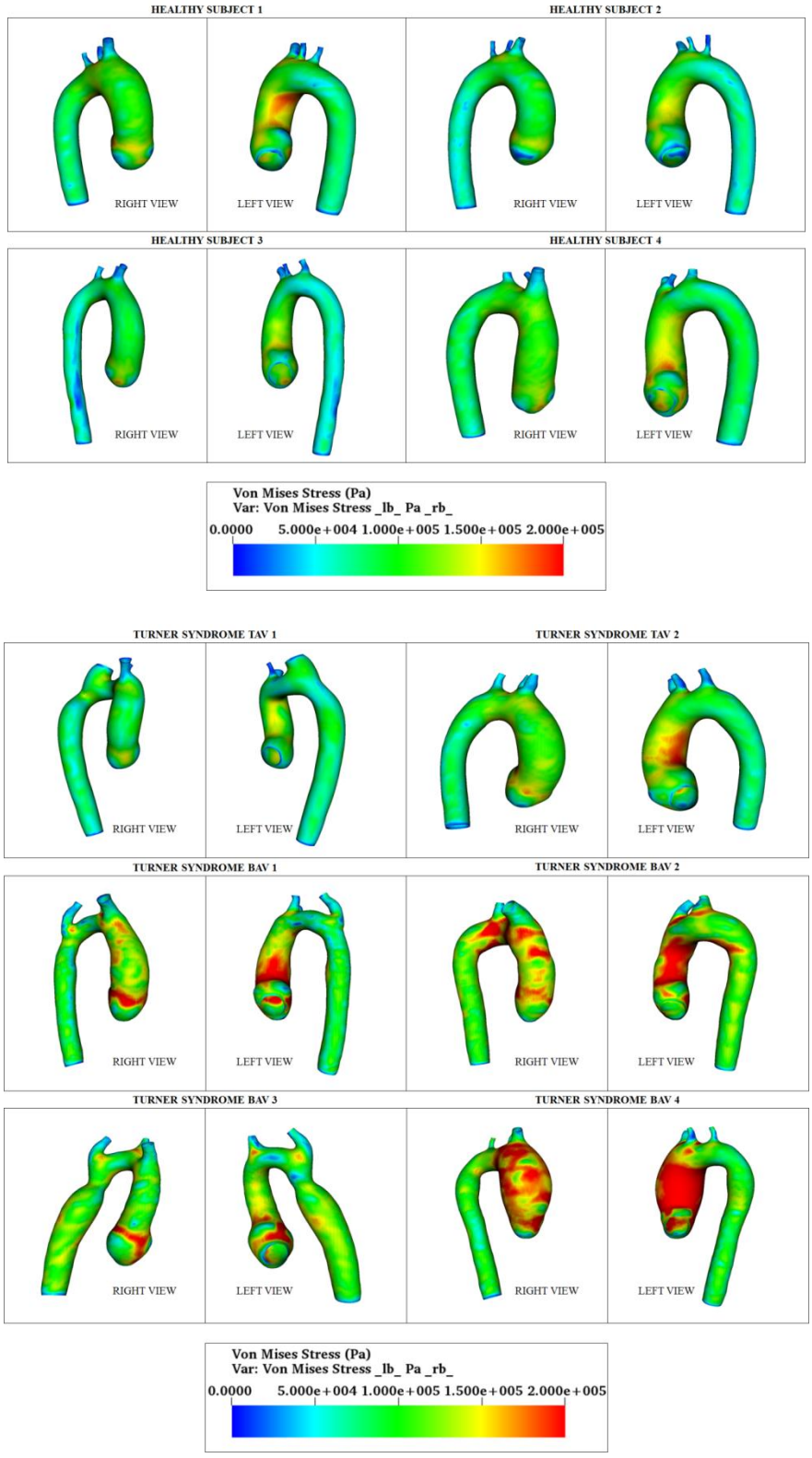

Figure 8.6: Comparison of von Mises stress contour plots corresponding to the 4 healthy controls and the 6 TS subjects analyzed in the study.

subject 2, healthy subject 3 and TAV-1. The maximum value of von-Mises stress was comparable for the aforementioned cases (< 10 percent difference) and was observed in the sinus (control) or the ascending aorta (TS). Furthermore, the stress in the descending aorta was significantly lower (~50000 Pa) as compared to the other cases (~100000 Pa). The distribution of von-Mises stresses over the entire thoracic aorta was similar for healthy subject 1, healthy subject 4 and TAV-2. The maximum values of mechanical stress were also comparable for these subjects (< 10 percent difference) and were greater than in healthy control 2, healthy control 3 and TAV-1 (24 percent). Besides, the maximum values were observed in the ascending aorta for healthy control 1 and TAV-2 as compared to healthy control 4. For healthy control 4, exclusion of the root generated negligible changes in the maximum stress. The anatomical location of stress concentration was also unchanged (Appendix: Figure G.5).

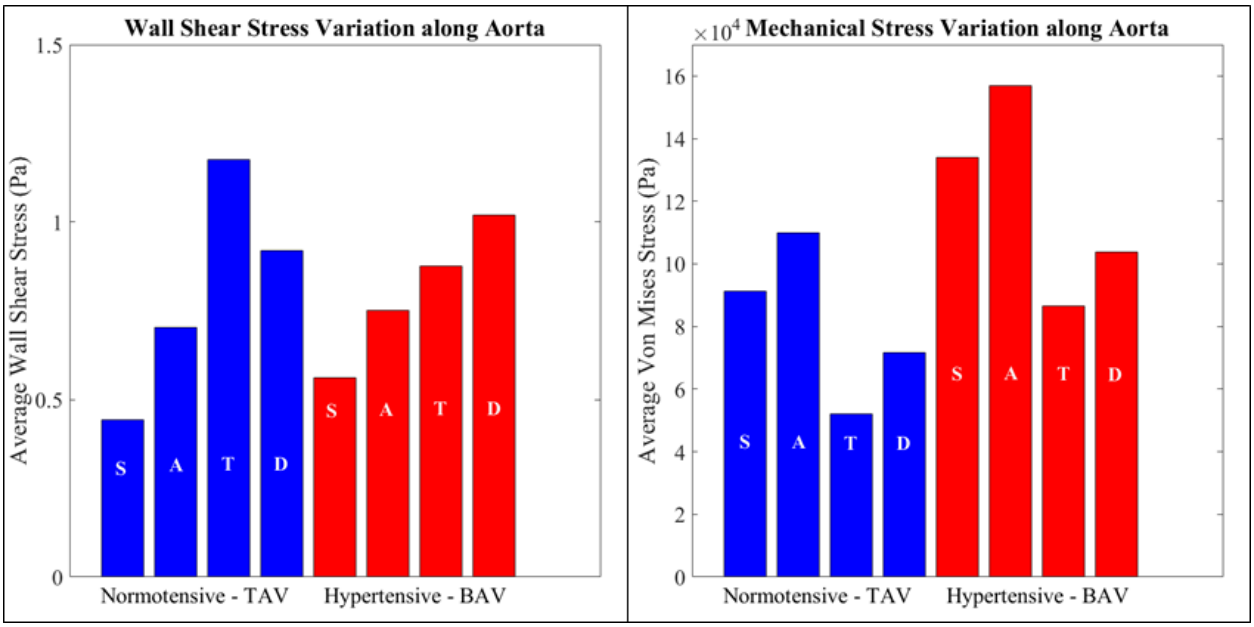

Figure 8.7: Bar-graphs describing the group-averaged variation in WSS and VM stress along the aorta length (Note: Blue bars – Normotensive subjects (healthy controls 1, 2, 3, 4, TS TAV-1, 2), Red bars – Hypertensive subjects (TS BAV-1, 2, 3, 4), S – Sinus, A – Ascending aorta, T – Transverse aorta, D – Descending aorta).

For the hypertensive subjects, the distribution of von-Mises stress at the STJ was similar for BAV-1 and BAV-3. Exclusion of the sinus for BAV-3 resulted in a different anatomical location of stress concentration and a significant reduction in the peak value of von-Mises stress (Appendix: Figure G.5). The maximum value of mechanical stress was observed in the sinus for these aforementioned subjects and the value for BAV-1 was greater than BAV-3 by 17 percent. High mechanical stresses observed on the inner and outer walls of the ascending aorta for BAV-4 were also observed in BAV-2. The maximum value of mechanical stress for the latter was lower by 17 percent. Moreover, the highest stress concentration for BAV-2 was observed in the transverse aorta and the same occurred in the ascending aorta for BAV-4. Regarding the impact of ETA, high mechanical stresses were distributed throughout the transverse segment (BAV-2). Table G.3 summarizes the locations of peak von-Mises stress for all the subjects. Additionally, the average von-Mises stress was computed for the sinus, ascending, transverse and descending aorta segments corresponding to aortic valve morphology. The group-averaged mean von-Mises stress is illustrated in Figure 8.7. For the normotensive subjects, the section-averaged von-Mises stress gradually increased (22 percent) from the sinus to the ascending aorta, following which the values decreased sharply in the transverse aorta (54 percent). Although higher group averaged mechanical stresses (sinus: 44% higher, ascending: 45% higher, transverse: 60% higher, descending: 42% higher) were obtained for the hypertensive group compared with normotensives, this trend was unchanged. Maximum Euclidean distance correlated highly (R-value:0.95, P-value<0.0005) with the peak value of von-Mises stress (Fig. 8.8). Concordance between the von-Mises stress at the spatial location corresponding to the maximum Euclidean distance (local) was also determined since the highest stress concentration does not always occur at the site of the largest aorta caliber (Table G.3). Similarly, the correlation between the

maximum Euclidean distance and the maximum value of von-Mises stress at the corresponding cross-section (local maximum) was evaluated. Good correlation was obtained for the local (R=0.86, P=0.001) and local maximum (R=0.74, P=0.01) values of mechanical stress (Figure 8.8).

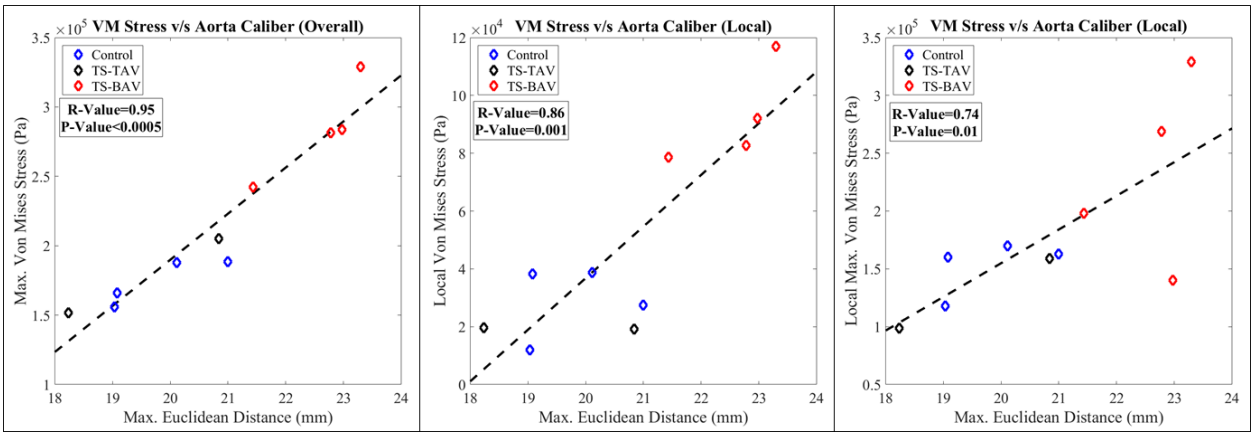

Figure 8.8: Linear regression analysis describing correlation between maximum VM stress, local or local maximum VM stress and maximum Euclidean distance (Note: Blue diamond marker – Controls, Black diamond marker – TS TAV, Red diamond marker – TS BAV).

8.3 *Discussion*

FSI computational modeling enabled to elucidate differences in hemodynamic and biomechanical variables for different TS phenotypes and healthy controls. Flow-induced (i.e. WSS) and mechanical forces (i.e. von-Mises stress) were 20 percent higher for TS, although the difference in maximum aortic radius was 10 percent. Computational FSI modeling provides a 3D representation of these aforementioned functional measures while simultaneously accounting for aortic lumen caliber, wall thickness, flow, cardiac pressure and material response of the vessel wall, unlike the 3D distance maps that only consider aortic lumen caliber. Furthermore no risk markers were identifiable for 11 percent of previously documented cases of aortic dissection in TS [29]. It is hypothesized that functional measures evaluated using the presented approach may serve as new indices to improve current risk stratification, pending validation against outcomes.

The maximum aortic size was observed in the aortic sinus for the majority of subjects, thereby emphasizing the importance of including the aortic root for dimensional measures of cardiovascular risk assessment in TS, which corroborates previous data [32]. Flow patterns at the 7 different stations outlined in Section 8.2.2 were in good agreement with those obtained previously for complete [190, 208] and truncated aortic models [58, 199], for the same cardiac output employed in this study (Appendix: Figure G.1). Secondary flow in the ascending aorta and skewing of the flow towards the outer wall was observed for the full aortic models of healthy and diseased subjects. A similar observation was obtained from computational models of pulsatile aortic blood flow in patients with CoA repair, validated using phase-contrast magnetic resonance images (PCMRI) [208]. The angular orientation of the aortic root relative to the left ventricle outflow could, hypothetically, influence these flow patterns in the ascending aorta, as observed previously from experiments of steady flow in thoracic aortic phantoms [209]. The location and orientation of the spiral flow in the ascending aorta and flow recirculation in the sinus corresponded well with previous computational [187, 190] and imaging studies of blood flow in the thoracic aorta [210]. Line plots describing variation in area averaged helicity density (Appendix: Figure G.3) for the truncated healthy aorta were in good agreement with the same obtained in an earlier study for steady [181] and transient [211] CFD simulations of aortic blood flow.

Good concordance was obtained between the regions of high and low shear identified in this study, with those reported previously for truncated [58, 200] and complete geometries [212, 213] of the thoracic aorta (Appendix: Figure G.4). PCMRI has been employed previously to map WSS distribution in the thoracic aorta for control subjects and patients with TS [210]. These studies indicated higher wall shear stress on the outer wall of the ascending aorta as compared to

the inner wall. Similar patterns of ascending aortic WSS distribution and relative variations in the average shear stress magnitude between normotensive (TAV) and hypertensive (BAV) were observed in this study for the full models (Figure 8.7). The difference of ~ 1mmHg (134 Pa) in the aorta wall pressure corresponding to the ascending and descending aorta has also been reported previously in FSI simulations of aortic blood flow in ascending aortic aneurysms [190]. Although the probability of plaque deposition is greater in the regions of low WSS (i.e. stagnation flow regions) [199], high shear stress concentration observed at the CoA in TAV-1, BAV-1, BAV-3 are less favorable and can potentially contribute to thinning and weakening of the aortic wall. Besides, distribution of shear stress and aortic wall pressure in the regions corresponding to the largest vessel caliber (i.e. in the aortic root or ascending segment) could be associated with changes in extracellular matrix protein expression and smooth muscle cell apoptosis [190, 214], potentially resulting in progressive dilatation.

The magnitude of arterial wall displacement obtained in this study was in good agreement with values reported elsewhere for diseased [65] and healthy aortas [201]. Significant displacements of the aortic root between the left-posterior sinus and anterior sinus for the healthy and diseased cases (right views in Figure 8.5) were also reported for stented aortic valves [202]. Large displacements of the healthy and diseased aortae could be attributed to lower aortic stiffness and hypertension, respectively. The magnitude of von-Mises stress for the healthy and diseased cases reported in this study was within the range of values computed previously for AAAs [198]. The importance of including the root in risk assessment in TS was highlighted by the observation of maximum stresses in the aortic sinus or STJ in half of the cases in this study (Table G.3). This finding was consistent with previous documented cases of aortic dissection that were reported to have occurred in proximal sites of the aorta [215]. Patterns of mechanical stress

distribution in the sinus and ascending aorta resembled the same observed in Marfan syndrome [65] and ascending aortic aneurysms [190] respectively. The high correlation coefficient obtained between the maximum von-Mises stress and maximum Euclidean distance (Fig. 8.8) has also been reported in previous studies involving AAAs [198] and ascending aortic aneurysms [216]. The regression analysis for the local and locally maximum von-Mises stress suggests that while measurements of aortic caliber in TS could provide an initial estimate of the risk of dissection, computational modeling would be necessary to determine regions that are most vulnerable to vessel wall rupture and thus dissection.

A computational methodology was described to simulate blood flow in the compliant aorta for mean flow conditions. Patterns describing the distribution of hemodynamic and biomechanical variables obtained using the proposed approach were in good agreement with those obtained using a similar, previously developed FSI model for ascending aortic aneurysms [190]. Transient simulations of flow over the complete cardiac cycle would significantly enhance the study, since they are more representative of physiological conditions in-vivo. Time-averaged WSS obtained from transient simulations can be considerably larger than the values obtained for the steady or quasi-steady case [217]. Besides, oscillatory shear index (i.e. temporal WSS oscillations) [212] obtained from unsteady simulations has been reported to significantly impact endothelial cell function. The accuracy achieved using unsteady computational modeling is often offset by higher computational costs and necessity for high performance computing resources [84]. The presented quasi-steady approach can be easily modified to simulate aortic flow at peak systole [186] and has relatively lower computational costs than transient simulations. Besides, quasi-steady FSI modeling of peak systolic aortic blood flow has been previously demonstrated to provide a promising option for risk stratification in ascending aortic aneurysms [216]. The

computational scheme presented here modeled the turbulence using the Reynolds-Averaged Navier-Stokes equations. Although advances in CFD modeling have enabled superior resolution of the flow field using Large Eddy Simulations (LES) [218], LES with FSI modeling would significantly increase computational costs, making it less suited for clinical applications. The present study assumed that blood behaves as a Newtonian fluid. A suitable Non-Newtonian rheological model [59] would have to be chosen to obtain more accurate estimates of flow patterns and WSS.

PCMRI for controls and TS patients [210, 219] can aid in validating flow patterns obtained using CFD or FSI [67]. Besides, PCMRI would provide a more accurate estimate of the inlet flow boundary conditions [220] and distribution of flow in the descending aorta and the aortic branch arteries. Simulated flow and shear stress distribution can significantly vary for different combinations of pressure and flow boundary conditions at the inlet and outlets of the computational domain [221, 222]. Although sensitivity of the simulated flow patterns with respect to these combinations was not performed in this study, this analysis would be necessary for better validation of the computational approach. The present study excluded the aortic valve [202] due to challenges in identifying the leaflet morphology from MR images. Besides, high WSS on the outer wall of the ascending aorta obtained in this study has been attributed previously to impingement of the fluid jet which stems from the morphology of valve leaflets and the resulting orifice [212]. It would be necessary to perform FSI simulations of aortic valve opening [79, 223-226] to thoroughly explain factors that result in skewing of ascending aortic flow towards the outer wall.

The present study approximated the aorta as a single-layered structure with a constant wall thickness. Variable wall thickness [221] and multi-layered models of the aorta wall [190]

are physiologically more representative of the vessel wall structure and provide an enhanced description of the biomechanics of aortic dissection [227, 228]. Simulated deformation of the vessel wall and resulting alterations in the flow variables are also sensitive to the choice of fixed or free structural boundary conditions [229]. Additionally, aortic root motion can result in larger displacements and stresses in the aorta wall, as observed in Marfan syndrome [66]. These observations emphasize the need to accurately track the motion of the vessel wall using dynamic images [61] to identify patient-specific structural boundary-conditions. Furthermore, a variety of isotropic material models including linear elastic [65], Raghavan-Vorp [190], Demiray [61] and anisotropic models such as Holzapfel-Gasser-Ogden [205] and Fung [55], have been proposed to approximate the mechanical response of the vessel wall in aortic disease similar to TS. Mechanical testing of resected aortic samples in TS has not been performed. The isotropic Arruda-Boyce material, employed to model the biomechanics of the arterial wall was an initial approximation and would have to be eventually substituted with a suitable material model derived using uniaxial or biaxial testing of tissue specimens. Moreover, intramural stresses predicted by isotropic material models can be significantly higher than the same obtained using anisotropic models, as observed in a recent study involving ascending aortic aneurysms [205]. Furthermore, material properties for ascending [55] and abdominal aortic aneurysms [230] have been previously estimated in-vivo using inverse computational methods. These iterative methods require dynamic computed tomography or CMR images [206] with high spatial resolution and corresponding temporally varying estimates of aortic pressure. Additionally, since the aorta is surrounded by hard and soft structures, the structural model would have to be suitably modified to include the effects of supporting tissue [201, 206].

In view of previous studies and current findings, the presented study indicates that the chosen computational FSI methodology to characterize flow and mechanical variables for the thoracic aorta is valid, and interestingly was able to indicate differences between TS and controls that may aid in the understanding for aortic disease in general and TS. It is proposed to eventually apply the FSI method presented in this pilot study, to additional aortic phenotypes and age-matched controls to describe changes of aortic morphology disease in TS over time. Overcoming simplifications in the flow and structural model and development of an improved computational method also forms the basis of future research.

Chapter 9

FSI Modeling using Patient-Specific Flow Conditions

Results from this chapter were presented at the 2016 BMES Annual Meeting, Minneapolis, MN

Information about flow velocity can be encoded into the phase of a detected signal using MR imaging [231]. Volume of flow at a vessel cross-section can be measured using phase-contrast methods, sensitized to the flow-velocity normal to the cross-section [231, 232]. As described in earlier chapters, the aortic lumen is comprised of pixels as observed in the MR images. Flow Q_j through the j^{th} pixel is computed as follows [231]:

$$Q_j = a_j \times v_{\perp j} \tag{9.1}$$

where $v_{\perp j}$ is the weighted-average, normal component of blood velocity through the j^{th} pixel with an area a_j. Flow through the vessel cross-section is obtained by summing the flow for all the N pixels that enclose the vessel lumen. For identical pixel areas (a), the total flow Q_{tot} is given as follows [231]:

$$Q_{tot} = Na\left[\frac{1}{N}\sum_{j=1}^{N} v_{\perp j}\right] = Av_{\perp} \tag{9.2}$$

Equation 9.2 indicates that the net flow is the product of lumen area (A) and the average normal component of blood flow velocity $v_{\perp}$. For a single slice acquired at a single phase in the cardiac cycle, the image where the intensity of the pixel is proportional to $v_{\perp j}$, a flow-encoding gradient is applied along the slice-selection direction of the imaging pulse sequence [231]. Additional details regarding the velocity mapping has been described elsewhere [231]. Measurements of the velocity vector for each pixel are also achievable using phase-contrast and require at least 4 velocity-encoded measurements [231]. 3D, 3-directional velocity encoding, temporally resolved

blood velocity acquisition is referred to as 4D-velocity acquisition [233]. 4D-velocity CMR imaging involves large datasets, requires considerable time for acquisition and depends on effective co-ordination relative to respiratory and cardiac motion [233]. It should be noted that 4D-velocity CMR imaging is referred to as PCMRI in this dissertation. PCMRI has been employed to visualize aortic blood flow patterns in subjects with BAV, TAV, quadricuspid aortic valve (QAV) and unicuspid aortic valve (UAV) [234, 235] (Figure 9.1). This technique has been recently adopted to image aortic flow and map the circumferential distribution of wall shear stress in subjects with TS [210] and Marfan syndrome [236].

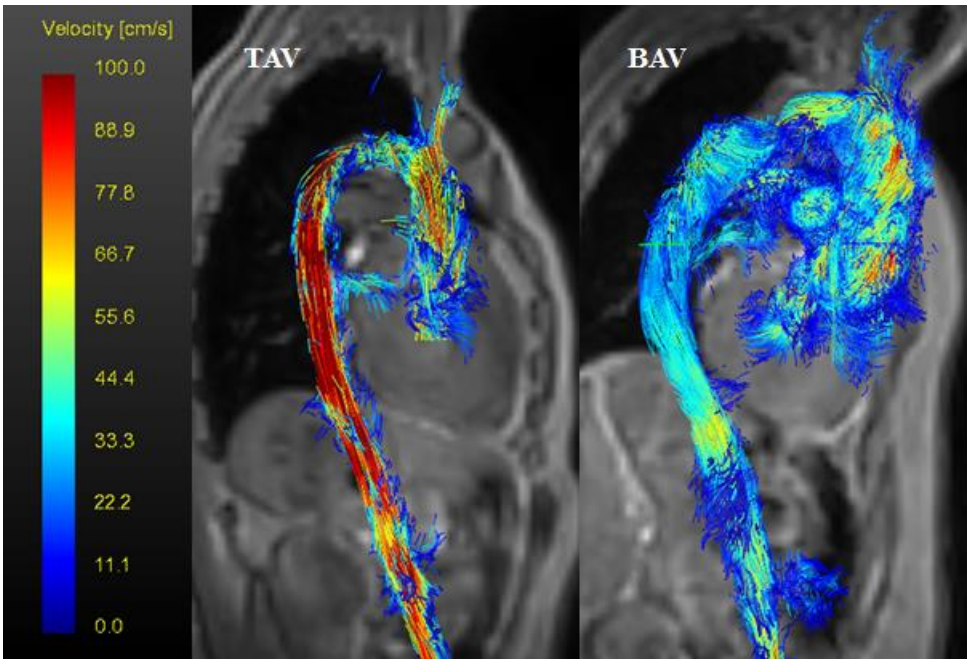

Figure 9.1: 3D visualization of peak systolic aortic blood flow in subjects with tricuspid and bicuspid aortic valve.

As discussed in Chapter 8, flow boundary conditions derived using PCMRI would provide an improved characterization of aortic disease based on hemodynamic functional variables [186]. In this chapter, the FSI methodology described in Chapters 7 and 8 is extended for peak-systolic flow simulations for a TS subject using flow conditions derived using phase-contrast (Section 9.1). An FSI methodology with enhanced outflow boundary conditions is then

described for two non-TS patients with aortic root dilatation (Section 9.2). This improved methodology combined with ascending and descending aortic flow volumes obtained using 4D-flow CMR imaging is then applied for functional characterization of aortic disease in 3 TS patients and one healthy control (Section 9.3).

9.1 *FSI Modeling using Flow and Pressure Outlets*

This section describes FSI modeling of aortic blood flow for one TS patient with a tricuspid aortic valve, ETA and CoA, using the methodology outlined in Chapter 7 and 8.

9.1.1 *Methods*

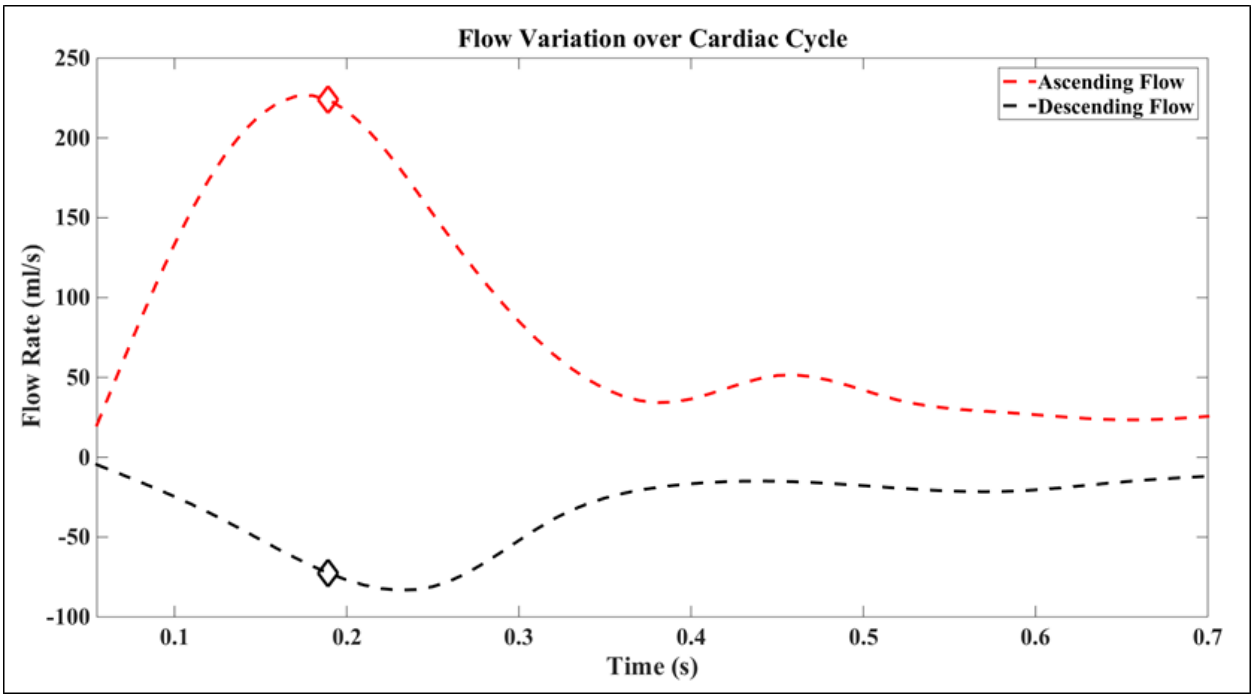

Figure 9.2: Flow variation over the cardiac cycle (Note: Red and black diamond markers indicate peak systolic flow for ascending and descending aortas).

PCMRI was acquired using a whole-body 1.5T Philips Achieva scanner (Philips Medical Systems, Best, The Netherlands). Imaging parameters included: a. Matrix Size – 144x144, b. Slice Thickness – 3, c. Pixel Size – 2.64 x 2.64 mm^2, d. Flip angle – 10°, Number of cardiac phases – 11. 4D flow data was analyzed using the GTFlow 2.2.15 software (GyroTools LLC,

Zurich, Switzerland) to compute temporal variation in ascending and descending aortic flow. It should be noted that the ascending aortic flow was determined at a cross-section just above the sinotubular junction [186]. Smoothing splines were fitted to the data using MATLAB (Mathworks Inc., Natick, MA) to approximate the flow waveforms (Fig. 9.2). Flow rates corresponding to the peak-systolic phase were then determined from the flow waveforms (red and black diamond markers in Fig. 9.2). Static diastolic scans (Chapter 6) were then employed to reconstruct the geometry of the aorta including the sinus (Chapter 8). Peak systolic ascending aortic flow corresponding to 13.5 lpm was applied as an inlet boundary condition, assuming a flat velocity profile (Chapter 8). The descending aortic flow at peak systole corresponded to 32 percent of the cardiac output (as compared to the assumption of 85 percent (Chapters 7,8))and the same was applied as an outflow boundary condition at the descending aortic outlet (Fig. 9.3). Static pressure corresponding to a peak systolic pressure of 120 mmHg was applied at the branch outlets.

The flow domain was discretized using 3 million tetrahedral cells. The centerlines based mesh generator outlined in Chapter 8 was also employed in this study. Additional details regarding the thermo-physical properties of blood and the turbulence model have been described previously (Chapter 7, 8). The vessel wall was discretized using 170000 quadrilateral shell elements. The proximal and distal ends of the aorta wall were constrained in all directions to ensure that the displacements of the vessel were physiological [190]. A FSI boundary condition was prescribed at the interface between the fluid and solid domains (Fig. 9.3). 2D cine MR images corresponding to the descending aorta were segmented using the thresholding algorithm written in MATLAB to identify the boundary of the pharyngeal airway (Chapter 4). Descending aortic compliance was then determined using the pressure-area relation described in Equation

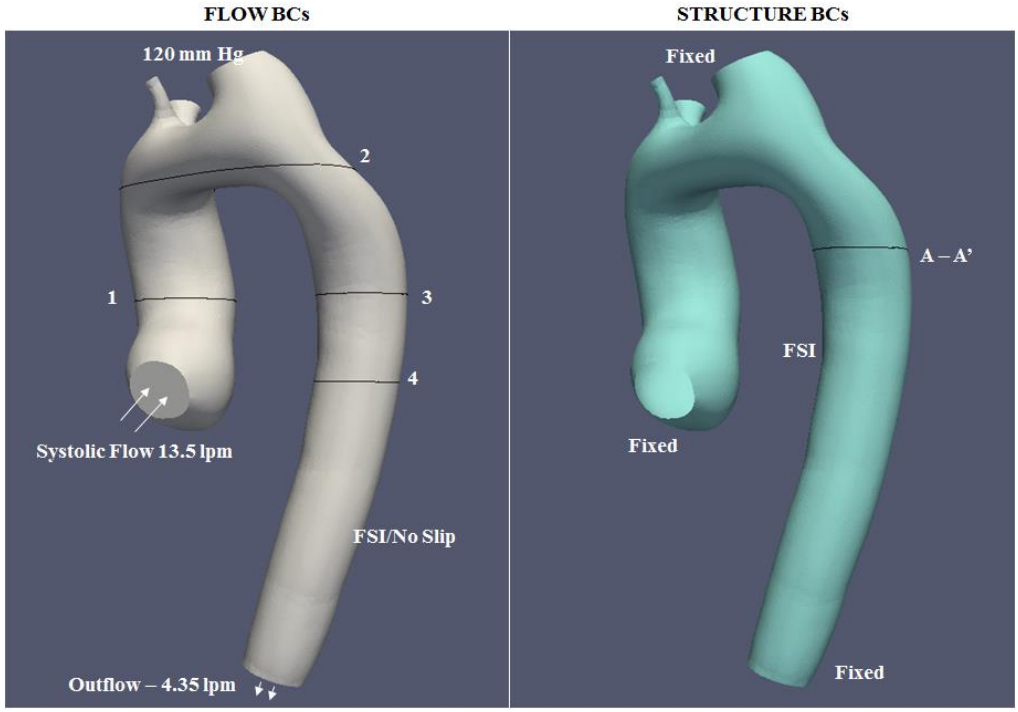

Figure 9.3: Summary of boundary conditions for flow and structural domains (Note: Velocities compared at stations 1,2,3,4, Compliance compared at station A-A').

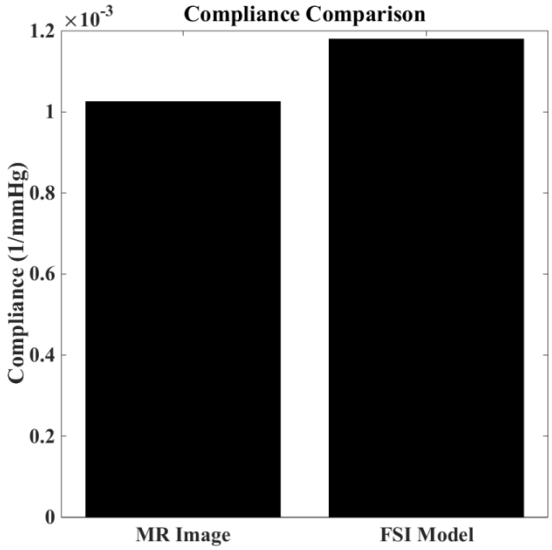

Figure 9.4: Comparison between compliance obtained from images and computational model.

4.1. Mechanical response of the aorta wall was approximated using the Arruda-Boyce material model (Chapter 7, 8) with 0.145 MPa as the initial guess value of the shear modulus. The shell thickness corresponded to 1.25 mm (Chapter 7). Constant velocity FSI simulations of peak

systolic aortic flow were performed using the ANSYS Multiphysics software (ANSYS Inc., Canonsburg, PA). The guess value of the shear modulus was iteratively changed until the compliance obtained from FSI simulations was within 10 percent of the observed values (Fig. 9.4). Accordingly, the shear modulus estimated using this iterative method was 0.225 MPa (55 percent higher than the initial guess value). Flow profiles were compared at 4 different cross-sections (Fig. 9.3): 1. Ascending aorta above sinotubular junction, 2. Transverse aorta upstream of CoA, 3, 4. Descending aorta downstream of CoA. Recognizing the low spatial resolution of the phase contrast MR images, the observed velocity profiles were interpolated on a finer grid using MATLAB, prior to comparison.

9.1.2 *Results and Discussion*

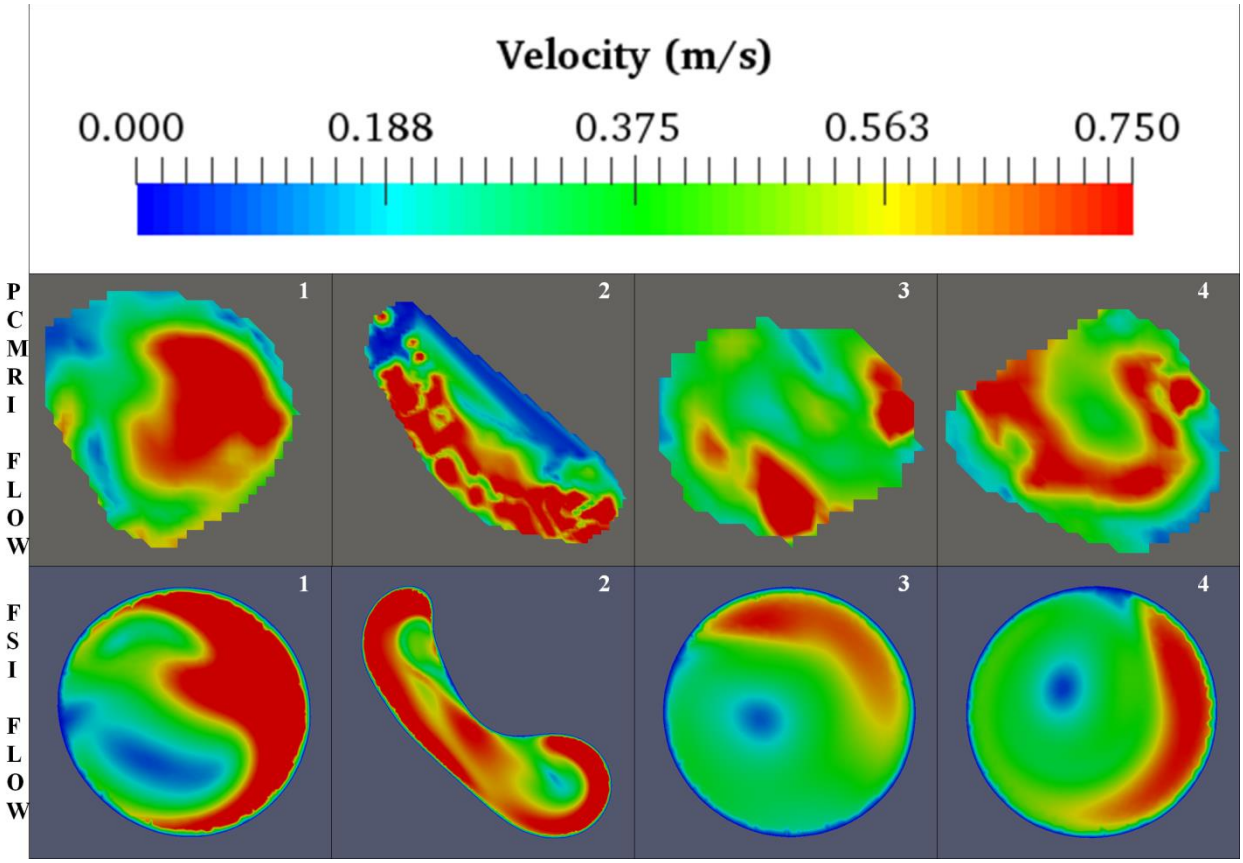

Figure 9.5: Station-to-station comparison between observed (PCMRI) and simulated (FSI) flow patterns (Note: Station 1 – Ascending aorta, Station 2 – Transverse aorta, Station 3, 4 – Descending aorta).

Figure 9.5 compares the observed (i.e. PCMRI) and simulated (i.e. FSI) flow patterns in the ascending aorta (station 1), transverse segment (station 2) and descending section (station 3, 4). At station 1 in the ascending aorta above the STJ, flow was observed to skew towards the outer wall of the ascending aorta. A similar observation was obtained from the FSI model. However, the circumferential extent of the outer wall skewing was greater for the simulated velocity profile. Differences were also observed in the spatial locations and extents of the low velocity regions. These differences could be potentially attributed to the exclusion of the aortic valve geometry as discussed previously in Chapter 8. In the transverse aorta (station 2), PCMRI predicted a high flow velocity in the proximity of the outer wall and the same was obtained in the FSI model. Furthermore, flow entering the transverse segment from the ascending aorta was observed to skew towards the outer wall. The circumferential extents of the skewed flow were greater for the FSI model as described previously for station 1. Larger differences between the model prediction and the observed velocity profiles were obtained on the descending aortic outflow upstream of the coarctation. Higher flow velocities were obtained from FSI simulations as compared to phase-contrast imaging. For stations 3 and 4 downstream of the coarctation, better agreement between simulated and imaged flow patterns were obtained for station 4. Skewing of the flow observed from the 4D images was also observed for the FSI model. However, the circumferential extent of the skewed flow was greater for the phase contrast images. Lower agreement in the transverse and descending sections could be attributed to the low spatio-temporal resolution of the images acquired in this study. Differences could also have arisen from the choice of outflow boundary conditions chosen in this preliminary analysis [237]. A recently concluded study has discussed the importance of employing outflow boundary conditions based on flow measurements from phase-contrast for the branch vessels and a

pressure outlet in the descending aorta [237]. It should be noted that the spatial resolution of the phase-contrast images was insufficient to evaluate systolic flow in the IA, LCCA and LSCA. Outflow and pressure outlets were thereby prescribed for the descending and branch vessel outlets respectively, as described previously in section 9.1.1. Furthermore, differences could have arisen due to the unsteadiness of the jet downstream of the coarctation and the same could be captured more effectively using LES simulations of aortic blood flow [59]. Additional differences could also be attributed to the differences in vessel compliance along the aorta and the choice of structural boundary conditions discussed in Chapter 8.

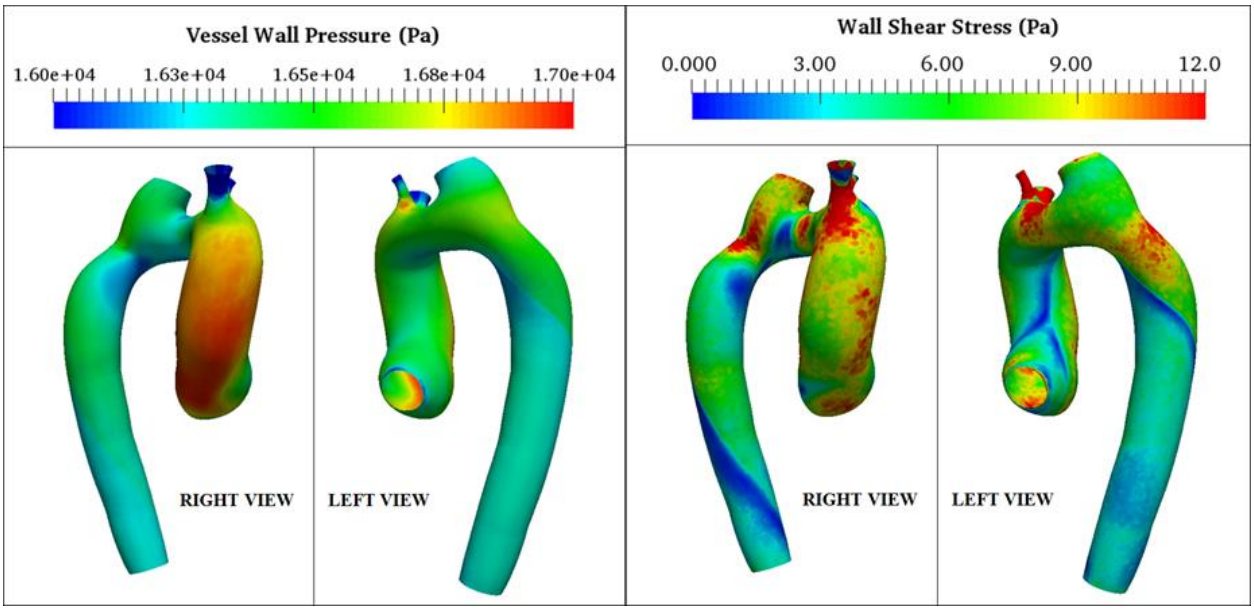

Figure 9.6: Surface maps indicating variation in vessel wall pressure and wall shear stress at peak systolic flow.

Aortic wall pressure was observed to decrease from the ascending aorta to the descending section. The highest wall pressure occurred at the sinotubular junction. A larger range of the aortic wall pressure (~7.5 mmHg) was obtained for FSI simulations with subject-specific division of the cardiac output between the branch vessels and descending aorta. Furthermore, the lowest wall pressure was observed in the innominate artery. The wall pressure decreased at the coarctation and recovered downstream of the constriction as observed previously for similar

aortic phenotypes analyzed for mean flow conditions (Chapter 8). High shear stresses were distributed in the sinus, outer wall of the ascending aorta, ETA and CoA. The greatest shear stress (~48 Pa) was observed at the constriction. As discussed previously in Chapter 8, high shear stresses could potentially weaken the vessel wall locally. High shear stress and vessel wall pressure above the STJ could increase the possibility of dilatation, subsequently enhancing the probability of Type-A dissection in this patient.

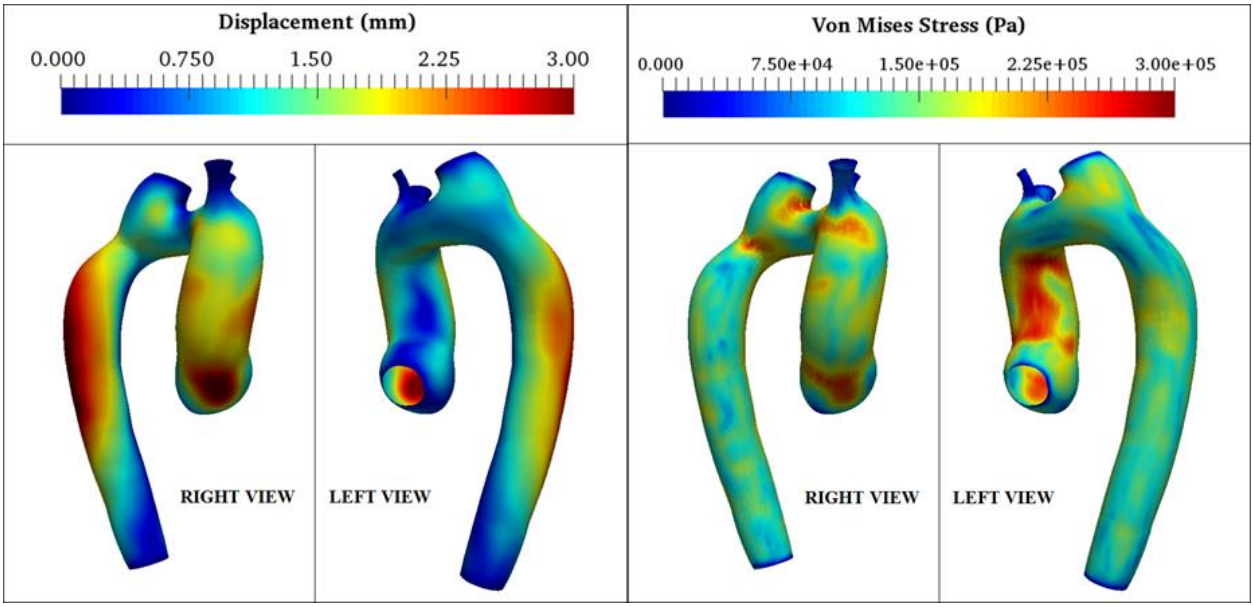

Figure 9.7: Surface maps indicating variation in vessel wall displacement and mechanical stress at peak systole.

Largest displacements of the vessel wall were observed at the STJ and midway in the descending section. It should be noted that the displacement distribution indicated in Fig. 9.7 corresponds to the optimized stiffness (i.e. 0.225 MPa). The methodology described to estimate the optimum stiffness of the descending aorta would potentially generate non-unique values of aortic stiffness based on some of the factors outlined below. Firstly, the thickness corresponding to 1.25 mm was assumed in this study. Besides, the thickness could potentially vary along the vessel length. Secondly, the choice of boundary conditions for the structural domain (i.e. constrained or radial degrees of freedom for the inlet and outlets) could influence the motion of the aortic wall.

Moreover, the choice of flow outlet boundary conditions would determine the distribution of flow-induced forces, subsequently influencing vessel wall displacements. Variations in the aortic pressure and diastolic geometry between cardiac cycles would also result in non-unique values of vessel compliance. Although computation of a 'zero pressure' geometry [55] would minimize errors associated with variability in the diastolic aortic geometry, temporal variation in the three-dimensional geometry of the aorta and corresponding aortic pressures would be necessary to evaluate the unstressed state [61]. Furthermore, the stiffness of supporting tissue would also have to be considered in computing the aortic stiffness in-vivo. The proposed iterative method does not provide information regarding the material response of the aortic wall. This implies that a Neo-Hookean constitutive model could generate the same compliance as that predicted by the chosen Arruda-Boyce model for a different set of material parameters.

Notwithstanding these limitations, the estimated shear modulus was within the range of values reported previously for ascending aortic aneurysms [190]. The lower distensibility (i.e. higher stiffness) reported for the subject chosen for this analysis was in good agreement with the same observed previously in patients with aortic coarctation [206]. High von-Mises stresses were observed on the inner and outer walls of the ascending aorta at the STJ. Concentration of stresses at these locations potentially increases the possibility of Type-A dissection. This observation further emphasizes the importance of including the root for subject-specific cardiovascular risk assessment in TS. Additionally, high stresses at the site of coarctation could also result in Type-B dissection. The magnitude of mechanical stress would potentially change as a result of the variability in the stiffness values estimated using the proposed method. The presented methodology would have to be suitably modified to account for differences in aortic distensibility of the ascending and transverse aorta.

9.2 *FSI Modeling using Enhanced Outlet Conditions*

In this section, a FSI methodology is presented using improved outflow boundary conditions. The proposed methodology is presented for two non-Turner syndrome subjects.

9.2.1 *Patient Clinical History, MR Imaging & Aortic Reconstruction*

Two subjects diagnosed with aortic root dilatation at the Aarhus University Hospital were selected for this analysis. The aortas for both patients dissected before surgical intervention. Cardiovascular MR images described in this section were acquired prior to vessel wall failure. Patient 1 (pre-dissection case 1) was a 41 year old male subject with Ehler-Danlos syndrome and patient 2 (pre-dissection case 2) was a 19 year old male subject at the time of MR image acquisition. Both subjects provided informed consent to participate in this study. Static diastolic CMR images for patient 1 were acquired using a Philips Achieva scanner (Philips Medical Systems, Best, The Netherlands). Imaging parameters included: Echo time – 2.202, Echo train length – 27, Flip angle – 90. A total of 160 sagittal images with a resolution of 528 x 528 pixels (1.51 pixels/mm) and slice thickness 1.5 were acquired for this patient. For patient 2, static diastolic images were acquired using a GE Signa HDxt scanner (GE Medical Systems, Waukesha, WI). Imaging parameters included: Echo time – 1.732, Echo train length – 1, Flip angle – 60. A total of 80 sagittal images with a resolution of 512 x 512 pixels (1.46 pixels/mm) and slice thickness 3.2 were acquired for the second subject. Sagittal images for both subjects were imported into Mimics (Materialise Inc., Plymouth, MI) for 3D reconstruction of the aortic geometries including the aortic sinus. Aorta geometries were smoothed and clipped at the inlet below the root and in the descending aorta outlet using Paraview (Kitware Inc., Clifton Park, NY). Centerlines were identified using VMTK to construct a 20 mm diameter cylindrical extension normal to the left ventricle as described in Chapter 8 for the Turner syndrome patients.

The extensions were merged with the respective aorta geometries, smoothed using Mimics and exported in the STL format for geometric and computational analysis.

9.2.2 *Geometric Parameter Estimation and Computational FSI Modeling*

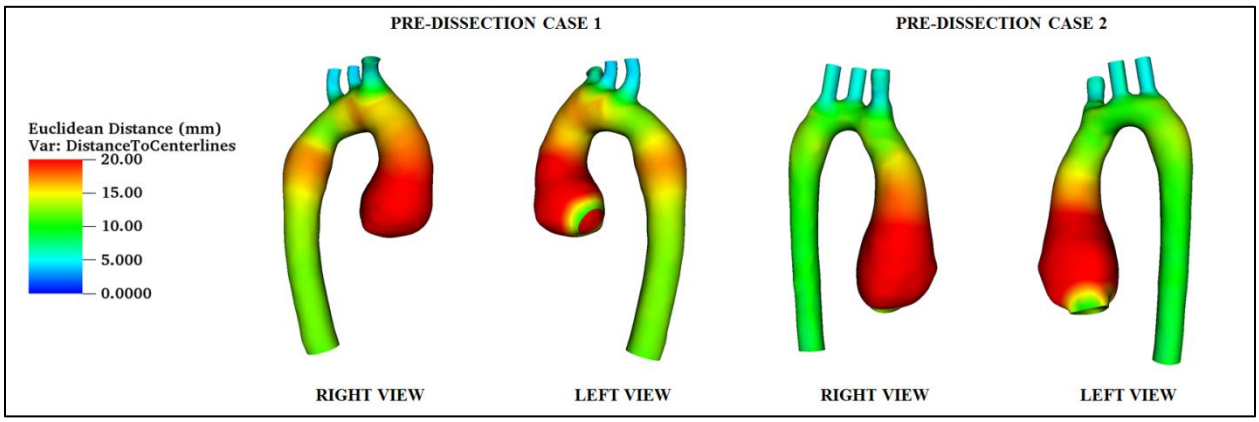

Figure 9.8: Contour plots describing variation in Euclidean distance for pre-dissection subjects 1 and 2.

Inlet and outlets of the computational domain were identified for the aorta geometries using Paraview. The supra-aortic vessels (i.e. IA, LSCA and LCCA) were extended four diameters normal to the vessel cross-section to ensure backflow stabilization [212]. Centerlines were generated for the resulting aorta geometries and Euclidean distance maps were generated using VMTK (Fig. 9.8) as described previously in Chapter 6, 7 and 8. As can be seen, the largest aorta caliber for both subjects (~44 mm) was observed in the root. For patient 1, the aorta radius increased at the end of the aortic arch by ~50 percent and again decreased downstream in the descending aorta. Transition in the aortic dimensions from the root to the ascending aorta was gradual for patient 1 (~33 percent change) as compared to patient 2 (~100 percent change). The average descending aortic radius for patient 2 was ~25 percent smaller compared to patient 1.

The aorta lumen was meshed using a centerlines based grid generation algorithm [204] available in VMTK. The flow domains for patients 1 and 2 were discretized using 2 million and 2.5 million tetrahedral cells respectively. Blood was assumed to be Newtonian with a density of

1060 kg/m^3 and a dynamic viscosity of 0.0035 Pa-s. Peak-systolic flow simulations were performed for a cardiac output corresponding to 16 liters per minute. 60 percent of the flow was assumed to exit the descending aorta [190]. Hydraulic diameters of the supra-aortic vessel outlets were then determined and outflow percentages were evaluated in a manner similar to Murray's law [164]. Accordingly, the outflow for the innominate arteries was 18 and 14 percent for patients 1 and 2 respectively. Similarly, the outflow percentages for the LCCA and LSCA were 11 percent and 13 percent each for patients 1 and 2 respectively. Pressure outlet boundary conditions with a target mass flow were defined at the outlets [238]. The static pressure corresponding to these outlets was a pulse pressure equivalent to 56 mmHg as measured previously for male subjects without hypertension [192]. It should be noted that specification of the target mass flow results in iterative adjustment of the pressure drop across each vascular segment to minimize the error between the predicted and simulated flow rates (Fig. 9.9).

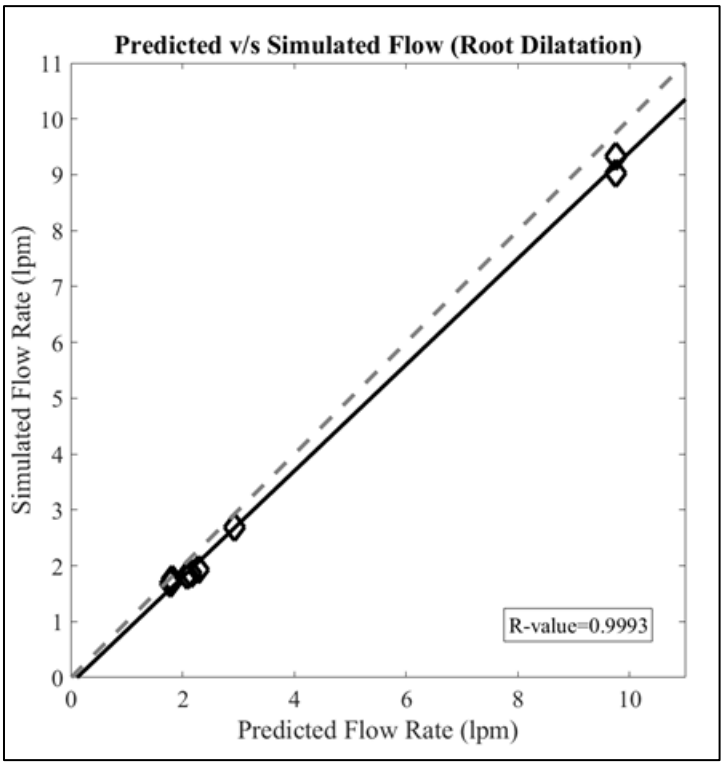

Figure 9.9: Correlation between predicted and simulated flow rates for the two subjects.

The k-ω SST model was chosen to model the turbulence as described in Chapter 7 and 8. A turbulence intensity corresponding to 2 percent was prescribed at the inlet and a length scale equivalent to 1 mm was assumed. The pressure, momentum and turbulence terms were discretized using a second-order upwind scheme. A pressure-based coupled formulation [89] was adopted for pressure-velocity coupling. A least-squares cell-based scheme was employed to evaluate gradients. The aorta wall for patients 1 and 2 were discretized using 130000 and 160000 quadrilateral shell elements respectively. Vessel density equivalent to 1100 kg/m^3 and a wall thickness corresponding to 2.3 mm was assumed for both patients [55, 227]. A nearly incompressible Arruda-Boyce constitutive model was employed to approximate the biomechanical response of the aorta wall. The initial shear modulus equivalent to 0.185MPa was obtained from previous measurements of mechanical properties of ascending aortic aneurysms [190]. The limiting network stretch was assumed to be 1.01. Computation of the unstressed or 'zero-pressure' aorta geometry was not necessary, since FSI simulations were performed for the pulse pressure as outlined previously. The inlet and outlets were constrained in all directions [65] to ensure that the resulting vessel wall displacements were physiological.

An FSI boundary condition was prescribed at the interface between the flow and solid domains. The mesh for the flow domain was moved using the ALE approach [67] to maintain the aforementioned condition throughout the simulation (Chapter 2). Specifically, the grid for the flow domain was smoothed using a diffusion based scheme [46] and remeshed at every coupling step to maintain mesh quality. Quasi-steady, constant velocity FSI simulations of aortic blood flow were performed using the ANSYS Multiphysics software. The ANSYS System Coupling code was employed to communicate forces from ANSYS Fluent to ANSYS Mechanical and relay the resulting displacements to ANSYS Fluent to update the flow variables and grid

(Chapter 2). Data exchange between the two solvers occurred for a time period corresponding to 0.68 s [190]. 25 coupling iterations were observed to be sufficient to ensure convergence of the data exchange quantities (i.e. forces and displacements). Post-processing of flow and mechanical variables was performed using VisIt [207].

9.2.3 *Results and Discussion*

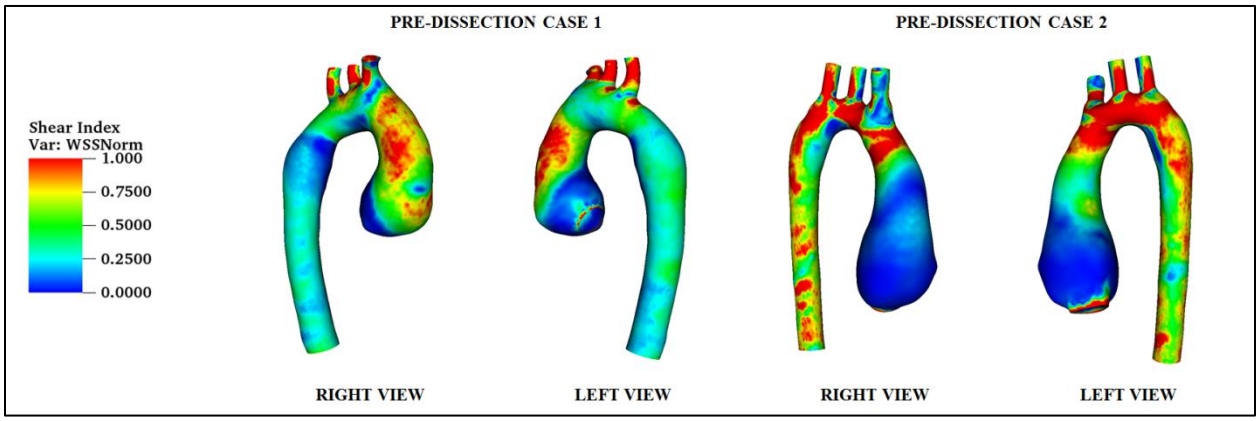

Figure 9.10: Contour plots of normalized wall shear stress for subjects with aortic root dilatation.

Color maps of the shear index or normalized wall shear stress are indicated in Fig. 9.10 for the two patients analyzed in this study. As can be seen, high shear stresses corresponding to patient 1 were observed in the supra-aortic vessels and junction between branch vessels and the transverse aorta. A region of low shear was observed in the sinus, in the proximity of the inlet. Skewing of flow towards the outer wall of the ascending aorta resulted in concentration of shear stresses on the proximal outer wall of the ascending aorta and in the aortic root. Low shear regions were observed at the start of the transverse aortic arch and in the dilated section of the descending aorta at the end of the aortic arch. Shear index increased downstream of the stagnation flow region in the descending aorta. For subject 2, high shear index was observed for the branch vessels and at the junction between the transverse section and supra-aortic vessels in a manner similar to patient 1. A region of low shear was observed at the end of the aortic arch. The

average shear indices for the transverse and descending aorta were 25 percent and 133 percent higher respectively than the same for patient 1, as a result of the lower lumen radius (Fig. 9.8). Low shear regions were observed throughout the aortic sinus for subject 2 as compared to patient 1. High shear was observed on the inner and outer walls of the ascending aorta in the proximity of the innominate artery. These results further emphasize the importance of including the aortic sinus since the angulation of flow leaving the left ventricle upstream of the valve leaflets could potentially vary between subjects and subsequently influence the distribution of shear stresses in the ascending aorta. The observations of low shear in the sinus were consistent with previous computational [187, 190] and experimental [239] studies. Besides, a low shear index corresponding to the aortic root could potentially increase the possibility of sinus rupture due to progressive dilatation [187].

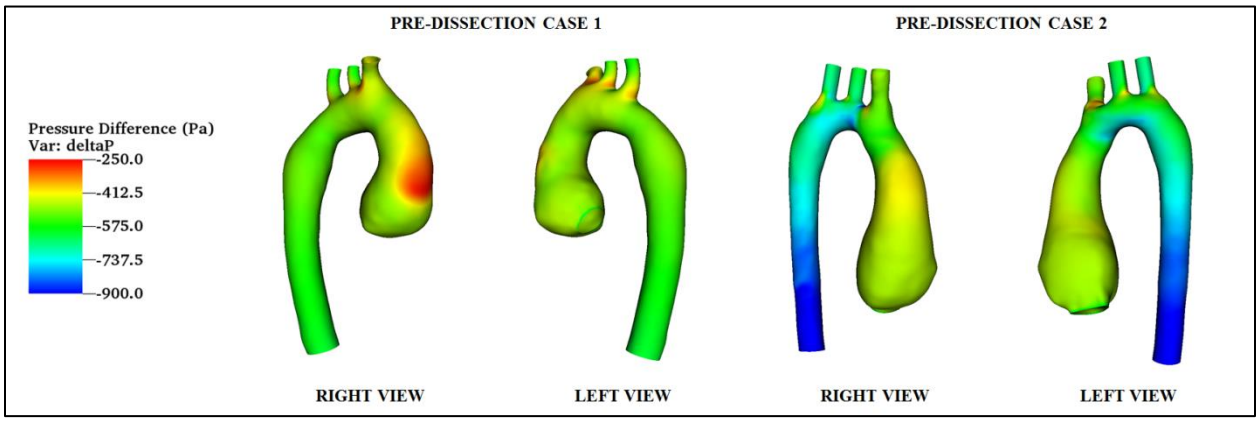

Figure 9.11: Surface maps of differential aortic wall pressure distribution for subjects with aortic root dilatation.

The pulse pressure (i.e. 56 mmHg) was subtracted from the nodal values of aortic wall pressure to generate contour plots of the differential aortic wall pressure distribution for the 2 patients considered in this analysis. As can be seen for subject 1, the differential aortic pressure decreased from the ascending aorta to the descending section. The wall pressure was greatest in the ascending aorta above the sinotubular junction (-250 Pa). The descending aorta was characterized by a nearly uniform aortic pressure (~-575 Pa). The range of aortic wall pressure

for patient 1 (~2.5 mmHg) was 150 percent higher than the same obtained for simulations involving mixed outflow and pressure outlet boundary conditions described in Chapter 8. For patient 2, the highest wall pressure was observed midway on the outer wall of the ascending aorta and was 65 percent lower than the same for patient 1. The wall pressure was observed to decrease from the sinus to the descending aorta in a manner similar to patient 1. The differential aortic wall pressure decreased from -575 Pa at the end of the aortic arch to -900 Pa at the descending aorta outlet due to the aortic taper. The range of aortic wall pressure for patient 2 (~3.7 mmHg) was 270 percent higher than the same for simulations involving pressure outlets for the supra-aortic vessels and outflow for the descending aorta outlet (Chapter 8). As discussed previously in Chapter 8, concentration of shear stress coupled with high aortic wall pressure is associated with vascular remodeling and subsequently generates morphological changes in the ascending aorta [187, 190].

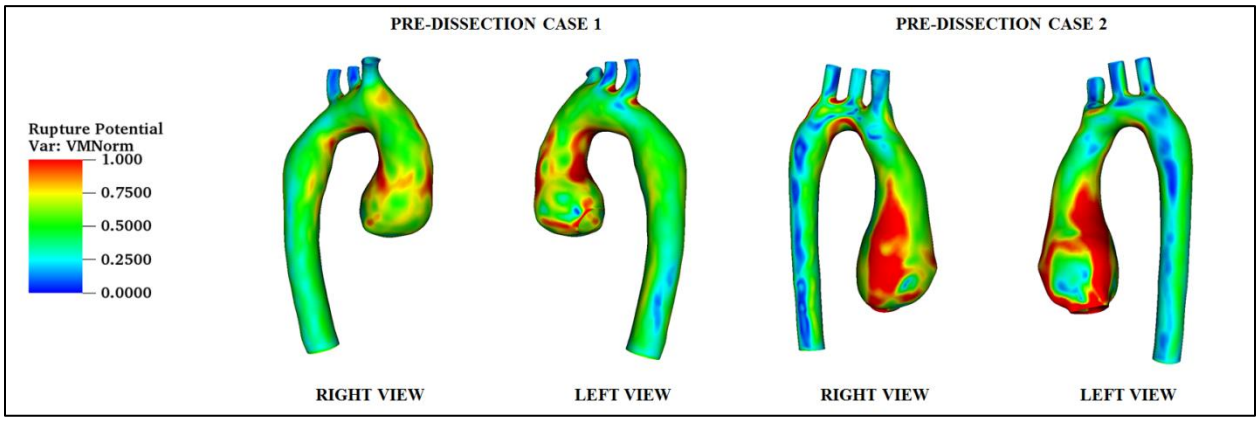

Figure 9.12: Contour plots of normalized mechanical stress for subjects with aortic root dilatation.

Nodal values of von-Mises stress were normalized by a value of 75 kPa to generate contour plots of the rupture potential (Fig. 9.12). Mechanical stresses were concentrated at the junction between the transverse aorta and supra-aortic vessels for the 2 subjects analyzed in this study. For patient 1, high mechanical stresses were uniformly distributed throughout the inner wall of the ascending aorta. Mechanical stress concentration was observed on the proximal outer

wall and at the sinotubular junction. The aortic sinus for patient 1 was characterized by a moderate rupture potential (~0.62). Stresses were also distributed on the inner wall of the transverse aorta and at the end of the aortic arch. For subject 2, high mechanical stresses were concentrated on the inner and outer walls of the ascending aorta in the proximity of the STJ. The sinus for patient 2 was characterized by a rupture potential that was 40 percent higher than the same for subject 1. Stresses were also concentrated on the inner wall of the transverse aorta in a manner similar to patient 1. The average rupture potential of the descending section for patient 2 (~0.25) was 50 percent smaller than the same for patient 1 (~0.5), as a result of a dilated descending aorta in the latter case.

It should be noted that evaluation of the rupture potential of the aorta for the 2 subjects was performed using computational FSI modeling without prior knowledge of the clinical outcome until all the analyses was completed. Both subjects were diagnosed with Type-A dissection in a follow-up visit. Although the presented computational analysis provided evidence of the high risk of vessel wall failure in the root and STJ, the accuracy in predicting the exact spatial location of the origin of arterial rupture was limited by the choice of the isotropic material model chosen in this study. Previous studies have emphasized the importance of modeling the biomechanical response of the aorta using the fiber-reinforced Hozapfel-Gasser-Ogden constitutive law [205] to obtain an improved estimate of mechanical stress magnitude and identification of regions that are most vulnerable to vessel wall failure. Tissue histology and characterization of mechanical properties using biaxial testing is necessary to implement the aforementioned anisotropic model [205]. Additionally ‘peel tests’ would have to be performed to assess the bond strength between the intimal and medial layers [227] and the structural model would have to be suitably modified to account for anisotropy in the radial direction.

9.3 *FSI Modeling for TS using Enhanced Outlet Conditions*

In this section, the FSI methodology presented in section 9.2 is applied to 3 Turner syndrome patients and one female volunteer to compare hemodynamic and biomechanical functional indices of aortic disease.

9.3.1 *Methods*

3 adult patients with karyotypically proven TS were recruited for this computational analysis. Additionally, one adult female volunteer was recruited to serve as a healthy control. The control was normotensive and the three TS subjects were hypertensive. The first patient (TS-1) had mild aortic valve regurgitation and ascending aortic dilatation. Patient 2 (TS-2) had ascending aortic dilation only and patient 3 (TS-3) had ETA. This study was approved by the ethical committee of The Central Denmark Region (#201250012) and was registered at ClinicalTrials.gov (#NCT01678274). The 3 TS patients and healthy control provided informed consent to participate in this study. Static diastolic and phase-contrast MR images were acquired for the four subjects using a whole-body 1.5T Philips Achieva scanner (Philips Medical Systems, Best, The Netherlands). The GTFlow software (GyroTools LLC, Zurich, Switzerland) was employed to analyze 4D flow data and compute the cardiac output and descending aortic flow at peak systole.

Diastolic scans were imported into Mimics (Materialise Inc., Plymouth, MI) image processing software to reconstruct subject-specific 3D geometries of the thoracic aorta using a thresholding algorithm. Smoothed aortic geometries were clipped using Paraview (Kitware Inc., Clifton Park, NY) at the inlet in the sinus and outlet in the descending aorta. The vascular modeling toolkit (VMTK) was employed to identify centerlines [240] for the individual clipped aortas and the same were employed to create a 20 mm diameter short flow extension directed

into the left ventricle. The extensions were merged with the thoracic aortic geometries using Mimics and smoothed geometries were exported in the STL format for geometric measurements and FSI modeling. Inlet and outlets for the computational domain were identified using Paraview. VMTK was employed to create artificial flow extensions approximately 4 diameters in length for the branch vessels. Euclidean distance maps were computed for the individual aorta geometries as described in Chapter 6. Hydraulic diameters of the supra-aortic vessel outlets were then evaluated to estimate the percentage outflow corresponding to the branch vessels in a manner similar to Murray's law [164]. Table 9.1 summarizes the cardiac output and percentage outflow corresponding to the descending aorta and supra-aortic vessels for the 4 subjects considered in this analysis.

Table 9.1: Cardiac output and percentage outflow for control and TS (Note: Cardiac output expressed in lpm).

	Control	**TS-1**	**TS-2**	**TS-3**
Cardiac Output	14.14	21.54	9.85	8.82
Descending Aorta	77%	72%	61%	68%
Innominate Artery	10%	13%	18%	15%
Left Common Carotid Artery	6%	5%	9%	7%
Left Subclavian Artery	8%	10%	12%	10%

The centerlines-based grid generation algorithm available in VMTK [204] was employed to discretize the aorta lumen using tetrahedral elements. Mesh resolutions for the flow domain were as follows: a) control – 1.7 million cells, b) TS-1 – 2.8 million cells, c) TS-2 – 2.2 million cells, d) TS-3 – 3 million cells. A mass flow boundary condition corresponding to the cardiac output (Table 9.1) was prescribed at the inlet of the flow domain. A flat inlet velocity profile was employed in this study [208]. Pressure-outlet boundary conditions with a target mass flow rate [238] was adopted for this analysis (Section 9.2). The static pressure corresponding to the outlets was the pulse pressure equivalent to 50 mmHg for the control and 84 mmHg for TS as measured

previously for normotensive and hypertensive female subjects [192]. Specification of the mass flow at the pressure outlet minimized the error between the predicted and simulated outflows by iteratively adjusting the pressure drop across the individual vascular segments (Fig. 9.13). Turbulence was modeled using the shear-stress transport model. A length scale corresponding to 1 mm was assumed and the turbulence intensity was set to 2 percent. Blood was modeled as a Newtonian fluid with a dynamic viscosity of 0.0035 Pa-s and density 1060 kg/m^3. A second order upwind scheme was employed to discretize the pressure, momentum and turbulence terms. Pressure-velocity coupling was achieved using a least-squares cell-based scheme.

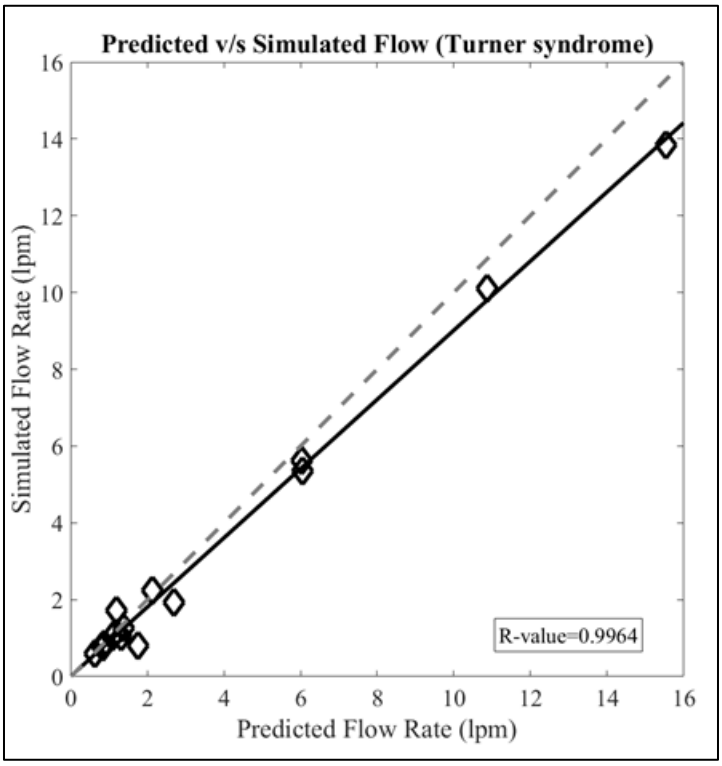

Figure 9.13: Correlation between predicted and simulated flow rates for control and TS patients.

Biomechanical response of the aorta wall was approximated using a nearly incompressible Arruda-Boyce material model. Density of the vessel wall was equivalent to 1100 kg/m^3. Vessel wall thickness definitions for the 4 subjects were as follows [227]: a) Control – 2 mm, b) TS-1 – 1.9 mm, c) TS-2, 3 – 1.8 mm. The limiting network stretch was equivalent to

1.01. The initial shear modulus was defined as follows: a) control – 0.1 MPa [196], b) TS-1 – 0.145 MPa [190], c) TS-2, 3 – 0.225 MPa [190]. ICEM-CFD (Ansys Inc., Canonsburg, PA) was used to discretize the vessel wall using 4 node quadrilateral shell elements. Vessel wall mesh resolutions for the 4 subjects were as follows: a) control – 120000 elements, b) TS-1 – 160000 elements, c) TS-2 – 135000 elements, d) TS-3 – 180000 elements. Since FSI simulations corresponded to the pulse pressure, the 'unstressed' configuration of the aorta [55] was not evaluated. Fixed boundary conditions were applied at the inlet and outlets [65]. A FSI boundary condition was prescribed at the interface between the lumen and arterial wall. Cells for the flow domain were moved using the ALE method as described in Chapter 2. Mesh quality was maintained by smoothing the grid using a diffusion-based scheme and frequent remeshing. Constant velocity FSI simulations were performed using the ANSYS Multiphysics software. Forces from ANSYS Fluent and ANSYS Mechanical were communicated using the ANSYS System Coupling code. Data exchange for the partitioned approach occurred for a time period corresponding to 0.68 s. Convergence of data exchange quantities was obtained within 25 coupling iterations. Hemodynamic and biomechanical variables were post-processed using VisIt.

9.3.2 *Results & Discussion*

Figure 9.14 summarizes the contour maps of Euclidean distance for the 4 subjects considered in this analysis. Largest aortic dimensions were observed in the root for the control, TS-1 and TS-3. It should be noted that the maximum aortic radius was observed in the posterior sinus for TS-1 and in the coronary sinus for the control and TS-3. Furthermore, the sinus radius for TS-1 (21.3 mm) was 12 percent higher than the control (19 mm) and 20 percent higher than the same for TS-3 (17.5 mm). The largest aortic diameter was observed midway in the ascending aorta for

TS-2 (21.3 mm). The average ascending aortic dimensions were comparable for the control and TS-3 and were ~30 percent lower than the same for TS-1, 2.

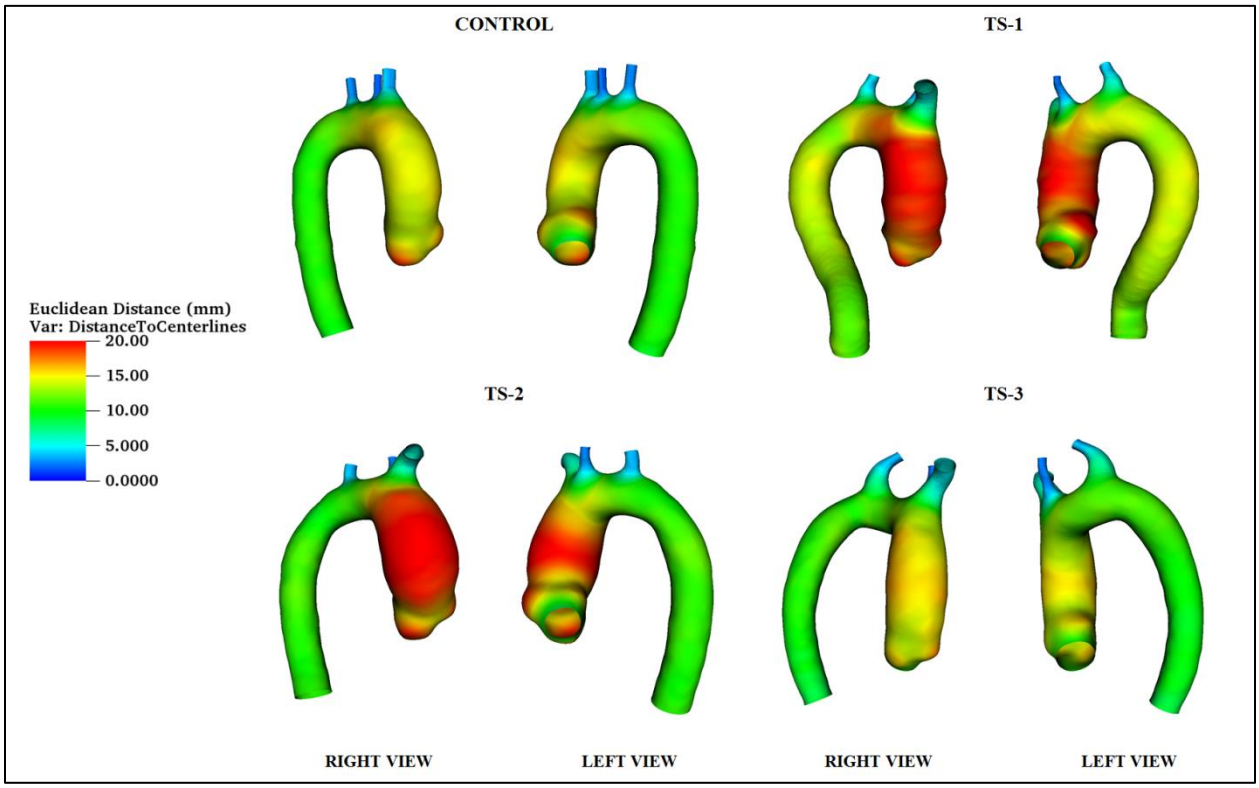

Figure 9.14: Contour maps of Euclidean distance from centerlines for control and TS patients.

Figure 9.15 summarizes the 3D distribution of wall shear stress for the 3 TS patients and control subject analyzed in this study. For the control, the highest WSS in the ascending aorta (10 Pa) was observed midway on the outer wall. The aortic wall pressure at the corresponding spatial location was 6330 Pa. It should be noted that the highest aortic wall pressure (6470 Pa) was also observed midway on the outer wall of the ascending aorta. The corresponding shear stress was 74 percent than the maximum shear stress in the ascending aorta. In the descending aorta, maximum shear (9.7 Pa) was obtained at the end of the aortic arch. The average shear stress corresponding to the ascending aorta (3 Pa) was comparable to the same for the descending section (3.2 Pa). High shear stresses were also concentrated at the junction between

the transverse aorta and supra-aortic vessels. Regions of low shear occurred in the sinus and the inner wall of the ascending aorta. The 3D distribution of shear for TS-1 was qualitatively similar to the same for the control subject. Maximum WSS in the ascending aorta (10.2 Pa) was obtained midway on the outer wall. The corresponding aortic wall pressure was 9370 Pa. Similar to the control case, the highest aortic wall pressure (9580 Pa) occurred at a different spatial location in the ascending aorta. The corresponding shear stress was 67 percent lower than the maximum value. Low shear regions were observed in the sinus, as obtained for the control subject. In the descending aorta, peak shear stress (14.5 Pa) occurred on the outer wall at the diaphragm. Additionally, shear stresses were concentrated at the end of the aortic arch and junction between the branch vessels and transverse section. The average ascending and descending aortic WSS for this subject were 3.4 and 18 percent higher respectively than the control.

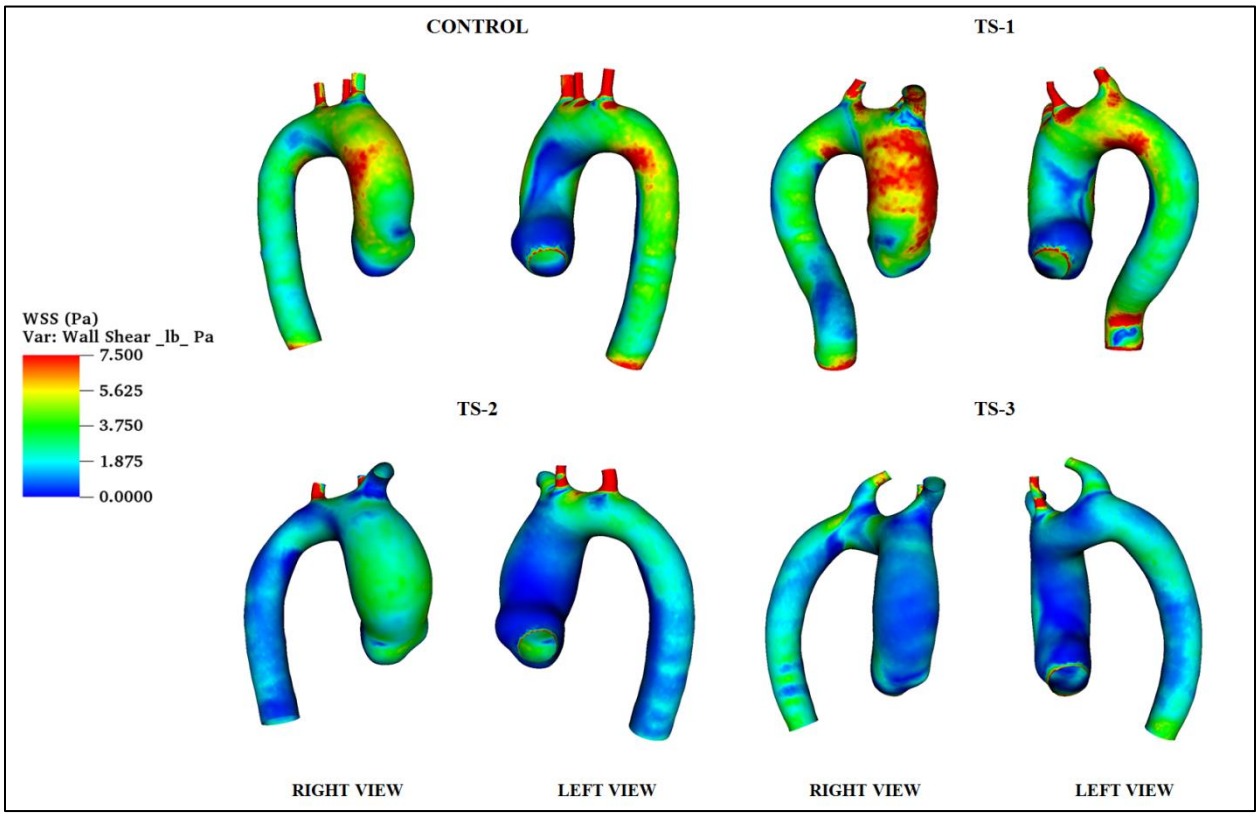

Figure 9.15: Contour maps of WSS variation at peak systole for control and TS patients.

For the subject with ascending aortic dilatation (TS-2), maximum aortic wall pressure (10990 Pa) was observed above the STJ. The corresponding shear stress was 1.8 Pa. Maximum shear stress in the ascending aorta (4.6 Pa) occurred at a different spatial location above the sinotubular junction. The corresponding aortic wall pressure was comparable (85 Pa difference) to the maximum value. In the descending segment, the greatest shear stress (5 Pa) was observed on the outer wall downstream of the LSCA. Shear stresses were also significant on the inner wall of the descending aorta at the end of the aortic arch and on the lateral left walls of the transverse aorta. Regions of low shear were observed downstream of the aortic arch, inner wall of the ascending aorta and sinus. The average shear in the ascending and descending sections was 46 percent and 59 percent lower respectively than the control case. For the subject with ETA (TS-3), maximum aortic wall pressure (11120 Pa) was obtained above the STJ in a manner similar to TS-2. Corresponding shear stress was 64 percent lower than the same for TS-2. Maximum shear stress in the ascending aorta (2.9 Pa) occurred midway on the outer wall. Aortic wall pressure at this spatial location was comparable (50 Pa difference) to the maximum value. In the descending segment, maximum shear was obtained downstream of the LSCA on the outer wall and was 6 percent higher than TS-2. Regions of low shear occurred on the inner wall of the descending aorta at the end of the aortic arch, in the sinus and inner wall of the ascending aorta. The average shear in the ascending and descending sections was 25 percent lower and 46 percent higher respectively than TS-2.

The peak displacement for the control subject (1.9 mm) occurred in the right lateral wall of the transverse aorta between the IA and LCCA. The same for TS-1 was also obtained in the right lateral wall of the transverse aorta and was 47 percent higher than the control. For the subject with ascending aortic dilatation (TS-2), the peak displacement magnitude was identical to

the control but was observed to occur between the left coronary and posterior sinus. For the subject with ETA (TS-3), the maximum displacement of the vessel wall was obtained in the right lateral wall similar to the control and TS-1. The maximum displacement was 8 percent lower than the control. Aortic displacements were in good agreement with the same obtained for patients with Marfan syndrome [65].

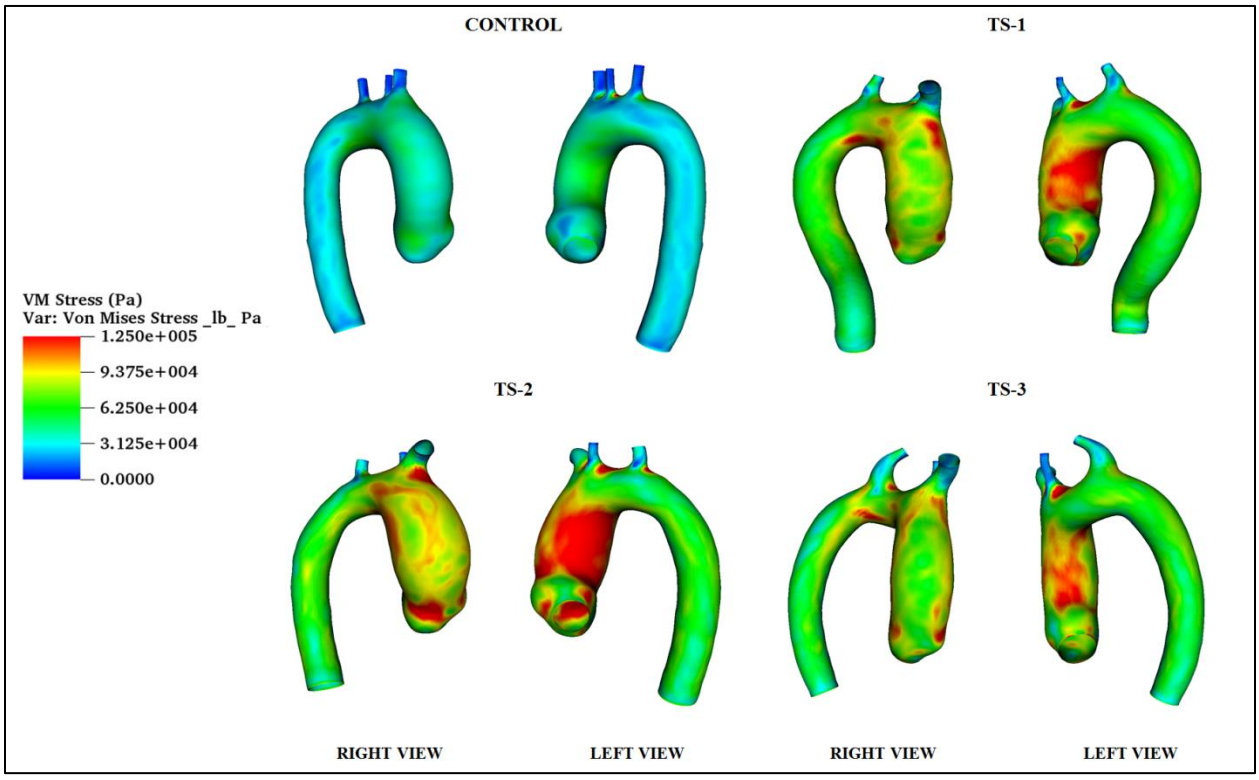

Figure 9.16: Contour maps of mechanical stress variation at peak systole for control and TS patients.

For all the subjects analyzed in the present study, high mechanical stress concentration was obtained at the junction between supra-aortic vessels and the transverse aorta (Fig. 9.16). For the control these highly stressed regions were observed between the LCCA and LSCA. The same for the TS patients occurred between the IA and LCCA. The maximum stress in the STJ for the control (65000 Pa) occurred in the proximity of the coronary sinus. For the subject with ascending aortic dilatation and valve regurgitation, the maximum stress in the STJ (150000 Pa) was obtained in the proximity of the posterior sinus. For the subject with ascending aortic

dilatation (TS-2), peak magnitude of the von-Mises stress in the STJ (190000 Pa) also occurred in the proximity of the posterior sinus. For TS-3, the maximum stress in the STJ (130000 Pa) was obtained in the proximity of the coronary sinus similar to the control. It should be noted that while stresses in the STJ correlated with the corresponding aortic diameter for the control, TS-1 and TS-2, lower concordance was obtained for TS-3. This could be attributed to the selection of higher vessel stiffness for FSI simulations involving TS-3. Stress distribution in the ascending aorta was qualitatively similar for all TS subjects. However, higher stresses in the inner wall were obtained for subjects with ascending aortic dilatation (TS-1, 2). Furthermore, higher stresses were observed on the outer wall of the ascending aorta for TS-2 as compared to TS-1 and TS-3. Mechanical stresses were also distributed in the inner wall of the transverse section for all TS subjects. Stress concentration occurred at the end of the aortic arch for TS-1 and TS-3. Patterns of von-Mises stress distribution in TS were in good agreement with the same for patients with ascending aortic aneurysms [55].

Although differences were observed in cardiac output, division of flow between the descending section and branch vessels, aortic pressure, vessel elasticity and wall thickness for the individual cases, qualitative similarities in the 3D distribution of functional variables were also obtained for the subjects analyzed in this pilot study. In a future study involving additional patients and controls, the presented methodology could be potentially employed to create ‘functional phenotypes’, similar to geometric phenotypes currently identified in TS. The proposed computational FSI model would have to be suitably modified to include measures of aortic distensibility (Section 9.1) and possible variations in the same between visits [177] for longitudinal analysis.

Chapter 10

Decoupled FSI, Transient FSI & Sensitivity Analysis

Results from this chapter were presented at the 2017 AIAA DCASS, Dayton, OH and at the 2017 BMES Annual Meeting, Phoenix, AZ

This concluding chapter firstly describes an alternate bi-directional FSI methodology for peak systolic analysis of functional variables in TS. Secondly, unsteady FSI simulations are presented for one TS patient to introduce hemodynamic and biomechanical functional variables based on temporal variations in the aortic flow and displacement of the vessel wall. Thirdly, the influence of blood rheology on shear stress distribution and wall thickness on mechanical stress is described for several aortic anomalies observed in TS.

10.1 *Decoupled 2-way FSI simulations of Aortic Blood Flow*

Two TS subjects were chosen for this analysis. The methodology described in this section was employed to evaluate visit-to-visit changes in geometric and functional variables for the 2 patients. It should be noted that the present analysis discusses longitudinal changes including the aortic root as compared to results presented in Chapter 7 (Section 7.2).

10.1.1 *Methods*

Static diastolic MR images for 2 TS patients with bicuspid aortic valve and hypertension were acquired for baseline and follow-up visits (5 years difference between the 2 visits). Additional details regarding image acquisition and reconstruction of the aortic geometry including the sinus have been described previously in Chapters 8 and 9. Flow extensions were generated for the supra-aortic vessels, approximately four diameters normal to the vessel cross-section [212] using the Vascular Modeling Toolkit as described previously in Chapter 9. Surface maps describing the

variation in Euclidean distance from the aorta centerlines were evaluated using VMTK [203]. Aorta geometries were discretized using a centerline-based tetrahedral grid generation algorithm [204] available in VMTK, as outlined previously in Chapter 7-9. Flow domain mesh resolutions for the 2 subjects were as follows: a) TS-1 (Visit 1) – 2.6 million cells b) TS-1 (Visit 3) – 2.9 million cells c) TS-2 (Visit 1) – 2.8 million cells d) TS-2 (Visit 3) – 3.1 million cells. Blood was modeled as a Newtonian fluid with a dynamic viscosity of 0.0035 Pa-s and density of 1060 kg/m^3. Constant velocity simulations of aortic blood flow were performed for a peak systolic cardiac output equivalent to 10 liters per minute. 60 percent of the flow was assumed to exit the descending aorta [190]. Hydraulic diameters of the supra-aortic vessel outlets were determined and outflow percentages were evaluated in a manner similar to Murray's law [164]. Pressure outlet boundary conditions with a target mass flow were defined at the outlets [238]. The static pressure corresponding to the outlets was the pulse pressure equivalent to 84 mmHg measured previously for hypertensive female subjects [192]. Specification of the mass flow at the pressure outlet minimized the error between the predicted and simulated outflows by iteratively adjusting the pressure drop across the individual vascular segments (Fig. 10.1).

Turbulence was modeled using the k-ω SST model as described previously in Chapter 7 and 8. A turbulence intensity corresponding to 2 percent was prescribed at the inlet and a length scale equivalent to 1 mm was assumed. The pressure, momentum and turbulence terms were discretized using a second-order upwind scheme. A pressure-based coupled formulation [89] was adopted for pressure-velocity coupling. A least-squares cell-based scheme was employed to evaluate gradients. Flow simulations were performed using ANSYS Fluent software. The surface mesh corresponding to the aorta wall and corresponding nodal forces arising from fluid shear and normal stresses were exported to ABAQUS using the 'export solution data' utility available in

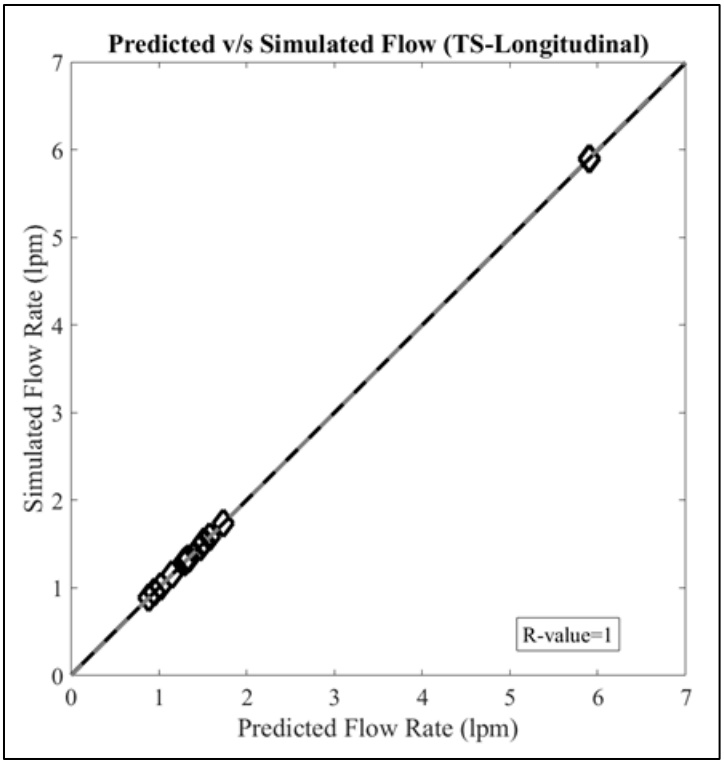

Figure 10.1: Correlation between predicted and simulated flow rates for the longitudinal analysis.

ANSYS Fluent [241]. Accordingly, the vessel wall was discretized using reduced integration triangular shell elements (S3R) [190] with a thickness of 1.5 mm [206]. Structural domain grid mesh resolutions were as follows: a) TS-1 (Visit 1) – 60000 shells b) TS-1 (Visit 3) – 57000 shells c) TS-2 (Visit 1) – 72000 shells d) TS-2 (Visit 3) – 72000 shells. Biomechanical response of the aorta wall was approximated using a nearly incompressible Arruda-Boyce material model. Density of the vessel wall was equivalent to 1100 kg/m^3. The limiting network stretch was equivalent to 1.01. The initial shear modulus for the baseline and follow-up visits was 0.87 MPa. The order of magnitude of the stiffness was similar to patients with descending aortic aneurysms [242] and Marfan syndrome [66]. Inlet and outlets were constrained in all directions [65]. Since simulations corresponded to the pulse pressure, the 'unstressed' configuration of the aorta [55] was not evaluated. Simulations of vessel wall motion in response to flow-induced forces were performed using ABAQUS/Standard software. The displaced aorta wall was remeshed in

ANSYS Fluent and the flow variables were updated as described previously in Chapter 9. It should be noted that the 'decoupled' FSI methodology described in this section was similar to the computational approach adopted to study the positional stability of aortic endografts for abdominal aortic aneurysms [243]. The output database (ODB) from ABAQUS was converted to the visualization toolkit format (VTK) using an open-source Python script [244], modified to suit triangular and quadrilateral shell elements. Geometric, hemodynamic and biomechanical variables were post-processed using Paraview, Tecplot 360, VisIt and Abaqus Viewer.

10.1.2 *Results and Discussion*

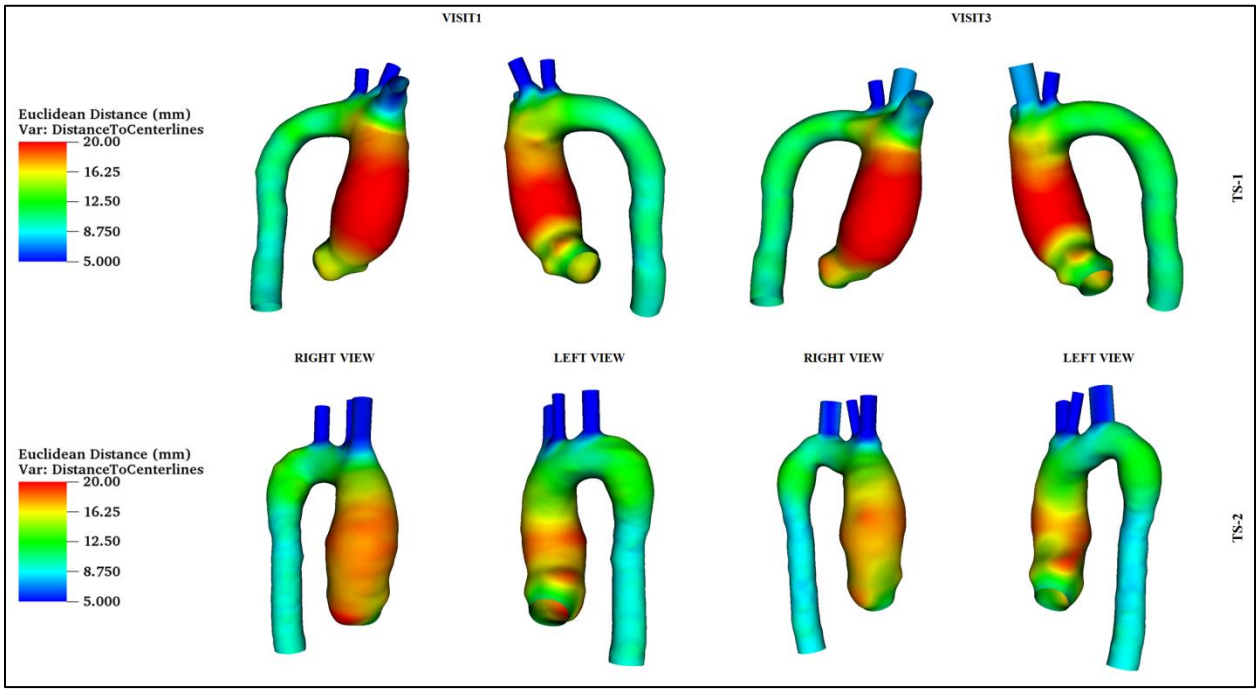

Figure 10.2: Contour maps of Euclidean distance describing visit-to-visit change in aortic geometry for TS-1, 2.

Figure 10.2 summarizes the contour maps of Euclidean distance for the 2 subjects (baseline and follow-up visit) considered in this analysis. Largest Euclidean distance was observed midway in the ascending aorta for TS-1 corresponding to the baseline (21.8 mm) and follow-up visit (22.2 mm). The maximum aortic diameter for this subject increased by 3 percent between visits. The maximum lumen radius was obtained in the inner wall for visit 1 and in the outer wall for visit 3.

For TS-2, the maximum Euclidean distance was obtained in the aortic root for the baseline (20.8 mm) and follow-up visit (19.3 mm). The maximum aortic diameter decreased by 7 percent between visits. For visit 1 and visit 3, the maximum lumen radius was observed in the coronary and posterior sinus respectively. Maximum aorta diameter in the ascending aorta for TS-2 was 35 mm for visit 1 and 3. The descending aortic radius for TS-1 increased moderately between visits. The same for TS-2 was observed to decrease from visit 1 to visit 3.

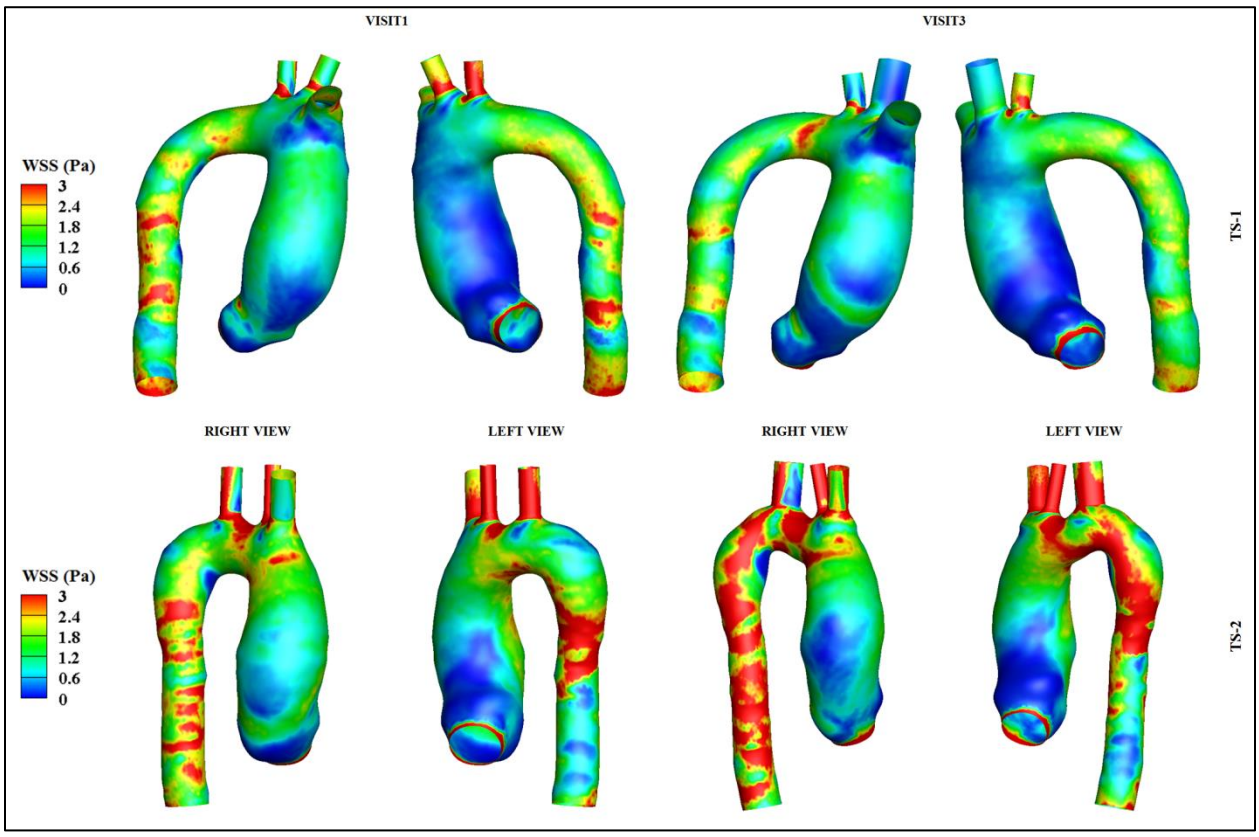

Figure 10.3: Contour maps of wall shear stress describing visit-to-visit change in hemodynamic functional variables for TS-1, 2.

Figure 10.3 summarizes the 3D distribution of wall shear stress for the 2 TS patients (baseline and follow-up visit) considered in this analysis. For TS-1, the highest WSS in the ascending aorta corresponding to the baseline visit (2.5 Pa) was observed at the sinotubular

junction. The spatial location was unchanged from visit 1 to visit 3. The magnitude of WSS was observed to decrease by 20 percent between visits. The maximum ascending aortic pressure for the baseline visit (11345 Pa) was obtained on the outer wall in the proximity of the aortic sinus. The same for the follow-up visit occurred on the outer wall midway in the ascending aorta and the magnitude was comparable (11285 Pa) to the first visit. Low shear was observed in the sinus and inner wall of the ascending aorta for both visits. The outer wall was characterized by a low shear region surrounded by regions of high shear stress [208]. The magnitude of WSS in this aforementioned region of high shear was greater for visit 3 as compared to visit 1. The spatial extent of the same was lower for the former case. The average ascending aortic WSS was comparable for the visits (0.86 Pa – visit 1, 0.84 Pa – visit 3). Concentration of shear stress was observed at the end of the aortic arch and at the supra-aortic vessels – transverse aorta junction for baseline and follow-up visits. The maximum shear stress in the descending aorta (4.9 Pa) was obtained in the proximity of the diaphragm for the baseline visit. The maximum WSS decreased by 25 percent between visits and occurred midway in the descending aorta for the follow-up visit. The average descending aortic WSS was 18 percent lower for visit 3.

For TS-2, the highest WSS in the ascending aorta corresponding to the baseline visit (3.5 Pa) was observed on the outer wall in the proximity of the innominate artery. The same for the follow-up visit was 14 percent higher and occurred on the lateral wall in the proximity of the IA. The maximum ascending aortic pressure for the baseline visit (11373 Pa) was obtained on the outer wall midway in the ascending aorta. The spatial location of maximum aortic wall pressure was unchanged for visit 3 and the magnitude (11415 Pa) was comparable to the first visit. Spatial extent of low shear regions in the sinus and inner wall of the ascending aorta were smaller compared to TS-1 and was unchanged between visits. The outer wall was characterized

by a low shear region surrounded by regions of higher shear stress as observed for TS-1. The average ascending aortic WSS was 50 percent higher than the same for TS-1 (visit 1 – 1.24 Pa, visit 3 – 1.3 Pa). High shear stresses were observed in the transverse aorta for the baseline and follow-up cases. The region of high shear stress concentration at the end of the aortic arch was observed only for the follow-up visit. A region of low WSS was obtained in the descending aorta downstream of the aortic arch. This region was smaller in size and strength for visit 1. High shear stresses were observed downstream of this aforementioned region of low shear for the baseline and follow-up visits. Maximum WSS in the descending aorta for visit 1 (8 Pa) occurred midway on the outer wall. The circumferential location of peak WSS differed from visit 1 to visit 3. Maximum descending aortic shear stress for the follow-up visit was 4 percent lower than baseline and was obtained on the lateral wall. The average descending aortic WSS for visit 3 (2.4 Pa) was 26 percent higher than the same for visit 1 (1.9 Pa).

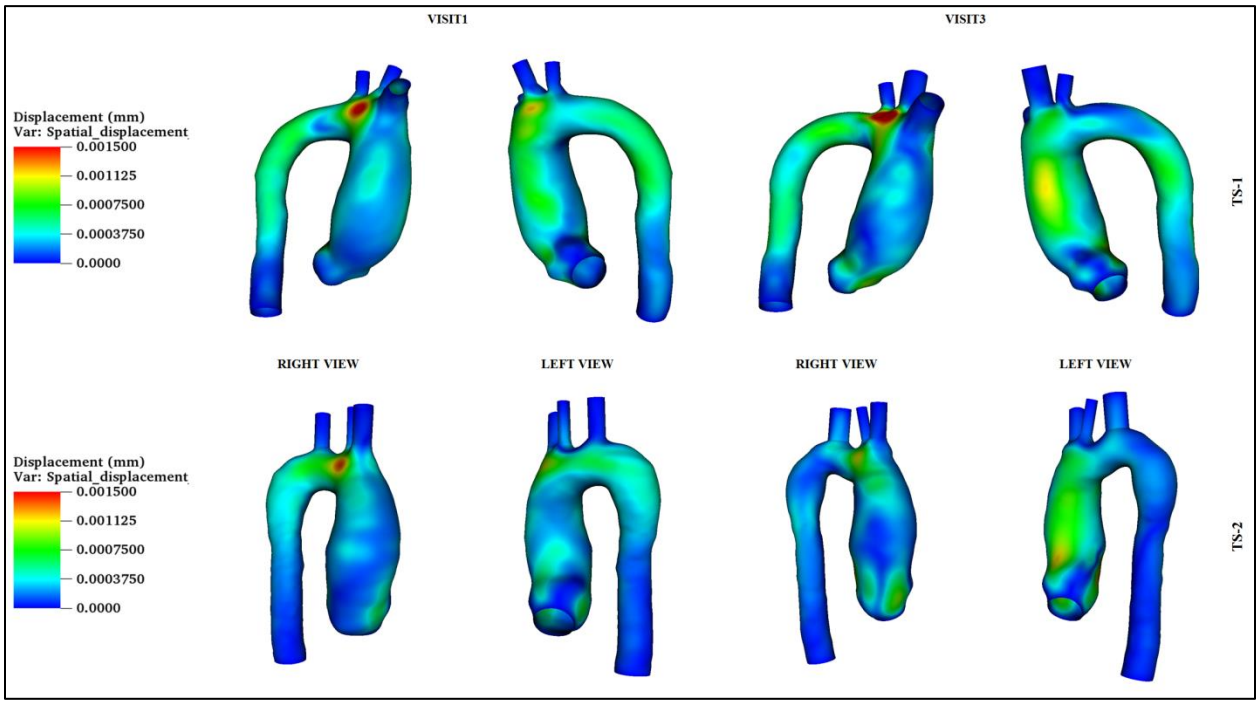

Figure 10.4: Contour maps of vessel wall displacement describing visit-to-visit change in biomechanical functional variables for TS-1, 2.

Figure 10.4 summarizes the 3D distribution of wall displacement for the 2 TS patients (baseline and follow-up visit) considered in this analysis. For TS-1, the peak displacement for the baseline visit (1.6 mm) occurred in the right lateral wall of the transverse aorta. The same for the follow-up visit was also obtained at the same spatial location and was 25 percent higher than the first visit. For TS-2, the peak displacement magnitude for the first visit was 13 percent lower than the corresponding value for TS-1 and was observed to occur in the right lateral wall of the transverse aorta. The largest vessel wall displacement for the follow-up visit was 7 percent lower than the baseline and was observed in the root between the coronary and posterior sinuses. Magnitudes of maximum vessel wall displacement and the corresponding spatial locations were in good agreement with the same obtained for fully coupled, 2-way FSI simulations of aortic blood flow in subjects with coarctation [206] and aortic valve prosthesis [202].

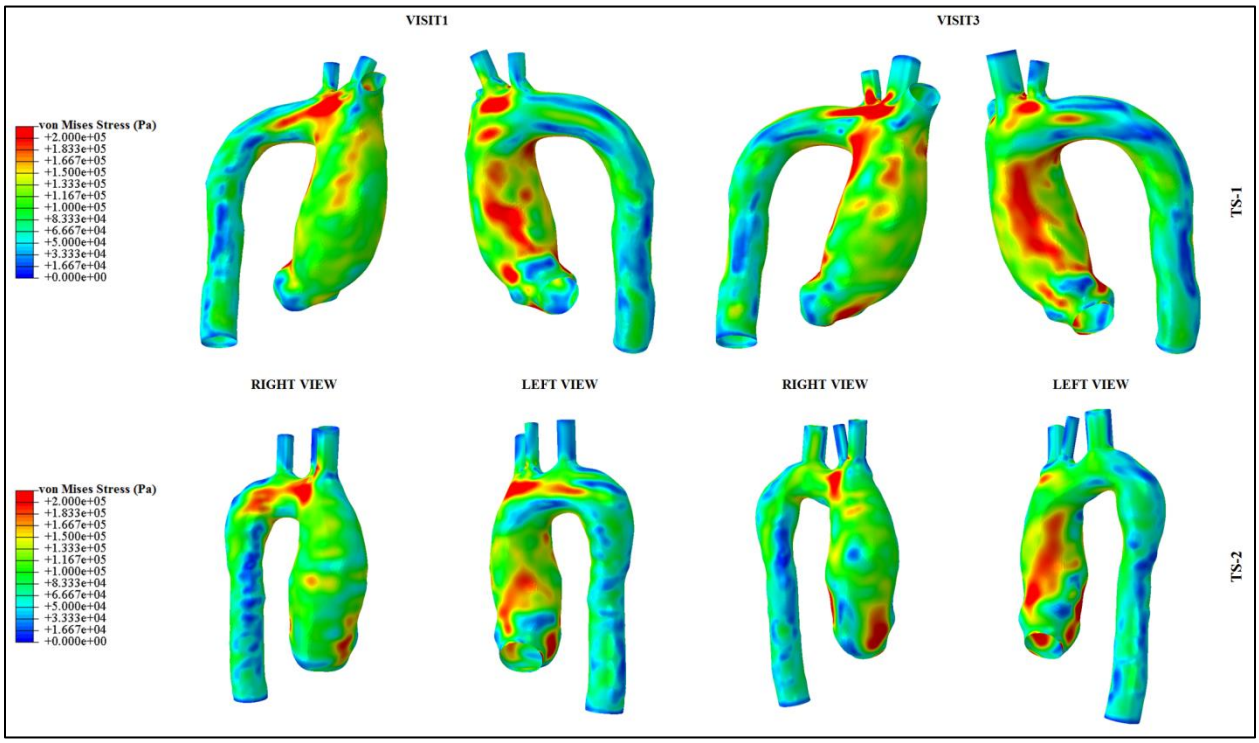

Figure 10.5: Contour maps of von-Mises stress describing visit-to-visit change in biomechanical functional variables for TS-1, 2.

Contour maps of mechanical stress variation at peak systole for the 2 TS patients (visit 1 and visit 3) are indicated in Figure 10.5. For both subjects, high von-Mises stresses were distributed in the inner wall of the ascending aorta, lateral walls of the transverse section and in the aortic root between the coronary and posterior sinuses. For the baseline visit corresponding to TS-1, the maximum magnitude of mechanical stress (0.32 MPa) was observed on the right lateral wall of the transverse aortic arch. The peak von-Mises stress in the inner wall of the ascending aorta was 32 percent lower (0.22 MPa) for this subject. The value corresponding to the aortic root was 0.28 MPa. For the follow-up visit, the spatial location of the maximum von-Mises stress (i.e. right lateral wall of transverse section) was unchanged. However, the magnitude was higher by 16 percent. The largest mechanical stress in the inner wall of the ascending aorta was 5 percent lower than the baseline visit. Besides, the spatial extent of high mechanical stresses in the inner wall was greater than visit 1. The magnitude of maximum von-Mises stress corresponding to the aortic sinus was unchanged between visits. Lower stresses were obtained between the left coronary and posterior sinus for visit 3. The region of high mechanical stress on the outer wall of the ascending aorta in the proximity of the IA was not observed for the first visit.

For the baseline visit corresponding to TS-2, highest mechanical stress (0.26 MPa) was observed in the right lateral wall of the transverse aortic arch. The maximum von-Mises stress in the inner wall of the ascending aorta was 9 percent lower than the corresponding value for TS-1. Besides, the stress in the inner wall was concentrated in the proximity of the STJ. Moreover, the peak mechanical stresses in the aortic root were 18 percent lower than the same obtained for TS-1. For the follow-up visit, the maximum von-Mises stress (0.29 MPa) occurred at the STJ. The corresponding value in the transverse aorta was 15 percent lower than the baseline visit.

Furthermore, the spatial extents of high mechanical stress in the transverse aorta were higher for visit 1. As compared to the first visit, significantly higher stresses were observed in the aortic root for the third visit. The peak von-Mises stress in the inner wall of the ascending aorta (0.22 MPa) for visit 3 was comparable to the values obtained for TS-1. The spatial extents of high mechanical stresses in this location were greater for the follow-up visit.

The 'decoupled' 2-way FSI methodology proposed in this section has several advantages: a) The proposed methodology does not require a specialized FSI communication interface like the MFX or System-Coupling coupling codes described in Chapter 2, 5, 7, 8 and 9 or the Mesh Based Parallel Code Coupling Interface (MPCCI) employed previously to communicate between ANSYS Fluent and ABAQUS for FSI simulations of aortic blood flow [188, 190]. b) The approach enables computation of vessel wall displacements using a structural solver (i.e. ABAQUS) that has several built-in and user-defined isotropic and anisotropic hyperelastic constitutive laws [61, 205], specifically developed to model the biomechanical response of the aorta wall. c) Remeshing of the flow domain following exchange of the deformed interface does not require the dynamic mesh motion option in ANSYS Fluent. d) Computational costs are lower than the fully coupled method (approximately 50 percent lower pre-processing and solution time on a workstation computer). Limitations of the proposed methodology include: a) The proposed method has been currently tested for small to moderate displacements of the aorta wall (1 to 2 mm). b) The approach is currently applicable for shell elements employed to model the aorta wall. c) The method necessitates node-to-node matching of the vessel wall and lumen grids at the FSI interface. Notwithstanding the aforementioned limitations, the decoupled methodology could be potentially employed for analysis of large patient datasets. Additionally, the employment of

the ABAQUS structural solver would enable a sensitivity analysis in a future study involving the choice of vascular material model on the 3D distribution of von-Mises stress [205].

10.2 *Transient 2-way FSI simulations of Aortic Blood Flow*

This section describes 2-way FSI simulations of transient aortic blood flow for 1 TS patient using subject specific inflow conditions derived using phase-contrast MR images.

10.2.1 *Methods*

A TS patient with tricuspid insufficiency and hypertension was selected for this analysis. Static, diastolic MR and phase contrast MR image acquisition, reconstruction of the aorta geometry and mesh generation for the flow and solid domains have been described for this subject in Section 9.3. 4D MR images were processed using the GTFlow software to compute the temporally varying flow in the ascending aorta. The length of the cardiac cycle was 0.5 s and the flow profile was approximated by a series of sine-functions. Blood was assumed to behave as a Newtonian fluid with a density of 1060 kg/m^3 and dynamic viscosity of 0.0035 Pa-s. Transient simulations were performed for a cardiac pressure of 140/90 mmHg (systole/diastole). A time varying velocity boundary condition was applied at the inlet face below the sinus assuming a flat profile [208]. Transient CFD simulations of aortic blood flow have been performed using several outflow boundary conditions including: a) Windkessel model at all outlets b) Windkessel model at supra-aortic vessel outlets and subject-specific pressure waveform in the descending aortic outlet c) Subject-specific mass-flow and pressure waveforms corresponding to the branch outlets and descending aortic outlets respectively d) Subject-specific mass-flow and zero static pressure corresponding to the branch outlets and descending aortic outlets respectively e) Zero static pressure at all outlets [59, 237]. Transient FSI simulations of blood flow in the abdominal aorta have been performed previously using a time-varying pressure outlet [245] and the same was

employed in the present study. The temporally varying pressure profile (Fig. 10.6) was applied at the branch vessel and descending aortic outlets using a user-defined function (UDF).

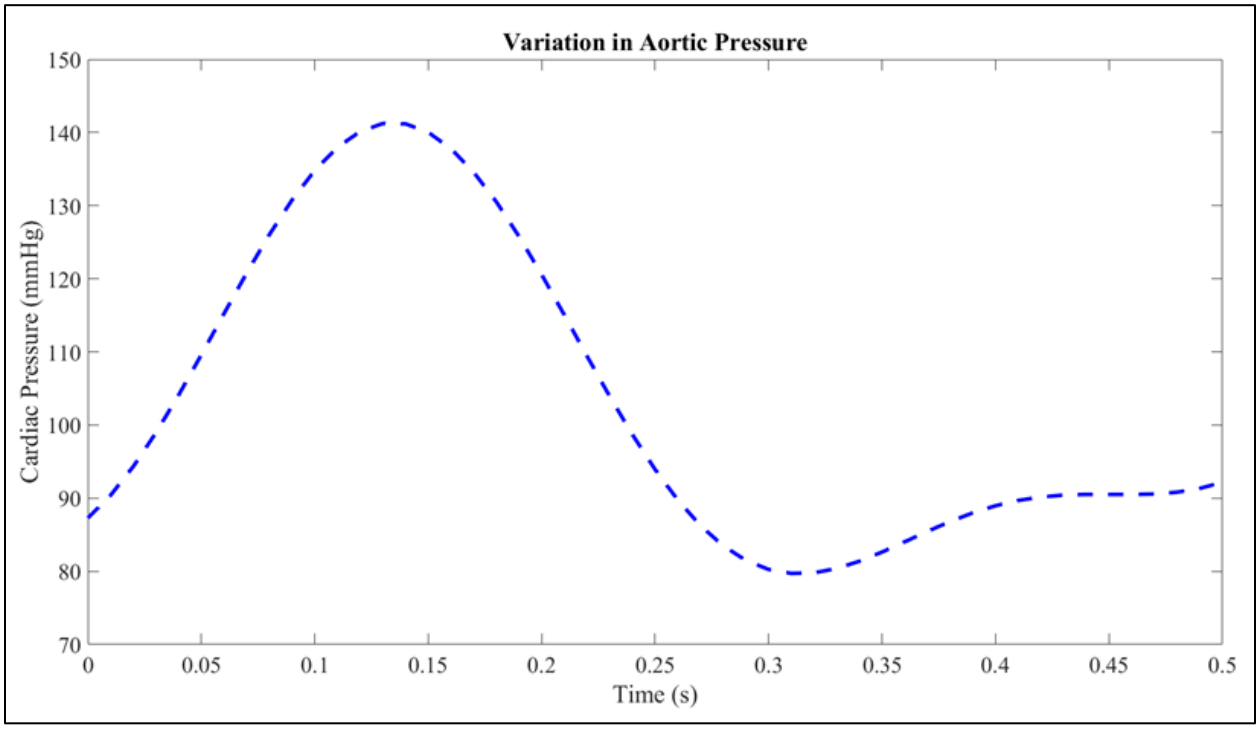

Figure 10.6: Temporally varying aortic pressure profile employed in transient FSI simulations.

The unsteady Navier-Stokes equations were discretized using a second order upwind scheme for the momentum terms. Pressure-velocity coupling was achieved using the Pressure Implicit Splitting Operator (PISO). The PREssure STaggering Option (PRESTO!) scheme was adopted for pressure interpolation at cell faces to enhance convergence and minimize numerical diffusion [188]. Gradients were evaluated using a least squares approach. The vessel wall was modeled using the nearly incompressible Arruda-Boyce material model with a density equivalent to 1040 kg/m^3 and an initial shear modulus corresponding to 1.05 MPa [242]. The limiting network stretch was 1.01 [68] and 1.7 mm wall thickness was assumed in this study [190]. A fixed boundary condition was assigned to the inlet and outlets. An implicit time stepping for the flow solver enabled a larger time step (0.01 s) as described in Chapter 5. 2-way FSI simulations

were performed for one full cardiac cycle using the ANSYS Multiphysics software. The System Coupling code described in Chapter 2, 5 and 9 was employed to communicate fluid forces and structural displacements between ANSYS Fluent and ANSYS Mechanical. The mesh for the flow domain was smoothed using a diffusion-based scheme. The grid was remeshed in every coupling step to minimize the possibility of highly skewed cells. Biomechanical and hemodynamic variables were post-processed using VisIt and Paraview.

10.2.2 *Results and Discussion*

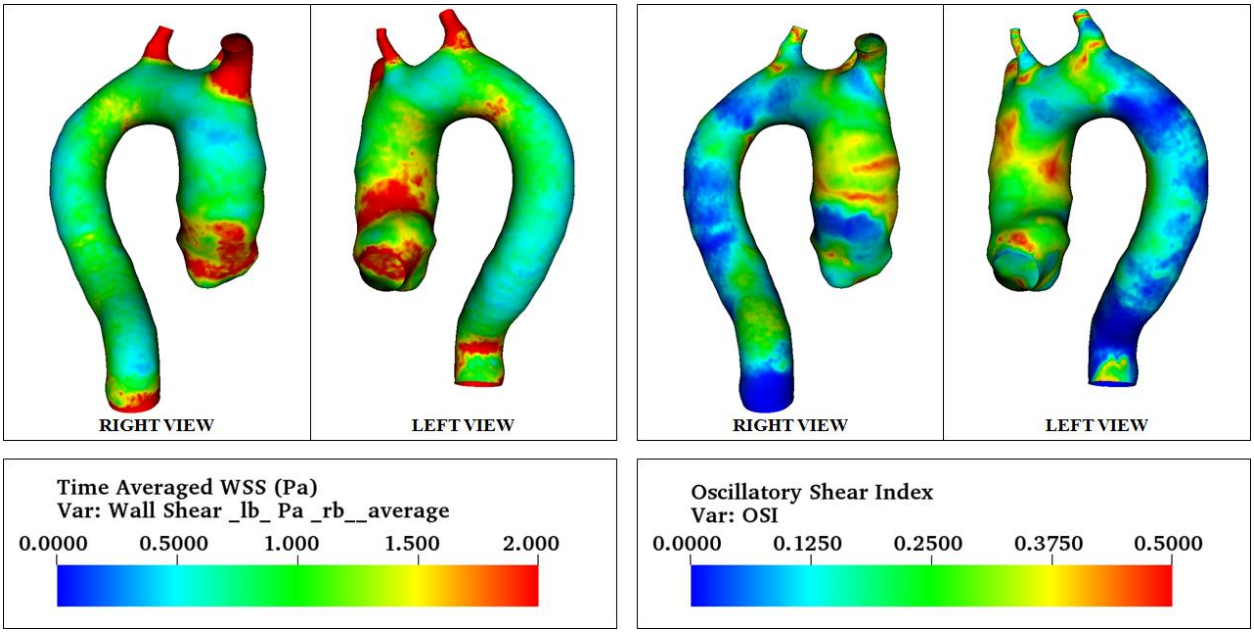

Figure 10.7: Contour maps of time-averaged WSS (TAWSS) and oscillatory shear index (OSI).

The shear stress averaged over one cardiac cycle (i.e. time-averaged wall shear stress (WSS)) was computed in Paraview (Fig. 10.7) and is given by [246],

$$\mathrm{TAWSS} = \frac{1}{T}\int_0^T \left|\overrightarrow{\mathrm{WSS}}\right| dt \qquad (10.1)$$

The centerlines for the aorta wall corresponding to the flow domain were then computed and the aorta was subdivided into its constituent branches using VMTK [240] for statistical analysis. The maximum TAWSS in the ascending aorta (2.7 Pa) was observed at the sinotubular junction. The

same in the transverse aorta was obtained on the right lateral wall and was 30 percent lower than the ascending segment. For the descending aorta, the maximum TAWSS occurred on the outer wall at the diaphragm and was 26 percent higher than the ascending aorta. The mean TAWSS for the descending and transverse sections was comparable (0.9 Pa) and was 35 percent lower than the ascending aorta. Furthermore, the peak systolic wall shear stresses for this subject in the ascending and descending aortas were 270 and 310 percent higher respectively than the corresponding values of TAWSS. These differences were consistent with previous studies involving 4D MR imaging of aortic blood flow in subjects with and without ascending aortic dilatation [247]. Additionally, the spatial location of the maximum WSS was different for the ascending aorta (STJ – unsteady flow, outer wall of ascending aorta – quasi-steady flow). Moreover, distribution of TAWSS in the sinus and inner wall of the ascending aorta reported in the present study (Fig. 10.7), was also obtained from CFD simulations of aortic blood flow in Marfan syndrome [187]. These observations further emphasize the importance of evaluating subject-specific 3D distribution of instantaneous and temporally averaged WSS, since shear stress influences growth and remodeling of the aortic wall as discussed in Chapters 8 and 9. The oscillatory shear index (OSI) is a measure of the difference between the magnitude and direction of the wall shear stress vector and is defined as follows [246],

$$\mathrm{OSI} = 0.5 \times \left(1 - \frac{\left| \int_0^T \overrightarrow{\mathrm{WSS}} dt \right|}{\int_0^T \left| \overrightarrow{\mathrm{WSS}} \right| dt} \right) \tag{10.2}$$

OSI was also evaluated using Paraview (Fig. 10.7) and a statistical analysis for the individual vascular segments was performed by subdividing the aorta geometry. The peak OSI (0.49) was identical for the ascending, transverse and descending segments. The same was obtained in the

inner wall midway in the ascending aorta, left lateral wall of the transverse aorta and inner wall of the descending aorta downstream of the aortic arch. The mean OSI was largest in the ascending aorta (0.25) and least in the descending section (0.11). The same for the transverse aorta was the average of the mean OSI values corresponding to the ascending and descending aorta. OSI has been described previously to impact endothelial cell function and subsequently influence progressive dilatation of the ascending aorta [212].

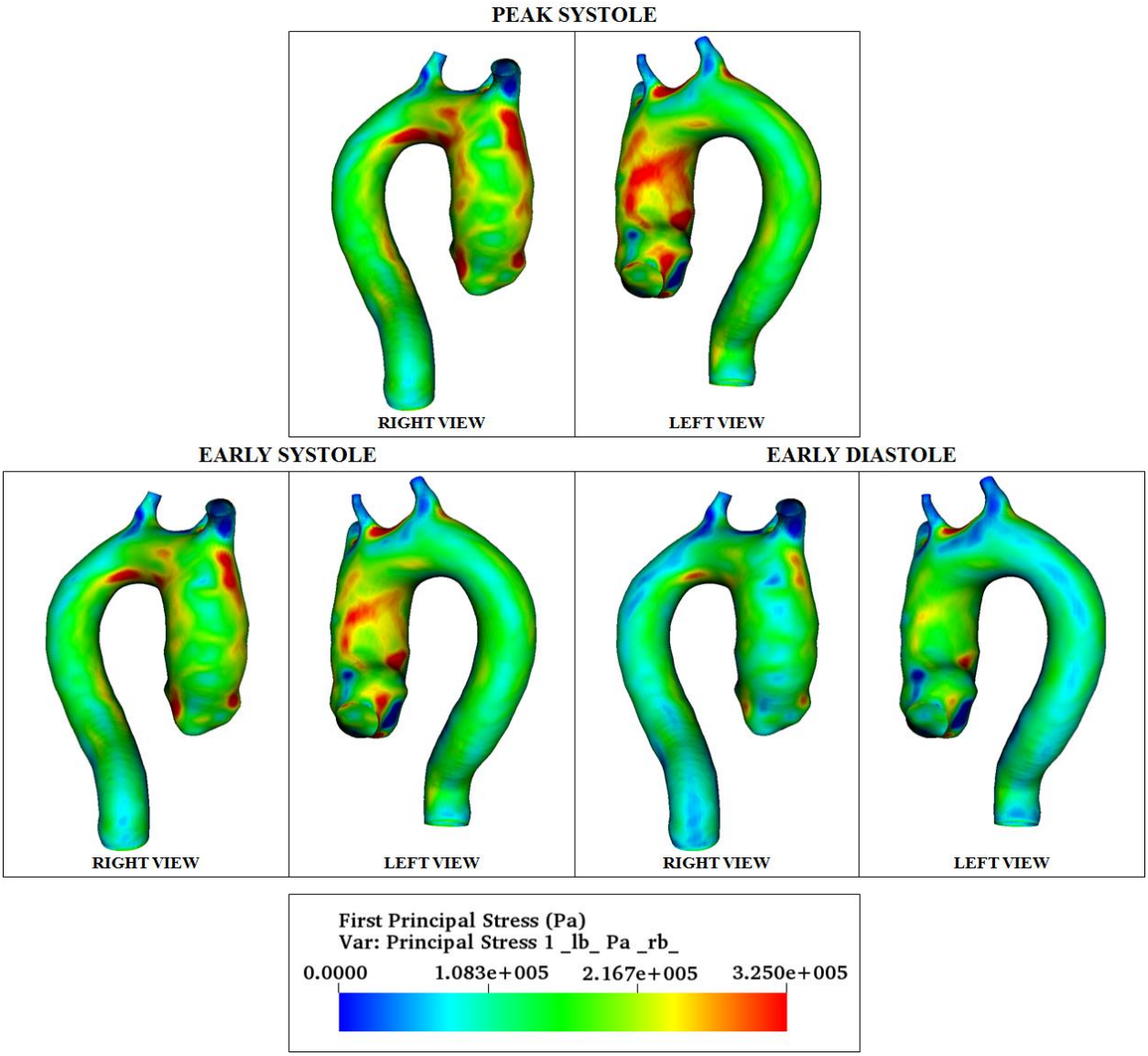

Figure 10.8: Contour maps of the first principal stress for early systole, peak systole and early diastole.

The first or maximum principal stress has been employed previously as a measure of fatigue damage to cardiac tissue under cyclic loading conditions [248] and the temporal variation of the same was evaluated in this study. Figure 10.8 describes the 3D distribution of the maximum principal stress in the aorta wall at three time points in the cardiac cycle: a) early systole b) peak systole c) late systole or early diastole. The maximum mechanical stress in the ascending aorta was observed in the proximity of the posterior sinus on the inner wall. The same for the transverse and descending aortas were obtained between the LCCA and LSCA and at the end of the aortic arch respectively. The spatial location of the maximum principal stress in the ascending, descending and transverse aortas were identical over the complete cardiac cycle. The peak value of the mechanical stress during early systole in the ascending (0.46 MPa), transverse (0.5 MPa) and descending (0.39 MPa) aortas increased by 11 percent at peak systole. The same decreased by 23 percent during early diastole. High mechanical stresses during systole were distributed throughout the inner wall of the ascending aorta, on the outer wall at the STJ and in the proximity of the innominate artery. The mechanical stress distribution was qualitatively similar to the same obtained from quasi-steady peak systolic simulations of aortic blood flow described previously in Chapter 9.3. Although the first principal stress has been employed previously to assess the durability of bio-prosthetic valves, cyclic variations in this stress measure could be potentially suitable in evaluating the risk of dissection of the vessel wall [190] over time. However, this would necessitate introduction of stress-softening terms and FSI modeling for multiple cardiac cycles. Although the simulation required 72 hours on a workstation with 128GB RAM, 3 cycles would have to be simulated to ensure periodicity [187]. High TAWSS in the supra-aortic vessels and low OSI in the descending aorta observed in Fig. 10.5 have also been reported in a recent CFD study of aortic blood flow involving static-pressure

outlet boundary conditions [237]. Recognizing the limitations of static pressure outlet boundary conditions in accurately predicting flow patterns in the thoracic aorta [237], the pilot FSI analysis presented in this section would be significantly enhanced in a future study by employing either Windkessel models or combined mass outflow (for the branch vessels) and static pressure outlet (for the descending aorta) boundary conditions [187]. The study would also have to be suitably modified to firstly evaluate the 'zero pressure' geometry [55] and subsequently compute the pre-stressed configuration of the vessel wall [206] prior to FSI analysis.

10.3 *Influence of Blood Rheology and Vessel Wall Thickness*

This section describes constant velocity 2-way FSI simulations of aortic blood flow for 3 aortic phenotypes observed in TS, using a non-Newtonian rheological model for blood and vessel wall thickness that varies continuously along the aorta length.

10.3.1 *Methods*

Clinical cardiac magnetic resonance imaging was performed on 3 Turner syndrome patients with the following aortic anomalies: Patient 1 - ascending aortic dilatation, Patient 2 - elongated transverse aorta, Patient 3 - coarctation. Static diastolic images were acquired on a 1.5T MRI scanner using a 8-channel cardiac coil at the Cincinnati Children's Hospital medical center [58]. Three-dimensional geometries of the thoracic aorta including the root were identified using a thresholding algorithm in Mimics. Centerlines for the smoothed aortic geometries were computed using VMTK and flow extensions were generated for the individual aortas as described previously. The flow-extensions were merged using Mimics and the geometries were exported in STL format for computational FSI modeling. The aorta lumen was discretized using a centerlines-based grid generation algorithm available in VMTK (Chapter 7-10). Approximately 3 million tetrahedral cells were employed for all the patients considered in this analysis. Blood

was modeled as incompressible, non-Newtonian and the Carreau-Yassuda model was employed to compute the viscosity of blood [249],

$$\mu(\gamma) = \mu_\infty + (\mu_0 - \mu_\infty)\left[1 + (\gamma\lambda)^2\right]^{(n-1)/2} \qquad (10.3)$$

where μ_∞ = 0.0035 Pa-s is the infinite shear rate, μ_0 = 0.056 Pa-s is the viscosity at zero shear, λ = 3.313 s is the relaxation-time and γ = 0.3568 is the power index [249]. The density of blood was 1060 kg/m^3. The influence of the non-Newtonian rheology was evaluated by comparing hemodynamic variables with the same obtained using the Newtonian assumption. It should be noted that for the Newtonian model, the dynamic viscosity of blood was 0.0035 Pa-s. Constant velocity flow computations [186, 190] were performed for a mean cardiac output corresponding to 5 liters per minute [191]. A flow boundary condition was defined at the inlet assuming a flat velocity profile and 85 percent of the flow was assumed to exit from the descending aorta [58]. The turbulence intensity was set to 2 percent and a 1 mm length scale was assumed. Static pressure corresponding to the pulse pressure was prescribed at the branch outlets [59]. The value was based on cardiac pressure measurements performed previously in female subjects [192]. Accordingly, a pulse pressure equivalent to 55 mmHg was employed for the three TS patients. Combined pressure and outflow boundary conditions have been adopted previously to model aortic blood flow in Marfan syndrome [187] and in thoraco-abdominal aortic aneurysms prior to and following elephant trunk repair surgery [188]. A high resolution advection scheme and turbulence numerics were chosen [187].

An in-house code based on VMTK and GMSH [128] was developed to model the aorta wall thickness as a function of the locally varying aorta diameter [221]. The local wall thickness was assumed to be approximately 7 percent of the local lumen caliber [221] and tetrahedral cells for the vessel wall were generated using GMSH. The influence of variation in vessel wall

thickness along the aorta length was evaluated by comparing mechanical variables for this case with the same obtained for FSI simulations involving a constant aorta wall thickness. For the latter case, the discretized surface geometry of the aorta wall was imported into ANSYS T-Grid (ANSYS Inc., Canonsburg, PA) mesh generation software. Triangular elements were extruded outward by 1 mm [65, 66] to generate prism elements for the vessel wall. The prism elements were then recombined into tetrahedral cells using ANSYS ICEM-CFD. This step enabled comparison between the constant and variable wall thickness structural models. The vessel wall was modeled using the nearly incompressible Arruda-Boyce constitutive law with an initial shear modulus corresponding to 1 MPa [242] and limiting network stretch equivalent to 1.01 [68]. The inlet and outlets were constrained in all directions [65, 66] to ensure that the resulting aortic displacements are physiological [190].

Parallel, 2-way FSI simulations were performed using the ANSYS multiphysics software (Ansys Inc., Canonsburg, PA) [84, 197]. An FSI boundary condition was applied at the interface between the flow and structural domains [79]. In order to maintain this aforementioned condition throughout the simulation, the lumen mesh was moved using the Arbitrary-Lagrangian Eulerian approach [67]. The mesh for the flow domain was updated using a displacement diffusion scheme [79]. The coupling data transfer control was set at 0.01 with an under relaxation factor equal to unity. Interpolation of flow-induced forces was not required during data exchange for each coupling step since the nodes for the fluid and solid domain were aligned at the FSI interface. Blood flow in the compliant aorta was modeled as quasi-steady [190] with data-exchange between the ANSYS CFX flow and ANSYS Mechanical structural solvers occurring for a total simulation time of 1s, which is approximately the length of a cardiac cycle. Flow and biomechanical solution variables were post-processed using Paraview, VMTK and VisIt.

10.3.2 *Results and Discussion*

Figure 10.9 compares the 3D distribution of aorta wall shear stress for the 3 TS patients, corresponding to the two rheological models. For the subject with the dilated ascending aorta, shear stresses were distributed along the length of the descending aorta and the maximum WSS was observed at the end of the aortic arch. The magnitude of peak WSS for the Carreau model (2.6 Pa) was 13 percent higher than the same for the Newtonian model. Regions of low WSS in the ascending aorta were observed in the inner wall and in the aortic root. A region of low shear surrounded by a region of high shear stress was observed on the outer wall of the ascending aorta. The maximum shear stress in the ascending section occurred on the right wall in the proximity of the innominate artery. The magnitude of the same was 10 percent lower for the Newtonian model. Maximum shear stress in the transverse aorta for the Newtonian model was 11 percent higher than the corresponding value for the Carreau-Yassuda model. The lower shear for the non-Newtonian model could be potentially attributed to lower blood flow velocity in the transverse section resulting from larger displacements for the variable vessel wall thickness structural model. For the patient with elongated transverse aorta, maximum shear stress was obtained on the outer wall of the transverse aorta, between the LCCA and LSCA. The maximum value for the Newtonian model (4.6 Pa) was comparable (< 5 percent difference) to the same for the non-Newtonian case. Additionally, high shear stress was distributed downstream of the LSCA in the descending section. The peak value of the descending aortic WSS for the Carreau model (4 Pa) was 14 percent higher than the Newtonian case. Maximum WSS in the ascending aorta occurred in the right wall in the proximity of the IA for both rheological models. The magnitude of the same was 32 percent higher for the non-Newtonian model. As compared to the patient with dilatation, shear stresses were distributed on the inner and outer walls of the

ascending aorta. In a manner similar to the first patient, the sinus was characterized by low WSS. For the patient with coarctation, the maximum shear stress occurred in the outer wall of the stenosis in the descending aorta. The magnitude of the same was 15 percent higher for the Carreau model. The spatial extent of the low shear region downstream of the coarctation was smaller for the Newtonian case. For the transverse aorta, maximum WSS was observed on the left lateral wall for both rheological models. The magnitude of the same was comparable (<5 percent difference) for the Newtonian (5.9 Pa) and non-Newtonian (6.2 Pa) cases. Similar to the patient with ETA, the sinus was characterized by low shear. Shear stresses were distributed on the inner and outer walls of the ascending aorta above the STJ. The maximum ascending aortic WSS occurred on the inner wall in the proximity of the IA and the magnitude was comparable for the Carreau-Yassuda and Newtonian models. Higher WSS for non-Newtonian rheological models has been reported previously for steady CFD simulations of aortic blood flow in healthy controls [211] and patients with thoracic aortic aneurysms [249]. The mean WSS for the ascending, transverse and descending sections corresponding to the two rheological models is indicated in Table 10.1.

Table 10.1: Average ascending, transverse and descending aortic wall shear stress corresponding to Newtonian and Carreau models.

Patient	Wall Shear Stress (Pa)					
	Newtonian			Carreau-Yassuda		
	Ascending	Transverse	Descending	Ascending	Transverse	Descending
Dilated	0.4	1	0.9	0.6	0.6	1
ETA	0.8	1.8	1	1	1.9	1.1
CoA	0.8	2.3	1.9	0.9	2.4	2

Figure 10.10 compares the 3D distribution of mechanical stress for the 3 TS patients, corresponding to the constant and variable wall thickness structural models. For the subject with

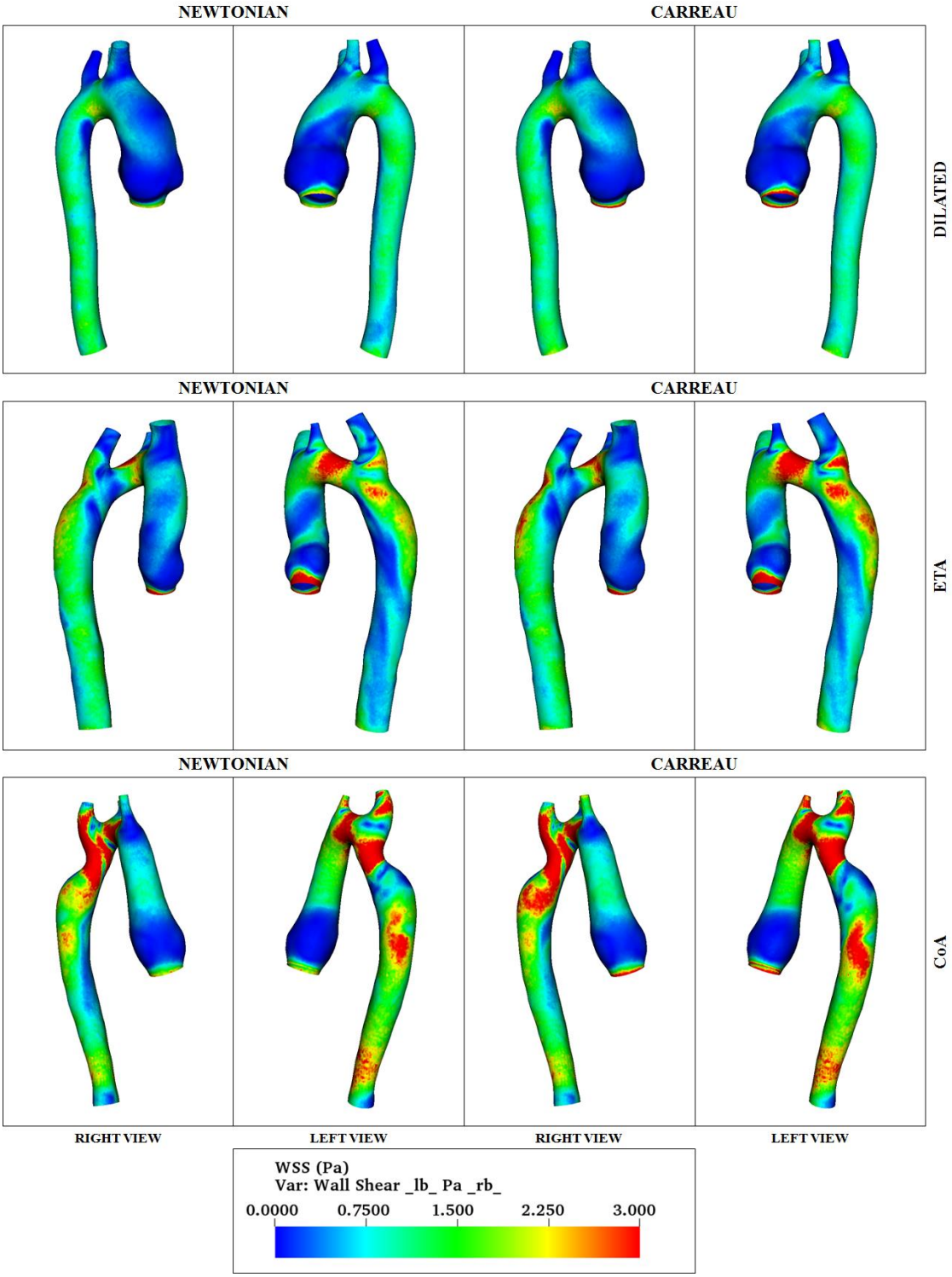

Figure 10.9: 3D contour maps of wall shear stress for dilated, ETA and CoA TS subjects corresponding to the Newtonian and non-Newtonian models.

the dilated ascending aorta, the maximum von-Mises stress occurred in the outer wall of the transverse aorta between the LCCA and LSCA. The magnitude of the peak mechanical stress for the variable wall thickness model (0.66 MPa) was 47 percent higher than the corresponding value for the constant wall thickness assumption. High mechanical stresses were distributed in the inner wall of the ascending aorta and the maximum ascending aortic mechanical stress was obtained in the proximity of the IA. The magnitude of the same for the constant wall thickness model was 6 percent lower than the corresponding value for the variable wall thickness case. Stresses were concentrated at the end of the aortic arch for both models and the maximum descending aortic mechanical stress for the variable wall thickness case was obtained at this location. Furthermore, stress concentration between the coronary sinuses occurred in the constant vessel wall thickness model. For the constant wall thickness model, the peak descending aortic von-Mises stress occurred on the outer wall downstream of the LSCA and the magnitude (0.25 MPa) was 21 percent lower than the same for the variable wall thickness case. Moreover, the high stress distribution in the outer wall, downstream of the end of the aortic arch was observed for the variable wall thickness model. For the subject with ETA, the maximum mechanical stress was obtained in the transverse aorta between the LCCA and LSCA, in a manner similar to the patient with aortic dilatation. The peak magnitude corresponding to the variable wall thickness case (0.49 MPa) was 48 percent higher than the corresponding value for the constant wall thickness assumption. Similar to the first patient, high stresses were distributed in the inner wall of the ascending aorta and the peak ascending aortic von-Mises stress was obtained in the proximity of the IA. The magnitude of the same for the variable wall thickness assumption (0.36 MPa) was 50 percent higher than the constant wall thickness model. In the descending aorta,

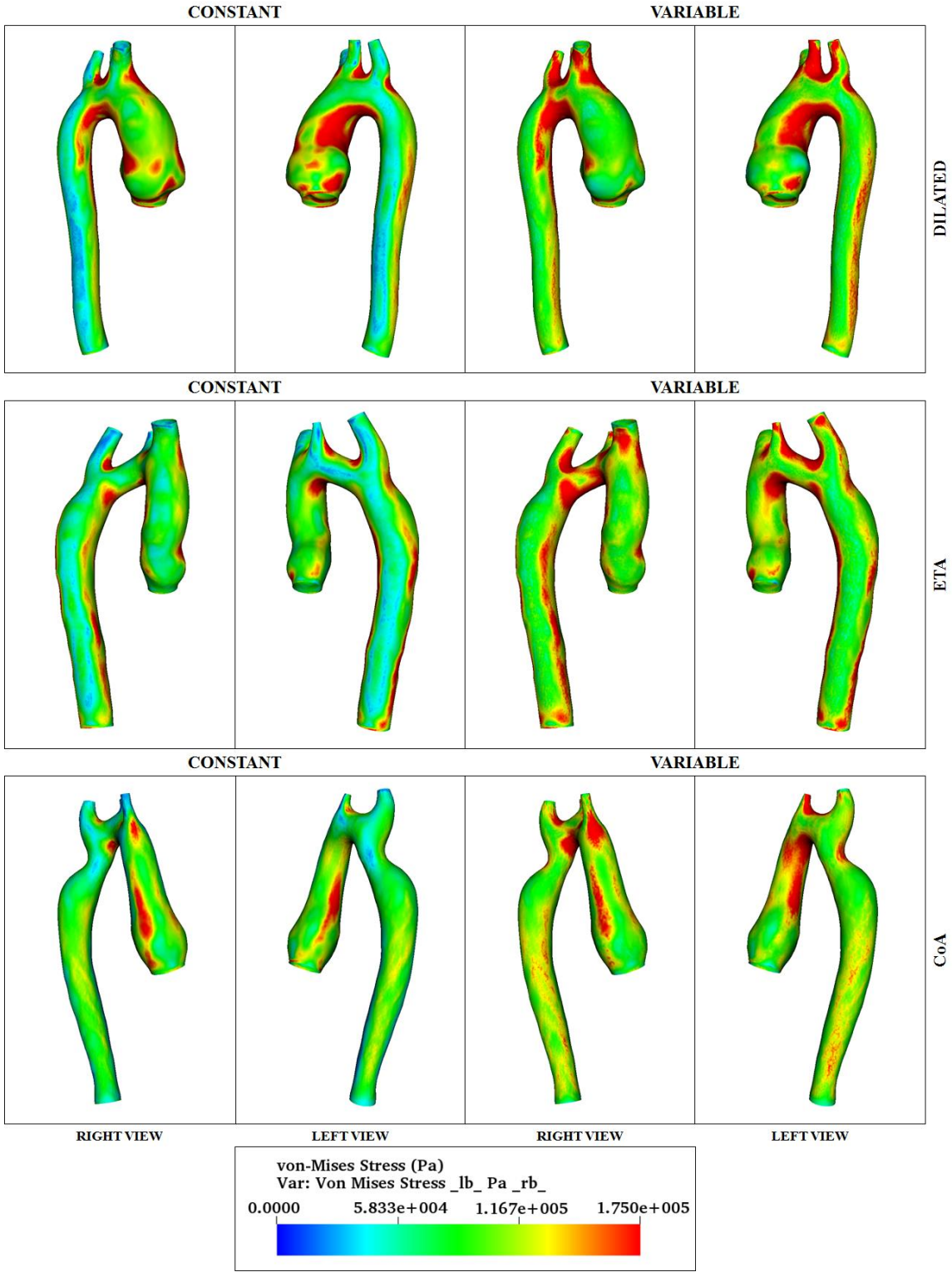

Figure 10.10: 3D contour maps of von-Mises stress for dilated, ETA and CoA TS subjects corresponding to a constant and variable wall thickness.

mechanical stress concentration was obtained throughout the inner wall from the end of the aortic arch to the descending aortic outlet. The peak value was obtained midway for both structural models. The magnitude of the same was 49 percent lower for the constant vessel wall thickness case. For the patient with coarctation, the maximum mechanical stress for the constant wall thickness case (0.25 MPa) was obtained in the inner wall of the ascending aorta proximal to the STJ. The same for the variable wall thickness occurred in the inner wall at the end of the aortic arch and was 28 percent higher than the constant wall thickness assumption. As compared to subjects with dilatation and ETA, higher stresses were observed on the outer wall of the ascending aorta for the subject with CoA. For the variable thickness model, stresses were distributed throughout the inner wall of the ascending aorta. The maximum magnitude of the ascending aortic stress for this model was 12 percent higher than the constant wall thickness assumption. The spatial location of peak ascending aortic stress was identical for both structural models. For the constant wall thickness model, the stress magnitude at the end of the aortic arch was 35 percent lower than the variable thickness case. The peak von-Mises stress in the descending section was obtained midway on the outer wall for both models. The stress magnitude for the constant wall thickness case at this location was 30 percent lower than the variable thickness model. Mechanical stress concentration observed at the coarctation for the variable thickness model, was not obtained for the constant wall thickness case. The mean von-Mises stress for the ascending, transverse and descending sections corresponding to the two models is indicated in Table 10.2. High mechanical stresses in the supra-aortic vessels were observed for the variable wall thickness models corresponding to all subjects analyzed in this study. Difference in stress distribution for the structural models was in good agreement with the same observed for subjects with descending thoracic aortic aneurysms [250]. Incorporation of

patient-specific anisotropic mechanical properties of the vessel wall, subject specific vessel wall thickness obtained from CT [250] and inclusion of supporting tissue elasticity in the structural model would significantly enhance the presented analysis. The flow model would be improved in a future study by performing simulations for peak systole and employing the outlet boundary conditions described in Sections 9.2, 9.3 and 10.1. A future study would also include control subjects and additional aortic phenotypes observed in TS.

Table 10.2: Average ascending, transverse and descending aortic von-Mises stress corresponding to constant and variable wall thickness models.

Patient	von-Mises Stress (MPa)					
	Constant Wall Thickness			Variable Wall Thickness		
	Ascending	Transverse	Descending	Ascending	Transverse	Descending
Dilated	0.13	0.15	0.08	0.12	0.2	0.11
ETA	0.1	0.11	0.1	0.12	0.17	0.12
CoA	0.09	0.09	0.07	0.11	0.15	0.11

10.4 *Summary*

- Longitudinal changes in thoracic aortic morphology for TS patients were evaluated using a novel continuous measurement method. Differences in aortic geometry including and excluding the aortic root for TS and controls were described using 3D distance maps.
- A quasi-steady, fully coupled FSI methodology was described for normotensive and hypertensive aortas using mixed pressure outlet and outflow boundary conditions, excluding the aortic root. The role of vessel wall elasticity on hemodynamic variables such as velocity, wall shear stress and helicity was discussed by comparing CFD and FSI simulations. The study was extended to compare the longitudinal change in hemodynamic and functional variables for TS patients.

- The influence of including the aortic sinus in the computational FSI model to identify regions in the aorta that were more vulnerable to progressive dilatation and vessel wall failure was described for mean flow conditions. Correlations between functional and geometric measures were evaluated.
- The proposed FSI methodology was employed for systolic flow simulations using subject-specific boundary conditions. The resulting flow patterns were compared with the same obtained from MR imaging. The methodology was utilized to iteratively compute the biomechanical properties of the descending aorta.
- An improved fully coupled, 2-way FSI methodology that employed pressure outlet boundary conditions based on the vascular resistances of the supra-aortic vessels and descending aorta was described for subjects with Type-A dissection. The proposed method was utilized to evaluate hemodynamic and biomechanical functional variables in TS and control subjects at peak systole, using subject-specific flow conditions derived from phase-contrast MR images.
- A decoupled 2-way FSI methodology was developed for constant velocity simulations of aortic blood flow at peak systole. The proposed method was utilized for longitudinal comparison of functional and geometric variables including the aortic sinus. Advantages and limitations of the proposed methodology were discussed.
- Transient, 2-way FSI simulations of aortic blood flow was presented for a hypertensive TS patient using subject-specific inflow conditions. Temporal changes in flow and mechanical variables were computed for a single cardiac cycle.
- The influence of blood rheology and variation in the thickness of the aortic wall on hemodynamic and biomechanical variables was assessed for mean flow conditions.

Chapter 11

Future Scope

For future work involving the upper airway project the following studies are proposed:

- Validation of virtual surgery geometries of the pharyngeal airway and supporting tissue using post-operative MR imaging.
- Inclusion of potential variations in tissue stiffness resulting from the surgery in the computational model.
- Analysis of additional controls and apneic patients with PCOS to estimate the biomechanical properties of the soft-palate using FSI and evaluating correlations between upper airway stiffness and clinical measures of OSA severity.
- Extending the fully-coupled quasi-steady FSI model presented in Chapter 5 to simulate the complete breathing cycle and evaluating temporal variations in the pre and post-operative displacements of the soft-palate.
- Inclusion of the tongue, epiglottis, lateral wall tissue, adenoids and posterior wall mucosa in the structural domain corresponding to the fully-coupled FSI model.
- Including neuromuscular response of airway tissue in the computational model.

For future work involving the aorta project the following studies are proposed:

- Inclusion of lumped parameter resistance boundary conditions at the supra-aortic vessel outlets and descending aortic outlet to model resistance of arteries downstream of the branch vessels and the abdominal aorta.

- Analysis of additional controls and TS patients using the decoupled 2-way FSI approach described in Chapter 10 using subject specific division of cardiac output derived from phase-contrast MR imaging.
- Comparison of arterial displacements and von-Mises stress obtained using the Arruda-Boyce model with the same obtained using isotropic arterial wall biomechanical models such as Raghavan-Vorp and Demiray that can be directly incorporated in the Abaqus software as user-defined materials.
- Inclusion of different isotropic mechanical properties for the inner and outer wall to evaluate the von-Mises stress at the interface between the adventia, media and intima.
- Evaluating mechanical properties of the aortic wall using the coupled or decoupled FSI methodologies and the average or patient-specific distensibility obtained using MR imaging.
- Pulsatile simulations of aortic blood flow for longitudinal comparison of flow and mechanical functional indices of cardiovascular disease in TS.

Appendix

Appendix A:

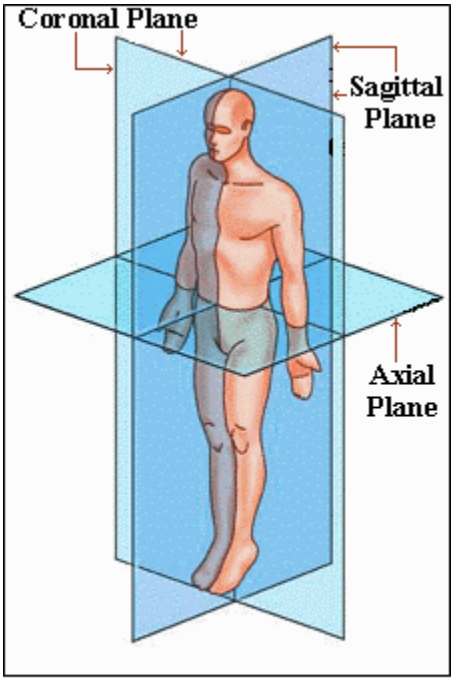

Source:
www.spineuniverse.com

Figure A.1: Anatomical plane definitions.

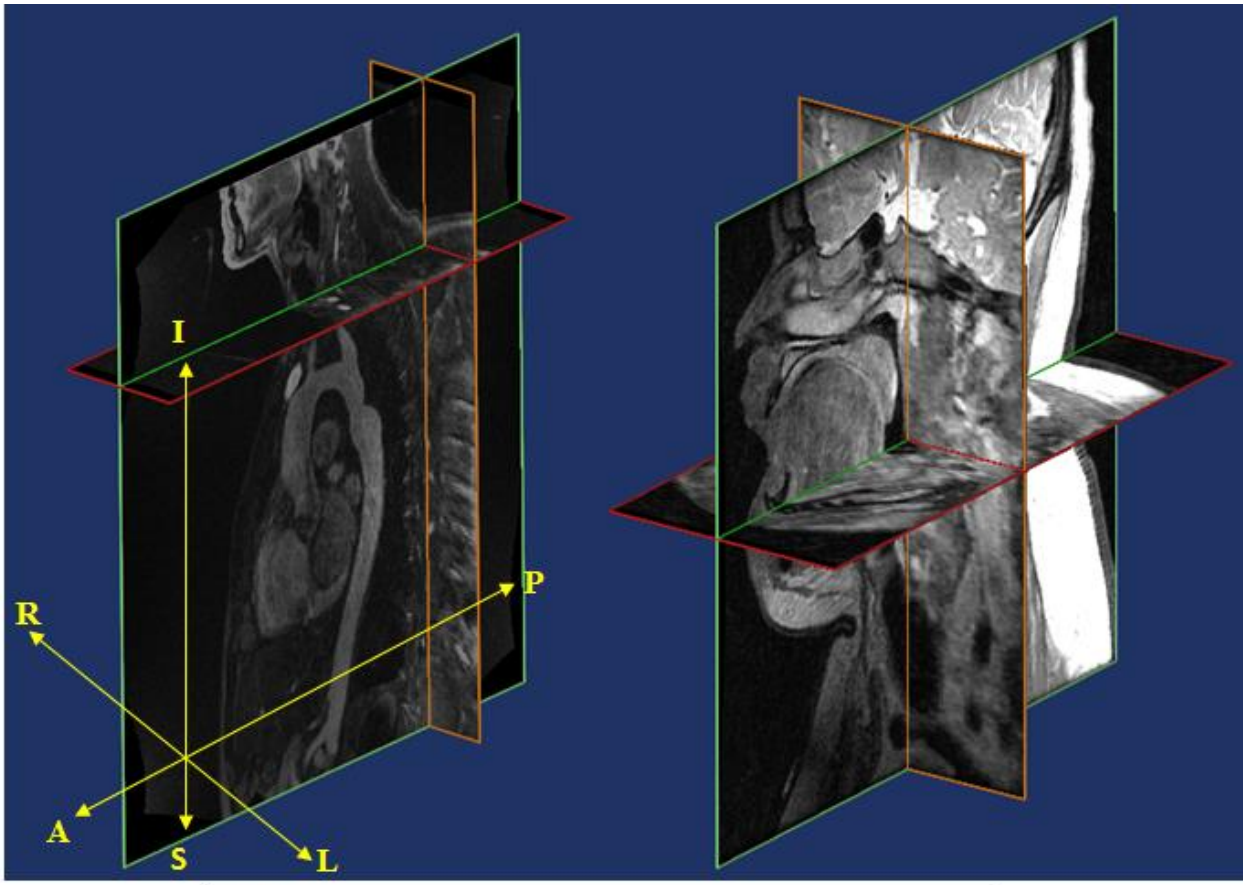

Note:
A-Anterior, P-Posterior, R-Right, L-Left, I-Inferior, S-Superior

Figure A.2: Anatomical directions indicated for MR images of the aorta and pharyngeal airway.

Appendix B:

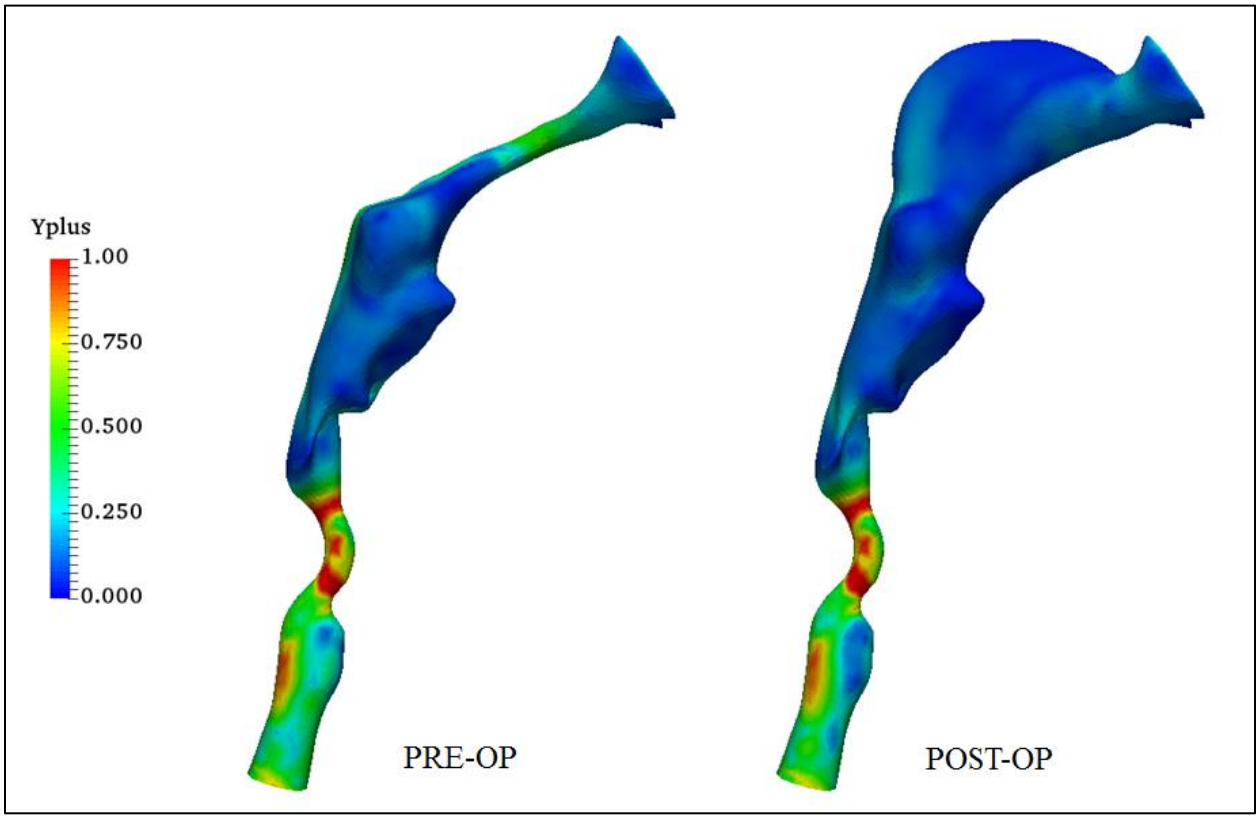

Figure B: Comparison of y+ distribution for pre and post-operative airways.

Appendix C:

Table C.1: Summary of patient clinical history for compliance estimation using tube-law (Note: Pressure (P_{crit}, CPAP1 and CPAP2) is in cm of water, 1 cm **of H_2O** ~ 100 Pa).

Patient No.	Age (years)	Gender	AHI	P_{crit}	CPAP1	CPAP2	OSA Severity (AHI Based)	OSA Severity (P_{crit} Based)
1	11	F	20.2	1.3	4	10	Severe	Severe
2	13	M	7.4	-1.7	3	6	Moderate	Moderate
3	17	M	8.2	-1.8	3	9	Moderate	Moderate
4	5	M	5	-11.6	4	8	Mild	Mild
5	3	M	6.8	-7.9	3	8	Moderate	Mild
6	5	F	13.1	6.6	8	15	Moderate	Severe
7	9	M	142.2	2	10	18	Severe	Severe
8	14	M	6.4	-4.3	3	7	Moderate	Moderate
9	4	M	9.3	-8.1	2	8	Moderate	Mild
10	7	M	8.7	1.3	7	12	Moderate	Severe
11	9	F	9.1	-3.8	4	6	Moderate	Moderate
12	3	F	5.9	-10	2	6	Moderate	Mild
13	10	M	4	-10.8	4	10	Mild	Mild
14	17	M	21.3	N/A	10	15	Severe	N/A
15	12	M	5.9	-0.2	4	8	Moderate	Moderate
16	9	M	6.1	7	10	14	Moderate	Severe

17	9	M	14.7	0.2	5	10	Severe	Severe
18	16	M	9.4	1.9	8	12	Moderate	Severe
19	8	M	7.5	-0.8	8	14	Moderate	Moderate
20	11	M	5.5	-8.4	5	10	Moderate	Mild
21	12	F	6.8	2.1	6	12	Moderate	Severe
22	12	M	13.8	-3.4	5	9	Moderate	Moderate

Table C.2: Summary of softest, narrowest locations in the pharyngeal airway.

Patient No.	Phenotype	S'_{soft} (Pa)	Location	$S'_{narrowest}$ (Pa)	Location
1	GROUP C	450	RG1	470	RG1
2	GROUP A	25	RG2	35	RG1
3	GROUP A	15	RG2	20	RG2
4	GROUP A	15	RG3	20	RG3
5	GROUP D	25	RG2	50	RG2
6	GROUP B	600	RP	695	RP
7	GROUP B	350	RP	1025	RG2
8	GROUP C	440	RP	950	RG1
9	GROUP C	220	RG1	220	RG1
10	GROUP C	220	RP	220	RP
11	GROUP B	150	RP	150	RP
12	GROUP A	625	RP	650	RP
13	GROUP A	1180	RP	3385	RG2
14	GROUP C	150	RP	185	RP
15	GROUP D	1000	RG1	1240	RP
16	GROUP D	380	RG2	630	RG2
17	GROUP D	35	RP	35	RP
18	GROUP D	30	RG2	30	RG2
19	GROUP D	220	RG1	900	RG2

20	GROUP A	160	RG2	420	RG2
21	GROUP A	60	RG2	60	RG2
22	GROUP B	270	RP	400	RG2

Table C.3: Summary of patient clinical history for compliance mapping study (Note: Pressure (P_{crit}, CPAP1 and CPAP2) is in cm of water, 1 cm **of H_2O** ~ 100 Pa).

Patient No.	Age (years)	Gender	AHI	BMI	P_{crit}	CPAP1	CPAP2
1	11	F	20.2	24.7	1.3	4	10
2	14	M	6.4	20.6	-4.3	3	7
3	4	M	9.3	20.4	-8.1	2	8
4	7	M	8.7	18.9	1.3	7	12
5	9	F	9.1	16.8	-3.8	4	6
6	3	F	5.9	22.1	-10	2	6
7	10	M	4	17.3	-10.8	4	10
8	17	M	21.3	30.5	N/A	10	15
9	12	M	5.9	27.1	-0.2	4	8
10	8	M	7.5	16.5	-0.8	8	14

Appendix D:

Table D.1: Summary of Turner syndrome clinical history (Note: Patient age corresponds to first visit. BAV – Bicuspid Aortic Valve, CoA – Coarctation, ETA – Elongated transverse aorta).

Patient	Age (years)	BAV	CoA	ETA
1	47	N	N	N
2	31	N	N	N
3	58	N	N	N
4	57	Y	N	N
5	38	N	N	Y
6	36	Y	N	Y
7	28	Y	Y	Y
8	38	Y	Y	Y
9	45	Y	N	Y
10	39	Y	Y	Y
11	25	Y	Y	Y
12	46	N	Y	N
13	40	N	Y	Y
14	42	N	Y	Y
15	44	N	Y	N

Table D.2: Passing-Bablok regression analysis comparing maximum aortic diameters obtained using manual and continuous methods (Note: Values in parenthesis indicate lower and upper bounds).

Visit	Intercept (95% CI)	Slope (95% CI)
1	4.01 (0.53 to 7.0)	0.85 (0.71 to 1)
2	0.48 (-3.59 to 3.82)	0.99 (0.85 to 1.16)
3	1.97 (-1.72 to 4.98)	0.97 (0.81 to 1.14)
All Visits	2.11 (0.14 to 4.09)	0.93 (0.84 to 1.02)

Table D.3: Summary of correlations of change between visits obtained using continuous and manual measurement methods (Note: F-test employed in all cases. F-value and corresponding critical value were compared in order to determine equivalence of the variances of change between visits obtained manually and continuously. For good concordance between methods test was performed to assess whether $F<F_{crit}$).

Case	F<Fcrit
Overall Visit 1 to 2	Y
Overall Visit 2 to 3	Y
Overall Visit 1 to 3	Y
Ascending Visit 1 to 2	Y
Ascending Visit 2 to 3	Y
Ascending Visit 1 to 3	Y
Transverse Visit 1 to 2	Y
Transverse Visit 2 to 3	N
Transverse Visit 1 to 3	Y
Descending Visit 1 to 2	N
Descending Visit 2 to 3	Y
Descending Visit 1 to 3	Y

Table D.4: Summary of Euclidean distance variation (mean ± standard deviation, mm) for the ascending and descending thoracic aorta in controls and TS (AA – Ascending Aorta, DA – Descending Aorta).

	Euclidean Distance	Controls	TS (Overall)	TS (V1)	TS (V2)	TS (V3)
AA	***Mean***	12.6 ± 1	13.4 ± 2.1	13.4 ± 2	13.4 ± 2.2	13.3 ± 2.3
	Maximum	14.8 ± 0.95	16.5 ± 2.7	16.8 ± 2.8	16.6 ± 2.8	16.1 ± 2.6
DA	***Mean***	9.5 ± 0.9	10.2 ± 1.3	10.3 ± 1.4	10.3 ± 1.4	10 ± 1.1
	Maximum	11.9 ± 1	13.2 ± 1.6	13.2 ± 1.5	13.4 ± 1.8	13 ± 1.5

Appendix E:

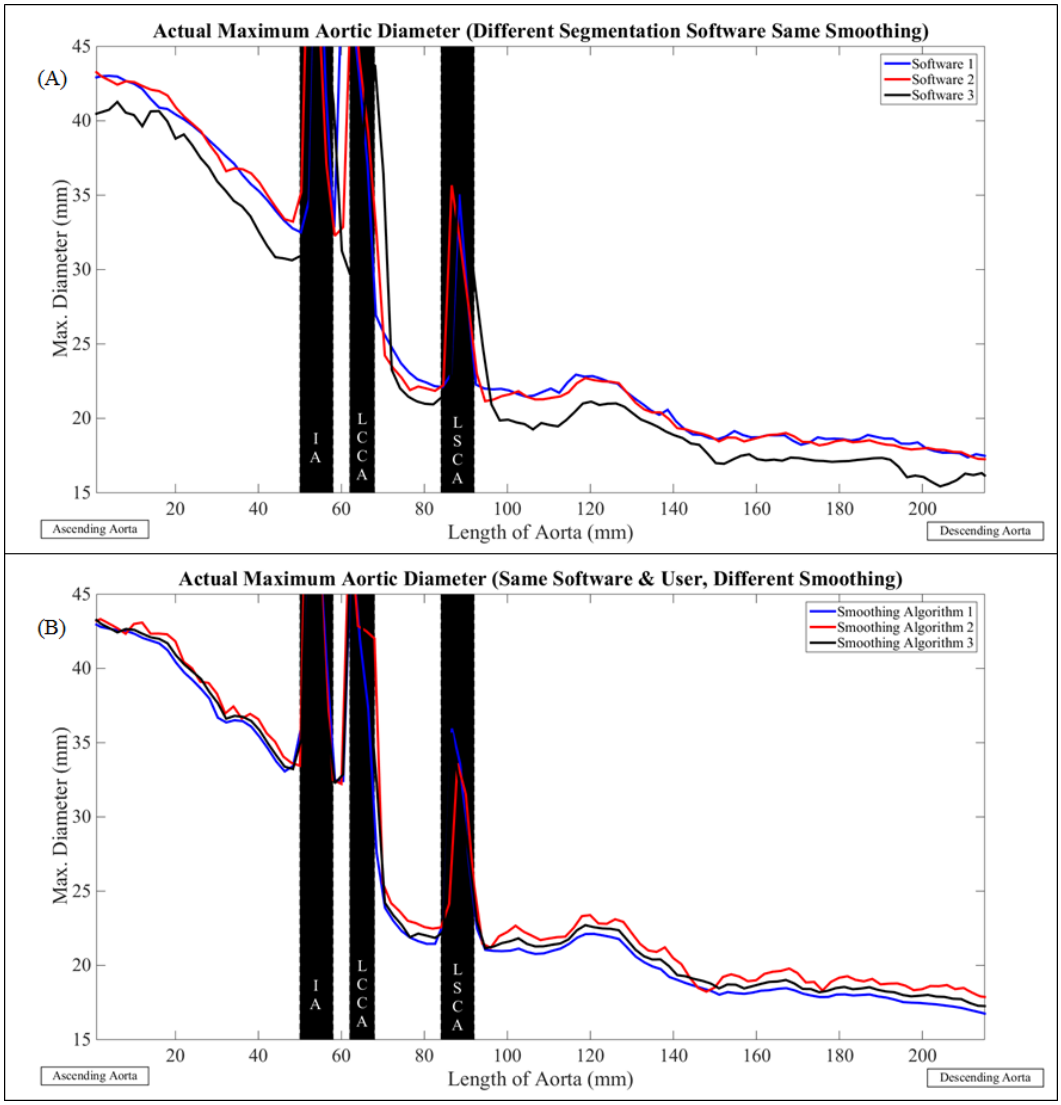

Figure E.1: Sensitivity of continuous measurements to choice of segmentation software and smoothing algorithm, exemplified for a subject with Turner syndrome (Subject 6). Figure 10A: Software 1 (solid blue line) – Mimics, Software 2 (solid red line) – ITK-Snap, Software 3 (solid black line) – 3D Slicer. Figure 10B: Smoothing Algorithm 1 (solid blue line) – C0 Smoothing, Smoothing Algorithm 2 (solid red line) – C1 Smoothing, Smoothing Algorithm 3 (solid black line) – Simple Smoothing. Aorta geometries were smoothed using OpenFlipper.

In order to evaluate the sensitivity of the continuous measurement methodology to the choice of segmentation software, the methodology was tested using both ITK-Snap [251] and 3D Slicer software (www.slicer.org) for identification of the aorta. The same threshold values were used

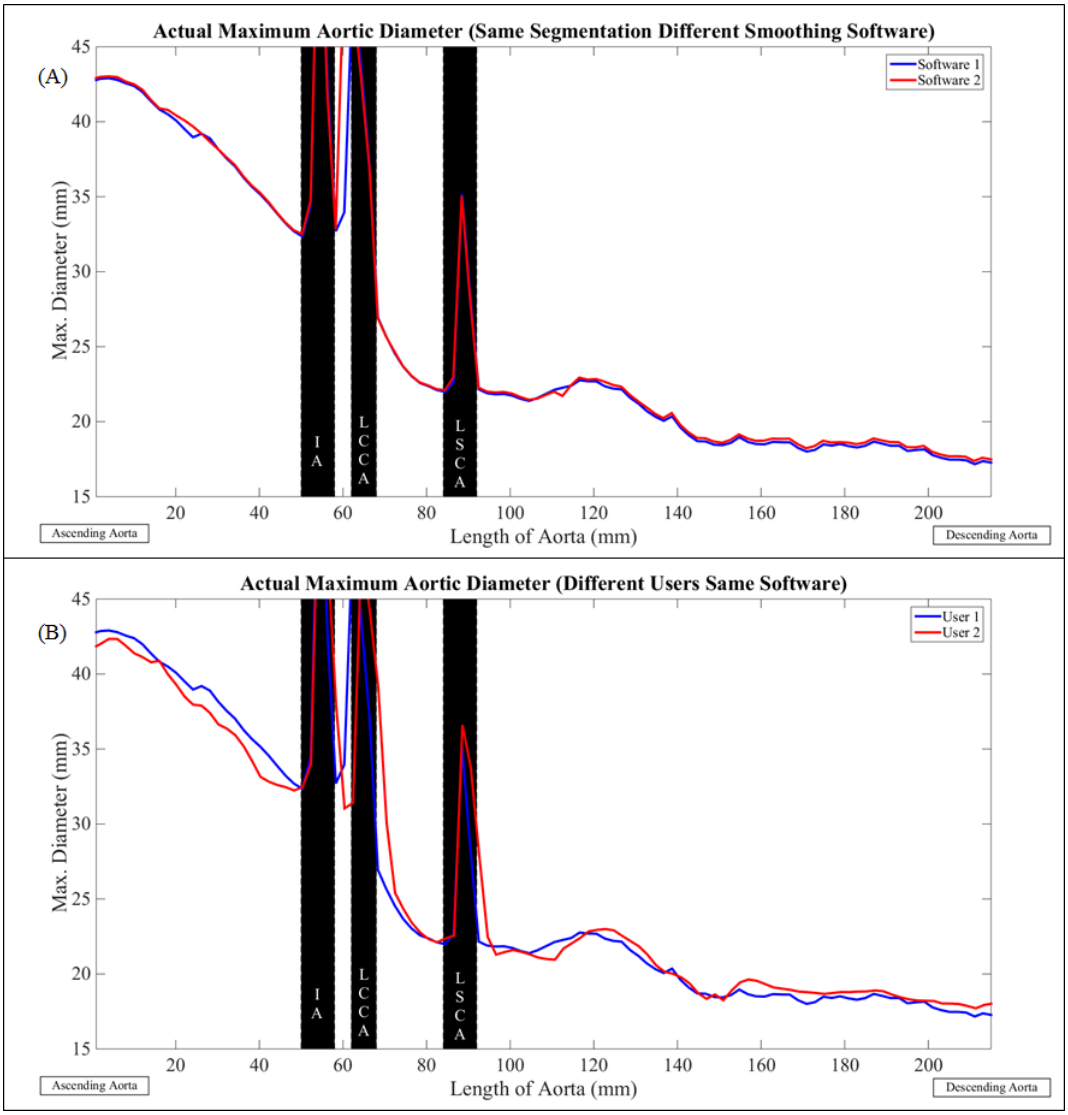

Figure E.2: Sensitivity of continuous measurements to choice of smoothing software and user, exemplified for a patient with Turner syndrome (Subject 6). Figure 11A: Segmentation of aorta performed using Mimics. Smoothing Software 1 (solid blue line) – Mimics, Smoothing Software 2 (solid red line) – OpenFlipper. Figure 11B: Solid blue line – User 1, Solid red line – User 2.

for the three different approaches to aortic segmentation. The simple, C0 and C1 smoothing algorithms available in the OpenFlipper software [252] were also tested, to assess the sensitivity of measurements to the choice of smoothing software and smoothing methodology (Figures E.1 and E.2). The simple or Laplacian smoothing method adjusts the location of each vertex to the geometric center of its neighboring vertices [253]. C0 smoothing assumes the individual curves

defining the surface to remain connected at common vertices and C1 smoothing ensures tangential continuity between the curves [254]. In order to evaluate inter-user variability in the measurements obtained continuously, aorta geometries reconstructed and smoothed by two users independently using Mimics were compared (Figure E.2).

Fig. E.1 depicts the sensitivity of continuous measurements to the choice of segmentation software and smoothing algorithm in a sample subject (Subject 6), and when comparing different segmentation software with identical smoothing, the maximum diameter measures obtained using Mimics and ITK-Snap were in good agreement compared to 3D Slicer (Difference between Mimics and ITK-Snap: -0.01 ± 2.5 mm, Difference between Mimics and 3D Slicer: -1.4 ± 3.6 mm, Difference between ITK-Snap and 3D Slicer: -1.4 ± 3.5 mm). Regarding the impact of using different smoothing algorithms exemplified for the same subject (Subject 6) in Fig. E.2, the diameters obtained using C0 and simple smoothing were comparable. The C1 smoothing resulted in a coarser lumen surface as compared to the C0 or simple smoothing (Difference between C0 and simple: 0.4 ± 0.6 mm, Difference between C0 and C1: 1 ± 1.5 mm, Difference between simple and C1: -0.5 ± 1.2 mm). Fig. E.2 indicates the sensitivity of continuous measures to choice of smoothing software and inter-user variability in the same subject (Subject 6). The inter-user variability in maximum diameter was 0.2 ± 2.3 mm, and the differences in measures resulting from selecting the simple smoothing available in Mimics or OpenFlipper was 0.3 ± 1.3 mm.

Appendix F:

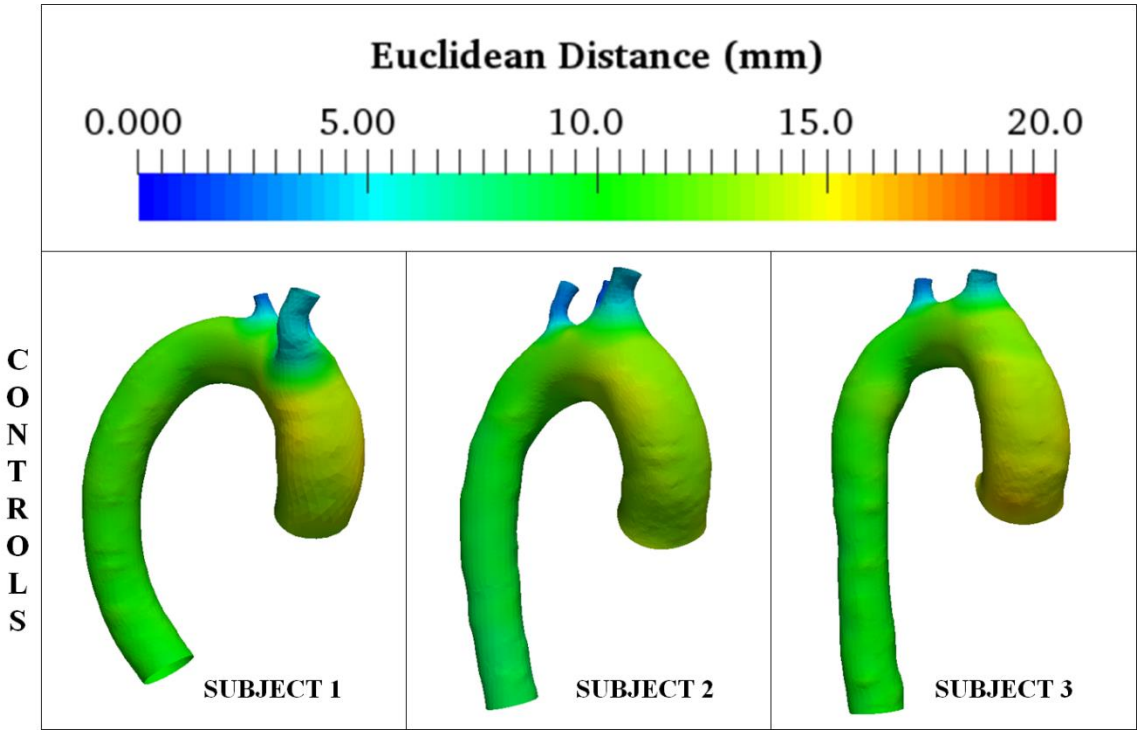

Figure F.1: Comparison of Euclidean distance maps for healthy controls.

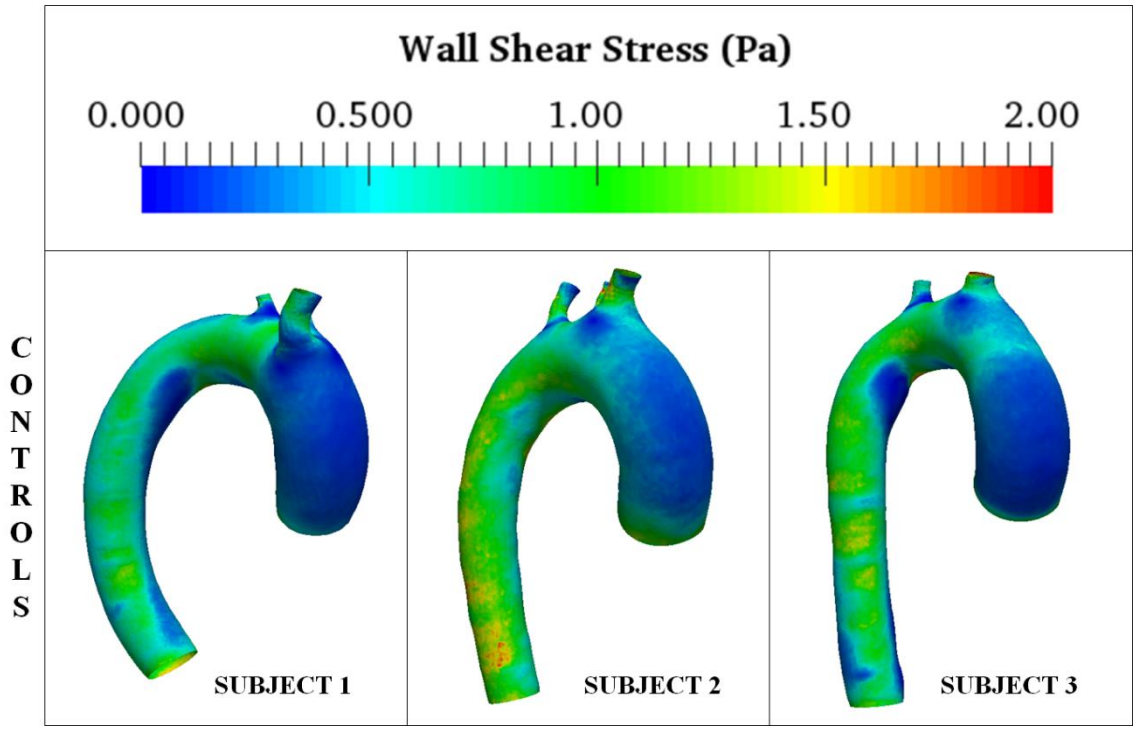

Figure F.2: Comparison of wall shear stress distribution for healthy controls.

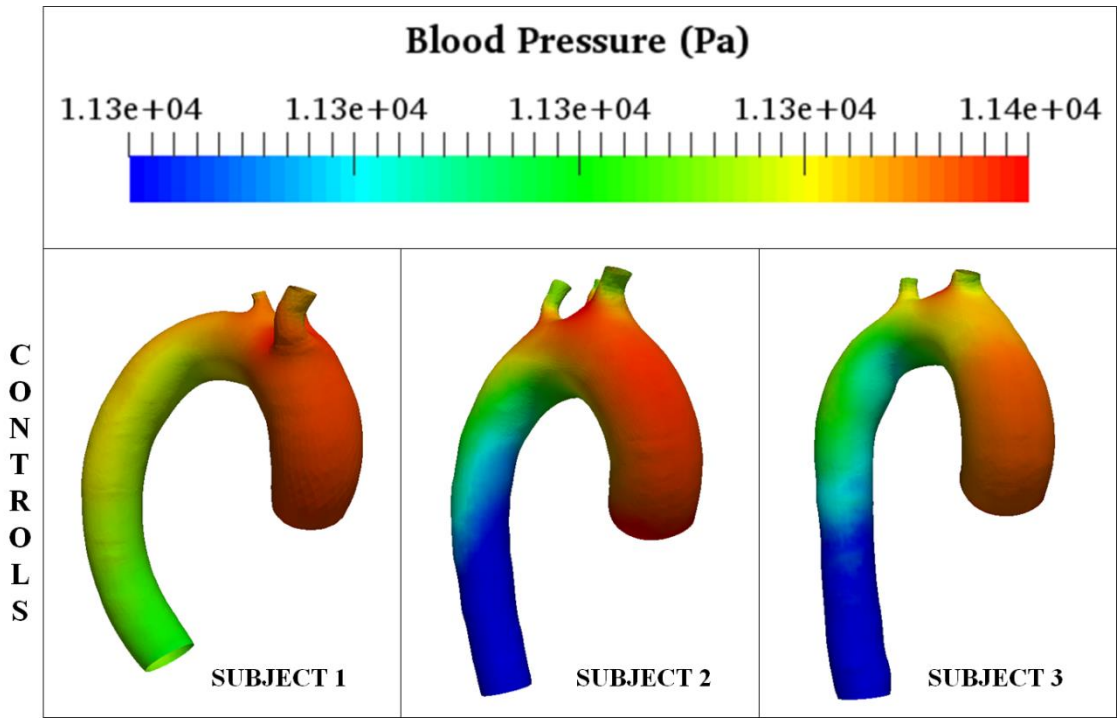

Figure F.3: Comparison of aorta wall pressure distribution for healthy controls.

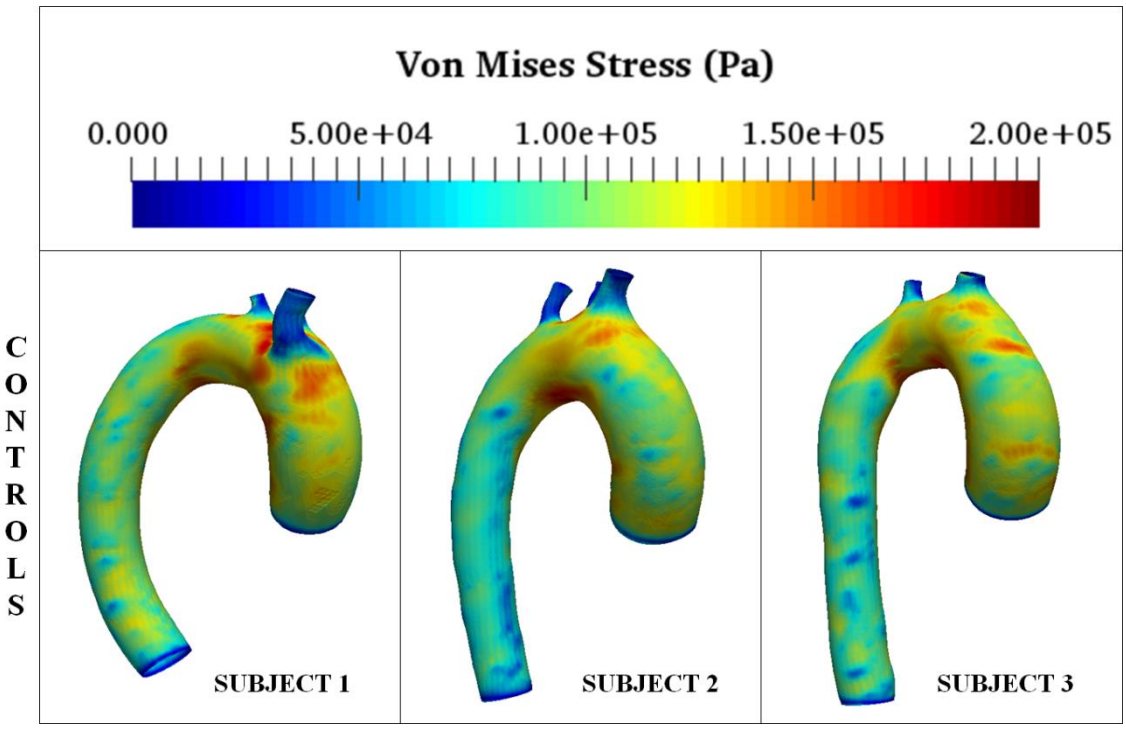

Figure F.4: Comparison of von-Mises stress distribution for healthy controls.

Appendix G:

Table G.1: Summary of patient clinical history, flow and mechanical parameters employed in the study (Note: HTN – Hypertension, ETA – Elongated transverse aorta, CoA – Coarctation, AA – Ascending aorta, MAP – Mean aortic pressure, Ct. - Control).

Subject	Age (yrs)	HTN	ETA	CoA	Dilatation (AA)	Dilatation (Root)	MAP (mmHg)	Cardiac Output (lpm)	Shear Modulus (MPa)
Ct. 1	40	N	N	N	N	N	85	5	0.145
Ct. 2	32	N	N	N	N	N	85	5	0.145
Ct. 3	34	N	N	N	N	N	85	5	0.145
Ct. 4	44	N	N	N	N	N	85	5	0.145
TAV 1	42	N	Y	Y	N	N	85	5	0.145
TAV 2	57	N	N	N	Y	N	85	5	0.145
BAV 1	49	Y	Y	Y	N	Y	118	5	0.225
BAV 2	56	Y	Y	N	N	Y	118	5	0.225
BAV 3	22	Y	Y	Y	N	Y	118	5	0.225
BAV 4	37	Y	Y	N	Y	N	118	5	0.225

Table G.2: Summary of mesh resolutions (element count) for the lumen (flow domain) and vessel wall (structural domain) (Note: Tetrahedral elements employed for flow domain, quadrilateral shell elements adopted for structural domain).

Subject	Flow Domain	Structural Domain
Control 1	2000000	124000
Control 2	2200000	140000
Control 3	1750000	122000
Control 4	2400000	136000
TAV 1	2900000	164000
TAV 2	2500000	141000
BAV 1	3100000	174000
BAV 2	2500000	140000
BAV 3	2700000	150000
BAV 4	2700000	156000

Table G.3: Locations of maximum Wall shear stress (WSS), Pressure, von-Mises (VM) stress, displacement and Euclidean distance (Note: LCCA – Left common carotid artery, LSCA – Left subclavian artery, IA – Innominate artery, CoA – Coarctation, STJ – Sinotubular junction).

Subject	Max. WSS	Max. Pressure	Max. VM Stress	Max. Displacement	Max. Euclidean Distance
Ct. 1	Transverse aorta - LCCA	Ascending aorta proximal to sinus	Ascending aorta distal	Transverse	Sinus
Ct. 2	Transverse aorta - LSCA	Ascending aorta proximal to sinus	Sinus	Transverse	Sinus
Ct. 3	Descending aorta	STJ	Sinus	Sinus	Sinus
Ct. 4	Transverse - IA LCCA junction	STJ	Transverse aorta	Sinus	Sinus
TAV 1	CoA	STJ	Ascending aorta (midway)	STJ	Sinus
TAV 2	Transverse - IA LCCA junction	Ascending aorta proximal to sinus	Ascending aorta proximal to STJ	Sinus	Sinus
BAV 1	Transverse - LCCA	STJ	Sinus	Sinus	Sinus
BAV 2	Transverse - LCCA	STJ	Transverse aorta	Ascending aorta	Sinus
BAV 3	CoA	Sinus	Sinus	Sinus	Sinus
BAV 4	End of aortic arch	STJ	Ascending aorta (midway)	Ascending aorta	Ascending aorta

Flow Patterns

Figure G.1 indicates flow patterns for healthy subject 4 and TS BAV-3 at the predefined 7 stations, for both the complete and truncated computational models. For the complete model corresponding to the control, a 'crescent-shaped' velocity profile was observed in the ascending aorta midway between the sinotubular junction and IA (station 1) that was skewed towards the outer aortic wall. Fully-developed secondary flows were observed at this location. The flow was skewed towards the inner wall and a 'crescent-shaped' velocity profile was also observed for the truncated model. Secondary flow began to develop at this location, as indicated by the small vortex on the inner wall. Secondary flow observed in station 1 for the full model was also observed at station 2. Flow patterns had a smaller stagnation flow region and a moderate change in the angular orientation of the counter-rotating eddies. The 'crescent shaped' velocity profile was also more distinct for the reduced model. In the transverse aorta arch, midway between the LCCA and LSCA (station 3), the secondary flow diminished and resembled a concentric circle for the complete model. Stronger secondary flow patterns and Dean vortices were observed at station 3 for the truncated model. For the complete model, secondary flow began to develop at station 4 and the pattern resembled a concentric circle. The flow accelerated due to the aortic taper with a moderate increase in secondary flow for the truncated model. In the descending aorta between the left pulmonary artery and left atrium (station 5), secondary flows were observed for both models. The size and orientation of the stagnation flow region on the inner wall was independent of inclusion of the aortic sinus. Tertiary eddies were observed for the complete aorta geometries. At station 6, secondary flow patterns were observed and at station 7, the flow was skewed towards the outer wall of the descending aorta for the full and reduced models.

At station 1 for the diseased case, skewing of flow towards the outer wall, fully-developed secondary flow and a 'crescent-shaped' velocity profile were observed for the complete model. Unlike in the control, large stagnation flow regions were not observed in the ascending aorta. Skewing of the flow towards the inner wall and a 'crescent-shaped' velocity profile were observed for the truncated model in a manner similar to the normal subject. At station 2, flow in the full model resembled a concentric circle. Flow accelerated at this location and was skewed towards the outer wall. The 'crescent shaped' velocity profile was more distinct in the ascending aorta proximal to the IA, for the reduced model. At station 3, secondary flow patterns began to develop for the complete model including weak tertiary eddies in the proximity of the outer wall. Secondary flow for the truncated model was less developed in the transverse aorta, between the LCCA and LSCA. At the aortic isthmus distal to the LSCA (station 4), weak secondary flow patterns were observed for both models. The magnitude of flow velocity was higher for the truncated case. A high jet velocity was observed downstream of the coarctation (station 5) for complete and truncated models. Differences between the full and reduced models were observed in the angular orientation of the jet and stagnation flow regions on the side walls of the descending aorta. Decay of the coarctation jet, secondary flow, reattachment of the flow with outer wall and a narrow stagnation flow region was observed at station 6 for the full and reduced models. This station was also characterized by formation of a tertiary eddy on the outer wall. At station 7, decay in the secondary flow was observed for the complete and truncated models, resulting in a flow pattern that resembled a concentric circle. Higher flow velocity in the TS patient could be attributed to smaller aortic caliber compared to the control. The tortuosity of the individual aortas generated asymmetry in the counter-rotating vortices unlike Dean flow [199].

Helicity

Figure G.2 summarizes contours of helicity at the seven discrete stations. The red contours represent clockwise rotation whereas the blue contours correspond to counterclockwise rotation. Helicity density was greatest in the transverse aortic arch for the complete and reduced models, including (FSI) and excluding (CFD) vessel elasticity. Additionally, the helicity density was non-zero in the ascending aorta for the complete models and was greater for TS BAV-3 as compared to healthy subject 4. Line plots describing variation in area-averaged helicity density H_a and absolute area-averaged helicity density H_{abs} for all models are summarized in Figure G.3. Markers indicating values of H_a and H_{abs} at the seven stations were superposed on these plots. For the healthy subject, helicity density was higher in the ascending (station 2) and transverse aorta (station 3) for the full model compared to the reduced case. The peak value of helicity density was observed at the end of the aortic arch for the reduced model. Decay of the swirl in the descending aorta was observed in all models. For the TS patient, variation in helicity was similar for the full and reduced models. The peak magnitude of helicity density in the transverse aorta was 3 times higher than the same for the control subject. The swirling flow increased gradually for the truncated models. Direction of the swirl apparently reversed, upstream of the coarctation (station 4) and the original direction was again recovered downstream of the constriction (station 5), following which the swirl was attenuated in the descending aorta as observed for the control. It should be noted that since area-averaged helicity plots consider the directionality of the individual helical structures, positive and negative values are observed as compared to the absolute area-averaged helicity plots. Low aortic tortuosity was associated with negligible values of helicity density in a previous computational study [181]. Significantly higher

helicity density in BAV-3 provided evidence of greater aortic tortuosity compared to healthy control 4.

Wall Shear Stress

Surface maps describing the variation in WSS for the healthy control 4 and TS BAV-3 (full and truncated models) are indicated in Figure G.4. For the complete model corresponding to the healthy subject, shear stress concentration was observed at the junctions between IA and LCCA, transverse aorta and LCCA and at the exit of the aortic arch on the inner wall. WSS was distributed on the outer wall of the ascending and descending aorta for this case. Regions of low shear were observed on the inner wall from the sinotubular junction to the outlet in the descending section. Additionally a region of low shear was observed in the posterior sinus. A non-uniform circumferential distribution of WSS was observed in the descending aorta (Fig. G.4). Location of maximum shear changed from the transverse aorta-LCCA-IA junction to the exit of the aortic arch following exclusion of the aortic root. Additionally, the maximum value decreased by 32 percent. WSS was distributed on the inner wall of the ascending aorta and outer wall of the descending section. Low shear regions were observed in the inner wall of the descending aorta and outer wall of the ascending aorta. Circumferential distribution of WSS downstream of the LSCA was more uniform compared to the complete model.

For the complete model corresponding to the TS case, high shear stresses were observed at the outer wall of the sinotubular junction and ascending aorta. Large values of WSS were distributed throughout the ETA and descending aorta at the coarctation. Low shear was observed downstream of the coarctation followed by a localized high shear region resulting from reattachment of the flow (right view in Fig. G.4). For the truncated geometry, low shear stresses were observed throughout the outer wall of the ascending aorta. Shear stress patterns

downstream of the constriction for the truncated model were similar to the complete model. Changes in WSS patterns in the ETA and at the coarctation were less significant when the root was excluded. The peak value of WSS was observed at the constriction for both cases and the magnitude decreased by 14 percent following exclusion of the sinus.

Mechanical Stress

Surface maps comparing the von-Mises stress distribution for the full and truncated models corresponding to healthy control 4 and TS BAV-3 are given in Figure G.5. For the control, high stresses observed in the inner ascending aorta wall and STJ were not observed when the root was excluded. The maximum magnitude of von-Mises stress was 0.19 MPa for the complete model and increased by 2 percent for the truncated model. The increase in the von-Mises stress and lower displacements for the truncated geometry could be attributed to the greater apparent structural rigidity of the arterial wall resulting from a shorter vessel length. The maximum stress occurred at the junction between the transverse aorta and LCCA. This location was unchanged following exclusion of the aortic sinus. For TS BAV-3, high localized stresses were observed in the ascending and descending aorta as compared to the healthy aorta. Stresses were concentrated on the inner ascending aorta wall in a manner similar to the control case. High stress regions also occurred in the transverse aorta in the proximity of the LCCA and LSCA as indicated in the right and left views. Furthermore, maximum stress values occurred at the sinotubular junction and a high stress concentration was observed along the entire aorta circumference at this location. High stresses were also observed in the inner side of the aortic root downstream of the inlet. When the root was excluded, peak mechanical stress was observed in the transverse aorta and was 27 percent lower than the complete model. Stress patterns in the transverse and descending sections resembled the same for the full model.

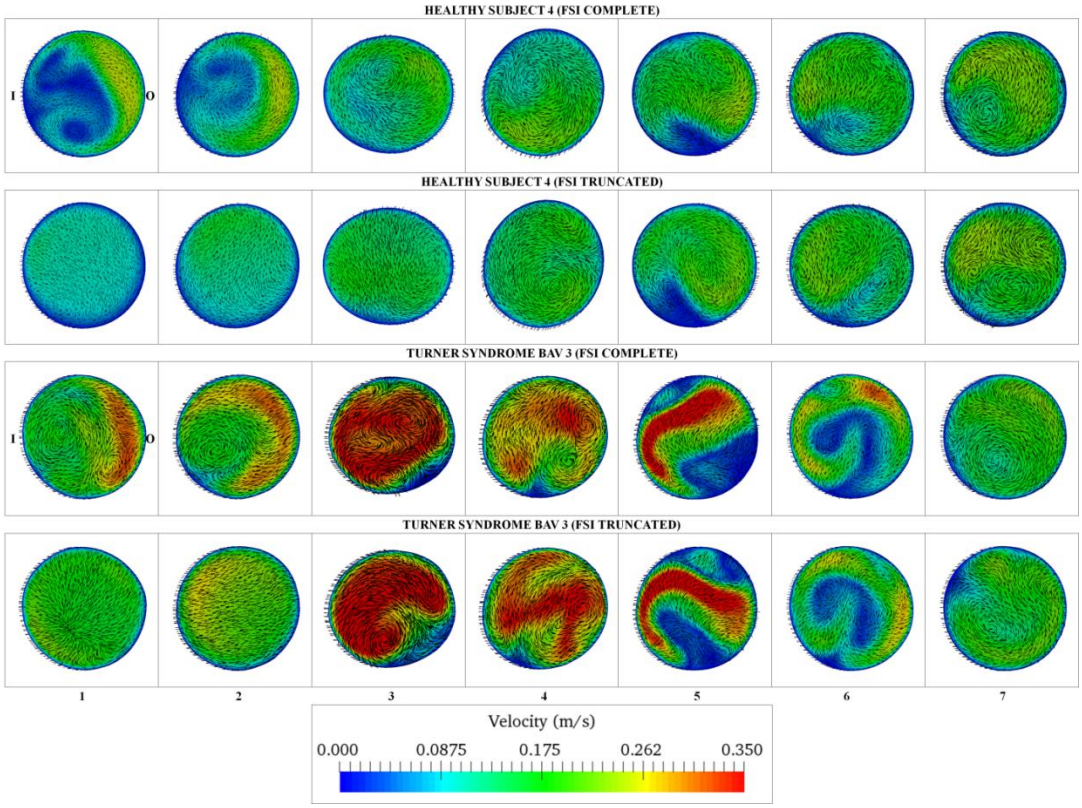

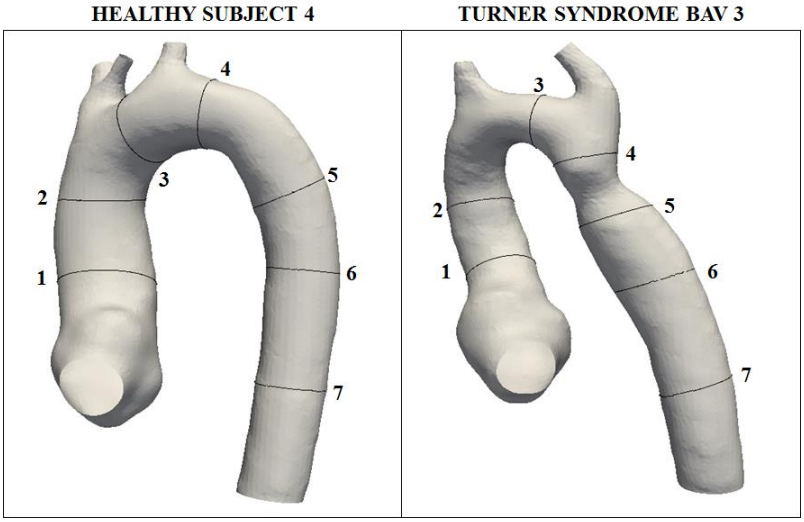

Figure G.1: Velocity contours (superposed vectors) describing flow patterns at 7 stations for healthy control 4 and TS BAV-3 corresponding to the full and truncated models (Note: Views are normal to the cross-section. I – Inner wall, O – Outer wall, Locations of the seven stations identified along the length of the aorta also shown for reference).

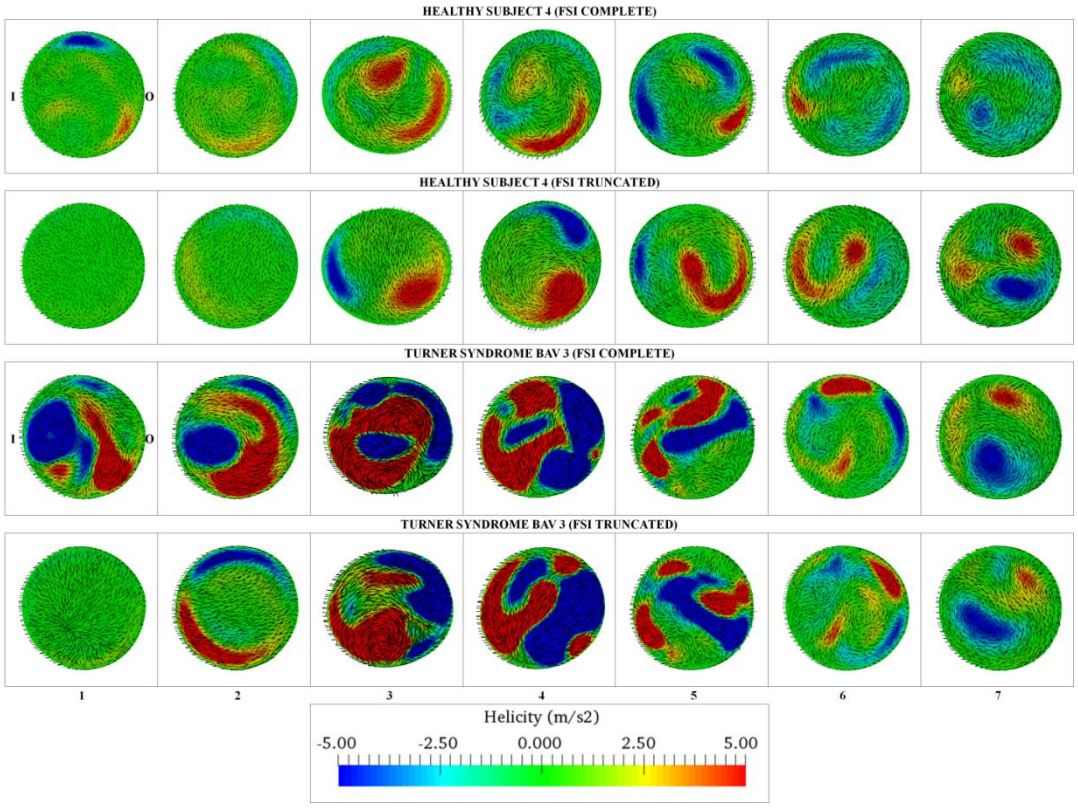

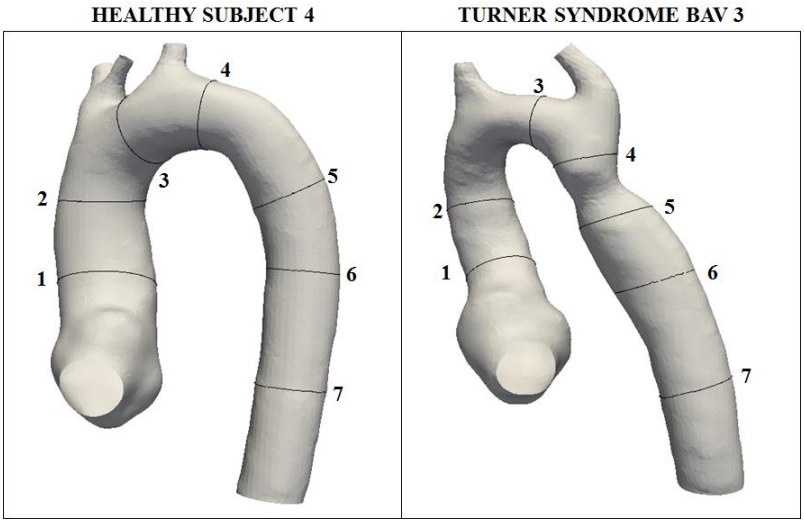

Figure G.2: Contours of helicity (superposed velocity vectors) describing the swirl at 7 stations for healthy control 4 and TS BAV-3 corresponding to the full and truncated models (Note: Red – clockwise helix, Blue – counterclockwise helix, Views are normal to the cross-section, I – Inner wall, O – Outer wall, Locations of the seven stations identified along the length of the aorta also shown for reference).

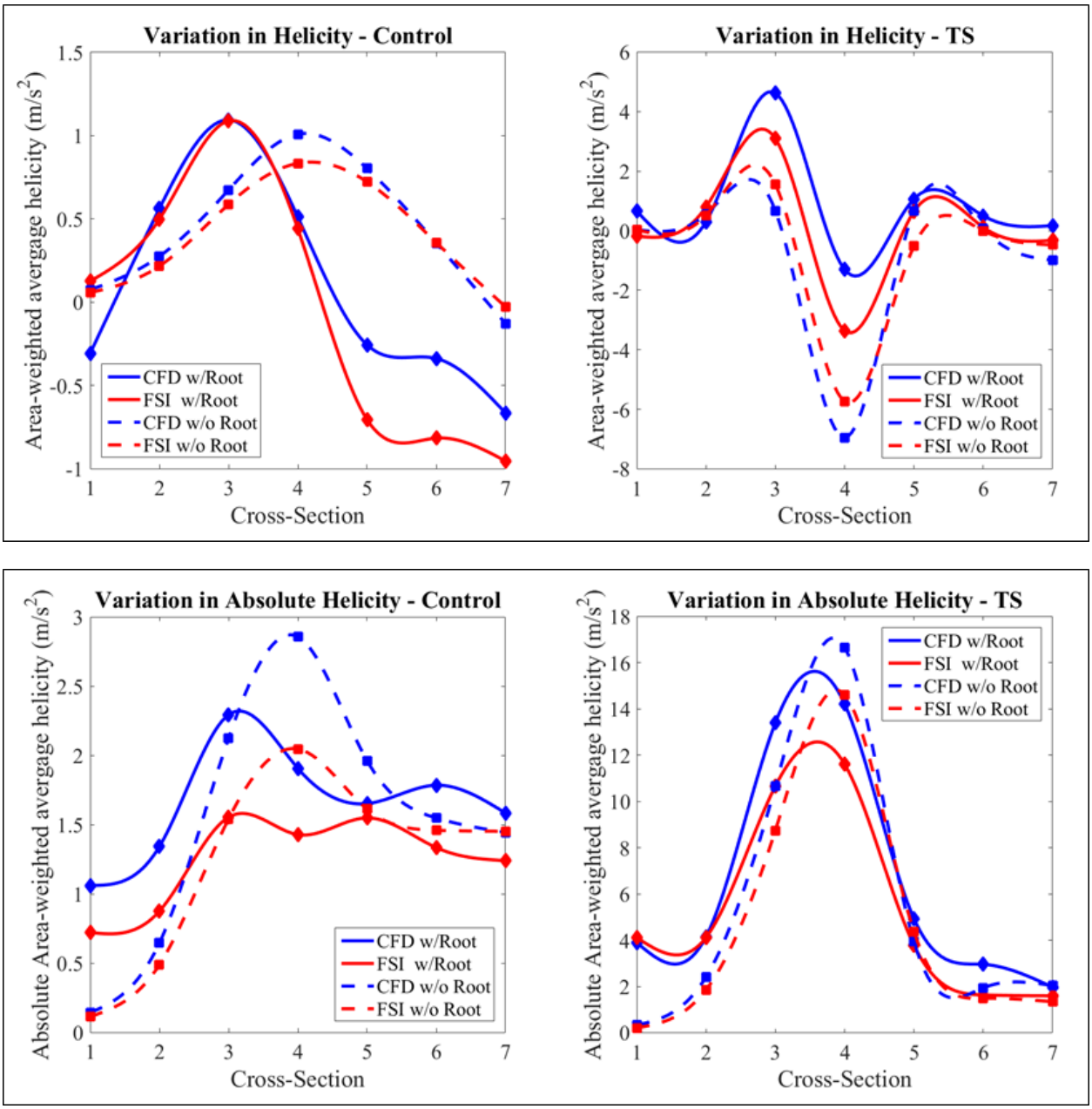

Figure G.3: Variation in area-averaged helicity density H_a and absolute area-averaged helicity density H_{abs} along the thoracic aorta for healthy control 4 and TS BAV-3 (All values in m/s^2. Blue solid line – CFD including root, Red solid line – FSI including root, Blue dashed line – CFD excluding root, Red dashed line – FSI excluding root, Helicity values at 7 stations indicated using diamond (Blue – CFD, Red – FSI) and square (Blue – CFD, Red – FSI) markers, Smoothing-spline fitted to data).

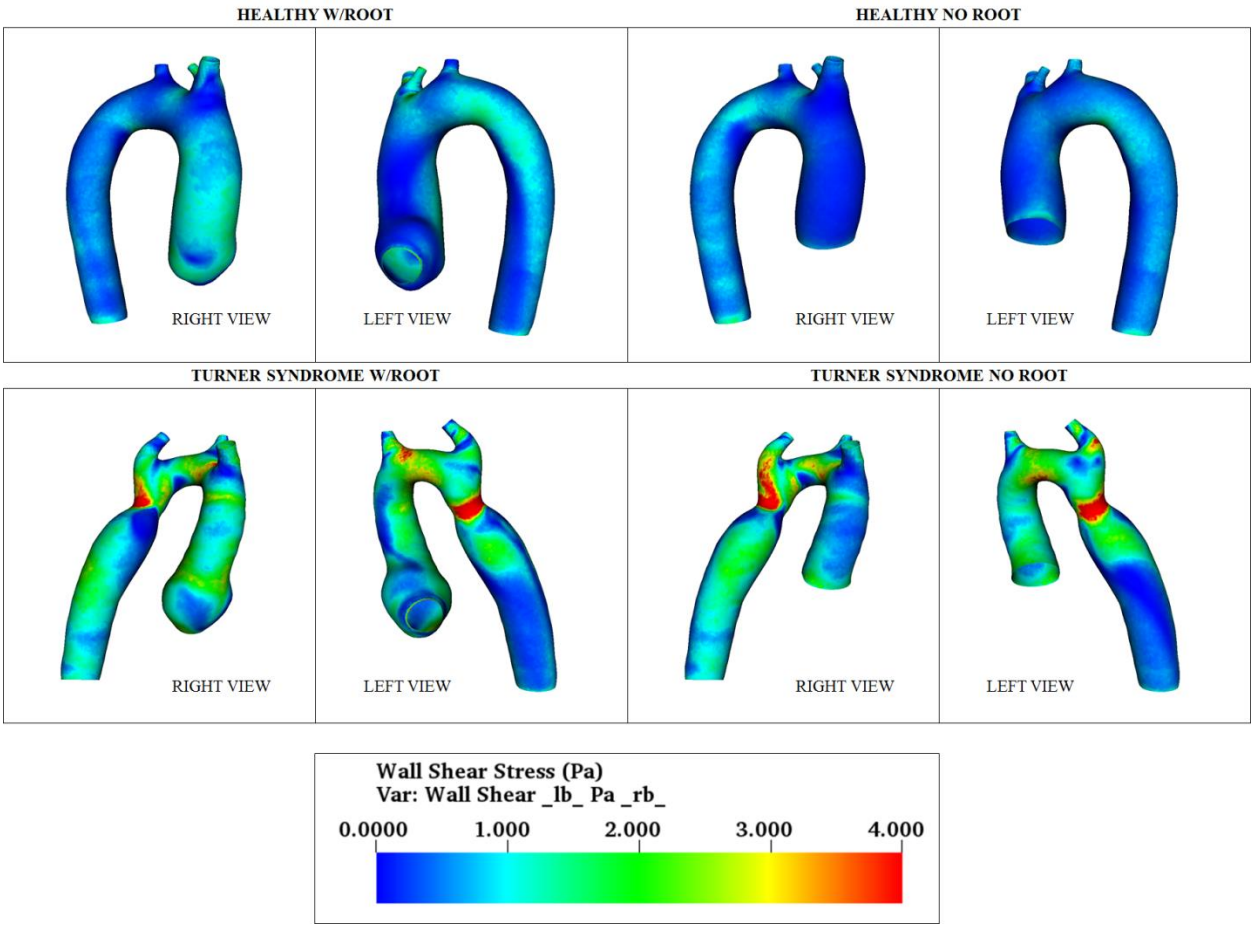

Figure G.4: Surface maps describing circumferential and axial variation in WSS for the complete and truncated aorta geometries corresponding to healthy control 4 and TS BAV-3.

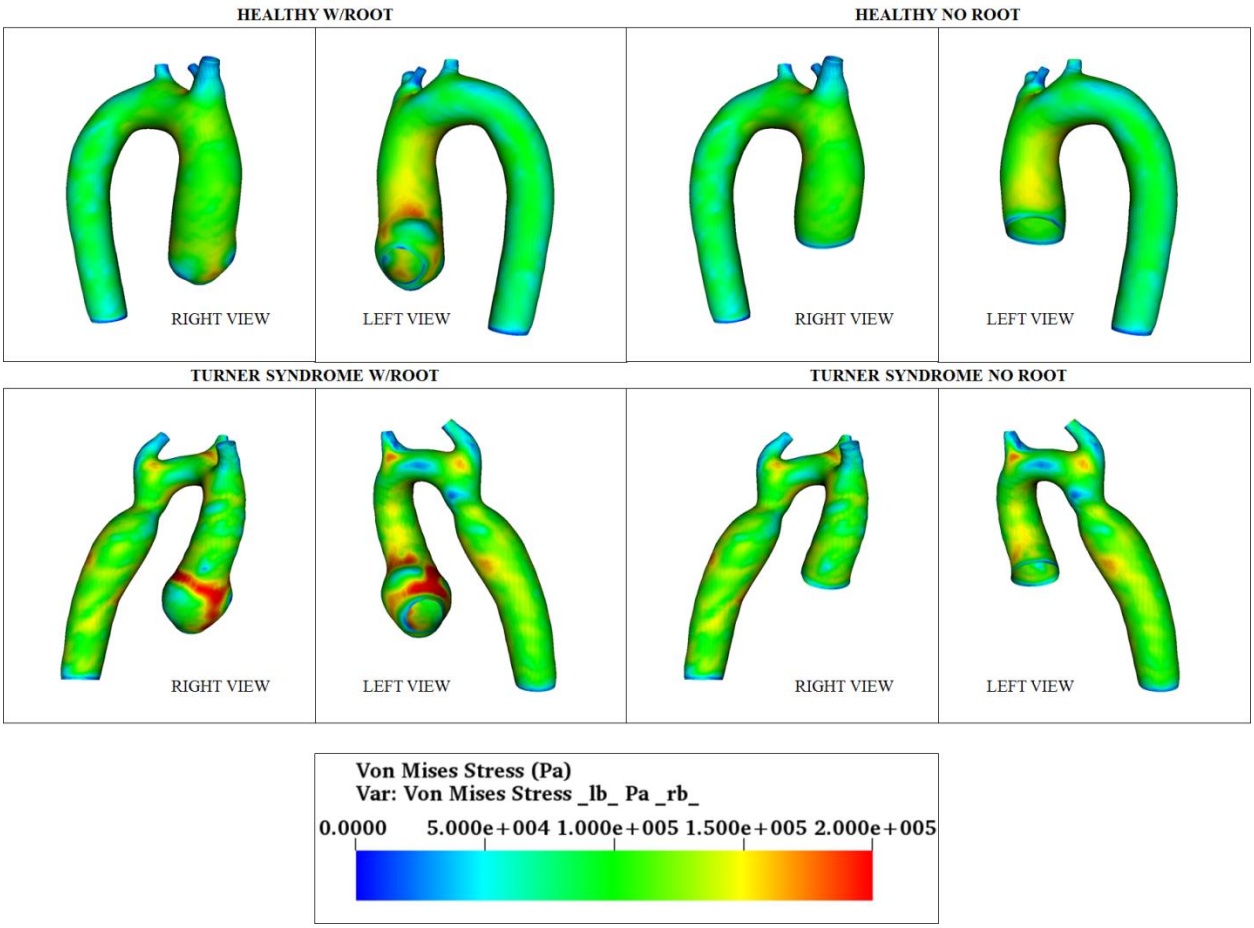

Figure G.5: Surface maps indicating circumferential and axial variation in Von-Mises stress for the complete and truncated aorta geometries corresponding to healthy control 4 and TS BAV-3.

Appendix H:

Planes were selected normal to the aorta cross-section to visualize the variation in flow patterns along the aorta length (Figure H.1). For the patient with a dilated ascending aorta, the flow accelerated from the ascending aorta to the descending section. Selection of the Carreau-Yassuda rheological model resulted in a higher flow velocity. For the patient with the elongated transverse aorta, the highest flow velocity was obtained in the transverse aorta between the LCCA and LSCA. Differences in flow patterns for the two rheological models were observed in the descending aortic taper for this subject. For the patient with aortic coarctation, the flow was observed to accelerate from the ascending aorta to the transverse aorta upstream of the stenosis. The velocity of the jet downstream of the coarctation was higher for the non-Newtonian model. Furthermore, flow reattachment occurred further downstream of the stenosis compared to the Newtonian case. The flow accelerated downstream of the coarctation due to the aortic taper for both rheological models. Line plots of area-averaged helicity were then plotted for the three subjects (Figure H.2) to assess the influence of blood rheology on the swirling flow patterns. For the subjects with ascending aortic dilatation and elongated transverse aorta, the area averaged helicity increased to a maximum positive value in the transverse section and then decreased in the descending aorta indicating a larger contribution of the counter-clockwise spiral. For the subject with coarctation, the sign of the area-averaged helicity at the coarctation changed from positive to negative. Downstream of the coarctation the contribution of the counter-rotating spirals was comparable. For the two rheological models tested, the differences in the helicity were similar for the three patients analyzed and also did not vary significantly along the aorta length. Furthermore, the maximum absolute area averaged helicity was highest for the patient with coarctation (14 m/s^2) and least for the subject with dilatation (0.7 m/s^2).

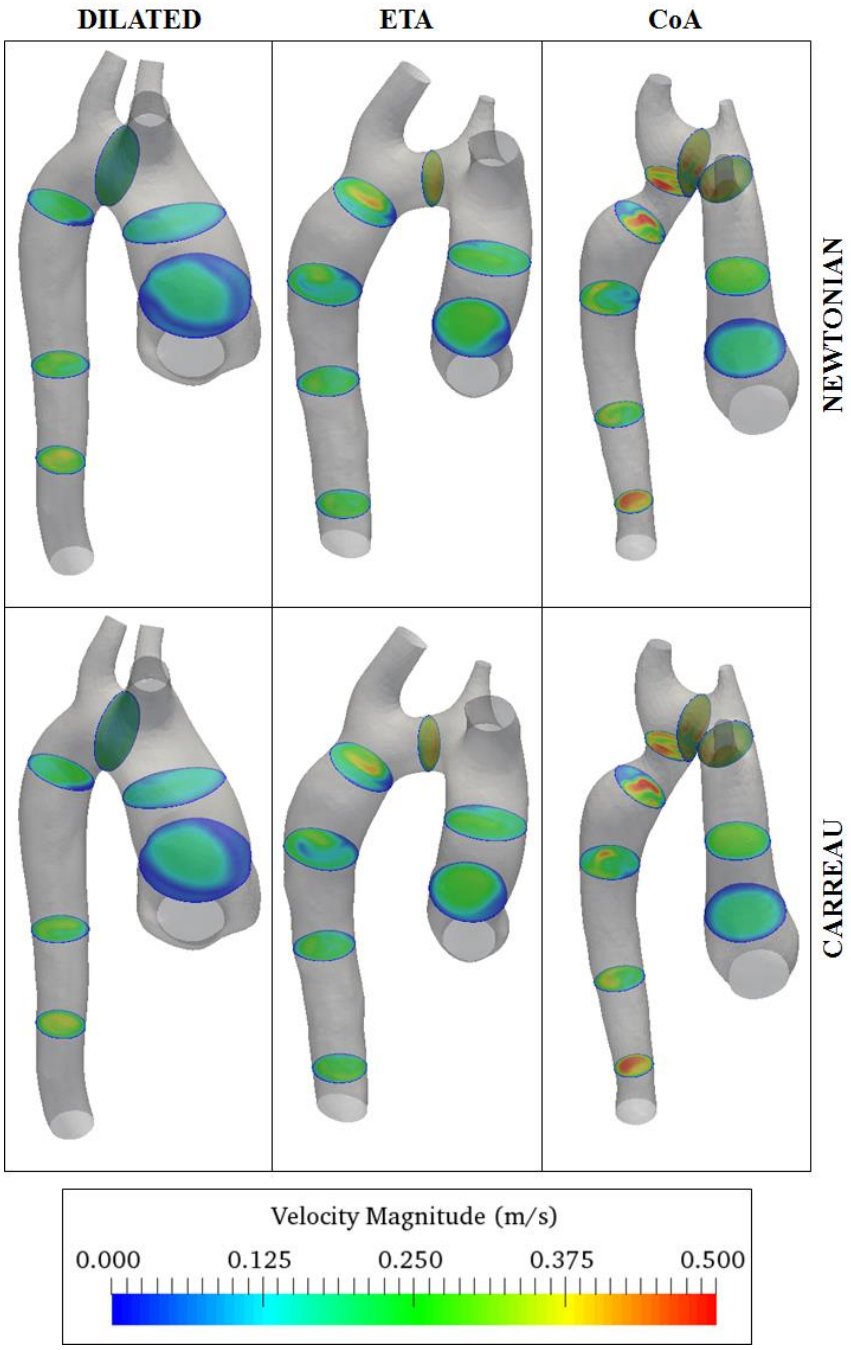

Figure H.1: Comparison between flow patterns for the dilated, ETA and CoA TS subjects corresponding to the Newtonian and non-Newtonian (i.e. Carreau-Yassuda) models.

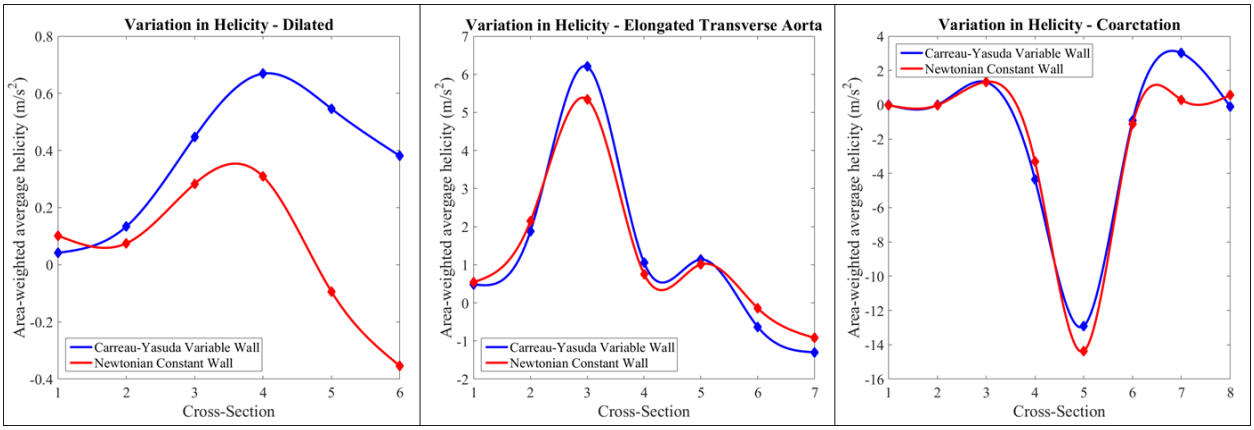

Figure H.2: Variation in area-averaged helicity density H_a along the thoracic aorta for the dilated, ETA and CoA TS subjects (All values in m/s^2. Blue solid line – non-Newtonian model, Red solid line – Newtonian assumption).

Figure H.3 summarizes the vessel wall displacements for the three TS patients considered in this study. For the patient with the dilated ascending aorta, the largest displacements were observed in the left walls of the ascending, transverse and descending aorta. Large displacements were also observed in the right wall of the transverse section. For the constant wall thickness, the maximum displacement (1.4 mm) occurred in the left wall midway in the descending aorta. For the variable wall thickness, the largest vessel wall motion was obtained in the left wall of the transverse aorta. The magnitude was 21 percent higher than the constant wall thickness case. Furthermore, the magnitude of vessel wall displacement in the ascending aorta was lower for the variable wall thickness case. For the subject with ETA, the greatest displacements of the aorta were obtained in the lateral walls of the descending aorta, downstream of the LSCA. The peak displacement (1.4 mm) for the constant wall case occurred midway in the left lateral wall of the descending aorta. The location of the same was unchanged for the variable wall case and the magnitude was 14 percent higher. Besides, higher vessel wall displacements were observed in the ascending and transverse aortas as compared to the constant wall thickness case. For the subject with coarctation, the peak arterial wall displacements were concentrated above the STJ in the ascending aorta. The maximum magnitude of wall displacement for the variable wall

thickness case (1.2 mm) was 20 percent higher than the constant wall thickness model. Vessel displacements were also observed in the descending section downstream of the coarctation.

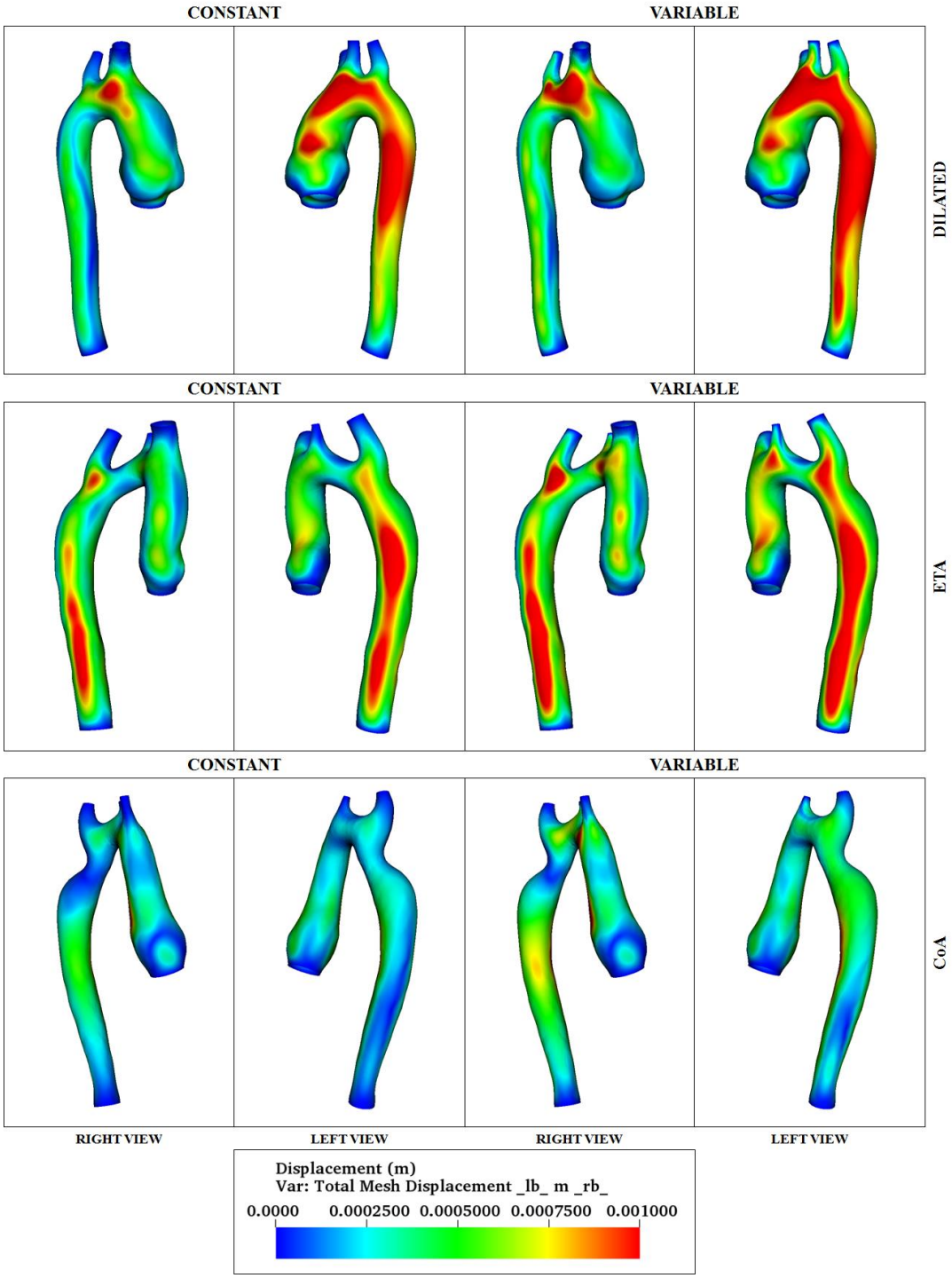

Figure H.3: 3D contour maps of vessel wall displacement for dilated, ETA and CoA TS subjects corresponding to a constant and variable wall thickness.

Bibliography

1. Mylavarapu, G., *Computational Flow Modeling of Human Upper Airway Breathing*. 2013.
2. Fogel, R.B., et al., *Increased Prevalence of Obstructive Sleep Apnea Syndrome in Obese Women with Polycystic Ovary Syndrome1*. J Clin Endocrinol Metab, 2001. **86**(3): p. 1175-1180.
3. Bilston, L.E. and S.C. Gandevia, *Biomechanical properties of the human upper airway and their effect on its behavior during breathing and obstructive sleep apnea.* J Appl Physiol, 2014. **116**(3): p. 314-324.
4. Ayappa, I. and D.M. Rapoport, *The upper airway in sleep: physiology of the pharynx.* Sleep Med Rev, 2003. **7**(1): p. 9-33.
5. Hillman, D.R., P.R. Platt, and P.R. Eastwood, *The upper airway during anaesthesia.* Br J Anaesth, 2003. **91**(1): p. 31-39.
6. Roberts, J.L., et al., *Assessment of pharyngeal airway stability in normal and micrognathic infants.* J Appl Physiol, 1985. **58**(1): p. 290-299.
7. Suratt, P.M., S.C. Wilhoit, and K. Cooper, *Induction of airway collapse with subatmospheric pressure in awake patients with sleep apnea.* J Appl Physiol, 1984. **57**(1): p. 140-146.
8. Epstein, L.J., et al., *Clinical Guideline for the Evaluation, Management and Long-term Care of Obstructive Sleep Apnea in Adults.* J Clin Sleep Med, 2009. **5**(3): p. 263-276.
9. Montazeri, A., E. Giannouli, and Z. Moussavi, *Assessment of Obstructive Sleep Apnea and its Severity during Wakefulness.* Ann Biomed Eng, 2012. **40**(4): p. 916-924.
10. Berry, R.B., M.M. Desa, and R.W. Light, *Effect of ethanol on the efficacy of nasal continuous positive airway pressure as a treatment for obstructive sleep apnea.* Chest, 1991. **99**(2): p. 339-343.
11. Schwartz, A.R., et al., *Obesity and Obstructive Sleep Apnea.* Proc Am Thorac Soc, 2008. **5**(2): p. 185-192.
12. Patil, S.P., et al., *A Simplified Method for Measuring Critical Pressures during Sleep in the Clinical Setting.* Am J Resp Crit Care, 2004. **170**(1): p. 86-93.
13. Ruehland, W.R., et al., *The new AASM criteria for scoring hypopneas: impact on the apnea hypopnea index.* Sleep, 2009. **32**(2): p. 150-7.
14. Weijerman, M.E. and J.P. de Winter, *Clinical practice: The care of children with Down syndrome.* Eur J Pediatr, 2010. **169**(12): p. 1445-1452.
15. Shott, S.R., et al., *Obstructive sleep apnea: Should all children with down syndrome be tested?* Arch Otolaryngol Head Neck Surg, 2006. **132**(4): p. 432-436.
16. Fleck, R.J., et al., *An adverse effect of positive airway pressure on the upper airway documented with magnetic resonance imaging.* JAMA Otolaryngol Head Neck Surg, 2013. **139**(6): p. 636-638.
17. Vgontzas, A.N., et al., *Polycystic Ovary Syndrome Is Associated with Obstructive Sleep Apnea and Daytime Sleepiness: Role of Insulin Resistance1*. J Clin Endocrinol Metab, 2001. **86**(2): p. 517-520.
18. Tasali, E., E. Van Cauter, and D.A. Ehrmann, *Polycystic Ovary Syndrome and Obstructive Sleep Apnea.* Sleep Med Clin, 2008. **3**(1): p. 37-46.

19. Waters, K.A., et al., *Obstructive sleep apnea: the use of nasal CPAP in 80 children.* Am J Resp Crit Care 1995. **152**(2): p. 780-785.
20. Sher, A.E., *Upper airway surgery for obstructive sleep apnea.* Sleep Med Rev, 2002. **6**(3): p. 195-212.
21. Sybert, V.P. and E. McCauley, *Turner's Syndrome.* N Engl J Med, 2004. **351**(12): p. 1227-1238.
22. Turner, H.H., *A syndrome of infantalism, congenital webbed neck, and cubitus valgus.* Endocrinology, 1938. **23**(5): p. 566-574.
23. Højbjerg Gravholt, C., et al., *Clinical and epidemiological description of aortic dissection in Turner's syndrome.* Cardiol Young, 2006. **16**(05): p. 430-436.
24. Mortensen, K.H., et al., *Abnormalities of the major intrathoracic arteries in Turner syndrome as revealed by magnetic resonance imaging.* Cardiol Young, 2010. **20**(02): p. 191-200.
25. Sybert, V.P., *Cardiovascular malformations and complications in Turner syndrome.* Pediatrics, 1998. **101**(1): p. E11.
26. Isselbacher, E.M., *Thoracic and Abdominal Aortic Aneurysms.* Circulation, 2005. **111**(6): p. 816-828.
27. Ho, V.B., et al., *Major Vascular Anomalies in Turner Syndrome: Prevalence and Magnetic Resonance Angiographic Features.* Circulation, 2004. **110**(12): p. 1694-1700.
28. Matura, L.A., et al., *Aortic Dilatation and Dissection in Turner Syndrome.* Circulation, 2007. **116**(15): p. 1663-1670.
29. Carlson, M. and M. Silberbach, *Dissection of the aorta in Turner syndrome: two cases and review of 85 cases in the literature.* J Med Genet, 2007. **44**(12): p. 745-749.
30. Elsheikh, M., et al., *Hypertension is a major risk factor for aortic root dilatation in women with Turner's syndrome.* Clin Endocrinol, 2001. **54**(1): p. 69-73.
31. Gutmark-Little, I. and P.F. Backeljauw, *Cardiac magnetic resonance imaging in Turner syndrome.* Clin Endocrinol, 2013. **78**(5): p. 646-658.
32. Mortensen, K.H., et al., *Prediction of aortic dilation in Turner syndrome - enhancing the use of serial cardiovascular magnetic resonance.* J Cardiovasc Magn Reson, 2013. **15**(1): p. 1-11.
33. Cleemann, L., et al., *Aortic Dimensions in Girls and Young Women with Turner Syndrome: A Magnetic Resonance Imaging Study.* Pediatr Cardiol, 2010. **31**(4): p. 497-504.
34. Hjerrild, B., et al., *Thoracic aortopathy in Turner syndrome and the influence of bicuspid aortic valves and blood pressure: a CMR study.* J Cardiovasc Magn Reson, 2010. **12**(1): p. 12.
35. Mortensen, K., et al., *Dilation of the ascending aorta in Turner syndrome - a prospective cardiovascular magnetic resonance study.* J Cardiovasc Magn Reson, 2011. **13**(1): p. 24.
36. Erbel, R., et al., *2014 ESC Guidelines on the diagnosis and treatment of aortic diseases.* Eur Heart J, 2014. **35**(41): p. 2873-2926.
37. Hiratzka, L.F., et al., *2010 ACCF/AHA/AATS/ACR/ASA/SCA/SCAI/SIR/STS/SVM Guidelines for the Diagnosis and Management of Patients With Thoracic Aortic Disease: A Report of the American College of Cardiology Foundation/American Heart Association Task Force on Practice Guidelines, American Association for Thoracic Surgery, American College of Radiology, American Stroke Association, Society of Cardiovascular Anesthesiologists, Society for Cardiovascular Angiography and Interventions, Society of*

Interventional Radiology, Society of Thoracic Surgeons, and Society for Vascular Medicine. Circulation, 2010. **121**(13): p. e266-e369.
38. Mortensen, K.H., N.H. Andersen, and C.H. Gravholt, *Cardiovascular phenotype in Turner syndrome--integrating cardiology, genetics, and endocrinology.* Endocr Rev, 2012. **33**(5): p. 677-714.
39. Mihaescu, M., et al., *Large Eddy Simulation and Reynolds-Averaged Navier–Stokes modeling of flow in a realistic pharyngeal airway model: An investigation of obstructive sleep apnea.* J Biomech, 2008. **41**(10): p. 2279-2288.
40. Mylavarapu, G., et al., *Validation of computational fluid dynamics methodology used for human upper airway flow simulations.* J Biomech, 2009. **42**(10): p. 1553-1559.
41. Xu, C., et al., *Computational fluid dynamics modeling of the upper airway of children with obstructive sleep apnea syndrome in steady flow.* J Biomech, 2006. **39**(11): p. 2043-2054.
42. Wootton, D.M., et al., *Computational fluid dynamics endpoints to characterize obstructive sleep apnea syndrome in children.* J Appl Physiol, 2014. **116**(1): p. 104-112.
43. Luo, H., et al., *Computational fluid dynamics endpoints for assessment of adenotonsillectomy outcome in obese children with obstructive sleep apnea syndrome.* J Biomech, 2014. **47**(10): p. 2498-2503.
44. Mihaescu, M., et al., *Large Eddy Simulation of the pharyngeal airflow associated with Obstructive Sleep Apnea Syndrome at pre and post-surgical treatment.* J Biomech, 2011. **44**(12): p. 2221-2228.
45. Mylavarapu, G., et al., *Planning human upper airway surgery using computational fluid dynamics.* J Biomech, 2013. **46**(12): p. 1979-1986.
46. Pirnar, J., et al., *Computational fluid-structure interaction simulation of airflow in the human upper airway.* J Biomech, 2015. **48**(13): p. 3685-3691.
47. Zhu, J.H., et al., *Passive movement of human soft palate during respiration: A simulation of 3D fluid/structure interaction.* J Biomech, 2012. **45**(11): p. 1992-2000.
48. Wang, Y., et al., *Fluid–structure interaction modeling of upper airways before and after nasal surgery for obstructive sleep apnea.* Int J Numer Method Biomed Eng, 2012. **28**(5): p. 528-546.
49. Zhao, M., et al., *Simulation of upper airway occlusion without and with mandibular advancement in obstructive sleep apnea using fluid-structure interaction.* J Biomech, 2013. **46**(15): p. 2586-2592.
50. Carrigy, N.B., et al., *Simulation of muscle and adipose tissue deformation in the passive human pharynx.* Comput Methods Biomech Biomed Engin, 2016. **19**(7): p. 780-788.
51. Xu, C., et al., *Modeling upper airway collapse by a finite element model with regional tissue properties.* Med Eng Phys, 2009. **31**(10): p. 1343-1348.
52. Bersvendsen, J., et al., *Automatic measurement of aortic annulus diameter in 3-dimensional Transoesophageal echocardiography.* BMC Med Imaging, 2014. **14**(1): p. 1-8.
53. Ntsinjana, H., et al., *Aortic arch shape is not associated with hypertensive response to exercise in patients with repaired congenital heart diseases.* J Cardiovasc Magn Reson, 2013. **15**(1): p. 101.
54. Arzani, A., et al., *A longitudinal comparison of hemodynamics and intraluminal thrombus deposition in abdominal aortic aneurysms.* Am J Physiol Heart Circ Physiol, 2014. **307**(12): p. H1786-H1795.

55. Martin, C., W. Sun, and J. Elefteriades, *Patient-specific finite element analysis of ascending aorta aneurysms.* Am J Physiol Heart Circ Physiol, 2015. **308**(10): p. H1306-H1316.
56. Nathan, D.P., et al., *Pathogenesis of Acute Aortic Dissection: A Finite Element Stress Analysis.* Ann Thorac Surg, 2011. **91**(2): p. 458-463.
57. Keshavarz-Motamed, Z., J. Garcia, and L. Kadem, *Fluid Dynamics of Coarctation of the Aorta and Effect of Bicuspid Aortic Valve.* PLoS ONE, 2013. **8**(8): p. e72394.
58. Chen, J., et al., *Numerical investigation of mass transport through patient-specific deformed aortae.* J Biomech, 2014. **47**(2): p. 544-552.
59. Prahl Wittberg, L., et al., *Effects of aortic irregularities on blood flow.* Biomech Model Mechanobiol, 2016. **15**(2): p. 345-360.
60. Nathan, D.P., et al., *Increased Ascending Aortic Wall Stress in Patients With Bicuspid Aortic Valves.* Ann Thorac Surg, 2011. **92**(4): p. 1384-1389.
61. Trabelsi, O., et al., *Patient specific stress and rupture analysis of ascending thoracic aneurysms.* J Biomech, 2015. **48**(10): p. 1836-1843.
62. Zelaya, J.E., et al., *Improving the Efficiency of Abdominal Aortic Aneurysm Wall Stress Computations.* PLoS ONE, 2014. **9**(7): p. e101353.
63. Humphrey, J.D. and G.A. Holzapfel, *Mechanics, mechanobiology, and modeling of human abdominal aorta and aneurysms.* J Biomech, 2012. **45**(5): p. 805-814.
64. Raghavan, M.L. and D.A. Vorp, *Toward a biomechanical tool to evaluate rupture potential of abdominal aortic aneurysm: identification of a finite strain constitutive model and evaluation of its applicability.* J Biomech, 2000. **33**(4): p. 475-482.
65. Singh, S.D., et al., *Biomechanical properties of the Marfan's aortic root and ascending aorta before and after personalised external aortic root support surgery.* Med Eng Phys, 2015. **37**(8): p. 759-766.
66. Singh, S.D., et al., *Effects of aortic root motion on wall stress in the Marfan aorta before and after personalised aortic root support (PEARS) surgery.* J Biomech, 2016. **49**(10): p. 2076-2084.
67. Chandra, S., et al., *Fluid-Structure Interaction Modeling of Abdominal Aortic Aneurysms: The Impact of Patient-Specific Inflow Conditions and Fluid/Solid Coupling.* J Biomech Eng, 2013. **135**(8): p. 081001-081001.
68. Trachet, B., et al., *An Animal-Specific FSI Model of the Abdominal Aorta in Anesthetized Mice.* Ann Biomed Eng, 2015. **43**(6): p. 1298-1309.
69. Bathe, K.-J. and E.N. Dvorkin, *A four-node plate bending element based on Mindlin/Reissner plate theory and a mixed interpolation.* Int J Numer Meth Eng, 1985. **21**(2): p. 367-383.
70. Maas, S.A., et al., *FEBio: Finite Elements for Biomechanics.* J Biomech Eng, 2012. **134**(1): p. 011005-011005.
71. *Fluid-structure Interaction: Modelling, Simulation, Optimization*, ed. H.-J. Bungartz and M. Schäfer. 2006: Springer-Verlag.
72. *Fluid-Structure Interaction and Biomedical Applications*, ed. T. Bodnár, G.P. Galdi, and Š. Nečasová. 2014: Springer Basel.
73. Tang, D., et al., *Image-based patient-specific ventricle models with fluid–structure interaction for cardiac function assessment and surgical design optimization.* Prog Pediatr Cardiol, 2010. **30**(1–2): p. 51-62.

74. Xenos, M., et al., *Patient-Based Abdominal Aortic Aneurysm Rupture Risk Prediction with Fluid Structure Interaction Modeling.* Ann Biomed Eng, 2010. **38**(11): p. 3323-3337.
75. Cheng, S., et al., *Effects of fluid structure interaction in a three dimensional model of the spinal subarachnoid space.* J Biomech, 2014. **47**(11): p. 2826-2830.
76. Malvè, M., et al., *FSI Analysis of the Coughing Mechanism in a Human Trachea.* Ann Biomed Eng, 2010. **38**(4): p. 1556-1565.
77. Donea, J., S. Giuliani, and J.P. Halleux, *An arbitrary lagrangian-eulerian finite element method for transient dynamic fluid-structure interactions.* Comput Methods Appl Mech Eng, 1982. **33**(1): p. 689-723.
78. van Loon, R., et al., *Comparison of various fluid–structure interaction methods for deformable bodies.* Comput Struct, 2007. **85**(11–14): p. 833-843.
79. Bavo, A.M., et al., *Fluid-Structure Interaction Simulation of Prosthetic Aortic Valves: Comparison between Immersed Boundary and Arbitrary Lagrangian-Eulerian Techniques for the Mesh Representation.* PLoS ONE, 2016. **11**(4): p. e0154517.
80. Peskin, C.S., *Numerical analysis of blood flow in the heart.* J Comput Phys, 1977. **25**(3): p. 220-252.
81. Jaiman, R., et al., *Combined interface boundary condition method for unsteady fluid–structure interaction.* Comput Methods Appl Mech Eng, 2011. **200**(1–4): p. 27-39.
82. Dang, H., Z. Yang, and Y. Li, *Accelerated loosely-coupled CFD/CSD method for nonlinear static aeroelasticity analysis.* Aerosp Sci Technol, 2010. **14**(4): p. 250-258.
83. Habchi, C., et al., *Partitioned solver for strongly coupled fluid–structure interaction.* Comput Fluid, 2013. **71**: p. 306-319.
84. Brown, A.G., et al., *Accuracy vs. computational time: Translating aortic simulations to the clinic.* J Biomech, 2012. **45**(3): p. 516-523.
85. He, T., *A CBS-based partitioned semi-implicit coupling algorithm for fluid–structure interaction using MCIBC method.* Comput Methods Appl Mech Eng, 2016. **298**: p. 252-278.
86. Mylavarapu, G., et al., *Computational Modeling of Airway Obstruction in Sleep Apnea in Down Syndrome: A Feasibility Study.* Otolaryngol Head Neck Surg, 2016. **155**(1): p. 184-187.
87. Spiegel, M., et al., *Tetrahedral vs. polyhedral mesh size evaluation on flow velocity and wall shear stress for cerebral hemodynamic simulation.* Comput Methods Biomech Biomed Engin, 2011. **14**(1): p. 9-22.
88. Menter, F.R., *Two-equation eddy-viscosity turbulence models for engineering applications.* AIAA J, 1994. **32**(8): p. 1598-1605.
89. Chen, Z.J. and A.J. Przekwas, *A coupled pressure-based computational method for incompressible/compressible flows.* J Comput Phys, 2010. **229**(24): p. 9150-9165.
90. Cheng, S., et al., *Viscoelastic properties of the tongue and soft palate using MR elastography.* J Biomech, 2011. **44**(3): p. 450-454.
91. Brown, E.C., et al., *Tongue stiffness is lower in patients with obstructive sleep apnea during wakefulness compared with matched control subjects.* Sleep, 2015. **38**(4): p. 537-44.
92. Greenleaf, J.F., M. Fatemi, and M. Insana, *Selected methods for imaging elastic properties of biological tissue.* Annu Rev Biomed Eng, 2003. **5**(1): p. 57-78.

93. Elad, D., R.D. Kamm, and A.H. Shapiro, *Tube law for the intrapulmonary airway.* J Appl Physiol, 1988. **65**(1): p. 7-13.
94. Fouke, J.M., et al., *Elastic characteristics of the airway wall.* J Appl Physiol, 1989. **66**(2): p. 962-967.
95. Shapiro, A.H., *Steady Flow in Collapsible Tubes.* J Biomech Eng-T ASME, 1977. **99**(3): p. 126-147.
96. Teng, Z., et al., *Study on Tracheal Collapsibility, Compliance, and Stress by Considering Nonlinear Mechanical Property of Cartilage.* Ann Biomed Eng, 2009. **37**(11): p. 2380-2389.
97. Isono, S., et al., *Static mechanics of the velopharynx of patients with obstructive sleep apnea.* J Appl Physiol, 1993. **75**(1): p. 148-154.
98. Isono, S., et al., *Anatomy of pharynx in patients with obstructive sleep apnea and in normal subjects.* J Appl Physiol, 1997. **82**(4): p. 1319-1326.
99. Amatoury, J., et al., *Onset of airflow limitation in a collapsible tube model: impact of surrounding pressure, longitudinal strain, and wall folding geometry.* J Appl Physiol, 2010. **109**(5): p. 1467-1475.
100. Subramaniam, D.R., et al., *Patient-Specific Identification Of Upper-Airway Tissue Compliance Using Medical Image Analysis*, in *American Thoracic Society 2014 International Conference B66. Novel and Traditional Lung Function Assessment* 2014, American Thoracic Society. p. A3564-A3564.
101. Nelson, L.E., et al., *The alpha2-adrenoceptor agonist dexmedetomidine converges on an endogenous sleep-promoting pathway to exert its sedative effects.* Anesthesiology, 2003. **98**(2): p. 428-36.
102. Ingrande, J. and H.J.M. Lemmens, *Dose adjustment of anaesthetics in the morbidly obese.* Briti J Anaesth, 2010. **105**(suppl 1): p. i16-i23.
103. Mahmoud, M., et al., *Effect of increasing depth of dexmedetomidine and propofol anesthesia on upper airway morphology in children and adolescents with obstructive sleep apnea.* J Clin Anesth, 2013. **25**(7): p. 529-541.
104. Issa, F.G. and C.E. Sullivan, *Upper airway closing pressures in obstructive sleep apnea.* J Appl Physiol, 1984. **57**(2): p. 520-527.
105. Pham, D.L., C. Xu, and J.L. Prince, *Current methods in medical image segmentation.* Annu Rev Biomed Eng, 2000. **2**(1): p. 315-337.
106. Shepp, L.A. and B.F. Logan, *The Fourier reconstruction of a head section.* IEEE T Nucl Sci, 1974. **21**(3): p. 21-43.
107. Kairaitis, K., et al., *Upper airway extraluminal tissue pressure fluctuations during breathing in rabbits.* J Appl Physiol, 2003. **95**(4): p. 1560-1566.
108. Kairaitis, K., et al., *Mandibular advancement decreases pressures in the tissues surrounding the upper airway in rabbits.* J Appl Physiol, 2006. **100**(1): p. 349-356.
109. Schwab, R.J., et al., *Upper airway and soft tissue anatomy in normal subjects and patients with sleep-disordered breathing. Significance of the lateral pharyngeal walls.* Am J Resp Crit Care, 1995. **152**(5): p. 1673-1689.
110. Barrera, J.E., *Sleep magnetic resonance imaging: Dynamic characteristics of the airway during sleep in obstructive sleep apnea syndrome.* Laryngoscope, 2011. **121**(6): p. 1327-1335.
111. Srodon, P.D., M.E. Miquel, and M.J. Birch, *Finite Element Analysis Animated Simulation of Velopharyngeal Closure.* Cleft Palate Craniofac J, 2011. **49**(1): p. 44-50.

112. Costantino, M.L., et al., *A numerical and experimental study of compliance and collapsibility of preterm lamb tracheae.* J Biomech, 2004. **37**(12): p. 1837-1847.
113. Eskandari, M., W. Kuschner, and E. Kuhl, *Patient-Specific Airway Wall Remodeling in Chronic Lung Disease.* Ann Biomed Eng, 2015: p. 1-14.
114. Flanagan, D.P. and T. Belytschko, *A uniform strain hexahedron and quadrilateral with orthogonal hourglass control.* Int J Numer Meth Eng, 1981. **17**(5): p. 679-706.
115. Berry, D.A., J.B. Moon, and D.P. Kuehn, *A Finite Element Model of the Soft Palate.* Cleft Palate Craniofac J, 1999. **36**(3): p. 217-223.
116. Stavness, I., J.E. Lloyd, and S. Fels, *Automatic prediction of tongue muscle activations using a finite element model.* J Biomech, 2012. **45**(16): p. 2841-2848.
117. Gerard, J.M., et al., *Non-linear elastic properties of the lingual and facial tissues assessed by indentation technique: Application to the biomechanics of speech production.* Med Eng Phys, 2005. **27**(10): p. 884-892.
118. Miller, K., et al., *Total Lagrangian explicit dynamics finite element algorithm for computing soft tissue deformation.* Commun Numer Meth En, 2007. **23**(2): p. 121-134.
119. Persak, S.C., et al., *Noninvasive estimation of pharyngeal airway resistance and compliance in children based on volume-gated dynamic MRI and computational fluid dynamics.* J Appl Physiol, 2011. **111**(6): p. 1819-1827.
120. Mihaescu, M., et al., *Computational Fluid Dynamics Analysis of Upper Airway Reconstructed from Magnetic Resonance Imaging Data.* Ann Otol Rhinol Laryngol, 2008. **117**(4): p. 303-309.
121. Mijailovich, S.M., et al., *Derivation of a finite-element model of lingual deformation during swallowing from the mechanics of mesoscale myofiber tracts obtained by MRI.* J Appl Physiol, 2010. **109**(5): p. 1500-1514.
122. Henke, K.G., *Upper airway muscle activity and upper airway resistance in young adults during sleep.* J Appl Physiol, 1998. **84**(2): p. 486-491.
123. Kairaitis, K., et al., *Pharyngeal mucosal wall folds in subjects with obstructive sleep apnea.* J Appl Physiol, 2015. **118**(6): p. 707-715.
124. Amatoury, J., et al., *Peripharyngeal tissue deformation and stress distributions in response to caudal tracheal displacement: pivotal influence of the hyoid bone?* J Appl Physiol, 2014. **116**(7): p. 746-756.
125. Subramaniam, D.R., et al., *Compliance Measurements of the Upper Airway in Pediatric Down Syndrome Sleep Apnea Patients.* Ann Biomed Eng, 2016. **44**(4): p. 873-885.
126. Subramaniam, D.R., et al., *Upper Airway Elasticity Estimation in Pediatric Down Syndrome Sleep Apnea Patients Using Collapsible Tube Theory.* Ann Biomed Eng, 2016. **44**(5): p. 1538-1552.
127. Prasad, R.N., et al., *Estimation of Airway Stiffness and Collapsibility in Children with Down Syndrome and Persistent Obstructive Sleep Apnea*, in *American Thoracic Society 2016 International Conference C109. PATHOGENESIS OF SDB: DOES IT MATTER?* 2016. p. A6375-A6375.
128. Geuzaine, C. and J.-F. Remacle, *Gmsh: A 3-D finite element mesh generator with built-in pre- and post-processing facilities.* Int J Numer Meth Eng, 2009. **79**(11): p. 1309-1331.
129. Järvinen, E., et al., *A method for partitioned fluid–structure interaction computation of flow in arteries.* Med Eng Phys, 2008. **30**(7): p. 917-923.

130. Inouye, J.M., et al., *Contributions of the Musculus Uvulae to Velopharyngeal Closure Quantified With a 3-Dimensional Multimuscle Computational Model.* Ann Plast Surg, 2016. **77**: p. S70-S75.
131. Lee, J., et al., *Semi-automatic segmentation for 3D motion analysis of the tongue with dynamic MRI.* Comput Med Imaging Graph, 2014. **38**(8): p. 714-724.
132. Shih, T.-H., et al., *A new k-ϵ eddy viscosity model for high reynolds number turbulent flows.* Comput Fluids, 1995. **24**(3): p. 227-238.
133. Wootton, D.M., et al., *Computational fluid dynamics upper airway effective compliance, critical closing pressure, and obstructive sleep apnea severity in obese adolescent girls.* J Appl Physiol, 2016. **121**(4): p. 925-931.
134. Sinha Roy, A., et al., *Air-puff associated quantification of non-linear biomechanical properties of the human cornea in vivo.* J Mech Behav Biomed Mater, 2015. **48**: p. 173-182.
135. van der Velden, W.C.P., et al., *Acoustic simulation of a patient's obstructed airway.* Comput Methods Biomech Biomed Engin, 2016. **19**(2): p. 144-158.
136. Ashaat, S. and A.M. Al-Jumaily, *Reducing upper airway collapse at lower continuous positive airway titration pressure.* J Biomech, 2016. **49**(16): p. 3915-3922.
137. Amatoury, J., et al., *Development and validation of a computational finite element model of the rabbit upper airway: simulations of mandibular advancement and tracheal displacement.* J Appl Physiol, 2016. **120**(7): p. 743-757.
138. Bathe, K.-J., E. Ramm, and E.L. Wilson, *Finite element formulations for large deformation dynamic analysis.* Int J Numer Meth Eng, 1975. **9**(2): p. 353-386.
139. Rashid, B., M. Destrade, and M.D. Gilchrist, *Mechanical characterization of brain tissue in compression at dynamic strain rates.* J Mech Behav Biomed Mater, 2012. **10**: p. 23-38.
140. Aycock, K.I., et al., *A Computational Method for Predicting Inferior Vena Cava Filter Performance on a Patient-Specific Basis.* J Biomech Eng, 2014. **136**(8): p. 081003-081003-13.
141. McConnell, K., et al., *Effect Of Dexmedetomidine On Upper Airway Collapsibility In Children With Down's Syndrome*, in *American Thoracic Society 2012 International Conference B70. SLEEP DISORDERED BREATHING: PATHOPHYSIOLOGY*. 2012, American Thoracic Society. p. A3595-A3595.
142. Birch, M.J. and P.D. Srodon, *Biomechanical Properties of the Human Soft Palate.* Cleft Palate Craniofac J, 2009. **46**(3): p. 268-274.
143. Malhotra, A., et al., *The Male Predisposition to Pharyngeal Collapse.* Am J Resp Crit Care 2002. **166**(10): p. 1388-1395.
144. Liu, Z.S., et al., *Snoring source identification and snoring noise prediction.* J Biomech, 2007. **40**(4): p. 861-870.
145. Vos, W., et al., *Correlation between severity of sleep apnea and upper airway morphology based on advanced anatomical and functional imaging.* J Biomech, 2007. **40**(10): p. 2207-2213.
146. Bates, A.J., et al., *Dynamics of airflow in a short inhalation.* J R Soc Interface, 2015. **12**(102).
147. Fabbri, S., et al., *Streptococcus mutans biofilm transient viscoelastic fluid behaviour during high-velocity microsprays.* J Mech Behav Biomed Mater, 2016. **59**: p. 197-206.

148. Luo, H., et al., *An immersed-boundary method for flow–structure interaction in biological systems with application to phonation.* J Comput Phys, 2008. **227**(22): p. 9303-9332.
149. Pelteret, J.P.V. and B.D. Reddy, *Computational model of soft tissues in the human upper airway.* Int J Numer Method Biomed Eng, 2012. **28**(1): p. 111-132.
150. Wei, W., et al., *Airflow behavior changes in upper airway caused by different head and neck positions: Comparison by computational fluid dynamics.* J Biomech, 2017. **52**: p. 89-94.
151. Wootton, D.M., et al. *Increased CFD Pharyngeal Airway Flow Resistance in Adolescent Girls with Polycystic Ovarian Syndrome and Obstructive Sleep Apnea Syndrome*. in *American Thoracic Society International Conference 2017 D30. NEW INSIGHTS INTO OBSTRUCTIVE SLEEP APNEA PATHOGENESIS*. 2017. American Thoracic Society.
152. Wagshul, M.E., et al., *Novel retrospective, respiratory-gating method enables 3D, high resolution, dynamic imaging of the upper airway during tidal breathing.* Magn Reson Med, 2013. **70**(6): p. 1580-1590.
153. Christen, D., et al., *Deformable image registration and 3D strain mapping for the quantitative assessment of cortical bone microdamage.* J Mech Behav Biomed Mater, 2012. **8**: p. 184-193.
154. Liao, D., J. Zhao, and H. Gregersen, *A novel 3D shape context method based strain analysis on a rat stomach model.* J Biomech, 2012. **45**(9): p. 1566-1573.
155. Phatak, N.S., et al., *Strain measurement in the left ventricle during systole with deformable image registration.* Med Image Anal, 2009. **13**(2): p. 354-361.
156. Subramaniam, D.R., et al., *Effect of airflow and material models on tissue displacement for surgical planning of pharyngeal airways in pediatric down syndrome patients.* J Mech Behav Biomed Mater, 2017. **71**: p. 122-135.
157. Qiu, J., et al., *A noninvasive approach to determine viscoelastic properties of an individual adherent cell under fluid flow.* J Biomech, 2014. **47**(6): p. 1537-1541.
158. Brown, E.C., et al., *Tongue Stiffness is Lower in Patients with Obstructive Sleep Apnea during Wakefulness Compared with Matched Control Subjects.* Sleep, 2015. **38**(4): p. 537-544.
159. Inouye, J.M., et al., *Contributions of the Musculus Uvulae to Velopharyngeal Closure Quantified With a 3-Dimensional Multimuscle Computational Model.* Ann Plast Surg, 2016. **77 Suppl 1**: p. S70-5.
160. Bilston, L.E. and S.C. Gandevia, *Biomechanical properties of the human upper airway and their effect on its behavior during breathing and in obstructive sleep apnea.* J Appl Physiol, 2014. **116**(3): p. 314-324.
161. Huang, Y., D.P. White, and A. Malhotra, *Use of Computational Modeling to Predict Responses to Upper Airway Surgery in Obstructive Sleep Apnea.* Laryngoscope, 2007. **117**(4): p. 648-653.
162. Zheng, X., et al., *A Computational Study of the Effect of False Vocal Folds on Glottal Flow and Vocal Fold Vibration During Phonation.* Ann Biomed Eng, 2009. **37**(3): p. 625-642.
163. Antiga, L., et al., *An image-based modeling framework for patient-specific computational hemodynamics.* Med Biol Eng Comput, 2008. **46**(11): p. 1097-1112.

164. Yap, C.H., X. Liu, and K. Pekkan, *Characterizaton of the Vessel Geometry, Flow Mechanics and Wall Shear Stress in the Great Arteries of Wildtype Prenatal Mouse.* PLoS ONE, 2014. **9**(1): p. e86878.
165. Piccinelli, M., et al., *A Framework for Geometric Analysis of Vascular Structures: Application to Cerebral Aneurysms.* IEEE Trans Med Imaging, 2009. **28**(8): p. 1141-1155.
166. Besl, P.J. and N.D. McKay, *A method for registration of 3-D shapes.* IEEE Trans Pattern Anal Mach Intell, 1992. **14**(2): p. 239-256.
167. Bruse, J.L., et al., *A statistical shape modelling framework to extract 3D shape biomarkers from medical imaging data: assessing arch morphology of repaired coarctation of the aorta.* BMC Med Imaging, 2016. **16**(1): p. 40.
168. Bruse, J.L., et al., *How successful is successful? Aortic arch shape after successful aortic coarctation repair correlates with left ventricular function.* J Thorac Cardiovasc Surg.
169. Bruse, J.L., et al., *Looks Do Matter! Aortic Arch Shape After Hypoplastic Left Heart Syndrome Palliation Correlates With Cavopulmonary Outcomes.* Ann Thorac Surg.
170. Auricchio, F., et al., *A simple framework to generate 3D patient-specific model of coronary artery bifurcation from single-plane angiographic images.* Comput Biol Med, 2014. **44**: p. 97-109.
171. Rosero, E.B., et al., *Agreement between methods of measurement of mean aortic wall thickness by MRI.* J Magn Reson Imaging, 2009. **29**(3): p. 576-582.
172. Passing, H. and Bablok, *A new biometrical procedure for testing the equality of measurements from two different analytical methods. Application of linear regression procedures for method comparison studies in clinical chemistry, Part I.* J Clin Chem Clin Biochem, 1983. **21**(11): p. 709-20.
173. Snedecor, G.W. and W.G. Cochran, *Statistical methods*. 1980: Iowa State University Press.
174. Warfield, S.K., K.H. Zou, and W.M. Wells, *Simultaneous truth and performance level estimation (STAPLE): an algorithm for the validation of image segmentation.* IEEE Trans Med Imaging, 2004. **23**(7): p. 903-21.
175. Wissmann, L., et al., *MRXCAT: Realistic numerical phantoms for cardiovascular magnetic resonance.* J Cardiovasc Magn Reson, 2014. **16**(1): p. 63.
176. van Ooij, P., et al., *Age-related changes in aortic 3D blood flow velocities and wall shear stress: Implications for the identification of altered hemodynamics in patients with aortic valve disease.* J Magn Reson Imaging, 2015: p. n/a-n/a.
177. Roccabianca, S., et al., *Quantification of regional differences in aortic stiffness in the aging human.* J Mech Behav Biomed Mater, 2014. **29**: p. 618-634.
178. Lin, A.E., B. Lippe, and R.G. Rosenfeld, *Further Delineation of Aortic Dilation, Dissection, and Rupture in Patients With Turner Syndrome.* Pediatrics, 1998. **102**(1): p. e12-e12.
179. Fazel, S.S., et al., *The aortopathy of bicuspid aortic valve disease has distinctive patterns and usually involves the transverse aortic arch.* J Thorac Cardiovasc Surg, 2008. **135**(4): p. 901-907.e2.
180. Kilner, P.J., et al., *Helical and retrograde secondary flow patterns in the aortic arch studied by three-directional magnetic resonance velocity mapping.* Circulation, 1993. **88**(5): p. 2235-2247.

181. Liu, X., Y. Fan, and X. Deng, *Effect of Spiral Flow on the Transport of Oxygen in the Aorta: A Numerical Study.* Ann Biomed Eng, 2010. **38**(3): p. 917-926.
182. Georgakarakos, E., et al., *The Role of Geometric Parameters in the Prediction of Abdominal Aortic Aneurysm Wall Stress.* Eur J Vasc Endovasc Surg, 2010. **39**(1): p. 42-48.
183. Valentín, A., et al., *Complementary vasoactivity and matrix remodelling in arterial adaptations to altered flow and pressure.* J R Soc Interface, 2009. **6**(32): p. 293-306.
184. Valentín, A. and J.D. Humphrey, *Evaluation of fundamental hypotheses underlying constrained mixture models of arterial growth and remodelling.* Philos Trans A Math Phys Eng Sci, 2009. **367**(1902): p. 3585-3606.
185. El Khoury, G., et al., *Repair of Bicuspid Aortic Valves in Patients With Aortic Regurgitation.* Circulation, 2006. **114**(1 suppl): p. I-610-I-616.
186. Goubergrits, L., et al., *The Impact of MRI-based Inflow for the Hemodynamic Evaluation of Aortic Coarctation.* Ann Biomed Eng, 2013. **41**(12): p. 2575-2587.
187. Singh, S.D., et al., *Aortic flow patterns before and after personalised external aortic root support implantation in Marfan patients.* J Biomech, 2016. **49**(1): p. 100-111.
188. Raffa, G.M., et al., *Early distal remodeling after elephant trunk repair of thoraco-abdominal aortic aneurysms.* J Biomech, 2016. **49**(12): p. 2398-2404.
189. Ku, D.N., *Blood Flow in Arteries.* Annu Rev Fluid Mech, 1997. **29**(1): p. 399-434.
190. Pasta, S., et al., *Difference in hemodynamic and wall stress of ascending thoracic aortic aneurysms with bicuspid and tricuspid aortic valve.* J Biomech, 2013. **46**(10): p. 1729-1738.
191. Wesseling, K.H., et al., *Computation of aortic flow from pressure in humans using a nonlinear, three-element model.* J Appl Physiol, 1993. **74**(5): p. 2566-2573.
192. Mitchell, G.F., et al., *Determinants of Elevated Pulse Pressure in Middle-Aged and Older Subjects With Uncomplicated Systolic Hypertension: The Role of Proximal Aortic Diameter and the Aortic Pressure-Flow Relationship.* Circulation, 2003. **108**(13): p. 1592-1598.
193. Horgan, O.C. and G. Saccomandi, *A description of arterial wall mechanics using limiting chain extensibility constitutive models.* Biomech Model Mechanobiol, 2003. **1**(4): p. 251-266.
194. Fung, Y.C., K. Fronek, and P. Patitucci, *Pseudoelasticity of arteries and the choice of its mathematical expression.* Am J Physiol Heart Circ Physiol, 1979. **237**(5): p. H620-H631.
195. Holzapfel, G.A., T.C. Gasser, and R.W. Ogden, *A New Constitutive Framework for Arterial Wall Mechanics and a Comparative Study of Material Models.* J Elast, 2000. **61**(1): p. 1-48.
196. Silver, F.H., D.L. Christiansen, and C.M. Buntin, *Mechanical properties of the aorta: a review.* Crit Rev Biomed Eng, 1989. **17**(4): p. 323-58.
197. Suzuki, T., et al., *Fluid structure interaction analysis reveals facial nerve palsy caused by vertebral-posterior inferior cerebellar artery aneurysm.* Comput Biol Med, 2015. **66**: p. 263-268.
198. Xenos, M., et al., *Progression of Abdominal Aortic Aneurysm Towards Rupture: Refining Clinical Risk Assessment Using a Fully Coupled Fluid–Structure Interaction Method.* Ann Biomed Eng, 2015. **43**(1): p. 139-153.

199. Liu, X., et al., *A numerical study on the flow of blood and the transport of LDL in the human aorta: the physiological significance of the helical flow in the aortic arch.* Am J Physiol Heart Circ Physiol, 2009. **297**(1): p. H163-H170.
200. Liu, X., et al., *Nitric Oxide Transport in Normal Human Thoracic Aorta: Effects of Hemodynamics and Nitric Oxide Scavengers.* PLoS ONE, 2014. **9**(11): p. e112395.
201. Crosetto, P., et al., *Fluid–structure interaction simulation of aortic blood flow.* Comput Fluid, 2011. **43**(1): p. 46-57.
202. Nestola, M.G.C., et al., *Computational comparison of aortic root stresses in presence of stentless and stented aortic valve bio-prostheses.* Comput Methods Biomech Biomed Engin, 2016: p. 1-11.
203. Subramaniam, D.R., et al., *Continuous measurement of aortic dimensions in Turner syndrome: a cardiovascular magnetic resonance study.* J Cardiovasc Magn Reson, 2017. **19**(1): p. 20.
204. Auricchio, F., et al., *Patient-specific analysis of post-operative aortic hemodynamics: a focus on thoracic endovascular repair (TEVAR).* Comput Mech, 2014. **54**(4): p. 943-953.
205. Pasta, S., et al., *Constitutive modeling of ascending thoracic aortic aneurysms using microstructural parameters.* Med Eng Phys, 2016. **38**(2): p. 121-130.
206. LaDisa, J.F., et al., *Computational Simulations for Aortic Coarctation: Representative Results From a Sampling of Patients.* J Biomech Eng, 2011. **133**(9): p. 091008-091008-9.
207. Childs, H., et al., *VisIt: An End-User Tool For Visualizing and Analyzing Very Large Data*, in *High Performance Visualization-Enabling Extreme-Scale Scientific Insight*, H.C. Wes Bethel, Charles Hansen, Editor. 2012, CRC Press. p. 357-372.
208. Wendell, D.C., et al., *The Impact of Cardiac Motion on Aortic Valve Flow Used in Computational Simulations of the Thoracic Aorta.* J Biomech Eng, 2016. **138**(9): p. 091001-091001-11.
209. Ha, H., et al., *The influence of the aortic valve angle on the hemodynamic features of the thoracic aorta.* Sci Rep, 2016. **6**: p. 32316.
210. Arnold, R., et al., *Magnetic resonance imaging 4-D flow-based analysis of aortic hemodynamics in Turner syndrome.* Pediatr Radiol, 2017. **47**(4): p. 382-390.
211. Liu, X., et al., *Effect of non-Newtonian and pulsatile blood flow on mass transport in the human aorta.* J Biomech, 2011. **44**(6): p. 1123-1131.
212. Rinaudo, A. and S. Pasta, *Regional variation of wall shear stress in ascending thoracic aortic aneurysms.* Proc Inst Mech Eng H, 2014. **228**(6): p. 627-638.
213. Tse, K.M., et al., *A computational fluid dynamics study on geometrical influence of the aorta on haemodynamics.* Eur J Cardiothorac Surg, 2013. **43**(4): p. 829-838.
214. Dolan, J.M., et al., *High Fluid Shear Stress and Spatial Shear Stress Gradients Affect Endothelial Proliferation, Survival, and Alignment.* Ann Biomed Eng, 2011. **39**(6): p. 1620-1631.
215. Bäck, M., et al., *Biomechanical factors in the biology of aortic wall and aortic valve diseases.* Cardiovasc Res, 2013. **99**(2): p. 232-241.
216. Pasta, S., et al., *In Silico Shear and Intramural Stresses are Linked to Aortic Valve Morphology in Dilated Ascending Aorta.* Eur J Vasc Endovasc Surg, 2017. **54**(2): p. 254-263.
217. Feintuch, A., et al., *Hemodynamics in the mouse aortic arch as assessed by MRI, ultrasound, and numerical modeling.* Am J Physiol Heart Circ Physiol, 2007. **292**(2): p. H884-H892.

218. Lantz, J. and M. Karlsson, *Large eddy simulation of LDL surface concentration in a subject specific human aorta.* J Biomech, 2012. **45**(3): p. 537-542.
219. Gravholt, C.H., et al., *Clinical practice guidelines for the care of girls and women with Turner syndrome: proceedings from the 2016 Cincinnati International Turner Syndrome Meeting.* Eur J Endocrinol, 2017. **177**(3): p. G1-G70.
220. Morbiducci, U., et al., *Inflow boundary conditions for image-based computational hemodynamics: Impact of idealized versus measured velocity profiles in the human aorta.* J Biomech, 2013. **46**(1): p. 102-109.
221. Reymond, P., et al., *Physiological simulation of blood flow in the aorta: Comparison of hemodynamic indices as predicted by 3-D FSI, 3-D rigid wall and 1-D models.* Med Eng Phys, 2013. **35**(6): p. 784-791.
222. Vignon-Clementel, I.E., et al., *Outflow boundary conditions for three-dimensional finite element modeling of blood flow and pressure in arteries.* Comput Methods Appl Mech Eng, 2006. **195**(29): p. 3776-3796.
223. Hsu, M.-C., et al., *Dynamic and fluid–structure interaction simulations of bioprosthetic heart valves using parametric design with T-splines and Fung-type material models.* Comput Mech, 2015. **55**(6): p. 1211-1225.
224. Piatti, F., et al., *Hemodynamic and thrombogenic analysis of a trileaflet polymeric valve using a fluid–structure interaction approach.* J Biomech, 2015. **48**(13): p. 3641-3649.
225. Cao, K., et al., *Simulations of morphotype-dependent hemodynamics in non-dilated bicuspid aortic valve aortas.* J Biomech, 2017. **50**: p. 63-70.
226. Weinberg, E.J., F.J. Schoen, and M.R.K. Mofrad, *A Computational Model of Aging and Calcification in the Aortic Heart Valve.* PLoS ONE, 2009. **4**(6): p. e5960.
227. Pasta, S., et al., *Effect of aneurysm on the mechanical dissection properties of the human ascending thoracic aorta.* J Thorac Cardiovasc Surg, 2012. **143**(2): p. 460-467.
228. Rajagopal, K., C. Bridges, and K.R. Rajagopal, *Towards an understanding of the mechanics underlying aortic dissection.* Biomech Model Mechanobiol, 2007. **6**(5): p. 345-359.
229. Long, C.C., et al., *Fluid–structure interaction simulations of the Fontan procedure using variable wall properties.* Int J Numer Method Biomed Eng, 2012. **28**(5): p. 513-527.
230. Raghavan, M.L., B. Ma, and M.F. Fillinger, *Non-Invasive Determination of Zero-Pressure Geometry of Arterial Aneurysms.* Ann Biomed Eng, 2006. **34**(9): p. 1414-1419.
231. Nayak, K.S., et al., *Cardiovascular magnetic resonance phase contrast imaging.* J Cardiovasc Magn Reson, 2015. **17**(1): p. 71.
232. Nayler, G.L., D.N. Firmin, and D.B. Longmore, *Blood flow imaging by cine magnetic resonance.* J Comput Assist Tomogr, 1986. **10**(5): p. 715-22.
233. Markl, M., P.J. Kilner, and T. Ebbers, *Comprehensive 4D velocity mapping of the heart and great vessels by cardiovascular magnetic resonance.* J Cardiovasc Magn Reson, 2011. **13**(1): p. 7.
234. Burk, J., et al., *Evaluation of 3D blood flow patterns and wall shear stress in the normal and dilated thoracic aorta using flow-sensitive 4D CMR.* J Cardiovasc Magn Reson, 2012. **14**(1): p. 84.
235. Entezari, P., et al., *From unicuspid to quadricuspid: the impact of aortic valve morphology on 3D hemodynamics.* J Cardiovasc Magn Reson, 2013. **15**(1): p. O79.
236. van der Palen, R.L.F., et al., *Altered aortic 3D hemodynamics and geometry in pediatric Marfan syndrome patients.* J Cardiovasc Magn Reson, 2017. **19**(1): p. 30.

237. Pirola, S., et al., *On the choice of outlet boundary conditions for patient-specific analysis of aortic flow using computational fluid dynamics.* J Biomech, 2017. **60**: p. 15-21.
238. Benim, A.C., et al., *Simulation of blood flow in human aorta with emphasis on outlet boundary conditions.* Appl Math Model, 2011. **35**(7): p. 3175-3188.
239. Bellhouse, B.J. and L. Talbot, *The fluid mechanics of the aortic valve.* J Fluid Mech, 2006. **35**(4): p. 721-735.
240. Antiga, L. and D.A. Steinman, *Robust and objective decomposition and mapping of bifurcating vessels.* IEEE Trans Med Imaging, 2004. **23**(6): p. 704-713.
241. Bluestein, D., et al., *Intraluminal thrombus and risk of rupture in patient specific abdominal aortic aneurysm – FSI modelling.* Comput Methods Biomech Biomed Engin, 2009. **12**(1): p. 73-81.
242. Nathan, D.P., et al., *Increased Wall Stress of Saccular Versus Fusiform Aneurysms of the Descending Thoracic Aorta.* Ann Vasc Surg, 2011. **25**(8): p. 1129-1137.
243. Prasad, A., et al., *A computational framework for investigating the positional stability of aortic endografts.* Biomech Model Mechanobiol, 2013. **12**(5): p. 869-887.
244. Liu, Q., J. Li, and J. Liu, *ParaView visualization of Abaqus output on the mechanical deformation of complex microstructures.* Comput Geosci, 2017. **99**: p. 135-144.
245. Molony, D.S., et al., *Fluid-structure interaction of a patient-specific abdominal aortic aneurysm treated with an endovascular stent-graft.* Biomed Eng Online, 2009. **8**(1): p. 24.
246. Soulis, J.V., et al., *Low Density Lipoprotein and Non-Newtonian Oscillating Flow Biomechanical Parameters for Normal Human Aorta.* Cardiol Res, 2016. **7**(2): p. 66-79.
247. Bieging, E.T., et al., *In vivo three-dimensional MR wall shear stress estimation in ascending aortic dilatation.* J Magn Reson Imaging, 2011. **33**(3): p. 589-597.
248. Martin, C. and W. Sun, *Simulation of long-term fatigue damage in bioprosthetic heart valves: effects of leaflet and stent elastic properties.* Biomech Model Mechanobiol, 2014. **13**(4): p. 759-770.
249. Lei, Y., et al., *Influence of virtual intervention and blood rheology on mass transfer through thoracic aortic aneurysm.* J Biomech, 2015. **48**(12): p. 3312-3322.
250. Shang, E.K., et al., *Impact of Wall Thickness and Saccular Geometry on the Computational Wall Stress of Descending Thoracic Aortic Aneurysms.* Circulation, 2013. **128**(11 suppl 1): p. S157-S162.
251. Yushkevich, P.A., et al., *User-guided 3D active contour segmentation of anatomical structures: Significantly improved efficiency and reliability.* NeuroImage, 2006. **31**(3): p. 1116-1128.
252. Möbius, J. and L. Kobbelt, *OpenFlipper: An Open Source Geometry Processing and Rendering Framework*, in *Curves and Surfaces: 7th International Conference, Avignon, France, June 24 - 30, 2010, Revised Selected Papers*, J.-D. Boissonnat, et al., Editors. 2012, Springer Berlin Heidelberg: Berlin, Heidelberg. p. 488-500.
253. Sorkine, O., et al. *Laplacian surface editing*. in *Proceedings of the 2004 Eurographics/ACM SIGGRAPH symposium on Geometry processing*. 2004. ACM.
254. Barsky, B.A. and T.D. DeRose, *Geometric continuity of parametric curves: three equivalent characterizations.* IEEE Comput Graph Appl, 1989. **9**(6): p. 60-69.

Publications

1. Subramaniam D. R., E. J. Gutmark, C. Trolle, K.H. Mortensen, S. Ringgaard, C. H. Gravholt, P. F. Backeljauw, I. Gutmark-Little, "Functional Characterization of Thoracic Aortic Disease in Turner Syndrome." (manuscript in preparation)

2. Subramaniam D. R., R. Arens, M.E. Wagshul, S. Sin, D.M. Wootton, E. J. Gutmark, "Biomechanics of the Soft-Palate in Sleep Apnea Patients with Polycystic Ovarian Syndrome." (manuscript submitted)

3. Subramaniam, D.R., Mylavarapu, G., Fleck, R.J., Amin, R.S., Shott, S.R., Gutmark, E.J., 2017. "Effect of airflow and material models on tissue displacement for surgical planning of pharyngeal airways in pediatric down syndrome patients." Journal of the Mechanical Behavior of Biomedical Materials 71, 122-135.

4. Subramaniam D. R., W. A. Stoddard, K. H. Mortensen, S. Ringgaard, C. Trolle, C. H. Gravholt, E. J. Gutmark, G. Mylavarapu, P. F. Backeljauw, I. Gutmark-Little, "Continuous measurement of aortic dimensions in Turner syndrome: a cardiovascular magnetic resonance study." Journal of Cardiovascular Magnetic Resonance 19(1):20.

5. Mylavarapu G., D. Subramaniam, R. Jonnagiri, E. J. Gutmark, R. J. Fleck, R. S. Amin, M. Mahmoud, S. L. Ishman and S. R. Shott. (2016). "Computational Modeling of Airway Obstruction in Sleep Apnea in Down Syndrome: A Feasibility Study." Otolaryngology – Head and Neck Surgery 155(1):184-7.

6. Subramaniam, D. R., G. Mylavarapu, K. McConnell, R. J. Fleck, S. R. Shott, R. S. Amin, E. J. Gutmark. (2016). "Upper Airway Elasticity Estimation in Pediatric Down Syndrome Sleep Apnea Patients Using Collapsible Tube Theory." Annals of Biomedical Engineering 44(5):1538-52.

7. Subramaniam, D. R., G. Mylavarapu, K. McConnell, R. J. Fleck, S. R. Shott, R. S. Amin, E. J. Gutmark. (2016). "Compliance Measurements of the Upper Airway in Pediatric Down Syndrome Sleep Apnea Patients." Annals of Biomedical Engineering 44(4):873-85.

Conference Presentations and Posters

1. D.R. Subramaniam, E.J. Gutmark, C. Trolle, S. Ringgaard, C.H. Gravholt, K.H. Mortensen, P.F. Backeljauw, I. Gutmark-Little, Transient Aortic Blood Flow Modeling for Cardiovascular Risk Assessment in Turner Syndrome in: Biomedical Engineering Society (BMES) 2017 Annual Meeting Phoenix, AZ.

2. D.R. Subramaniam, E.J. Gutmark, I. Gutmark-Little, Evaluating the Influence of Vessel Wall Thickness and Blood Rheology on Hemodynamic and Mechanical Variables in Turner Syndrome in: 2017 Dayton Cincinnati Aerospace Sciences Symposium (DCASS) Dayton, OH.

2. D.R. Subramaniam, E.J. Gutmark, C. Trolle, S. Ringgaard, C.H. Gravholt, P.F. Backeljauw, I. Gutmark-Little, Patient-Specific Computational Modeling of Aortic Blood Flow in Turner Syndrome in: Biomedical Engineering Society (BMES) 2016 Annual Meeting Minneapolis, MN.

3. D.R. Subramaniam, E.J. Gutmark, G. Mylavarapu, C. Trolle, S. Ringgaard, C.H. Gravholt, P.F. Backeljauw, I. Gutmark-Little, Longitudinal Comparison of Aortic Flow Variables and Mechanical Stresses in Turner Syndrome in: Biomedical Engineering Society (BMES) 2016 Annual Meeting Minneapolis, MN.

4. I. Gutmark-Little, D.R. Subramaniam, G. Mylavarapu, W.A. Stoddard, E.J. Gutmark, C. Trolle, S. Ringgaard, P.F. Backeljauw, K.H. Mortensen, C.H. Gravholt, Monitoring for Aortic Dilatation Using Continuous Aortic Dimensions in Turner Syndrome in: ENDO 2016 Annual Meeting Boston, MA.

5. D.R. Subramaniam, E.J. Gutmark, G. Mylavarapu, I. Gutmark-Little, Evaluating the influence of vessel elasticity on hemodynamic variables in healthy and diseased aortae in: 2016 Dayton Cincinnati Aerospace Sciences Symposium (DCASS) Dayton, OH.

6. W.A. Stoddard, G. Mylavarapu, D.R. Subramaniam, E.J. Gutmark, C.H. Gravholt, C. Trolle, S. Ringgaard, P.F. Backeljauw, I. Gutmark-Little, Analysis of Automatically Sampled Aorta Geometry in Turner Syndrome Patients in: Biomedical Engineering Society (BMES) 2015 Annual Meeting Tampa, FL.

7. D.R. Subramaniam, G. Mylavarapu, R.J. Fleck, R.S. Amin, S.R. Shott, E.J. Gutmark, Assessing The Effectiveness Of Upper Airway Surgery Using Computational Modeling Of Airway Collapse in: Biomedical Engineering Society (BMES) 2015 Annual Meeting Tampa, FL.

8. D.R. Subramaniam, G. Mylavarapu, E.J. Gutmark, A Novel CFD-FEA Approach to Evaluate

Mechanical Properties of Pharyngeal Airway Tissue from Magnetic Resonance Images in: 2015 Dayton Cincinnati Aerospace Sciences Symposium (DCASS) Dayton, OH.

9. G. Mylavarapu, D.R. Subramaniam, E.J. Gutmark, R.J. Fleck, R.S. Amin, S. L. Ishman, S.R. Shott, Virtual Surgery for Children with OSA: Computational Modeling of the Airway for Surgical Planning in: 2015 Triological Combined Sections Meeting Coronado, CA.

10. D.R. Subramaniam, G. Mylavarapu, R.J. Fleck, S.R. Shott, R.S. Amin, E.J. Gutmark, Estimation of Soft Tissue Elasticity surrounding Upper Airway from MR Imaging and Tube Law Method in: Biomedical Engineering Society (BMES) 2014 Annual Meeting San Antonio, TX.

11. D.R. Subramaniam, G. Mylavarapu, J. Chen, R.J. Fleck, R.S. Amin, S.R. Shott, E.J. Gutmark, Patient Specific Identification of Upper-Airway Tissue Compliance Using Medical Image Analysis in: 2014 American Thoracic Society (ATS) International Conference San Diego, CA.

12. D.R. Subramaniam, G. Mylavarapu, E.J. Gutmark, Estimation of soft tissue compliance in the upper airway and its relation to clinically relevant parameters in: 2014 Dayton Cincinnati Aerospace Sciences Symposium (DCASS) Dayton, OH.

13. D.R. Subramaniam, E.J. Gutmark, An Image Processing and Edge Detection Toolbox for Biomedical and Engineering Image Analysis in: 2013 Dayton Cincinnati Aerospace Sciences Symposium (DCASS) Dayton, OH.